

TECHNISCHE UNIVERSITÄT MÜNCHEN

Fakultät für Medizin

# Magnetic Resonance Imaging of Bone with Ultrashort Echo Time

Sophia Kronthaler

Vollständiger Abdruck der von der Fakultät für Medizin der Technischen Universität München zur Erlangung des akademischen Grades einer

Doktorin der Naturwissenschaften (Dr. rer. nat.)

genehmigten Dissertation.

Vorsitz: Prof. Dr. Gabriele Multhoff

Prüfer\*innen der Dissertation:

1. Prof. Dimitrios Karampinos, Ph. D.
2. Prof. Dr. Björn H. Menze
3. Assoc. Prof. Edwin H. G. Oei, Ph. D.

Die Dissertation wurde am 06.10.2022 bei der Technischen Universität München eingereicht und durch die Fakultät für Medizin am 16.05.2023 angenommen.

# Abstract

Osteoporosis is a common disease characterized by trabecular bone loss and increased bone fracture risk at proximal skeletal sites, resulting in decreased quality of life for patients and significant socioeconomic healthcare costs. Although there is a strong clinical need for osteoporosis screening, current methods are invasive and have limitations in diagnostic precision and fracture risk prediction. Magnetic resonance imaging (MRI) is a non-invasive technique that can measure a wide range of quantitative parameters that are directly related to fundamental tissue properties and are candidates for magnetic resonance (MR) biomarkers in a variety of diseases. A particular category of MRI acquisition techniques with so-called ultrashort echo time (UTE) imaging can sample the MRI signal of bone before it is lost due to transverse relaxation. UTE imaging is a powerful tool for measuring signals from tissues with short  $T_2^*$  relaxation times ( $T_2^* \ll 1$  ms) that are not detectable with conventional MRI techniques. State-of-the-art UTE MRI techniques have recently been proposed as a potential alternative to x-ray based imaging modalities that either require a high radiation dose or can fail to predict fracture risk in osteoporosis screening.

The present cumulative thesis bundles three journal publications in the field of  $u\tau e$  MRI. The first two publications focused on qualitative imaging to improve radiological diagnostics and the last one addressed quantitative imaging in the context of the use of quantitative biomarkers in osteoporosis research.

In particular, the first publication studied qualitative high-resolution UTE imaging of spinal fractures and specifically the importance of accurate knowledge of the gradient waveform in this context. The artifacts caused by deviations in the readout gradient were investigated and subsequently corrected using a gradient impulse response function (GIRF). Previously, no systematic investigation of the impact of gradient imperfections in high-resolution UTE musculoskeletal (MSK) imaging had been conducted. At first, trajectory errors were analyzed and corrected using simulations and phantom measurements. Thereafter, in a study of spine fractures, a comparison of UTE in vivo spine images with computed tomography (CT) images confirmed the diagnostic value of an elaborate UTE image correction method for high-resolution imaging.

The second publication focused on rapid qualitative imaging of short  $T_2^*$  tissues while simultaneously imaging water and fat. Therefore, the original concept of Dixon single-echo water-fat separation was extended to UTE imaging and a novel sUTE-Dixon-susceptibility weighted imaging (SWI) method was developed. The proposed method allows for the removal of unwanted low-frequency background phases, to perform a separation of water and fat, and SWI processing from a single echo complex UTE image. The formulated smoothness-constrained inverse problem solves the water-fat problem while removing undesirable low-frequency phase terms. As a result, no additional calibration scans are required to remove unwanted phase components, as were previously required. Another novel aspect of the formulation is the use of a tissue mask in the regularizer, and phase scaling to prevent phase wraps during the undesirable low-frequency phase estimation update steps. The proposed method was used in a thoracolumbar spine study which investigated vertebral fractures and edema replacing several MR sequences and an additional CT examination with a single UTE sequence. The study

demonstrated that the proposed method improved radiological assessment and diagnosis of fractures as well as edema without the need for an additional CT scan.

Finally, the third journal publication explored the feasibility of extracting quantitative biomarkers at short echo times (TEs), which add to the quantitative imaging of trabecular bone to assess bone health. Thus, UTE imaging was used to assess the influence of local field inhomogeneities on the signal of trabecularized bone marrow at short TE. Previous work predicted a Gaussian signal decay behavior at short TEs through simulations and theoretical analysis. This study is the first in vivo measurement and analysis of signal at short TEs in trabecular bone in the presence of fat. Furthermore, realistic simulations were carried out using masks generated from real trabecular bone structures. Finally, the influence of a Gaussian decay on  $R_2^*$  and proton density fat fraction (PDFF) mapping was investigated in Cartesian scans for bone marrow chemical shift encoding (CSE)-MRI at 3T. The study demonstrated, that  $R_2^*$  can be underestimated when using short TEs and a water-fat model with an exponential  $R_2^*$  decay model in multi-TE gradient echo (GRE) acquisitions of trabecularized bone marrow.

In conclusion, the methods developed in this thesis improve bone imaging both qualitatively and quantitatively. The developed techniques presented in the first and second publication were and are being used in ongoing research investigations and medical studies that include CT-like imaging and qualitative bone imaging. The results presented in the third publication lay a foundation for quantitative imaging of trabecular bone, which is valuable in future study of trabecular bone and development of quantitative biomarkers for osteoporosis screening.

# List of Included Journal Publications

The present dissertation is based on the following three journal publications:

- JP-I **Kronthaler, S.**, Rahmer, J., Börnert, P., Makowski, M.R., Schwaiger, B.J., Gersing, A.S., Karampinos, D.C., Trajectory correction based on the gradient impulse response function improves high-resolution UTE imaging of the musculoskeletal system. *Magn Reson Med.* 2021; 85: 2001– 2015. doi:10.1002/mrm.28566
- JP-II **Kronthaler, S.**, Boehm, C., Feuerriegel, G., Börnert, P., Katscher, U., Weiss, K., Makowski, M.R., Schwaiger, B.J., Gersing, A.S., Karampinos, D.C., Assessment of vertebral fractures and edema of the thoracolumbar spine based on water-fat and susceptibility-weighted images derived from a single ultra-short echo time scan. *Magn Reson Med.* 2022; 87: 1771– 1783. doi:10.1002/mrm.29078
- JP-III **Kronthaler, S.**, Diefenbach M.N., Feuerriegel, G., Boehm, C., Zamskiy, M., Makowski, M.R., Baum, T., Sollmann, N., Karampinos, C. D., On quantification errors of  $R_2^*$  and proton density fat fraction mapping in trabecularized bone marrow in the static dephasing regime. *Magn Reson Med.* 2022; 88( 3): 1126- 1139. doi:10.1002/mrm.29279

The above three journal publications are referred to as JP-I, JP-II and JP-III, respectively. Please refer to Chapter 7 for publication abstracts.

# List of Related Publications

The author contributed also to the following subject-related journal publications (ordered by year of appearance):

- J10 Feuerriegel, G.C., **Kronthaler, S.**, Boehm, C., Renz, M., Leonhardt, Y., Gassert, F., Foreman, S.C., Weiss, K., Wurm, M., Liebig, T., Makowski, M.R., Schwaiger, B.J., Karampinos, D.C., Gersing, A.S., Diagnostic value of water-fat-separated images and CT-like susceptibility-weighted images extracted from a single ultrashort echo time sequence for the evaluation of vertebral fractures and degenerative changes of the spine. *European Radiology* epub. (2022)
- J9 Leonhardt, Y., **Kronthaler, S.**, Feuerriegel, G., Karampinos, D.C., Schwaiger, B.J., Pfeiffer, D., Makowski, M.R., Koerte, I.K., Liebig, T., Woertler, K., Steinborn, M.-M., Gersing, A.S., CT-like MR-derived Images for the Assessment of Craniosynostosis and other Pathologies of the Pediatric Skull. *Clinical Neuroradiology* epub. (2022)
- J8 Sollmann, N., Kirschke, J.S., **Kronthaler, S.**, Boehm, C., Dieckmeyer, M., Vogele, D., Kloth, C., Lisson, C.G., Carballido-Gamio, J., Link, T.M., Karampinos, D.C., Karupppasamy, S., Beer, M., Krug, R., Baum, T., Imaging of the Osteoporotic Spine – Quantitative Approaches in Diagnostics and for the Prediction of the Individual Fracture Risk. *RoFo* epub. (2022)
- J7 Feuerriegel, G.C., Kopp, F.K., Pfeiffer, D., Pogorzelski, J., Wurm, M., Leonhardt, Y., Boehm, C., **Kronthaler, S.**, Karampinos, D.C., Neumann, J., Schwaiger, B.J., Makowski, M.R., Woertler, K., Gersing, A.S., Evaluation of MR-derived simulated CT-like images and simulated radiographs compared to conventional radiography in patients with shoulder pain: a proof-of-concept study. *BMC Musculoskeletal Disorders*. 23:122. (2022)
- J6 Gassert, F.T., Kufner, A., Gassert, F.G., Leonhardt, Y., **Kronthaler, S.**, Schwaiger, B.J., Boehm, C., Makowski, M.R., Kirschke, J.S., Baum, T., Karampinos, D.C., Gersing, A.S., MR-based proton density fat fraction (PDFFF) of the vertebral bone marrow differentiates between patients with and without osteoporotic vertebral fractures. *Osteoporosis International*. 33:487–496. (2022)
- J5 Probst, F.A., Burian, E., Malenova, Y., Lyutskanova, P., Stumbaum, M.J., Ritschl, L.M., **Kronthaler, S.**, Karampinos, D.C., Probst, M., Geometric accuracy of magnetic resonance imaging – derived virtual 3-dimensional bone surface models of the mandible in comparison to computed tomography and cone beam computed tomography: A porcine cadaver study. *Clinical Implant Dentistry and Related Research*. 23(5): 779–788. (2021)
- J4 Leonhardt, Y., Gassert, F.T., Feuerriegel, G., Gassert, F.G., **Kronthaler, S.**, Boehm, C., Kufner, A., Ruschke, S., Baum, T., Schwaiger, B.J., Makowski, M.R., Karampinos,

D.C., Gersing, A.S., Vertebral bone marrow T2\* mapping using chemical shift encoding-based water-fat separation in the quantitative analysis of lumbar osteoporosis and osteoporotic fractures. *Quantitative Imaging in Medicine and Surgery*. 11(8):3715–3725. (2021)

J3 Schwaiger, B.J., Schneider, C., **Kronthaler, S.**, Gassert, F.T., Böhm, C., Pfeiffer, D., Baum, T., Kirschke, J.S., Karampinos, D.C., Makowski, M.R., Woertler, K., Wurm, M., Gersing, A.S., CT-like images based on T1 spoiled gradient-echo and ultra-short echo time MRI sequences for the assessment of vertebral fractures and degenerative bone changes of the spine. *European Radiology*. 31:4680–4689. (2021)

J2 Sollmann, N., Löffler, M.T., **Kronthaler, S.**, Böhm, C., Dieckmeyer, M., Ruschke, S., Kirschke, J.S., Carballido-Gamio, J., Karampinos, D.C., Krug, R., Baum, T., MRI-Based Quantitative Osteoporosis Imaging at the Spine and Femur. *Journal of Magnetic Resonance Imaging*. 54:12–35. (2020)

J1 Gersing, A.S., Bodden, J., Neumann, J., Diefenbach, M.N., **Kronthaler, S.**, Pfeiffer, D., Knebel, C., Baum, T., Schwaiger, B.J., Hock, A., Rummeny, E.J., Woertler, K., Karampinos, D.C., Accelerating anatomical 2D turbo spin echo imaging of the ankle using compressed sensing. *European Journal of Radiology*. 118:277–284. (2019)

The author contributed also to the following subject-related conference abstracts (ordered by year of appearance):

C18 **Kronthaler, S.**, Boehm, C., Weiss, K., Makowski, M. R., Karampinos, D. C., On quantification errors of R2\* and PDFf mapping in trabecularized bone marrow induced by the static dephasing regime, in: Proc of 29th Scientific Meeting of ISMRM, Virtual Conference, p. 443, [oral presentation] (2021) **ISMRM Summa Cum Laude Merit Award**

C17 **Kronthaler, S.**, Boehm, C., Börnert, P., Katscher, U., Weiss, K., Makowski, M. R., Schwaiger, B. J., Gersing, A. S., Karampinos, D. C., Simultaneous assessment of vertebral fractures and edema of the thoracolumbar spine on water-fat and SW images derived from a single-TE UTE scan, in: Proc of 29th Scientific Meeting of ISMRM, Virtual Conference, p. 527, [oral presentation] (2021)

C16 Boehm, C., Diefenbach, M. N., **Kronthaler, S.**, Meineke, J., Weiss, K., Makowski, M. R., Karampinos, D. C., Quantitative susceptibility mapping in water-fat regions using in-phase echoes introduces significant quantification bias, in: Proc of 29th Scientific Meeting of ISMRM, Virtual Conference, p. 3972, [digital poster] (2021)

C15 Boehm, C., Sollmann, N., Meineke, J., **Kronthaler, S.**, Ruschke, S., Dieckmeyer, M., Weiss, K., Zimmer, C., Makowski, M. R., Baum, T., Karampinos, D. C., Preconditioned water-fat total field inversion: application to spine quantitative susceptibility mapping (QSM), in: Proc of 29th Scientific Meeting of ISMRM, Virtual Conference, p. 792, [oral presentation] (2021)

C14 Zamskiy, M., **Kronthaler, S.**, Weidlich, D., Ball, I., Gersing, A.S., Makowski, M.R., Herzen, J., Karampinos, D.C., Bone imaging of the spine and pelvis using an improved 3D adiabatic inversion recovery-prepared ultrashort TE sequence at 3T, in: Proc. of ESMRMB 2020, Virtual Conference, p. L01.36, [lightning talk] (2020)

- C13 **Kronthaler, S.**, Rahmer, J., Börnert, P., Gersing, A.S., Schwaiger, B.J., Krug, R., Karampinos, D.C., Bias and correction method of UTE trajectory errors in the depiction and relaxometry of deep articular cartilage, in: Proc of 28th Scientific Meeting of ISMRM, Virtual Conference, p. 2755, [digital poster] (2020)
- C12 **Kronthaler, S.**, Böhm, C., Weidlich, D., Diefenbach, M.N., Karampinos, D.C., Simultaneous imaging of trabecular and cortical bone by analyzing the multi-echo signal decay at UTEs and conventional TEs, in: Proc of 28th Scientific Meeting of ISMRM, Virtual Conference, p. 2767, [digital poster] (2020)
- C11 Böhm, C., Weidlich, D., **Kronthaler, S.**, Karampinos, D.C., On the carbon footprint of ISMRM's Annual Meeting: analysis and implications to the ISMRM 2020, in: Proc of 28th Scientific Meeting of ISMRM, Virtual Conference, p. 4156, [digital poster] (2020)
- C10 Böhm, C., **Kronthaler, S.**, Meineke, M.N.D.J., Karampinos, D.C., Sampling and modeling UTE signals is important to estimate bone marrow susceptibility, in: Proc of 28th Scientific Meeting of ISMRM, Virtual Conference, p. 3212, [digital poster] (2020)
- C9 Böhm, C., Oscanoa, J., **Kronthaler, S.**, Diefenbach, M.N., Gersing, A., Meineke, J., Karampinos, D.C., Highly accelerated compressed-sensing-based field-mapping is possible for body QSM applications, in: Proc of 28th Scientific Meeting of ISMRM, Virtual Conference, p. 3209, [digital poster] (2020)
- C8 Zöllner, C., **Kronthaler, S.**, Ruschke, S., Eggers, H., Rahmer, J., Börnert, P., Braren, R.F., Franz, D., Karampinos, D.C., Correcting gradient chain-induced fat quantification errors in multi-echo SoS acquisition using the gradient impulse response function, in: Proc of 28th Scientific Meeting of ISMRM, Virtual Conference, p. 0517, [oral-power pitch] (2020) **ISMRM Magna Cum Laude Merit Award**
- C7 Zöllner, C., **Kronthaler, S.**, Ruschke, S., Rahmer, J., Peeters, J.M., Eggers, H., Börnert, P., Braren, R.F., Karampinos, D.C., Trajectory correction in high-resolution gated golden-angle radial Dixon imaging using the gradient impulse response function, in: Proc of 28th Scientific Meeting of ISMRM, Virtual Conference, p. 3387, [digital poster] (2020)
- C6 **Kronthaler, S.**, Rahmer J., Börnert P., Karampinos D.C., Trajectory correction in high-resolution ultrashort echo-time (UTE) imaging based on the gradient impulse response function (GIRF) improves MSK image quality, in: ISMRM Workshop on Data Sampling and Image Reconstruction, Sedona, Arizona, USA, p.28, [poster] (2020)
- C5 Zöllner, C., **Kronthaler, S.**, Ruschke, S., Eggers, H., Rahmer, J., Börnert, P., Karampinos, D.C., Correcting gradient chain-induced blurring and quantification errors in multi-echo SoS Dixon acquisition using the gradient impulse response function, in: ISMRM Workshop on Data Sampling and Image Reconstruction, Sedona, Arizona, USA, p. 28, [oral presentation] (2020)
- C4 Zöllner, C., **Kronthaler, S.**, Boehm, C., Ruschke, S., Diefenbach, M., Franz, D., Karampinos, D.C., Fat deblurring in golden angle radial stack-of-stars multi-echo gradient echo for navigator-gated high-resolution water-fat imaging, in: ISMRM Workshop on MRI of Obesity and Metabolic Disorders, Singapore, [oral presentation] (2019)

- C3 **Kronthaler, S.**, Rahmer, J., Börnert, P., Karampinos, D.C., Trajectory correction for ultrashort echo-time (UTE) imaging based on the measurement of the gradient impulse response function (GIRF) with a thin-slice method, in: Proc of 27th Scientific Meeting of ISMRM, Montreal, Canada, p. 0924, [power pitch poster] (2019) **ISMRM Magna Cum Laude Merit Award**
- C2 Zöllner, C., **Kronthaler, S.**, Boehm, C., Ruschke, S., Diefenbach, M., Franz, D., Hock, A., Beck, G.M., Peeters, J.M., Karampinos, D.C., Fat deblurring in golden angle radial stack-of-stars multi-echo gradient echo for navigator-gated high-resolution water-fat imaging, in: Proc of 36th Annual Meeting of ESMRMB, Rotterdam, Netherlands. [oral presentation] (2019)
- C1 **Kronthaler, S.**, Diefenbach, M.N., Ruschke, S., Meineke, J., Eggers, H., Boernert, P., Karampinos, D.C., Time interleaved multi-gradient-echo imaging with UTE and non-UTE sampling for simultaneous PDFP, T2\* and magnetic susceptibility mapping of cortical bone, in: Proc of 26th Scientific Meeting of ISMRM, Paris, France, p. 5157, [electronic poster] (2018)



# Contents

<b>Abstract</b>	<b>I</b>
<b>List of Included Journal Publications</b>	<b>III</b>
<b>List of Related Publications</b>	<b>IV</b>
<b>1 Introduction</b>	<b>1</b>
1.1 Clinical Relevance . . . . .	1
1.2 Thesis Purpose . . . . .	2
1.3 Thesis Structure . . . . .	3
<b>2 Importance of Bone Imaging in the Context of Osteoporosis</b>	<b>4</b>
2.1 Introduction to Bone Biology and Physiology . . . . .	4
2.2 Osteoporosis Overview . . . . .	6
2.3 Measuring Bone Quality . . . . .	7
<b>3 Ultrashort Echo Time Imaging</b>	<b>11</b>
3.1 Fundamentals of Short $T_2$ MRI . . . . .	11
3.2 UTE Sequence Aspects . . . . .	15
3.3 UTE Imaging of Bone . . . . .	19
<b>4 Water-Fat Separation Techniques</b>	<b>22</b>
4.1 UTE Multi-TE Sequences . . . . .	22
4.2 Signal Models for Water-Fat Separation . . . . .	23
4.3 Water-Fat Separation using CSE-MRI . . . . .	24
4.4 Water-Fat Separation in Short $T_2/T_2^*$ Tissue . . . . .	25
4.5 Fat Suppression with CSE-Based Methods . . . . .	25
4.6 Single-TE Dixon Methods . . . . .	26
<b>5 Radial Sampling of k-space</b>	<b>28</b>
5.1 Nyquist Theorem and Undersampling . . . . .	28
5.2 Readout Oversampling . . . . .	29
5.3 Non-Cartesian Reconstruction . . . . .	30
5.4 Motion Robustness . . . . .	31
5.5 Off-Resonance Sensitivity . . . . .	32
5.6 Scan Time and Acceleration . . . . .	32
<b>6 Compliance with Ethical Standards</b>	<b>35</b>
<b>7 Comprising Journal Publications</b>	<b>36</b>
7.1 Journal Publication I . . . . .	36
7.2 Journal Publication II . . . . .	53
7.3 Journal Publication III . . . . .	68

<b>8 Discussion</b>	<b>84</b>
8.1 Review of Existing Literature . . . . .	84
8.2 Present Work . . . . .	88
8.3 Perspectives . . . . .	92
<b>9 Conclusion</b>	<b>93</b>
<b>Acknowledgments</b>	<b>94</b>
<b>List of Abbreviations</b>	<b>96</b>
<b>List of Figures</b>	<b>99</b>
<b>List of Tables</b>	<b>102</b>
<b>Bibliography</b>	<b>103</b>

# 1 Introduction

Tomographic imaging techniques provide a view of the internal structure of the human body and are therefore an essential part of modern medicine. Among many existing techniques, magnetic resonance imaging (MRI) is a technique to image the human body non-invasively. MRI emerged from several fundamental inventions made in the 1970s by Raymond Damadian who discovered different relaxation times in mouse tumors [1], Paul Lauterbur who laid the foundation for spatial encoding [2], Sir Peter Mansfield who invented selective excitation [3], Richard Ernst who introduced two-dimensional (2D) Fourier transform (FT) imaging [4], and finally Hugh Clow and Ian Young who produced the first published human head image. Due to problems of low signal intensity and high sensitivity to motion, body magnetic resonance (MR) was not really established until the 1990s. Advances and innovations on hardware, sequence design and faster computational power accelerated the development during the last decades. Aside from imaging anatomy and pathology, MR can nowadays be used to investigate organ function, to perform real-time imaging, to study in vivo chemistry, and even to conduct brain activation studies. The breakthrough of MRI was further supported by its powerful multi-contrast ability. MRI allows to observe a wide range of different parameters including proton density, susceptibility, diffusion, flow, temperature and even more complex quantities like tissue perfusion, permittivity and conductivity. MRI offers not only high spatial resolution but also excellent soft-tissue contrast. Because of these advantages, MRI is nowadays recognized as the leading modality for diagnostic imaging of numerous common diseases, in particular cancer and stroke. Particularly, the absence of ionizing radiation makes MR a valuable tool in both clinical and research settings. The signal detected in MRI emerges from the tissue itself and is not generated externally. In contrast computed tomography (CT), measures the attenuation of x-ray beams as they pass through the tissue. The examination procedure with MR does not pose a hazard to the patient's health, which is particularly valuable for patients who receive long-term monitoring after therapy and is thus preferable to other imaging modalities that use x-rays.

## 1.1 Clinical Relevance

Osteoporosis is a metabolic bone disorder that affects around over 200 million people [5] and is associated with an extraordinary burden for healthcare systems. Osteoporosis is more common in the elderly and bone fractures result in excess morbidity and mortality in elderlies. The disease is characterized by low bone mass, which makes bones fragile and susceptible to fractures. Therefore, bone constitution, geometry, and quality are critical in determining the fracture risk. Despite the availability of numerous effective treatments, osteoporosis is regularly undertreated and underestimated, partly because it is a clinically silent disease until it manifests itself in the form of fractures. Many elderly patients are not screened for osteoporosis and therefore remain untreated. Consequently, screening, long-term monitoring and management of risk factors for osteoporosis are essential to avoiding both physical and financial burdens. Aside from osteoporosis, degenerative changes to vital bone structure like

in the spine have significant medical and socioeconomic implications. According to Parenteau et al. [6], a large percentage of the population has radiological signs of spinal degeneration, which are typically found in the cervical or lumbar spine. Therefore, the assessment of bone constitution and bone health is highly desirable to improve the screening and long-term monitoring of patients, especially as they undergo interventions. However, the measurement of bone mineral density normally requires ionizing radiation such as x-ray imaging, dual-energy x-ray absorptiometry (DXA) or CT. In particular, DXA which is nowadays the most commonly used method for osteoporosis prediction, has a low accuracy in predicting fracture risk and frequently misclassifies osteoporotic bone as healthy [7].

## 1.2 Thesis Purpose

In almost all forms of proton MRI, that is used in clinical practice, healthy adult cortical bone has a short  $T_2$  and shows no signal. The lack of signal has previously been used to visualize bone with high-resolution imaging and can help to detect abnormalities [8]. However, the absence of signal makes it difficult to measure tissue properties such as density,  $T_1$  or  $T_2$ . Furthermore, high-resolution MRI is not feasible in all areas of the body due to motion. Thus, the leading modality for bone research today is still CT.

To extend the applicability of MRI to short  $T_2$  tissues, further efforts have been made to develop special short  $T_2$  sequences. The first major conventional strategies to image short  $T_2$  signals include single point imaging (SPI) [9] and ultrashort echo time (UTE) imaging [10]. It was only later, after SPI and UTE were invented, that the field had been expanded by zero echo time (ZTE) methods [11]. Promising results of recent applications have fueled general interest in short  $T_2$  imaging [12] and MR manufacturers are increasingly following with commercial deployments of new advances. Qualitative visualization of cortical bone with short  $T_2$  sequences has become increasingly common in recent years in research settings and even in clinical routine [13]. The wide range of UTE sequences to manipulate the image contrast, the flexibility to adjust echo time and flip angle led the field of short  $T_2$  imaging to focus on UTE imaging for quantitative bone measurements [14]. Yet, in vivo UTE imaging, qualitative and quantitative, of proximal sites have been proven to be more challenging because of scan time, gradient infidelities and signal-to-noise ratio (SNR). Further, direct trabecular bone imaging is technical challenging because of the fast decaying bone signal that is surrounded by fat.

This thesis addressed the major challenges in clinical UTE imaging in the context of qualitative bone visualization and osteoporosis research. Firstly, high-resolution imaging suffers from artifacts caused by gradient errors that can significantly degrade image quality and affect diagnostic accuracy. Secondly, time efficient single echo time UTE sequences provide information only on short  $T_2$  tissues and lack robust water and fat separation. And finally, due to the technical challenges in direct trabecular bone imaging, UTE acquisition techniques have not been considered in quantitative imaging. Thus, the aim of this thesis was to develop techniques to improve qualitative imaging for radiological diagnostics of bone pathologies and to improve quantitative imaging related to the use of quantitative biomarkers in osteoporosis research. Therefore, the aim was to perform high-quality high-resolution in vivo UTE CT-like imaging in proximal sites such as the spine and hip on a clinical scanner.

### 1.3 Thesis Structure

In Chapter 2, a short introduction to bone properties and the importance of bone imaging in the context of osteoporosis is given. A concise overview of the physical background and employed techniques in the assessment of short  $T_2^*$  tissue components is given in Chapter 3. A description of the employed UTE imaging sequences is given in Section 3.2. Chapter 4 provides an overview over general water and fat separation techniques and in particular water-fat separation in short  $T_2/T_2^*$  tissues. Summaries of the three embedded journal publications can be found in Chapter 7, followed by the original manuscripts. Finally, an overall discussion on the implications of the present work and its literature context is given in Chapter 8.

## 2 Importance of Bone Imaging in the Context of Osteoporosis

In this chapter, osteoporosis and its diagnosis are discussed. In Section 2.1, a brief background on bone is given. In Section 2.2, osteoporosis and its consequences are described and the importance of early osteoporosis diagnosis is explained. Furthermore, the current imaging and mechanical methods of osteoporosis diagnosis and monitoring are presented.

### 2.1 Introduction to Bone Biology and Physiology

Bone is a type of connective tissue that constitutes the major component of the musculoskeletal (MSK) system. It is a dynamic structure composed of both living tissues, such as bone cells, fat cells, and blood vessels, as well as non-living materials such as water and minerals [15, 16]. Bone tissue is a hard and lightweight composite material. It has a relatively high compressive strength but low tensile strength. Bone tissue, although essentially brittle, can have some elasticity due to its organic components, which is mainly made up of collagen. Bones give the body a framework and have many other important tasks. Bones provide a surface for attaching muscles and act as levers that allow many complex movements. In addition, many bones protect softer internal organs. Finally, bone tissue stores calcium, a mineral essential for the activity of nerve and muscle cells. The bone marrow is the site of formation of red blood cells, certain white blood cells, and blood platelets [16, 17]. To understand the properties of bone tissue, it is important to understand the macrostructural and microstructural organization of bone tissue.

#### 2.1.1 Macrostructural Organization of Bone

In general, bone is separated into cortical (or compact) and trabecular (or cancellous) types. Trabecular bone consists of trabeculae, in the shape of plates and rods organized in the direction of stress experienced by the bone. The trabeculae make the bone lighter compared to cortical bone and provide space for blood vessels and fat marrow. Trabecular bone has a typical bone volume fraction of 5-30% depending on anatomical location and age [16]. In contrast to trabecular bone, cortical bone is much less porous and has a relatively high bone mineral density with few blood vessels and with a porosity between 4-17% depending on age [18, 19]. Typically, both types of bone, cortical and trabecular, are distinguished by their degree of porosity or density. However, the true differentiation comes from a histological evaluation of the tissue's microstructure [16]. The exact distribution and ratio of cortical to trabecular bone varies depending on the overall function of the bone in question. For instance, at the end of a long bone, such as the femur, bone has a thin dense cortical shell with a porous, cancellous interior. The middle part of long bones, also named diaphyse, have a sandwich structure that comprises a dense thick cortical layer on the outer surface and a thin, reinforcing cancellous structure within [16, 20]. In humans, cortical thickness ranges

from several tenths of a millimeter to some millimeters, while a trabecula is typically around 50–300  $\mu\text{m}$  thick [21].

### 2.1.2 Microstructural Organization of Bone

The underlying microstructure of the bone consists of 3-6  $\mu\text{m}$  thick lamellae that occur in both trabecular and cortical bone. The lamellae, or bone matrix, are formed from mineralized collagenous sheets, which are a staggered arrangement of the basic bone components: 20-40% collagen type I molecules, 50-70% hydroxyapatite mineral platelets, 5-10% water, and a small fraction of non-collagenous proteins [20, 22]. In adult humans, there are two types of primary bone that are distinguished by their microscopic organization: primary lamellar bone and primary osteons. Primary lamellar bone is found mainly at the periosteal surface and is characterized by a series of parallel lamellae. It can become quite dense and has only few vascular canals. An osteon consists of lamellae that wrap in concentric layers (3-8 lamellae) around a central channel called the Haversian canal. Osteons look like cylinders running roughly parallel to the long axis of the bone and are about 200-250  $\mu\text{m}$  in diameter. Haversian canals house the blood vessels, lymph vessels and nerves that supply the bone tissue with nutrients. Perpendicular to the Haversian canals, are Volkmann's canals, which connect osteons with each other and the surface of the cortical bone [16]. The many small holes in and between the osteons are called lacunae, which accommodate a specific type of bone cell named osteocytes. The lacunae are connected to each other and to Havers' canal via smaller canals called canaliculi, thus forming the lacunar-canalicular system. The lacunar-canalicular system supplies the osteocytes with nutrients and removes the metabolic waste they produce. Osteocytes are thus involved in bone remodeling, and the lacunar-canalicular system also enables communication between osteocytes [20, 22]. In cortical bone, water comprises in total 20% of the total volume. It essentially exists in 2 compartments: within pores and bound to the bone matrix. The amount of pore water, found in Haversian canals, Volkmann's canals, and the lacunar-canalicular system, reflects intracortical porosity. Bound water primarily contributes to the mechanical behavior of bone by giving collagen the ability to provide elasticity or plasticity to the bone tissue. The amount of bound water decreases with age, as does fracture resistance [20, 23].

In trabecular bone, lamellae form rod and plate like structures, each about 200  $\mu\text{m}$  thick, that create a complex, often described as spongy, network. The bone tissue comprises only about 25–30% of the total tissue volume, with the remainder being marrow space. The lamellae are arranged more or less parallel to the trabecular surface. Extremely rarely, complete osteons can be found in a trabecula and osteons in trabeculae are usually smaller than those in the cortex. Rather, so-called hemiosteons are found. These hemiosteons have similar remodeling properties (as osteons) but they do not have the circular appearance of entire osteons. Because they are attached to the bone marrow cavity and can draw their blood supply from there, they do not require or contain a central vascular canal.

### 2.1.3 Bone Marrow

Bone marrow is located in the central cavities of axial and long bones and may or may not be trabecularized, depending on its location in the body. There are two main types of bone marrow, which differ in composition and vascularization: yellow and red bone marrow. Yellow bone marrow is composed of  $\sim 80\%$  fat cells, also named adipocytes, 15% water and 5% protein and is rich in carotenoid. Yellow bone marrow is primarily located in the appendicular

skeleton. Red bone marrow is composed of both hematopoietic cells, i.e. blood forming cells and fat cells. In particular, red marrow is typically composed of 40-60% lipids, 30-40% water and 10-20% protein. Additionally, it is rich in hemoglobin and red blood cells. Red bone marrow is the place for blood cell production and has a rich vascular system. With increasing age, red bone marrow is converted to yellow bone marrow, a process that continues throughout life and follows a pattern that progresses from the peripheral to the central skeleton. Within a single bone, the conversion from red to yellow marrow starts distally and spreads proximally. At age 25, adult bone marrow distribution is achieved. At this time, red bone marrow is found in the axial skeleton (spine, sternum, ribs, and pelvis) making bone a primary blood-forming organ [22, 24].

#### 2.1.4 Remodeling of Bone

Bone tissue is not in a state of rest but is undergoing constant remodeling to repair microfractures caused by daily activity and in response to external stimuli, such as mechanical stress and impact. There are two types of bone cells involved in this process: osteoclasts and osteoblasts. Osteoclasts resorb old bone tissue, whereas osteoblasts form new bone tissue. The resorption of old bone tissue and the formation of new bone tissue are generally in dynamic balance to maintain the overall volume of the bone. The newly deposited matrix then undergoes a primary ( $\sim$  several weeks) and a secondary ( $\sim$  several months) mineralization process to reach its full mechanical capacity [22]. Trabecular bone is highly responsive to metabolic stimuli and has a turnover rate approximately eight times higher than cortical bone. The high turnover rate of trabecular bone makes it an ideal target for detecting bone loss in the early stages of osteoporosis [22].

## 2.2 Osteoporosis Overview

Osteoporosis is a systemic skeletal disease characterized by loss of bone mass and deterioration of the microarchitecture of bone tissue, with a consequent increase in bone fragility and susceptibility to fractures [25, 26]. Bone loss in osteoporosis refers to the loss of trabecular as well as cortical bone mass. Trabecular bone volume is reduced, and the remaining trabeculae are thinner and less connected. Cortical bone becomes more porous as more resorption cavities are created. At the cellular level, osteoporosis is the result of imbalanced osteoblastic and osteoclastic activity, which leads to a reduced formation to resorption rate [22].

The occurrence of osteoporosis is high: it is estimated that 200 million people worldwide currently are affected by osteoporosis [5]. The incidence of osteoporosis increases with advancing age. Projections have shown that an increase of morbidity is expected, due to an ageing population and demographic change [27]. Numerous factors can contribute to osteoporosis, including genetic conditions, malnutrition or hormonal imbalances. Women in general have a higher risk of developing osteoporosis, especially after menopause. Menopause, which typically occurs in women around the age of 50, decreases the production of oestrogen, a hormone that suppresses osteoclastic activity and promotes osteoblastic activity [28]. In Western countries, osteoporosis affects about 30% of all post-menopausal women, leading to one or more fragility fractures in  $\sim$ 40% of these women during their lifetime [28, 29]. Although women are more likely to develop osteoporosis, 15-30% of all men are expected to experience at least one fragility fracture during their lifetime [30].

Osteoporotic fractures significantly impair the health-related quality of life and lead to



premature mortality [31–33]. This makes osteoporosis a public health concern [30]. The most common fractures in osteoporosis are estimated to be vertebral fractures of the spine and the second most common are hip fractures [25]. Hip fractures usually result in a high number of hospitalizations and surgical treatments. Unlike hip fractures, vertebral fractures often remain hidden and can stay asymptomatic. As a result, the start of treatment is often drastically delayed. Undetected fractures are particularly problematic as the risk of future vertebral, hip and forearm fractures drastically increases [34]. Osteoporosis may be present in a patient for many years without apparent consequences, with no obvious symptoms that would prompt the patient to seek medical advice.

The primary goal of treating osteoporosis is the prevention of osteoporotic fractures by strengthening the skeleton and decreasing fall frequency [25]. Besides recommendations of adaption of lifestyle factors, such as physical activity and good nutrition, pharmacological interventions are available. Yet, there is presently no widely applicable method to fully restore skeletal strength [35]. Under the aspects mentioned in this chapter, reliable early diagnosis, long-term therapy monitoring, and thus prevention of osteoporotic bone loss are of particular importance.

## 2.3 Measuring Bone Quality

### 2.3.1 Diagnostic Techniques to Measure Bone Mineral Density

Bone fragility assessment has fundamentally changed with the emergence of non-invasive methods for determining bone mineral density (BMD). Imaging-based BMD measurements are nowadays the conventional method to grade osteoporosis in the clinical setting. The BMD is rated by a scale developed by the world health organization (WHO), that is based on the comparison of a patient’s BMD with that of a healthy young adult [36]. BMD measurements are mainly performed in the lumbar spine and proximal femur. However, since 2013, the femoral neck has been recognized increasingly as a reference site for epidemiological studies [37, 38].

Currently, the standard diagnostic modality for osteoporosis is DXA. DXA, which was introduced to clinical routine in 1987, is a well-standardized and easy-to-use technique with high precision [38] and low radiation dose. DXA is nowadays the best established method for in vivo BMD measurements. However, it has several limitations: Firstly, DXA is a 2D measurement technique, which makes areal BMD susceptible to bone size. DXA, with the unit of  $\frac{g}{cm^2}$  describes BMD only within the projected area. Thus, individuals with a small body frame will have lower areal BMD and will end up with an overestimated fracture risk. Secondly, the spinal vertebrae and hip bone are sensitive to degenerative changes which can result in an increased areal density and consequently in an underestimated fracture risk. In addition, DXA may also mistake osteoporosis for demineralizing diseases, which have completely different pathologies and require different treatment plans [22, 38]. In particular, it has been shown that DXA-derived BMD values of subjects with and without osteoporosis overlap [39, 40]. Finally, DXA has a low fracture risk prediction accuracy, only 44% of non-vertebral fractures were found to occur in women categorized as osteoporotic by DXA [7].

Quantitative computed tomography (QCT) is a technique that reports volumetric BMD based on three-dimensional (3D) projection images. The result is therefore not biased by bone shape and size. To perform quantitative CT, a standard CT scanner with a calibration phantom underneath the patient is used and density values are measured in milligrams

hydroxyapatite per  $cm^3$ . Quantitative CT has some important advantages over DXA: First, QCT allows true volumetric measurements of the lumbar spine and proximal femur, which are independent of the body size. Second, due to volumetric measurements, assessment of purely trabecular bone is achieved. Trabecular bone measurements are more sensitive to monitoring changes with disease and therapy [41]. Further, cross-sectional studies have shown that QCT BMD of the spine allows better discrimination of individuals with fragility fractures [42].

The effective radiation dose for DXA measurements is relatively low compared to standard radiographic examinations (see Table 2.1) [38, 43]. However, the effective dose for a volumetric 3D QCT scan in the spine is five times higher than an equivalent X-ray of the spine. Finally, it should be noted that BMD, as a sole indicator of bone fragility and fracture risk, is questionable. As bone strength is an integral result of numerous factors, of which BMD is only one. Bone quality refers to architecture, turnover, damage accumulation (eg, micro-fractures), and mineralization [44]. In addition, BMD measurements are not able to distinguish between bone tissue and pore space. Thus, BMD does not reflect the extent of porosity or the actual degree of mineralization of bone.

Examination	Anatomical location	Effective dose ( $\mu Sv$ )
high-resolution QCT (HR-QCT)	distal tibia or radius	< 3
DXA	spine or hip	5 - 20
Radiograph	lumbar spine (sagittal)	300
3D QCT	spine, L1 - L2	1500
3D QCT	hip	2900
CT	abdomen	8000

**Table 2.1:** Effective radiation doses for x-ray based imaging methods. Table adapted from [38].

### 2.3.2 Diagnostic Techniques to Measure Bone Quality

Compared with BMD measurements that are well standardized and part of clinical routine, techniques for measuring bone quality in vivo are mainly used in research applications. To measure bone quality primarily the bone microstructure is investigated which is more challenging.

To assess bone architecture, HR-QCT was introduced. The highest resolution of HR-QCT is approximately 30–60  $\mu m$  [22] which is achievable in peripheral sites, such as the distal tibia or radius [45]. This technology has several drawbacks. In particular, it is limited to peripheral skeletal sites and therefore does not provide direct insight into bone quality in the lumbar spine or proximal femur that are common sites for osteoporotic fragility fractures [46]. However, the effective radiation doses are small compared to BMD measurements and recent reviews have highlighted the current and potential future role of QCT for osteoporosis diagnosis and monitoring [38].

Finally, although bone biopsy can determine both porosity and mineralization, it is not suitable for repeated use because of the inherent invasiveness. Therefore, a technique capable of accurately and non-invasively assessing both the matrix and mineral phases of bone in vivo would be highly desirable. MRI, with the absence of ionizing-radiation and the ability to measure multiple parameters, is a realistic alternative.

### 2.3.3 MRI-based Quantitative Osteoporosis Imaging

There are three main classes of MRI-based imaging modalities for osteoporosis: 1) Methods that indirectly assess trabecular bone microstructure via signal from the bone marrow 2) Methods investigating bone marrow properties such as density, composition and fat spectrum and 3) Methods assessing more direct imaging of bone tissue. An overview over all methods is given in Table 2.2.

In the context of quantitative MRI, studies dating back to the 1990s introduced  $T_2^*$ -mapping and high-resolution trabecular bone imaging. Both techniques measure bone marrow to indirectly assess bone microstructure, that is relevant in the context of osteoporosis [8, 47, 48]. High-resolution trabecular bone imaging takes advantage of the fact that solid tissues, such as bone, have a short  $T_2^*$ . Trabecular bone appears dark in most clinical sequences, revealing the bone matrix as voids within the marrow signal. Consequently, the goal of MRI acquisition is to maximize the bone marrow (BM) signal and enhance the contrast to the cancellous bone [8, 46, 49]. However, to achieve high resolution, long scan times and motion sensitivity are challenging. Therefore, high-resolution trabecular bone imaging is not suitable for in vivo spine imaging so far.

$T_2^*$  mapping reflects the tissue's magnetic susceptibility properties, as local magnetic field gradients lead to spin dephasing and thus short  $T_2^*$ . In the area of bone marrow, bone is more diamagnetic than marrow and the bone matrix organization is thus represented in the  $T_2^*$  maps. It has been demonstrated that  $T_2^*$  correlates with the density and orientation of trabecular bone. However,  $T_2^*$  mapping cannot distinguish between susceptibility sources and thus leads to an increased relaxation rate for both paramagnetic and diamagnetic susceptibility sources. Furthermore,  $T_2^*$  mapping is affected by anisotropic orientation of the trabecular bone microstructure [8, 50].

A relatively new development that overcomes the drawbacks of  $T_2^*$  mapping is quantitative susceptibility mapping (QSM). QSM reconstructs the tissue's magnetic susceptibility from the phase information of MRI gradient-echo data. In general, QSM has been proven to be capable of providing quantitative and reproducible data on magnetic susceptibility of different tissues of the body [51, 52]. Yet, QSM is still a newly developed method and in early stages of validation for clinical utility [53].

In the 2000s, MRI studies started to demonstrate that BM plays a key role in bone health and metabolism, with BM changes becoming increasingly apparent in osteoporosis patients [54, 55]. MRI techniques to investigate the BM fat fraction include magnetic resonance spectroscopy (MRS) and chemical shift encoding-based water-fat MRI (CSE-MRI).

Recently, methods have been developed that directly measure signal from spins originating from trabecular or cortical bone. The direct detection of the bone tissue signal itself is a challenging task due to the extremely rapid signal decay of the bone matrix, low SNR and the presence of high signals from long  $T_2$  water and fat. A couple of MR techniques have been developed to capture the short tissue components, such as UTE imaging and ZTE imaging. The technical aspects of this class of sequences are presented in Chapter 3. While early MRI methods predominantly exploited the BM signal to image the trabecular microstructure of bone, newer approaches such as UTE imaging and QSM allow for more direct imaging of bone tissue and have only recently been applied to spine imaging.

Technique	Basis of tissue signal	Advantages	Disadvantages
High-resolution trabecular bone (TB) imaging	Resolving the TB matrix as signal void within the bone marrow signal.	- Direct depiction of TB matrix	- Long scan times and high motion sensitivity - Not applicable for in vivo spine imaging
$T_2^*$ / QSM	Indirect assessment of TB microstructure by exploiting magnetic susceptibility effects.	- Multi-echo gradient-echo sequences available on most systems - Moderate resolution can be adequate	- Indirect measurement of TB microstructure - $T_2^*$ mapping known to be affected by the anisotropic orientation of the TB microstructure - QSM requires an extensive processing pipeline and is still in early stages of validation
UTE imaging	Bound and free water protons in bone are accessed by acquiring data at ultrashort echo times. Long $T_2$ tissue components are suppressed (e.g., with an adiabatic inversion recovery pulse).	- Direct measurement of bone signal - Computed tomography-like image contrast for assessment of bone	- Low spatial resolution (due to rather long scanning times) - Low signal-to-noise ratio after long $T_2$ tissue component suppression
MRS	Water and fat signals can be differentiated based on their different chemical shift characteristics.	- High availability, implementation provided by the majority of available MRI systems - High spectral resolution - High robustness of water-fat signal identification - High accuracy and sensitivity, especially for low fat content - Possibility of characterization of mono-, di-, and polyunsaturated triglycerides	- Moderate scanning times - Moderate correlation of fat fraction to BMD - Limited spatial coverage or very long scanning times - Manual planning of a specific voxel of interest (VOI) needed - Restrictions regarding the minimum required size for the VOI - On-site expertise required for the processing of the acquired spectra
CSE-MRI	Water and fat signals are acquired simultaneously and are then separated according to a chemical shift encoding-based model.	- Moderate to high availability for modern MRI systems - High spatial resolution - High water-fat tissue signal contrast - High robustness of water-fat signal identification - High accuracy for proton density fat fraction (PDFF) definition after addressing confounding factors - Moderate correlation of fat fraction to BMD - Possibility of characterization of triglyceride composition - Large spatial coverage in reasonable scanning times	- Consensus on optimized protocols for different $B_0$ field strengths is still needed - Water-fat signal swap artifacts can arise from inaccurate $B_0$ field map estimations

**Table 2.2:** Overview of major advantages and disadvantages of the different MR techniques currently applied to quantitative osteoporosis imaging at the spine and femur, including information on the basis of the tissue signal. Table adapted from [26].

## 3 Ultrashort Echo Time Imaging

In this chapter, the specific requirements for measuring tissue signals with short  $T_2$  relaxation time are discussed. First, a background is provided on the basic principles and concepts that apply to all existing short  $T_2$  MRI techniques. Then, UTE imaging is described in detail in Section 3.2. Finally, the application of UTE imaging in bone is presented in Section 3.3.

### 3.1 Fundamentals of Short $T_2$ MRI

The MR signal from short  $T_2$  tissues characteristically decays rapidly, so they produce little or no signal at the echo time (TE)s used in conventional clinical imaging and therefore appear dark. Most clinical scanners have a minimum echo time of 1-2 ms with conventional scanning methods [10]. All techniques used in short  $T_2$  imaging have evolved from a limited number of fundamental principles that determine sequence design, signal detection, data processing, and hardware requirements.

#### 3.1.1 Principles

Conventional echo sequences barely detect signals from short  $T_2$  tissues because the signal is lost by a factor of  $\sim e^{-t/T_2^*}$  until the echo is formed and detected by the echo time  $t = TE$ . Figure 3.1 illustrates the challenges of shortening TE in a gradient echo sequence. To form a gradient echo the signal is dephased and rephased with a readout gradient  $G_r$ . To achieve a slice-selective excitation, a gradient  $G_s$  is played out during the excitation pulse, which is followed by a rephasing lobe after the radio frequency (RF) excitation pulse. To excite a thin slice under a gradient of finite strength, frequency-selective RF pulses require a correspondingly small bandwidth, resulting in a long pulse duration. Lastly, phase encoding is achieved by a gradient  $G_p$ . The formation of the gradient echo, slice encoding, and phase encoding prevents achieving shorter TEs.

Thus, the first fundamental principle of short  $T_2$  MRI is, that the signal of the free induction decay (FID) is measured as soon as possible after the signal excitation. This yields the following implications: 1) No slice selection, 2) Radial center-out encoding and 3) Ramp-sampling or excitation under the encoding gradient. Instead of a slice-selective excitation, short  $T_2$  imaging often employs non-selective volume excitation as shown in Figure 3.2A. In almost all short  $T_2$  sequences, spatial encoding is then achieved by 3D Fourier encoding. Data acquisition is performed along radial trajectories that start in the k-space center. With echo-based MRI techniques, the echo time is defined by the time at which the k-space center was measured. The same definition of TE has widely been adopted for short  $T_2$ -imaging even though most of the techniques work without actual echo formation. Thus, in short  $T_2$  MRI, TE is defined at the beginning of the data acquisition window, whereas in gradient-echo sequences TE is defined in the middle of the acquisition window. To avoid losing time after the excitation, in UTE imaging the data acquisition starts already during the ramping up of the readout gradients. Similarly, in ZTE imaging, the gradient is switched on before the excitation such that it is already present when excitation is performed.

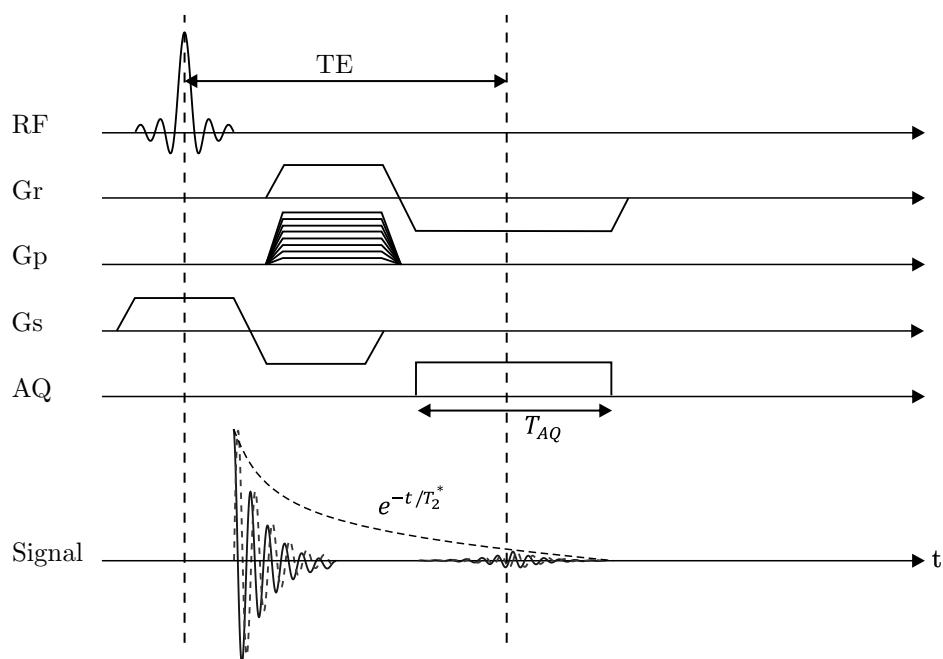


**Figure 3.1:** Gradient Echo: The first readout gradient  $G_r$  with positive polarity after the excitation RF pulse causes a dephasing of the spins. This dephasing is recovered by a second gradient with opposite polarity. After a time interval  $TE$ , the time integral of both gradients match and an echo is generated. The real and imaginary parts are shown as a solid black and dotted line, respectively. Slice selection is achieved with a frequency selective RF pulse and a slice encoding gradient  $G_s$ .  $TE$ : echo time; RF: radio-frequency pulse;  $G_r$ : readout encoding gradient;  $G_s$ : slice encoding gradient;  $G_p$ : phase encoding gradient; AQ: receiver channel;  $T_{AQ}$ : time of the acquisition window.

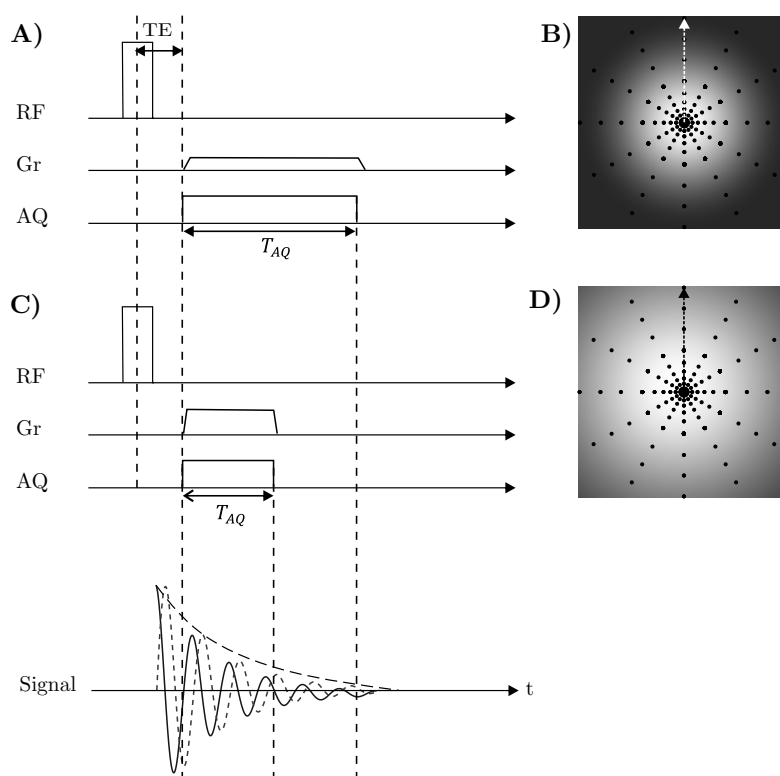


**Figure 3.2:** Free Induction Decay measurement with a UTE sequence: The signal's real and imaginary parts are shown as a solid black and dotted line, respectively. A) After the RF excitation pulse, data acquisition starts as soon as possible. TE is defined from the center of the RF pulse to the start of data acquisition. B) K-space representation of A). Data acquisition begins at the center of k-space with a radial center-out readout (along arrow). The signal decay during the data acquisition window  $T_{AQ}$  reduces the signal at the outer k-space points, resulting in blurring in the image space. C-D) To reduce  $T_2^*$  blurring, stronger readout gradients are used to traverse k-space faster and reduce  $T_{AQ}$ . TE: echo time; RF: radio-frequency pulse;  $G_r$ : readout encoding gradient; AQ: receiver channel;  $T_{AQ}$ : time of the acquisition window.

A second fundamental principle of short  $T_2$  MRI is that the signal decay during data acquisition still affects the spatial resolution. Figure 3.2B shows how the signal decay along each spoke translates to k-space. In mathematical terms, the apodization in k-space is equivalent to a convolution with a kernel in the image domain which results in blurring [56]. The width of the kernel is reciprocal to the width of the apodization function. To avoid resolution loss, as a result all image data must be acquired within a small time range  $T_{AQ}$  after excitation. In Figure 3.2C-D, a stronger readout gradient is used to shorten  $T_{AQ}$  and reduce apodization of k-space signal. It was shown by Rahmer et al that in order to approach the encoded resolution, the acquisition range  $T_{AQ}$  should approximately match  $T_2^*$  [57]. In general, high-resolution short  $T_2$  MRI requires both rapid encoding and large gradient time-integrals, and thus strong gradients. Due to the strong gradients a high resonance bandwidth is required. Therefore, short  $T_2$  imaging is generally more SNR-limited than conventional MRI.

In summary, the two principles introduced in this chapter, early acquisition start and short acquisition time, determine all basic schemes of short  $T_2$  sequences and their associated k-space sampling patterns.

### 3.1.2 Basic Sequences

The main sequences used in short  $T_2$  MRI are continuous time imaging (CTI), SPI, ZTE imaging, and UTE imaging. Table 3.1 shows the main advantages and disadvantages of each sequence.

In CTI and SPI, pure phase encoding is used and the acquisition starts after the phase encoding gradient was played out [58]. Consequently, each k-space point is acquired at a fixed time TE and thus spatial resolution is not affected by  $T_2^*$  blurring. The k-space points are usually chosen to lie on a Cartesian grid, which allows for a quick and easy reconstruction. However, only one k-space point is acquired per excitation which implies long scan times and low SNR efficiency. In addition, the resolution directly affects TE which is large compared to other short  $T_2$  sequences. The main difference between CTI and SPI is that in CTI the phase encoding gradient starts after the RF excitation and data acquisition after the phase encoding. In SPI, the RF excitation and data acquisition are performed in the presence of the gradient. Thus, CTI has longer TEs and lower RF excitation pulse bandwidth compared to SPI. Yet, SPI is a relatively silent sequence since gradients are ramped up slowly between data acquisition [59].

In UTE imaging [10, 60–64] and ZTE imaging [11, 65–68] pure frequency encoding is used to traverse radially through k-space. Per excitation, data is acquired continuously along a radial spoke. The angle of the spoke is altered from repetition to repetition. In a typical UTE experiment the encoding gradient is turned on immediately after the transmit/receive dead time, and data acquisition starts during the ramp-up of the readout gradient. The minimum TE in UTE imaging refers to the time the system needs to switch from transmit to receive. Due to the ramp sampling, the k-space center is traversed at a lower speed which results in non-equidistant k-space locations and longer acquisition time  $T_{AQ}$ . UTE sequences are therefore known to be more affected by  $T_2^*$  blurring. To decrease  $T_{AQ}$ , typically the slew rate of the gradients are large which results in strong eddy currents. Ramp sampling and its associated drawbacks are avoided in ZTE imaging by ramping up the gradient before the excitation. As in SPI, in ZTE high-band width (BW) RF pulses are needed which limit the available flip angle (FA) and increase specific absorption rate (SAR). A major aspect of ZTE sequences is silent scanning. A nearly silent scan is possible by adjusting the gradients between excitations rather than turning them off. Since the gradient is always switched on, k-space



	Disadvantages	Advantages
CTI	<ul style="list-style-type: none"> <li>- Long scan times</li> <li>- Low SNR</li> <li>- Very large TE (TE <math>\sim</math> resolution)</li> </ul>	<ul style="list-style-type: none"> <li>- No <math>T_2^*</math> blurring</li> <li>- Cartesian sampling</li> <li>- Lower BW excitation</li> </ul>
SPI	<ul style="list-style-type: none"> <li>- Long scan times</li> <li>- Low SNR</li> <li>- Large TE (TE <math>\sim</math> resolution)</li> <li>- High-BW excitation pulse</li> <li>- High-BW acquisition</li> </ul>	<ul style="list-style-type: none"> <li>- No <math>T_2^*</math> blurring</li> <li>- Cartesian sampling</li> <li>- Silent</li> </ul>
UTE	<ul style="list-style-type: none"> <li>- TE limited by the hardware's transmit/receive switch time (TE <math>\approx</math> 40-200 <math>\mu</math>s)</li> <li>- High sensitivity to eddy currents, trajectory correction needed</li> <li>- Longer <math>T_{AQ}</math> due to ramp up, results in stronger <math>T_2^*</math> blurring</li> </ul>	<ul style="list-style-type: none"> <li>- 2D and 3D techniques available</li> <li>- Larger FA range</li> <li>- Lower BW excitation</li> <li>- variety of contrast manipulations (FA, TE)</li> </ul>
ZTE	<ul style="list-style-type: none"> <li>- High-BW RF excitation (higher SAR, limited FA)</li> <li>- Only 3D</li> <li>- Limited intrinsic contrast</li> <li>- Higher sensitivity to background signal</li> </ul>	<ul style="list-style-type: none"> <li>- Silent</li> <li>- Very short TEs (TE <math>\approx</math> 4-10 <math>\mu</math>s)</li> <li>- Higher resolution than UTE</li> <li>- Robust against off-resonance effects</li> <li>- Robust against eddy currents</li> </ul>

**Table 3.1:** Overview of major advantages and disadvantages of basic techniques for short  $T_2$  MRI. Table adapted from [69].

encoding starts instantaneously after excitation and the data points encoded during dead time are lost leading to a gap in the k-space center. The missing data points are recovered either via a second set of scans or with algebraic reconstruction [69].

SPI and CTI are rarely used in vivo and are mainly applied for imaging materials or in combination with other short  $T_2$  techniques [70, 71]. For in vivo MRI, UTE and ZTE imaging are currently most widely used techniques. There are also many hybrid forms of the four techniques, which will not be discussed further in this chapter. More information can be found in [12, 69].

## 3.2 UTE Sequence Aspects

This chapter will focus on the individual building blocks of the most common UTE sequences.

### 3.2.1 RF Excitation

In general, relaxation during excitation must be considered if the excitation pulse duration is significant relative to  $T_2$  of the excited tissue. A typical excitation pulse used on a 3T system

has an amplitude of about  $B_1 \approx 10 \mu T$ . Thus, a  $90^\circ$  rectangular pulse requires a minimum duration of around

$$T_{pulse} = \frac{FA}{360^\circ \cdot \gamma_H \cdot B_1} = \frac{90^\circ}{360^\circ \cdot 42.6 \frac{MHz}{T} \cdot 10 \mu T} \approx 0.58 \text{ ms} \quad (3.1)$$

with  $\gamma_H$  being the gyromagnetic ratio of hydrogen. Since the duration of the pulse is of the same order of magnitude as  $T_2^*$  of cortical bone, the relaxation during excitation is substantial [10]. Further, relaxation during the pulse reduces the actual FA and makes the FA  $T_2$  dependent [68]. In UTE imaging, the length of the RF pulse is directly related to TE. A common assumption is that the relaxation starts at the magnetic center of the RF pulse, for symmetric waveforms the center of the pulse [72]. Thus, the TE is commonly defined from the center of the pulse, which is not entirely correct and an assumption. In conclusion, the aim of UTE imaging is to use small FAs, high  $B_1$  amplitude, and short excitation pulses. Based on the used excitation RF pulses, common UTE sequences can be divided in the following categories: 2D UTE sequences, 3D non-selective sequences, and 3D volume selective sequences.

Conventional ideal 2D sequences use a sinc shaped slice excitation pulse. To avoid an increasing TE in 2D UTE sequences, two half-sinc excitation pulses are used with opposite slice encoding gradients for each line in k-space (see Figure 3.3A). The two k-space lines are then summed up to a signal corresponding to what would have been produced with a full sinc excitation. The idea is that the imaginary parts of the excited slice profile, which have opposite polarity for each half-sinc excitation, cancel each other out in the summation. After each half-sinc excitation pulse, the excited signal is sampled in-plane with a center-out radial encoding [73]. 2D UTE sequences have the advantage to excite a single slice which reduces the field of view (FOV) and therefore scan time. However, motion and eddy currents can disturb the slice profile between each excitation which leads to a remaining imaginary parts and artifacts. Thus, 2D sequences are very susceptible to motion and eddy currents artifacts [74, 75].

For 3D sequences a spatially non-selective RF excitation is followed by 3D radial encoding. Three-dimensional center-out radial sampling of k-space is used with an isotropic distribution of radial lines. A common method to distribute the lines is along a 3D spiral. This sampling pattern, also known as Koosh ball acquisition, allows for very short TEs (see Figure 3.3B). However, an isotropic resolution requires an isotropic FOV which prolongs the scan time. A variation of the Koosh ball acquisition is the 3D Cones trajectory [76] where a twist is added to the radial spoke of the Koosh ball trajectory. As more twist is added, fewer total readouts are required which reduces the total scan time.

Another 3D approach is stack-of-stars (SOS) encoding (see Figure 3.3C). After the non-selective excitation pulse, a phase encoding gradient in slice direction is applied. The phase encoding gradient has a variable duration depending on the encoding of the k-space in the slice direction. Immediately after the phase encoding gradient, in-plane radial encoding is performed from the center out. Due to the variable duration of the phase encoding gradient, the readout gradients start at a slightly different time point for the different slice encodings. Thus, TE changes slightly with slice encoding. However, the center k-space point is acquired with the shortest TE. High-frequency k-space points in the slice direction have a larger TE and therefore lower signal that introduces a blurring. Both acquisition techniques, SOS and Koosh ball, have a 3D encoded k-space, and the signal is reconstructed at Cartesian k-space points with gridding. An advantage of the SOS acquisition compared to the Koosh ball acquisition is that anisotropic FOVs and anisotropic resolution are possible, which can be

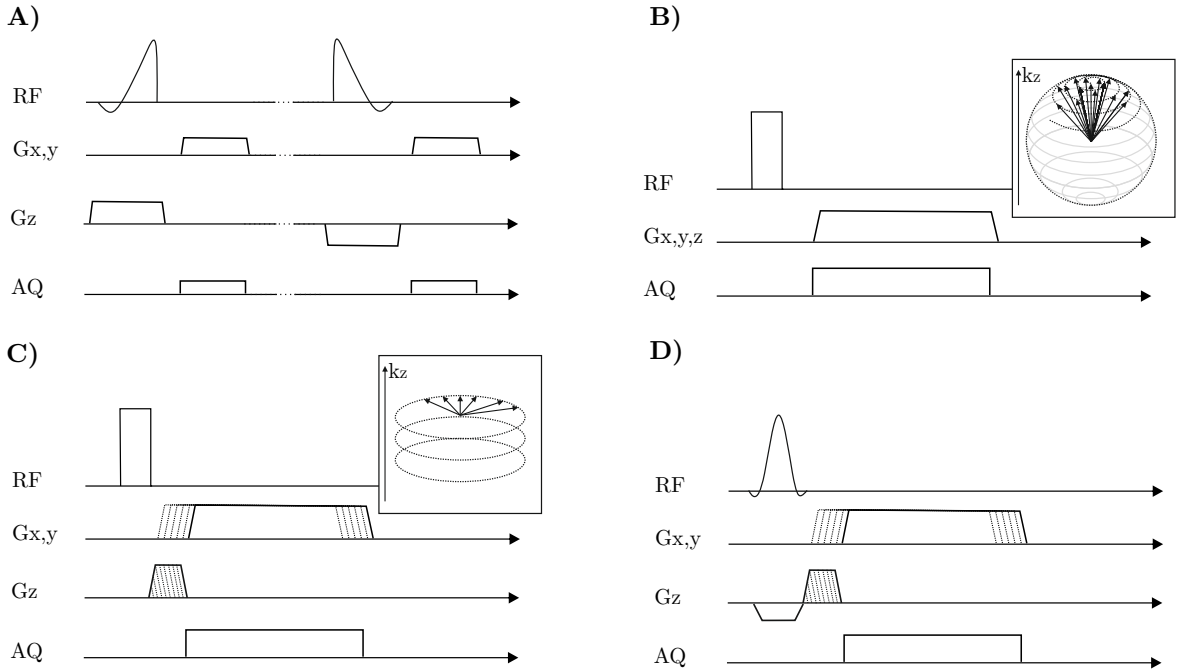


**Figure 3.3:** UTE sequence diagrams: In all sequences,  $G_{x,y}$  encodes the imaging plane and  $G_z$  the slice direction. A) 2D UTE sequence with two half-sinc slice selective RF pulses that belong to the acquisition of one k-space spoke. The slice excitation gradient has opposing polarities for each half pulse excitation, which result in a conventional sinc pulse slice profile. B) 3D non-selective excitation pulse followed by 3D radial Koosh ball readout. C) 3D non-selective excitation pulse followed by a slice phase encoding gradient  $G_z$  and a SOS in-plane radial readout. D) 3D volume-selective excitation combined with the same 3D SOS encoding as in C). RF: radio-frequency pulse;  $G_{x,y}$ : imaging plane encoding gradient;  $G_z$ : slice encoding gradient;  $k_z$ : k-space in slice direction; AQ: receiver channel; SOS: stack-of-stars.

used to decrease scan time. Further, the Cartesian phase-encoded slice-dimension does allow for faster reconstruction, since only 2D gridding is needed. However, the acquisition of thin slices prolongs TE for higher frequencies and results in blurring [57, 77]. Both 3D methods, Koosh ball and SOS, have a considerable drawback. A very large volume must be excited and encoded to prevent folding, which prolongs scan time.

Alternatively, there is a volume-selective variant of the 3D SOS method (see Figure 3.3D). A thick layer is excited with a selective RF pulse to prevent folding. Phase encoding is performed within the excited volume along the slice encoding direction. The volume excitation prolongs the minimum TE since a longer pulse is necessary as well as a refocusing gradient. If a large volume is excited, the additional time is comparably small, e.g.  $\sim 50 \mu s$  at a layer thickness of 300 mm (3T MR system, Ingenia Elition X, Philips Healthcare, The Netherlands). However, TE is dependent on the thickness of the excited volume [78, 79].

### 3.2.2 Readout Gradient

In all UTE imaging sequences data acquisition starts during the ramp up of the gradient fields. Thus, UTE imaging relies on high temporal accuracy and spatial linearity of the gradient

fields. However, eddy currents generated by the dynamic gradient field variations, timing inaccuracies, coupling between gradient coils, mechanical resonances, and gradient amplifier nonlinearities cause deviations from nominal gradient dynamics. Eddy currents arise from the self-inductance and cross-inductance of gradient coils, and from the cross-inductance between gradient coils and other conductive structures of the scanner, such as shim coils or parts of the cryostat. The distorted gradient shape leads to severe alterations in signal intensity and can significantly degrade UTE image quality [69, 80]. In modern clinical MR scanners gradient distortions are addressed by various means, such as actively shielded gradients to reduce induced currents in the cryostat and gradient pre-emphasis to minimize eddy current effects during gradient switching. However, many rapid and non-Cartesian sampling schemes are still vulnerable to small residual deviations of the acquisition trajectories and further pre- and post-compensations schemes have to be applied to prevent degradation of the reconstructed images. Both pre- and post-compensation correction methods require a precise knowledge of the dynamic gradient fields. Several techniques have been proposed for the characterization of non-Cartesian trajectories, including approaches based on raw UTE data itself [81, 82], methods that require calibration scans [83–85], impulse-response characterization of the gradient system [86] using modified MRI sequences [87–92] or dedicated nuclear magnetic resonance (NMR) field probes [93–95].

### 3.2.3 Contrast

In general, with negligible TEs, all tissues contribute according to their spin density and steady-state magnetization which results in images with relatively low intrinsic contrast. If TE is small compared to the tissue’s  $T_2$  the signal  $S$  at time TE can be approximated as follows:

$$S(TE) \sim \rho \left(1 - e^{-\frac{TR}{T_1}}\right) e^{-\frac{TE}{T_2}} \approx \rho \left(1 - e^{-\frac{TR}{T_1}}\right) \quad \text{for } TE \ll T_2 \quad (3.2)$$

Due to the short TE,  $T_2^*$  contrast in a UTE image is low.  $T_1$  image contrast is controlled by sequence parameters such as excitation flip angle or repetition time (TR). Short RF excitation pulses with small flip angles are used in UTE imaging and therefore UTE images have a small  $T_1$  weighting. Larger  $T_1$  weighting, with large flip angles, is possible for UTE imaging but requires long pulses which possibly lead to  $T_2$  decay during the pulse.

### 3.2.4 Techniques for $T_2/T_2^*$ Contrast

Several methods have been proposed for long  $T_2$  suppression, all of which can be classified into two groups. The first group consists of methods that combine images acquired with different TEs to generate  $T_2$  contrast. The other group of long  $T_2$  suppression methods are based on RF pulses and magnetization preparation. The most common technique is to subtract a later gradient echo image, which contains signal only from long  $T_2$  species, from the first FID image [60]. Dual-echo UTE sequences and multi-echo UTE sequences acquire the FID signal followed by a multi-echo gradient echo data acquisition (see also Chapter 4). The signal of the FID consists of short and long  $T_2$  signal, while the signal of the subsequent echoes consists of mostly long  $T_2$  components due to the larger TE. By combining or subtracting the images at different TEs the signal of long  $T_2$  species is suppressed. Combining images from multi-echo gradient echoes at different TEs can provide high  $T_2$  contrast [13, 57, 96–101] without the need for  $T_2^*$  fitting. Long  $T_2$  suppression based on subtraction is a fast and simple approach and provides a reference image that is useful for diagnosis. However, the image

subtraction method has several limitations. First, the combination of images at different TEs need a weighting factor to account for long  $T_2^*$  signal decay. Usually, the weighting factor is empirically tuned to achieve the desired contrast. Thus, the simultaneous suppression of long  $T_2$  species with differing  $T_2^*$  values is not achievable. Further, the refocusing needed for the multi-echo readout is sensitive to eddy-current induced artifacts and noise [69, 84, 102]. Finally, image subtraction decreases the SNR of short  $T_2$  components. The FID image contains short  $T_2$  signal and noise, while the echo image mainly contains noise at the locations of short  $T_2$  components. A subtraction then increases the noise level by a factor of  $\sqrt{2}$  and consequently decreases SNR by a factor of  $\sqrt{2}$  [102].

Instead of the acquisition of multiple echoes long  $T_2$  components can be suppressed by magnetization preparation. Various schemes for long  $T_2$  component saturation [103, 104], inversion recovery [13, 99] and the combination thereof exist [102]. The original method prepares the magnetization with a long rectangular, low-power  $90^\circ$  pulse followed by a dephaser [105]. Short  $T_2$  components lose coherence during the long RF pulse and thus are barely affected [103], while long  $T_2$  components are flipped into the transverse plane, where they are dephased by a crusher [102]. Long  $T_2$  saturation techniques are SNR and contrast efficient, but are very sensitive to off-resonance and inhomogeneous  $B_1$  fields.

Another method to suppress long  $T_2$  components is inversion recovery (IR) that selectively suppresses long  $T_2$  components with a particular  $T_1$  [105]. Commonly adiabatic inversion pulses are employed which have a high tolerance towards  $B_0$  and  $B_1$  inhomogeneities. With the adiabatic pulses the longitudinal magnetization of long  $T_2$  components are inverted and data acquisition starts when the magnetization of long  $T_2$  species cross zero [106]. While the magnetization of long  $T_2$  components follow the effective field of the adiabatic pulse, the short  $T_2$  components dephase during the inversion pulse because of the fast relaxation rate of short  $T_2$  components. Consequently, after the inversion pulse the short  $T_2$  species get saturated, having a near-zero value of the longitudinal magnetization. Methods based on IR are  $T_1$  selective and typically the inversion time is chosen such that fat is suppressed. As water has  $T_1 > 1000$  ms, and fat has  $T_1 \sim 300$  ms, the  $T_1$ -recovery for water is slower and its steady-state magnetization is lower than the one for fat [107]. Alternatively, dual-adiabatic inversion recovery pulses were employed to invert and null signals from long  $T_2$  water and fat, respectively [13, 63]. Finally, conventional fat suppression is also useful in UTE when imaging short  $T_2$  components. Conventional techniques, such as fat-selective saturation pulses have been used in UTE imaging [13, 102]. Fat suppression methods can be applied in addition to long  $T_2$  suppression.

All magnetization preparation-based techniques have the ability to create highly short  $T_2$  selective images, with a high tolerance towards  $B_0$  and  $B_1$  inhomogeneities if adiabatic pulses are employed. In general, magnetization preparation techniques require more scan time than multi-echo methods and are limited due to their high SAR.

### 3.3 UTE Imaging of Bone

Most bone pathologies necessitate either qualitative visualization of bone structures or quantification of bone mineral density. There are two possible ways to assess bone signal: indirectly from bone water with UTE sequences or directly from hydroxyapatite using  $31\text{P}$  imaging [10, 69, 108, 109].

Qualitative methods to image bone with UTE MR methods are presented in Table 3.2. While early UTE methods were mostly employed on human bone specimens or in vivo on

extremities, UTE imaging is nowadays possible on more proximal sites like the spine or pelvis. For the assessment of cortical bone, single UTE and ZTE sequences were applied to detect signal from both bound water and pore water in bone. One method to visualize cortical bone relies on the inversion of the UTE, or ZTE, image contrast such that cortical bone appears bright. Due to the short TE, UTE images have a highly proton density (PD) weighted contrast and the inverted signal magnitude highlights areas with a high proton density where acquired signal is low. It was shown that UTE imaging has potential advantages regarding tissue contrast when compared to conventional gradient echo imaging [110–112]. An advantage of the single UTE magnitude inversion method is the relatively high SNR and short scan time when compared with long  $T_2$  suppression techniques. However, the signal of long  $T_2$  components, such as water and fat, is present and not suppressed which limits the application to cortical bone. On the other side there are IR-UTE-based, UTE echo subtraction and fat suppressed UTE sequences which provide efficient suppression of long  $T_2^*$  tissues, allowing bound water imaging with CT-like bone contrast. Finally, besides UTE sequences qualitative bone imaging was achieved by conventional clinical fast spin echo (FSE) and conventional short TE gradient echo imaging [13]. Both sequences can acquire signal from tissues with, compared to the UTE sequences, relatively long  $T_2/T_2^*$ , such as water in large pores in cortical bone.

IR-UTE techniques have been used in quantitative studies of cortical bone, primarily ex vivo in human cortical bone specimens from the femoral or tibial midshafts [14, 113, 114]. Further, using specific  $T_2$  filter strategies to isolate signals from bound water or pore water, some studies have been able to extract signals from total water, bound water, and pore water individually [115, 116]. An alternative approach measured multiple UTEs at different TEs and bi-component  $T_2^*$  analysis to distinguish between bound water  $T_2^*$  and pore water  $T_2^*$  and their fractions [117]. In comparison with histology or micro-CT measurements, the studies indicated that in human cortical bone: Firstly, pore water proton density correlated positively with cortical bone porosity and negatively with BMD. And secondly, bound water proton density correlates positively with cortical bone stiffness, strength, and toughness to fracture. In trabecular bone, first quantitative studies were performed with IR-UTE-based sequences ex vivo [118], which characterized trabecular bone density and total water content. In a first feasibility study, IR-UTE spine measurements were performed in vivo in the spine to characterize the structure of trabecular bone which provided similar information regarding bone quality when compared with micro-CT [119].

MRI technique	Sequence parameter ( $T_2^*/TE$ )	Visualized proton pool	Application
FSE	Relatively long $T_2^*$	Water in large pores in cortical bone	Ex vivo in human bone specimens [120, 121]
Short TE gradient echo (GRE)	Relatively long $T_2^*$ TE $\sim 1\text{--}1.5$ ms	Water in large pores in cortical bone	In vivo in the tibia [122]
Single UTE	Ultra-short $T_2^*$ of $\sim 200 - 500 \mu s$ TE $\sim 40 - 200 \mu s$	Bound and pore water in cortical bone	In vivo in the tibia and lower extremities [60, 62, 63] Ex vivo in human bone specimens [121, 123–125] In vivo in the spine [126, 127]
IR-UTE	Ultra-short $T_2^*$ of $\sim 200 - 500 \mu s$ TE $\sim 40 - 200 \mu s$	Bound water in cortical and trabecular bone	In vivo in the lower extremities, knee and skull [128–131] In vivo in the hip and spine [119, 132, 133]
Fat suppression UTE	Ultra-short $T_2^*$ of $\sim 200 - 500 \mu s$ TE $\sim 40 - 200 \mu s$	Bound and pore water in cortical and trabecular bone	Ex vivo, wrist [118]; In vivo, knee, lower leg [104, 134]
Echo subtraction UTE	Ultra-short $T_2^*$ of $\sim 200 - 500 \mu s$ TE $\sim 40 - 200 \mu s$	Bound and pore water in cortical bone	In vivo in the knee [97] In vivo in the abdomen, pelvic region, lower extremities and skull [96]
ZTE	Shortest $T_2^*$ TE $\sim 0 \mu s$	Bound and pore water in cortical bone	In vivo in the shoulder [111], skull, dental [11, 135–137] Ex vivo in bone specimens [138]

**Table 3.2:** Overview of major qualitative MRI techniques for bone imaging and application. Table modified from [13].

## 4 Water-Fat Separation Techniques

Water-fat separation algorithms are frequently used in clinical practice for fat suppression, generating water-fat-separated images, and fat quantification. Water-fat separation methods take advantage of the chemical shift-induced phase difference between water and fat signals and are therefore also known as chemical shift encoding-based (CSE) MRI. CSE-MRI techniques typically necessitate the acquisition of multiple images at different TEs and, as a result, have a longer scan time [139–142].

### 4.1 UTE Multi-TE Sequences

To acquire multiple images at different TEs, various multi-TE UTE sequences have been developed [143]. The simplest method is to separately acquire multiple UTE images with different TE values in successive repetitions (see Figure 4.1A). While this approach provides

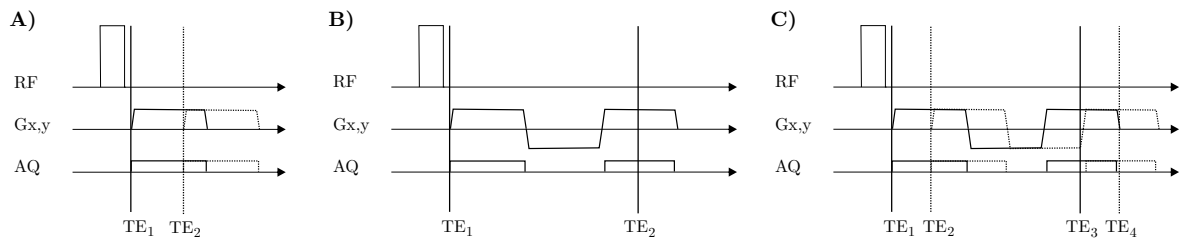


**Figure 4.1:** UTE multi-TE sequence diagrams. a) UTE multi-acquisition technique: The various TEs (shown is here a dual-echo acquisition) are acquired in successive sequence repetitions. The difference between two successive repetitions are depicted with the solid and dotted lines. While this acquisition scheme provides greater TE flexibility, it reduces scan time efficiency. b) UTE multi-echo technique: The various TEs are acquired in each sequence repetition. This method reduces the scan time when compared to the multi-acquisition method. However, TE is constrained by the system’s smallest achievable echo distance and thus also by the desired spatial resolution. c) Interleaved UTE multi-echo techniques: Multiple echoes are acquired after each RF excitation. The entire multi-TE readout is shifted between repetitions, allowing for more flexible TEs. Thus, the interleaved acquisition method combines the scan time efficiency of multi-echo readout with the multi-acquisition method’s greater TE flexibility. RF: radio-frequency pulse; Gx,y: imaging plane encoding gradient; AQ: receiver channel.

a high degree of flexibility in selecting individual TEs, it comes at the expense of low scan time efficiency due to the requirement of a sequence acquisition for each TE. Because of the sequential nature of this approach, physiological variations and motion can have different effects on the various TEs and may influence the quality of the water-fat reconstruction results. Although temporal interleaving of the different acquired TEs within a single scan can reduce



the impact of physiological variations and motion, this approach still has a low scan time efficiency.

To improve the scan time efficiency of UTE multi-acquisition methods, sequences that acquire multiple TEs within one repetition of the UTE sequence have been developed (see Figure 4.1B). In the UTE multi-echo approach, multiple echoes are acquired after each signal excitation. Multi-echo gradient acquisition techniques are prone to phase errors which are caused by hardware imperfections such as eddy currents or delays. To avoid such phase errors, approaches with monopolar readouts, instead of bipolar readouts, are often preferred.

Certain optimal TEs are preferred to reduce errors during the water-fat separation. The distance between two successive TEs is limited by the system's gradient slope, maximal gradient strength, and spatial resolution because the spatial resolution is directly proportional to the time integral of the readout gradient. The monopolar readout further increases the minimum distance between two echoes. To put it another way, in order to achieve optimal TEs for water-fat processing, the UTE multi-echo acquisition technique limits the maximum achievable spatial resolution, particularly at higher magnetic fields like 3T. Approaches combining UTE multi-acquisition and UTE multi-echo have been developed to combine increased scan time efficiency and high spatial resolution. Therefore, multiple gradient echoes are acquired within one repetition of the UTE sequence. In addition, the UTE sequence is repeated with a small shift in the gradient echo chain. To combine all acquired echoes, the acquired data is interleaved during the reconstruction. This interleaved UTE multi-echo technique combines high flexibility in selecting optimal TEs while maintaining the time efficient multi-echo readout (see Figure 4.1C).

## 4.2 Signal Models for Water-Fat Separation

To correctly process multi-TE UTE data with CSE-MRI, it is important to have a clear understanding of the signal models used in CSE-MRI. In a single voxel, the time evolution of the complex MR signal  $s(t_n)$  can be expressed generally as follows [144]

$$s(t_n) = \sum_{p=0}^P \rho_p e^{-i\phi_p} e^{(i\omega_p - R_{2,p}^*)t_n} \quad (4.1)$$

with  $t_n$  as the time at the  $n$ -th echo,  $\rho_p$  as the magnitude of the  $p$ -th chemical species,  $\phi_p$  as the phase after the RF-excitation,  $\omega_p$  as the resonance frequency and  $R_{2,p}^*$  as the transverse relaxation rate. Most Dixon techniques assume that only two chemical species in the target tissue contribute to the MR signal. With this assumption the number of model parameters can be reduced and subsequently the number of required echoes.

An additional assumption is that all peaks, including water, decay at the same relaxation rate  $R_2^*$ . Under these assumptions, in water-fat imaging (WFI) a multi-peak single- $R_2^*$  model is widely used, as follows:

$$s(t_n) = \rho_0 e^{-i\phi_0} e^{(i\omega_0 - R_2^*)t_n} + \sum_{p=1}^P \rho_p e^{-i\phi_p} e^{(i\omega_p - R_2^*)t_n} \quad (4.2)$$

$$= (\rho_0 e^{-i\phi_0} + \sum_{p=1}^P \rho_p e^{-i\phi_p} e^{i(\omega_p - \omega_0)t_n}) e^{(i\omega_0 - R_2^*)t_n} \quad (4.3)$$

$$= (W + c(t_n)F) e^{(i2\pi f_B - R_2^*)t_n} \quad (4.4)$$

$$\text{with } f_B = \frac{\omega_0}{2\pi}; W = \rho_0 e^{-i\phi_0}; c(t_n) = \sum_{p=1}^P \alpha_p e^{i\delta\omega_p t_n}$$

where  $W$  and  $F$  denote the complex water and fat signals, respectively,  $f_B$  is defined as the real-valued field map which accounts for phase accumulated from off-resonance effects due to  $B_0$  main field inhomogeneities. Further,  $\alpha_p$  denotes the the p-th relative fat peak amplitude and  $\delta\omega_p$  the chemical shift frequency difference between water and the p-th fat peak of the employed fat model.

### 4.3 Water-Fat Separation using CSE-MRI

Dixon developed the first water-fat separation algorithm based on the acquisition of two TEs, which is often referred to as the "two-point Dixon method" [139, 145] and is denoted in this chapter as the "two-TE Dixon method." Two TEs are acquired exactly when the water and fat signals are in-phase (IP) ( $c(t_1) = +1$ ) and out-of-phase (OP) ( $c(t_2) = -1$ ), respectively. The two acquired TEs are then used to solve for the real valued  $W$  and  $F$  by adding and subtracting the IP and OP MR images. This simple method relies on the assumption of  $f_B = 0$ , a single-fat peak model and the neglect of  $R_2^*$  decay effects ( $R_2^* \rightarrow \infty$ ). Since the original two-TE Dixon method assumes zero-field map terms, water-fat separation is known to fail in regions of large  $B_0$  field inhomogeneities.

To account for  $B_0$  field variations, the three-TE Dixon technique was introduced, in which three TEs are acquired at IP and OP echo times. The off-resonance induced phase map is estimated and used to calculate water and fat separated images [141]. The three-TE Dixon technique was later extended, such that the off-resonance induced phase map is calculated from only two TEs. This so-called extended two-TE technique replaces the magnitude based method by making use of the complex IP and OP images which allows to calculate the off-resonance induced phase map from only two TEs [146]. Both, the three-TE Dixon and extended two-TE Dixon, methods can improve water-fat separation accuracy by taking  $f_B$  into account [145, 147]. Despite the fact that the image quality of the fat-water separation improves when the field map is estimated, a water-fat swap will still occur in areas with large phase variations due to  $B_0$  field inhomogeneity. Most early two- and three-TE methods have the limitation of assuming a single fat peak, which only accounts for a portion of the fat signal and leads to an underestimation of the fat content. Furthermore, the early methods did not account for additional confounding factors such as  $T_1$  or  $T_2^*$  bias, which is critical for fat quantification.

In addition to the two-TE and three-TE Dixon methods, alternative methods have been proposed to solve the water-fat problem. Due to the field-map term the water-fat problem is non-convex and non-linear. As an alternative approach Reeder et al. introduced the iterative decomposition with echo asymmetry and least squares estimation (IDEAL) method, which is a sophisticated fitting technique [142, 152]. The IDEAL approach uses a matrix formulation and iteratively linearizes the non-linear problem to solve for the parameters in the signal model such as water and fat. As a result, the IDEAL technique allows arbitrary echo times and thus more flexible acquisitions, which potentially improves SNR for signal model fitting. The IDEAL method can be expanded for fat quantification to take into account confounding elements like the multipeak fat spectrum and  $T_2^*$  bias [152, 153]. However, the IDEAL technique relies on a good initialization of the field map. Another approach to solving the water-fat problem is to reformulate the problem using the variable projection (VARPRO) method to

decouple the estimation of the water and fat signals from the estimation of the field map [237]. For fat quantification, the IDEAL and VARPRO methods can also be extended to account for confounding factors such as the multiplex fat spectrum and  $T_2^*$  bias [152]. Recently, a generalized formulation for multi-echo gradient-echo-based chemical species separation for all MR signal models described by a weighted sum of complex exponentials with phases linear in echo time was introduced [144].

The image quality of the water-fat separated images improves, when the field map is estimated. However, phase wraps can still occur in areas with large  $B_0$  field inhomogeneities which cause large phase variations and, consequently, water-fat swaps in the water and fat separated images. To remove such phase wraps, Dixon methods were extended with frequently used phase unwrapping techniques such as region growing [148, 149], polynomial fitting [150], or by solving Poisson's equations [151]. An important assumption of most phase unwrapping methods is that the  $B_0$  field varies smoothly across the image [145]. The field map's solution, however, depends on the initial guess because the fitting problem has multiple local minima [145, 154]. To improve field map estimations which is particularly important for fat quantification, region growing algorithms [155] or sophisticated complex fitting algorithms [156–159] are needed.

#### 4.4 Water-Fat Separation in Short $T_2/T_2^*$ Tissue

There are several approaches to separate fat signal from water in imaging of short  $T_2$  tissues. One approach combines ultrashort echo time with spectroscopic imaging (UTESI) [125, 160], a successful technique not only for separating water and fat but also for separating different chemical species. However, the UTESI approach suffers from slice profile distortions, errors in the radial k-space trajectories, including chemical shift artifacts, and off-resonance artifacts. In another approach, the IDEAL algorithm is extended to include a k-space formulation to apply accurate water-fat separation to non-Cartesian trajectories [143]. Thus, the k-space based IDEAL formulation corrects effects of  $R_2^*$  decay and includes a multi-peak spectral fat model. Wang et al. showed that the combined k-space based UTE IDEAL method provided high contrast imaging of the short  $T_2$  tissues with robust water-fat separation [143]. A major limitation of UTE Dixon methods is the assumption that water is a single  $T_2$  compartment in the imaged voxel, which is not necessarily true, for example, in cartilage, tendon, or meniscus, where long and short  $T_2^*$  species are present. To overcome this limitation, one possible approach is to incorporate prior knowledge about the different water compartments into the signal model, similar to the multi-frequency modeling of the fat spectrum. However, this approach needs a high number of echoes and high SNR. It is important to note that these assumptions imply that the  $T_2^*$  obtained with the proposed model is an average value for all species and all compartments within a voxel. Beyond water-fat imaging, UTE Dixon was used to suppress long  $T_2$  components which proves itself beneficial in pseudo-CT imaging or in the context of positron emission tomography (PET) attenuation map generation [161–165].

#### 4.5 Fat Suppression with CSE-Based Methods

Magnetization preparation techniques are most commonly used in clinical protocols for fat suppression because they are easy to implement and compatible with a variety of MR imaging sequences. Examples of common magnetization preparation techniques are fat saturation, water excitation, short-tau inversion recovery (STIR), spectral presaturation with

inversion recovery (SPIR) or spectral attenuated inversion recovery (SPAIR). Even though magnetization-based fat suppression techniques can be very useful for morphological and quantitative imaging in UTE imaging, using conventional fat suppression methods is difficult. Chemical shift-based fat saturation techniques, for example, fail due to the broad spectrum of short  $T_2^*$  tissue, which results in unwanted signal loss of the signal in addition to those of fat (see also Section 3.2.4). Chemical shift encoding (CSE)-based methods have lower SAR and are more robust against  $B_0$  and  $B_1$  field inhomogeneities than magnetization preparation techniques. Two- and three-TE Dixon methods provide different image contrasts for better diagnosis, including IP, OP, water only, and fat only images. The IDEAL method also produces a PDFF for fat quantification in addition to the aforementioned four images. The main drawback of CSE-based methods is the lengthy scan time and the requirement for complex post-processing methods.

## 4.6 Single-TE Dixon Methods

Single-TE Dixon methods directly decompose fat and water components from a single complex MR image [166]. Single-TE Dixon methods have shorter acquisition times than multi-TE methods because only one complex TE image is required, and were thus first investigated in the context of dynamic imaging [166]. At specific echo times, when the phase between water and fat components is  $\theta(t) = \frac{\pi}{2}$ , fat is contained in the imaginary part and water in the real part of the signal. The original single-echo Dixon method exploits this property and separates water and fat by simply acquiring data at a specific echo time and taking the real and imaginary part of the signal respectively. Note that  $\theta(t)$  is defined as:

$$\theta(t) = \angle(c(t_n)) \quad (4.5)$$

Neglecting  $T_2^*$  decay effects, Equation 4.4 can be rewritten as:

$$s(t_n) = (|W| + |F| c(t_n)) e^{i\phi_{bulk}(t_n)} \quad (4.6)$$

$\phi_{bulk}$  represents all phase terms that water and fat share as a common phase, which comprises contributions from spatially dependent field  $B_0$  inhomogeneities ( $\phi_B = 2\pi f_B$ ), eddy currents, signal delays in the receiver chains, and phase contributions due to the  $B_1$  transmit/receive phase [167]. When the relative phase of the water and fat signals is  $\frac{\pi}{2}$ , the noise performance is optimal, however Ma et al. extended the technique to flexible TEs. Under the assumption that  $\phi_{bulk}$  is zero, water and fat can be estimated as follows:

$$|F| = \frac{\text{Im}\{s(t_n)\}}{\sin(\theta(t_n))} \quad (4.7)$$

$$|W| = \text{Re}\{s(t_n)\} - |F| \cos(\theta(t_n)) \quad (4.8)$$

with Re and Im being the real and imaginary part of the measured signal respectively. To remove phase-errors, which was important due to the non-optimal TE, Ma et al. used a region growing algorithm [167]. The assumption that  $\phi_{bulk}$  is zero only holds, if the  $B_0$  field map is homogeneous. In practice, however, the assumption of a homogeneous  $B_0$  field map is invalid, and the field map must be obtained by pre-calibration (e.g., using multi-TE Dixon measurement). Various techniques for removing unwanted phase terms have previously been reported, including those that use additional reference scans [134, 166] or that use a region

growing algorithm to estimate the unwanted phase terms [167]. Additional reference scans result in longer scan times and errors due to patient motion or other sources of inconsistency.

Different single-TE Dixon methods were presented in the context of short  $T_2^*$  imaging, either for fat suppression [97, 134], long  $T_2$  suppression [97] or water-fat imaging [97]. Jang et al [134] combined the single-TE Dixon method with a dual-echo UTE acquisition. To correct phase errors an additional field map scan was acquired. The non-UTE image was then processed with single-TE Dixon to generate a fat map. Fat suppression in the UTE image was achieved using the fat image obtained from the non-UTE image. The single-TE Dixon method produced accurate fat and water separation that was unaffected by the short  $T_2^*$  signal decay which turned out to be an advantage over the two-TE Dixon method. Jang et al demonstrated that, when compared to the two-TE Dixon method, the two-TE Dixon method estimated fat and water signals incorrectly in tendons due to short  $T_2^*$  signal decay. Further, the flexibility in selecting the TE for the second echo is an advantage of their single-TE Dixon with dual-UTE method. The conventional two-TE Dixon method's echo spacing is constrained by imaging parameters such as spatial resolution and field of view. In a recent work, using a UTE-Cones-dual echo steady state (DESS) sequence and single-TE Dixon processing, Jang et al [97], demonstrated UTE fat suppressed images of the osteochondral junction, tendons, menisci, and ligaments in the knee joint, as well as cortical bone and aponeurosis in the lower leg. With  $T_1$ -weighting, the FID-like  $S^+$  image displayed the typical UTE image contrast. Because of the longer TE, the echo-like  $S^-$  image had a higher  $T_2$  weighting. The initial  $\phi_{bulk}$  was calculated from the intrinsic signal properties of the  $S^+$  and  $S^-$  images before separating water and fat from both images with single-TE Dixon processing. The method effectively suppressed fat in both  $S^+$  and  $S^-$  images without the need for any additional acquisitions or preparation pulses. However, if there are significant  $B_0$  field inhomogeneities that cannot be compensated for by  $B_0$  shimming,  $\phi_{bulk}$  may grow to the point where an additional reference scan is required to avoid significant errors in single-TE Dixon.

## 5 Radial Sampling of k-space

For all UTE sequences, the sampling of k-space starts in the k-space center and follows a radial, center-out, sampling pattern. Due to the distinct non-Cartesian geometry of the trajectory as well as the different temporal ordering of the k-space acquisition, radial sampling of k-space offers unique imaging properties. Compared to the Cartesian sampling pattern, some of these non-Cartesian properties bring advantages, while others have disadvantages.

### 5.1 Nyquist Theorem and Undersampling

In radial scanning, data is acquired along a series of rotated lines in k-space known as "spokes". As in the Cartesian case, the distance between two samples in k-space along a spoke is typically selected from a given FOV size

$$dk = \frac{1}{FOV}. \quad (5.1)$$

The number of samples  $n$  per spoke is determined by a certain initial resolution  $dx$  with

$$n = \frac{FOV}{dx}. \quad (5.2)$$

In the radial case, the spatial resolution additionally depends on the number of spokes  $n_s$ . Usually,  $n_s$  is chosen such that the distance  $dk'$  (see Figure 5.1) between samples on adjacent spokes is less than or equal to  $dk$  [168, 169]. With a simple geometrical derivation [168, 169] it can be shown that with

$$n_s = \pi \cdot n \quad \text{with} \quad dk' \stackrel{!}{=} dk \quad (5.3)$$

an isotropic spatial resolution is guaranteed for the radial center-out sampling scheme, as it is used in UTE imaging. For radial sampling, with a readout from  $-k_{max}$  to  $+k_{max}$ , only half the number of spokes are needed to cover the k-space since the spokes are acquired by increasing the angle from  $0^\circ$  to  $180^\circ$ . In UTE imaging the spokes are acquired by increasing the angle from  $0^\circ$  to  $360^\circ$ . As an alternative to serially incrementing the angle, a golden angle or pseudo golden angle ordering may be used, which offers a more motion robust recording of the k-space information and adds free-breathing and self-navigation properties [170, 171]. While the requirement in equation 5.3 enables to obtain high-quality images, it prolongs the data acquisition by a factor of  $\pi$  relative to that of a corresponding fully-sampled Cartesian data set. This factor is highly undesirable as it increases the overall duration of the examination and hinders the use of radial techniques in the clinical setting. However, in practical imaging scenarios it is often tolerable to acquire only a reduced number of spokes. Figure 5.2 shows images of the point spread function (PSF) and corresponding reconstructions of the Shepp-Logan phantom, obtained using a radial trajectory with a full dataset according to Equation 5.3 which is defined as a radial sampling density of 100%. For a data set with 100% radial sampling density the PSF has a distinct peak in the center. If the number of spokes is reduced to a much lower value, for example a radial density of 5 %, the central part of the PSF remains unchanged. However, it can be seen that gaps appear in a certain radius,

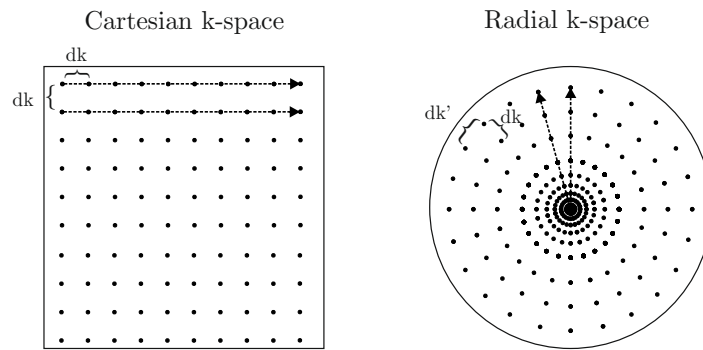


**Figure 5.1:** Illustration of the Cartesian (left) and radial center-out (right) sampling scheme. Shown are sampling points in k-space with  $dk$  and  $dk'$  being the distance between to sampling points. The arrows depict the readout direction and sampling points that are acquired during one acquisition.

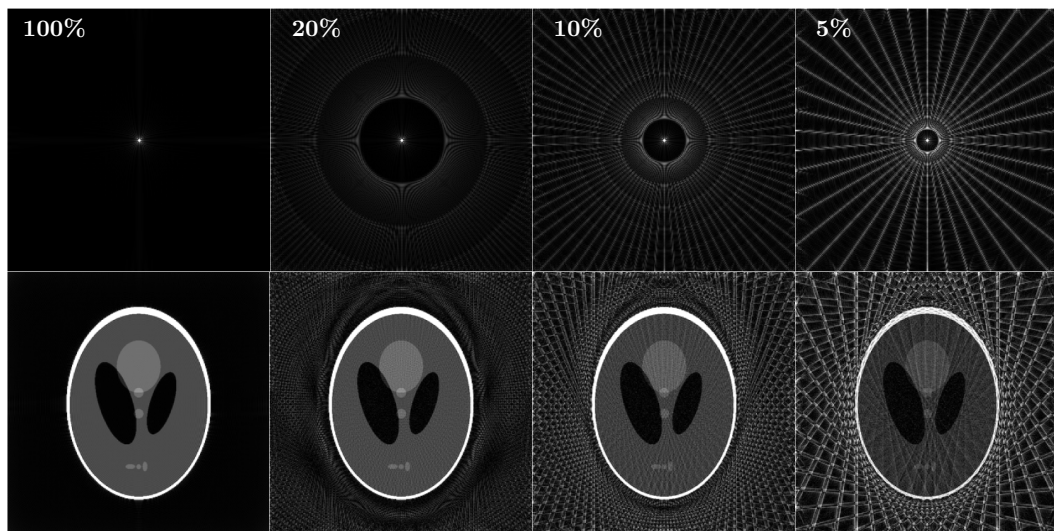


**Figure 5.2:** Point spread function (top row) and corresponding reconstruction of the Shepp-Logan phantom (bottom row) for variable radial density. A radial density of 100% corresponds to  $\pi \cdot n$  number of spokes.

creating a streak pattern in the outer areas. In conclusion, undersampling in radial imaging results in streaking artifacts with much lower intensities than corresponding undersampling artifacts, such as folding, in Cartesian sampling. Reducing the angular spacing of the radial spokes by factors of 2 to 4 results in relatively negligible and often tolerable artifacts [69].

## 5.2 Readout Oversampling

In MRI, k-space sampling is discrete and the object reconstruction in image space is periodic. Therefore, aliasing effects occur when the sampled points in k-space are too far apart, causing adjacent copies to overlap in image space. For a fixed spatial resolution, this problem can be eliminated by readout oversampling. To oversample in the readout direction,  $dk$  is decreased by increasing either the sampling rate or the gradient strength. A smaller  $dk$  increases the FOV while maintaining the spatial resolution. For radial imaging, an oversampling factor

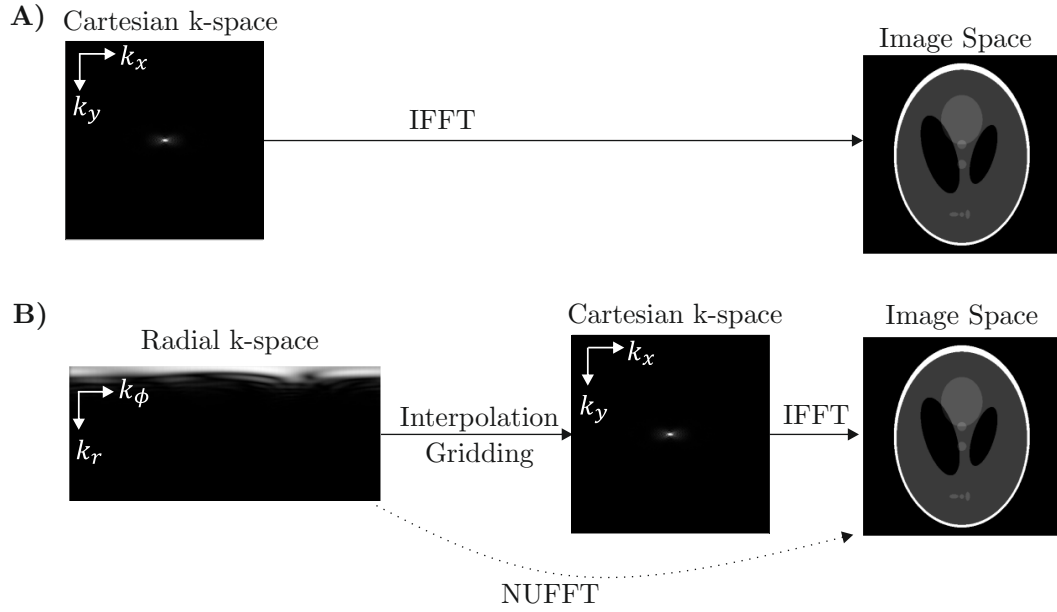


**Figure 5.3:** Cartesian and non-Cartesian reconstruction pipeline. A) The Cartesian k-space data is transformed to image space data by a straightforward IFFT. B) The non-Cartesian k-space data is gridded to a Cartesian k-space before the Fourier transform of k-space to image space. The NUFFFT directly transforms any non-Cartesian data from k-space to image space. IFFT: inverse fast Fourier transform; NUFFT: non-uniform fast Fourier transform;  $k_x, k_y$ : Cartesian k-space coordinates;  $k_\phi, k_r$ : polar k-space coordinates.

of 2 is usually chosen [168, 169, 172]. In contrast, in the Cartesian sampling scheme, this strategy is limited to only one spatial direction, and oversampling in the other direction, the phase encoding direction, requires additional acquisition steps that increase scan time. In the radial case, this limitation does not exist, and readout oversampling can be used in two directions within the imaging plane. In particular, radial imaging has an advantage over Cartesian imaging at anatomical locations that are central to the body. For example, radial imaging is commonly used in abdominal examinations and cardiac imaging where aliasing effects from the extremities require a large FOV. In summary, when imaging large objects with high spatial resolution, radial scanning can offer shorter acquisition time compared to Cartesian scanning.

### 5.3 Non-Cartesian Reconstruction

Due to the non-equidistant sampling positions, the reconstruction of the non-Cartesian data requires additional steps compared to the Cartesian image reconstruction (Figure 5.3). In Cartesian image processing a straightforward inverse fast Fourier transform (IFFT) translates k-space data to image space data which can not be directly applied to the non-Cartesian data. Two common approaches for processing radial data are: complex back projection [173] and interpolation on a Cartesian grid before Fourier transform [174, 175] also referred to as gridding. As a popular alternative to conventional gridding, there is the Non-Uniform Fast Fourier Transform, which can be applied directly to any non-Cartesian trajectory. The idea of gridding is to take each data point and add its contribution to the surrounding grid



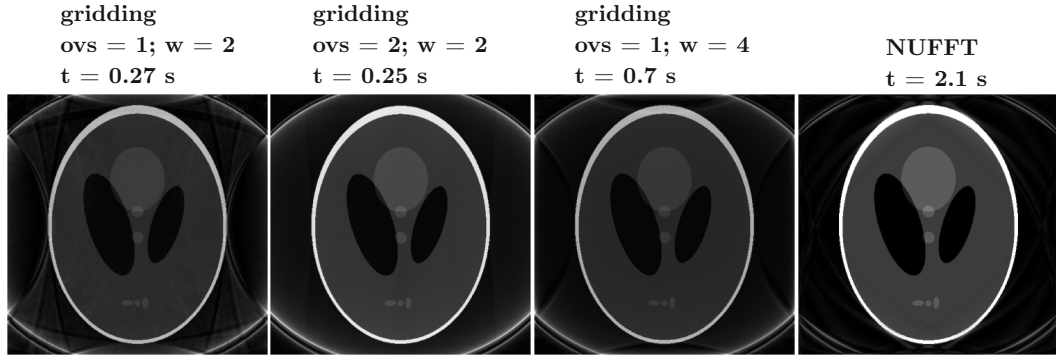


**Figure 5.4:** Comparison of gridding parameters and NUFFT. Regridding reconstruction without oversampling ( $ovs = 1$ ) shows clearly visible aliasing artifacts. Regridding reconstruction with artificially increased FOV ( $ovs = 2$ ) shifts the artifacts away from the object. A wider kernel ( $w = 4$ ) increases computation time yet also reduces aliasing artifacts. NUFFT: non-uniform fast Fourier transform; ovs: gridding oversampling factor;  $w$ : kernel width in  $dk$ ;  $t$ : computation time for an image with  $512 \times 512$  pixels.

points. Thus, each data point is conceptually considered to be convolved with a small kernel. In this way, each data point is resampled at the neighboring grid points. As a result, a density estimation is required to correct for an uneven concentration of sample points in certain areas of k-space. As the image space reconstruction from a discrete k-space grid is a periodic function, side lobes outside the FOV are aliased back into the FOV. For this reason, an oversampling of the gridding matrix is frequently employed. This increases the distance between the neighboring object copies and shifts the aliased side lobes away from the object. Thus, visible artifacts in the image plane are reduced. The extended FOV is cropped at the end of the reconstruction procedure to restore the initial FOV. As with gridding, reconstruction fidelity and reconstruction time is a trade-off between the complexity of the interpolator and the oversampling of k-space (see Figure 5.4). Either a kernel wide enough to extend to the neighboring grid points is chosen, or a finer grid which corresponds to a gridding oversampling factor greater than 1. In the non-uniform fast Fourier transform (NUFFT), a separate, unique interpolation function is considered for each data sample. The computation of these interpolation functions for each data sample requires significant setup time. However, once the functions are computed, the functions can be used repeatedly, which is particularly advantageous for iterative model-based reconstructions.

## 5.4 Motion Robustness

The major benefit of radial sampling is a relatively lower sensitivity to object motion during the data acquisition which is explained by two main reasons. First, the superior robustness is a consequence of the fact that conventional Cartesian sampling is rather vulnerable to motion. Cartesian methods have unique frequency- and phase-encode directions. Due to the shift property of the Fourier transform, any motion in the image space translates into a phase modulation in the Fourier space and causes ghosting artifacts for Cartesian sampling [168, 172]. Ghosting artifacts are usually structured noise appearing as repeated versions of the main object and most commonly emerge along the phase-encode direction. Ghosting can be compensated [169], yet most of the correction methods rely on an assumed motion model

and residual artifacts can remain in the image. Unlike Cartesian methods, radial sampling does not have unique frequency- and phase-encode directions. Noise from moving anatomic structures does not propagate as discrete ghosts along a single phase-encode direction, but it is distributed more diffusely across the entire image as blurring or streaking. The artifacts occur at a certain distance from the moving object so that the error is spread more homogeneously over the image plane. Secondly, in radial acquisition, the center of k-space is oversampled, and the spokes contain a certain degree of redundant information. During the reconstruction, the center of k-space is averaged and errors in single acquisitions are balanced out. Further, the redundancy can be exploited to identify and correct for motion when the signal from the k-space center changes between readouts. The oversampling of the k-space center, which improves motion robustness, together with the general absence of ghosting artifacts provides a high potential of radial imaging for examinations of regions that are highly affected by motion [176, 177].

## 5.5 Off-Resonance Sensitivity

In radial imaging, off-resonance effects deviate from the related signal shifts in Cartesian gradient echo imaging. Off-resonance effects arise due to a certain distribution of resonance frequencies which arise from different origins. First, global magnetic field variations due to  $B_0$  inhomogeneities of the main magnetic field. To reduce off-resonance due to  $B_0$  non-uniformity typically shimming is applied. Second, local susceptibility induced magnetic field variations at susceptibility boundaries of the object, in particular at air-tissue interfaces. Third, chemical shifts due to the inter and intramolecular chemical environment of the tissue, in particular between water and fat. All these frequency deviations cause an additional phase term in the tissues signal which causes phase modulations in the received spatial information.

In Cartesian imaging, the k-space is sampled with equidistant  $dk$  along the frequency encoded readout direction. Thus, the signal modulation from the off-resonance adds an overall linear phase along the readout direction. In image space, the linear phase translated to a shift in the readout direction, where the shift distance depends on the local offset of the resonance frequency. In other words, object areas that are affected strongly by off-resonance effects are shifted in the readout direction, whereas areas with small off-resonance effects remain unchanged. In particular, water and fat have a frequency difference of approximately 3.5 ppm. Consequently, if the system's resonance frequency is set to water, the fat signal will be shifted and water-fat boundaries show artifactual white or dark bands (see Figure 5.5).

In radial imaging, the readout direction in k-space varies for all repetitions and the experienced phase evolution causes a shift with a different orientation for each radial spoke. As a result, off-resonance effects arise as a blurring in the image or a ringing depending on the frequency offset. In particular, the chemical shift effect between water and fat has a strong impact on the appearance of the tissue interface (see Figure 5.5). To reduce fat blurring typically the pixel bandwidth is increased. Besides the increased bandwidth, fat or water can be suppressed using magnetization preparation (see Section 3.2.4) or water-fat separation techniques (see Chapter 4) [69, 139, 178, 179].

## 5.6 Scan Time and Acceleration

3D radial scanning can be relatively time-consuming especially for large FOVs and requires acceleration of the data acquisition. Most modern MR systems use parallel imaging (PI),

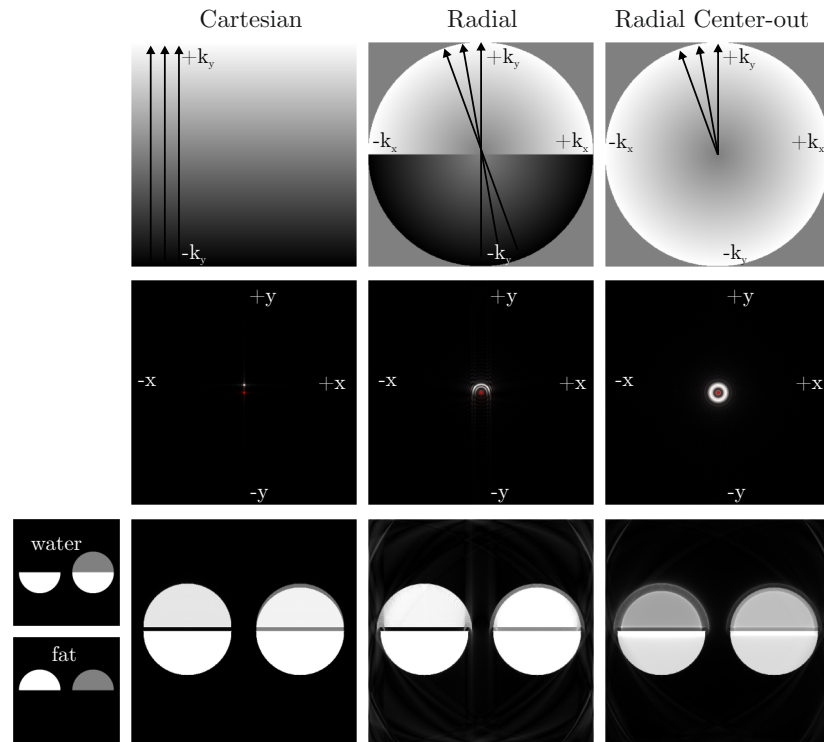


**Figure 5.5:** Off-resonance artifacts obtained for Cartesian, radial and radial center-out sampling. Graphical acquisition time maps are shown in the top row of the corresponding k-space trajectories (arrows). Points acquired at the beginning of the acquisition window are represented with darker shading and points acquired at the end of the acquisition window are represented with light shading. The phase accumulated due off-resonance effects leads to distortions. Middle row shows the PSF in k-space for water (on resonance) in red and for fat (frequency shift of 440 Hz) in white. Bottom row shows reconstructions of a water-fat phantom left. In the water map, the white represents voxels that contain 100% water, and gray represents 50% water. Similarly, in the fat map 100% fat is shown in white, and 50% fat gray. PSF: point spread function;  $k_x, k_y$ : Cartesian k-space coordinates;  $x, y$ : Cartesian images space coordinates.

such as sensitivity encoding (SENSE), where information about coil placements and coil sensitivities can be used to reduce the number of phase encoding steps and decrease scan time [180, 181].

Further, commonly slight angular undersampling (as discussed in section 5.1) is performed without significant degradation of image quality. To achieve realistic in vivo scan times, one of the new ways to handle undersampled datasets is to identify the MR mechanisms affecting a given protocol and integrate them into a single comprehensive signal model. That is, encompassing not only spatial but also hardware settings such as transmit/receive coil profiles. The reconstruction process then consists of estimating the most likely values by solving a complex inverse problem. The model-based reconstruction is usually iterative and includes a data fidelity term (i.e., the current reconstruction estimate must match the measured data) and regularization terms that help compensate for the missing data. These are combined into a cost function that penalizes the differences between the signal model and the measured data, so that the optimal solution can be determined by minimizing the value of this function. One of the most effective data-driven approaches is compressed sensing (CS), which takes advantage of the fact that MR images are sparse in some areas [182, 183].

Finally, trajectories can be optimized such that the k-space area covered per TR is increased. Examples for such sampling schemes are spiral [77, 130] or cone [76, 184] shaped trajectories. However, the length and shape of the trajectory is limited by the gradient specifications and the the tissue's  $T_2$ .

## 6 Compliance with Ethical Standards

All investigations performed in studies involving human participants were in accordance with the ethical standards of the institutional and/or national research committee and with the 1964 Helsinki declaration and its later amendments or comparable ethical standards. Informed consent was obtained from all individual participants included in the studies.

# 7 Comprising Journal Publications

## 7.1 Journal Publication I:

### **Trajectory correction based on the gradient impulse response function improves high-resolution UTE imaging of the musculoskeletal system**

The publication entitled *Trajectory correction based on the gradient impulse response function improves high-resolution UTE imaging of the musculoskeletal system* was published in *Magnetic Resonance in Medicine* (ISSN: 0740-3194) [185]. The manuscript was authored by Sophia Kronthaler, Jürgen Rahmer, Peter Börnert, Marcus R. Makowski, Benedikt J. Schwaiger, Alexandra S. Gersing, Dimitrios C. Karampinos. It is available online (DOI: 10.1002/mrm.28566) as an open access article under the terms of the Creative Commons Attribution-NonCommercial-NoDerivs License. Preliminary results were also presented in the conference contribution C8, which was awarded with an ISMRM Magna Cum Laude Merit Award and invited for a power pitch at the ISMRM annual meeting 2019. Additional to that, parts of the work were presented as a poster C6 at the ISMRM Workshop on Data Sampling and Image Reconstruction 2020. A summary of the publication is provided in Section 7.1.1 the author contributions are listed in Section 7.1.2 and the full text is included subsequently on the following pages.

#### 7.1.1 Abstract

##### **Purpose**

UTE sequences typically acquire data during the ramping up of the gradient fields, which makes UTE imaging prone to eddy current and system delay effects. The purpose of this work was to use a simple gradient impulse response function (GIRF) measurement to estimate the real readout gradient waveform and to demonstrate that precise knowledge of the gradient waveform is important in the context of high-resolution UTE musculoskeletal imaging.

##### **Methods**

The GIRF was measured using the standard hardware of a 3 Tesla scanner and applied on 3D radial UTE data (TE: 0.14 ms). Experiments were performed on a phantom, in vivo on a healthy knee, and in vivo on patients with spine fractures. UTE images were reconstructed twice, first using the GIRF-corrected gradient waveforms and second using nominal-corrected waveforms, correcting for the low-pass filter characteristic of the gradient chain.

##### **Results**

Images reconstructed with the nominal-corrected gradient waveforms exhibited blurring and showed edge artifacts. The blurring and the edge artifacts were reduced when the GIRF-

corrected gradient waveforms were used, as shown in single-UTE phantom scans and in vivo dual-UTE gradient-echo scans in the knee. Further, the importance of the GIRF-based correction was indicated in UTE images of the lumbar spine, where thin bone structures disappeared when the nominal correction was employed.

## **Conclusion**

The presented GIRF-based trajectory correction method using standard scanner hardware can improve the quality of high-resolution UTE MSK imaging.

### **7.1.2 Author contributions**

The first author performed the experiments (MR measurements); programmed the magnetic resonance pulse sequence (propriety hardware, specific libraries, and software from Philips Medical Systems, Best, The Netherlands), implemented the reconstruction using Matlab (Mathworks, Natick, MA) and a reconstruction toolbox (ReconFrame, Gyrotools, Switzerland). With the help and consultation from the coauthors, the first author designed the experiment, manufactured the GIRF measurement phantom, measured the GIRF, analyzed and interpreted the data, and wrote the paper.

# Trajectory correction based on the gradient impulse response function improves high-resolution UTE imaging of the musculoskeletal system

Sophia Kronthaler<sup>1</sup>  | Jürgen Rahmer<sup>2</sup>  | Peter Börnert<sup>2</sup> | Marcus R. Makowski<sup>1</sup> | Benedikt J. Schwaiger<sup>1</sup> | Alexandra S. Gersing<sup>1</sup> | Dimitrios C. Karampinos<sup>1</sup>

<sup>1</sup>Department of Diagnostic and Interventional Radiology, Technical University of Munich, Munich, Germany

<sup>2</sup>Philips Research, Hamburg, Germany

## Correspondence

Sophia Kronthaler, Department of Diagnostic and Interventional Radiology, Klinikum rechts der Isar, Technische Universität München, Ismaninger Str. 22, 81675 Munich, Germany.  
Email: sophia.kronthaler@tum.de

## Funding information

The present work was supported by the European Research Council (grant agreement no. 677661, ProFatMRI) and Philips Healthcare

**Purpose:** UTE sequences typically acquire data during the ramping up of the gradient fields, which makes UTE imaging prone to eddy current and system delay effects. The purpose of this work was to use a simple gradient impulse response function (GIRF) measurement to estimate the real readout gradient waveform and to demonstrate that precise knowledge of the gradient waveform is important in the context of high-resolution UTE musculoskeletal imaging.

**Methods:** The GIRF was measured using the standard hardware of a 3 Tesla scanner and applied on 3D radial UTE data (TE: 0.14 ms). Experiments were performed on a phantom, in vivo on a healthy knee, and in vivo on patients with spine fractures. UTE images were reconstructed twice, first using the GIRF-corrected gradient waveforms and second using nominal-corrected waveforms, correcting for the low-pass filter characteristic of the gradient chain.

**Results:** Images reconstructed with the nominal-corrected gradient waveforms exhibited blurring and showed edge artifacts. The blurring and the edge artifacts were reduced when the GIRF-corrected gradient waveforms were used, as shown in single-UTE phantom scans and in vivo dual-UTE gradient-echo scans in the knee. Further, the importance of the GIRF-based correction was indicated in UTE images of the lumbar spine, where thin bone structures disappeared when the nominal correction was employed.

**Conclusion:** The presented GIRF-based trajectory correction method using standard scanner hardware can improve the quality of high-resolution UTE musculoskeletal imaging.

## KEYWORDS

eddy currents, gradient imperfections, k-space trajectory distortions, MRI, short  $T_2^*$  species, UTE imaging

This is an open access article under the terms of the Creative Commons Attribution-NonCommercial License, which permits use, distribution and reproduction in any medium, provided the original work is properly cited and is not used for commercial purposes.

© 2020 The Authors. Magnetic Resonance in Medicine published by Wiley Periodicals LLC on behalf of International Society for Magnetic Resonance in Medicine



## 1 | INTRODUCTION

A variety of tissue components have short  $T_2$  relaxation times.<sup>1,2</sup> In conventional MRI, short- $T_2$  tissues appear as signal voids and are not directly visible.<sup>3</sup> UTE imaging is an approach that allows the detection of such short- $T_2$  signal components. UTE sequences have received increasing interest, especially in studies of the musculoskeletal (MSK) system, thanks to their ability to visualize short- $T_2$  tissue components such as those within cartilage,<sup>4</sup> knee menisci,<sup>5</sup> ligaments,<sup>6</sup> tendons, cortical bone,<sup>7</sup> and other similar examples.<sup>7-10</sup> Many of the above MSK tissues are associated with thin structures and therefore require high-resolution imaging. For instance, cartilage in the knee measures between 2 and 7 mm thick and has been shown to include short- $T_2$  components with  $T_2$  relaxation times in the order of 1 to 4 ms.<sup>11-13</sup> Separately, the mean thickness of cortical bone in the lumbar spine is found to be on the order of 0.3 mm, with short  $T_2$  relaxation times of 0.1 to 1 ms.<sup>7,14-16</sup>

UTE imaging is usually implemented along non-Cartesian trajectories to achieve data acquisition at UTEs. Data are acquired as soon as possible after the RF excitation and during the ramping up of the readout gradient. Due to the high slew rate and the time-varying gradients, effects including system delays, eddy currents, and the filter characteristics of the entire gradient chain can significantly degrade UTE image quality.<sup>3,17</sup> To obtain high-quality UTE images, a precise knowledge of the dynamic gradient fields, employed to perform the non-Cartesian spatial encoding, is required. Clinical scanners use preemphasis compensation and actively shielded gradients to minimize k-space trajectory deviations. However, the gradient waveform preemphasis is typically optimized for conventional clinical acquisition needs and for scanning with Cartesian sequences. The hardware preemphasis is calibrated to meet defined filter characteristics and is limited by a finite number of time constants to correct long-term eddy currents,<sup>18</sup> rendering them not perfect for correcting short time-constant eddy currents.<sup>19,20</sup>

A number of different techniques for the characterization of non-Cartesian trajectories have been proposed, including methods that require calibration scans and measure the gradient waveforms using either special NMR field probes<sup>21-23</sup> or the MRI scanner hardware.<sup>24-30</sup> Other techniques aim to extract such supporting information for k-space trajectory correction directly from the measured raw data without any calibration scans.<sup>31,32</sup> Once the gradient waveform is estimated, the corrected k-space trajectories are used for image reconstruction. Different approaches have been presented specifically in the context of UTE imaging, including methods that measure the actual k-space trajectories immediately before each UTE measurement for a given set of scan parameters<sup>33-35</sup> or that calibrate eddy current models individually to the scan parameters to obtain an appropriate

correction for arbitrary UTE scan settings.<sup>17,36,37</sup> Approaches that measure the actual k-space trajectories prior to each acquisition lengthen the total scan time, whereas model-based approaches necessitate a model that accurately considers not only eddy current effects but also other system delays and potentially mechanical vibrations. To better capture the different factors affecting the final actual gradient waveforms and to remove unnecessary model assumptions, it has been shown that the gradient system can be comprehensively characterized by the gradient impulse response function (GIRF).<sup>24,38</sup> Once the GIRF is estimated, arbitrary gradient waveforms, generated from any type of pulse sequence, can be corrected without any assumptions about the underlying mechanisms generating the gradient waveform deviations. GIRF measurements can be performed using either special NMR field probes<sup>21-23,38</sup> or using the thin slice method in simple phantoms.<sup>24,30,39-41</sup> It has been recently shown how gradient imperfections can impose spatially dependent artifacts in UTE images, which compromise the bone water quantification accuracy.<sup>42,43</sup> However, to the best of the author's knowledge, there has been no systematic investigation of the impact of gradient imperfection in high-resolution UTE MSK imaging.

The purpose of this work is to 1) propose a k-space trajectory correction for UTE imaging based on GIRF measurements using the thin slice method, which does not rely on additional hardware, and 2) apply the proposed correction method in high-resolution MSK UTE imaging. The proposed GIRF-based UTE trajectory correction method was first validated in a phantom and then was applied in vivo to study the influence of the trajectory correction, especially with regard to the high-frequency features in high-resolution UTE imaging of MSK tissues.

## 2 | METHODS

### 2.1 | Measurement of the GIRF

The GIRF measurement was based on a method introduced by Rahmer et al<sup>40</sup> and was simplified for the application in high-resolution UTE imaging. The following section summarizes key concepts of the applied GIRF measurement: A common assumption in most techniques applied in gradient chain characterization is that the MRI gradient chain can be modeled by a linear time-invariant system.<sup>19</sup> Such a system can be described by the impulse response function  $h(t)$ , which is equivalent to the time-domain response of the system to an idealized point impulse.<sup>44</sup> Under the linear time-invariant system assumption, the gradient chain is thus described by the GIRF in the context of MRI. The convolution of the input gradient with the GIRF yields the real gradient as it is played out in the scanner bore.

$$g_{real}(t) = \int_{-\infty}^{+\infty} h(t-\tau) \cdot g_{input}(\tau) d\tau \quad (1)$$

Equation (1) can be transformed to the frequency domain, resulting in

$$G_{real}(\omega) = H(\omega) \cdot G_{input}(\omega), \quad (2)$$

where  $H(\omega)$  is the gradient modulation transfer function (GMTF), which is the Fourier transform of the GIRF.<sup>40</sup>

To measure the behavior of the gradient system, Duyn et al.<sup>30</sup> introduced a method based on the excitation of a thin slice yielding the generation of a virtual 1D probe without needing any additional hardware (Figure 1A). The signal obtained from this 1D test probe was then used to measure the response of a test gradient, applied along the direction of the slice selection gradient. The difference between the measured signal phase with gradients applied with positive and negative gradient polarity, respectively, yielded the linear response that is only related to the test gradient.<sup>39</sup> In order to account for the spatial variation of the system response, several slices at different off-center locations were excited. Rahmer et al. added a phase encoding gradient in order to measure the 3D GIRF. They showed that looking at the 3D GIRF, one finds that second order components are negligible; thus, the 3D

GIRF measurement could in principle be replaced by a 1D GIRF measurement without changing the outcome.

Therefore, in this work a simplified measurement method was applied that measures the signal from 4 slices per gradient axis to estimate the first order response. A second order polynomial was fitted per gradient axis to only improve the quality of the fit (Supporting Information Figure S3). The real gradient waveform was calculated using the first order component of the fitted phase.

The GIRF was measured in a spherical phantom (diameter 166 mm, volume 2 liters) filled with CuSO<sub>4</sub>-doped water, resulting in a  $T_1 \approx 280$  ms and a  $T_2 \approx 240$  ms (values at 3 Tesla [T]). An excitation pulse with length 1.6 ms, maximum amplitude of 5.45  $\mu$  Tesla, and a flip angle of 45° was used to excite a 1.5 mm thick slice. To establish a high spectral density in the frequency range of interest for the GIRF measurements, a chirp waveform was played out as the input gradient with a frequency range of 0.1 to 10.0 kHz and an acquisition window of 80 ms, resulting in a frequency resolution of 12.5 Hz (Figure 1B). The acquisition window was determined based on a compromise between high-frequency resolution and adequate signal for the phantom's relaxation times. During the acquisition time, the gradient frequency increased linearly. To avoid ringing in the frequency response, the time-domain gradient waveform was ramped down by the multiplication with a half-Gaussian.<sup>38</sup> The measurement

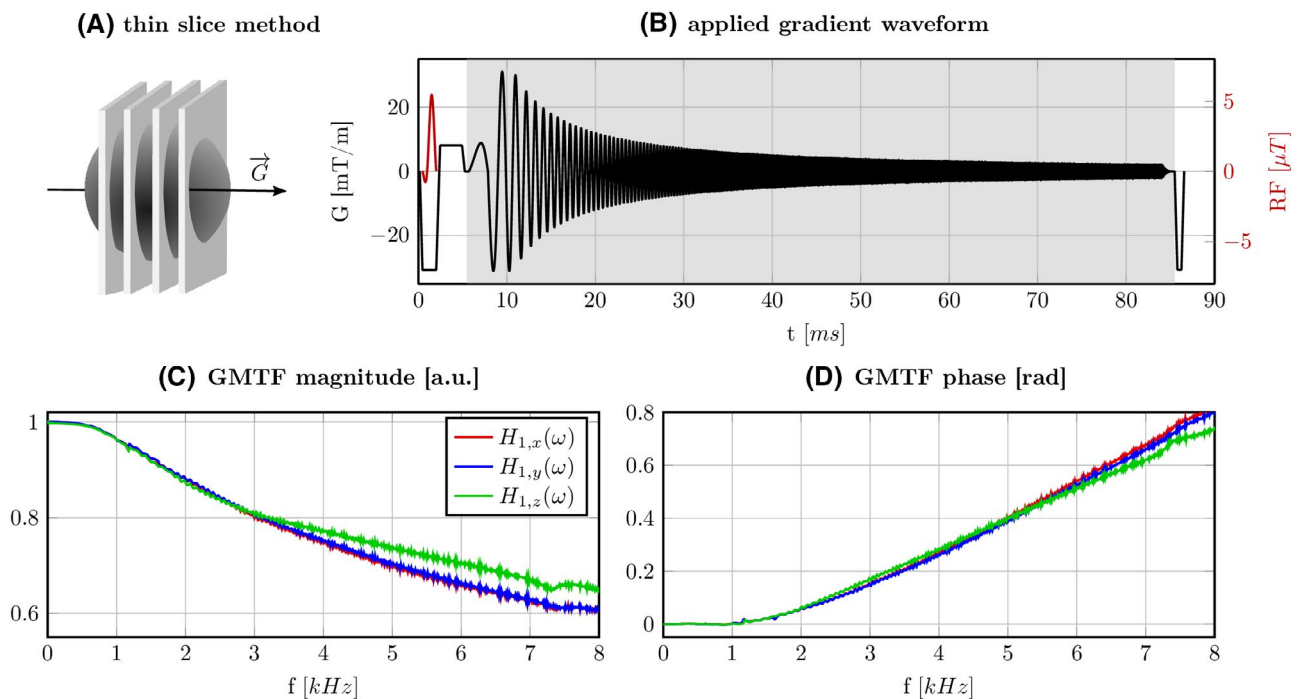


**FIGURE 1** Measurement of the GIRF: (A) Schematic diagram of the thin-slice method based on 4 slices per gradient direction. 1D information along the gradient direction is obtained by applying the slice encoding parallel to the measurement direction. (B) The applied chirp gradient waveform in the time domain (black) and the excitation RF pulse (red). The data acquisition window is indicated by the gray background color. (C,D) Measured spectra of the first-order GMTF  $H_1(\omega)$ . The colors indicate measurements of different gradient directions. Presented are the magnitude and phase in the range of 0 kHz to 8 kHz. GIRF, gradient impulse response function; GMTF, gradient modulation transfer function

was performed in 4 parallel slices located at distances of  $-26.25$  mm,  $-8.75$  mm,  $8.75$  mm, and  $26.25$  mm from the iso-center and repeated along all 3 gradient axes (Supporting Information Figure S3A-D). The chirp test gradient response was then calculated using the difference in the phase evolution of the measurements performed with positive and negative readout polarities. The following parameters were used for the GIRF measurement: TR of 2 s; slice thickness of 1.5 mm; 40 averages; sampling dwell time of  $1.28$   $\mu$ s; and 62,500 sampling points. The acquisitions of the 4 slices were interleaved and excited during 1 TR. The total scan time required for the acquisition of the GIRF measurement was defined as  $\text{TR} \times 40 \text{ averages} \times 2 \text{ polarities} \times 3 \text{ directions}$  and was equal to 4 min.

## 2.2 | UTE pulse sequence and image reconstruction

To measure the signal of tissues with short  $T_2^*$  values, a 3D UTE stack-of-stars sequence was employed<sup>45</sup> with a nonselective RF pulse. The excitation was followed by a variable-duration slice encoding gradient and a movable readout gradient. After the sampling of the FID at  $TE_1$ , a gradient echo with an opposite gradient readout polarity at  $TE_2$  was acquired (Figure 2A). The FID and the gradient echo were acquired during a single excitation along 1 radial “spoke.” An inner loop is defined along the rotation angle and an outer loop along  $k_z$ . All spokes within 1 slice were acquired with a uniform, constant azimuthal angle sampling pattern. The minimal FID readout time depended on the RF transmit–receive

switching time of the system. All images were acquired on a 3 Tesla system (Elition X, Philips Medical Systems, Best, the Netherlands).

The GIRF correction was applied as a part of the image reconstruction process.<sup>22,46,47</sup> To this end, the input gradient waveform was convolved with the measured GIRF to predict the real gradient waveform. This convolution can be simplified in the Fourier domain as a multiplication of the Fourier-transformed input gradient waveform with the GMTF. The predicted gradient waveform was used to calculate the k-space positions of the acquired data points. The GIRF correction provided the correction of the whole gradient waveform, including both the FID and the gradient echo.

The nominal correction was based on the default reconstruction of the manufacturer. The nominal gradient waveform applied during FID sampling was calculated by convolving the ideal gradient waveform with a simple, analytic, vendor-parameterized model of the system GMTF. This model was identical for all physical gradient axis. As a result of this convolution the input waveform was slightly smoothed and delayed. Regarding radial gradient echoes, eddy-current induced gradient delays can cause k-space shifts. The used radial acquisition scheme allowed for a simple spoke alignment correction<sup>48</sup>: the signals along spokes with opposed readout directions were correlated in image space to retrieve a phase offset.<sup>49,50</sup> Each spoke was corrected in image space by the estimated linear phase offset, which corresponds to a shift in k-space. The employed k-space spoke alignment for the echoes only shifted the k-space signal and did not affect the sampled k-space locations; therefore, the spoke-aligned gradient waveform is not displayed in Figure 2.

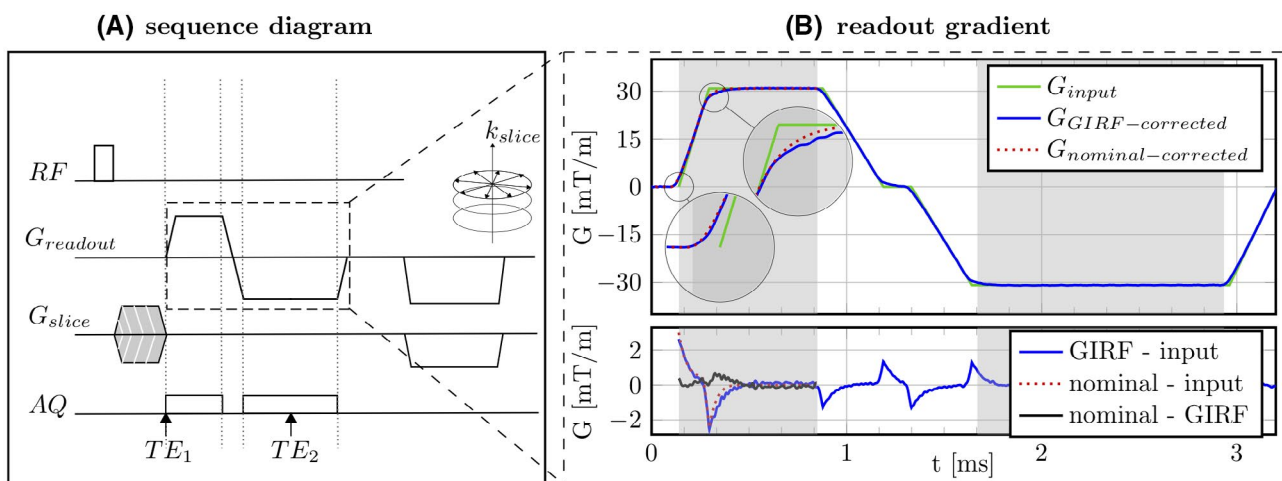


**FIGURE 2** UTE stack-of-stars pulse sequence diagram. (A) After the excitation and the 3D time encoding, the FID readout begins at time  $TE_1$ , followed by a gradient echo readout with  $TE_2$  using a gradient with opposite polarity to the FID. (B) The whole dual-echo UTE gradient waveform as a function of time after the RF excitation. The gradient echo readout was shifted to achieve a specific  $TE_2$  in which water and fat were in-phase. The data acquisition windows are indicated by the gray background color. Shown are the input gradient waveform  $G_{\text{input}}$ , GIRF-corrected gradient waveform, and nominal-corrected gradient waveform. In the nominal correction, only the FID readout gradient was corrected, and thus the nominal-corrected gradient was plotted solely for the FID readout. Bottom plot shows the error between the input gradient, GIRF-corrected gradient, and nominal-corrected gradient

For the reconstruction, an image reconstruction toolbox (ReconFrame, Gyrotools, Switzerland) was used to grid the data in 2 dimensions with the corresponding k-space trajectories, to Fourier transform in 3D, and to perform SENSE unfolding in the third Cartesian-sampled dimension. For the gridding, a Kaiser-Bessel kernel was used with a kernel width of 4 k-space sampling steps and a gridding oversampling factor of 1.25. The density was precompensated with weights that were estimated by counting the number of sampling points per ring segment. After the gridding, the image was normalized with the Fourier-transformed kernel function.

### 2.3 | Phantom measurements

A UTE stack-of-stars, high-resolution dual-echo scan was performed coronally in a phantom with an internal structure. The images were then reconstructed using 2 different trajectories: the nominal- and the GIRF-corrected trajectory. The employed sequence parameters were TE 0.14 ms/ 2.2 ms, TR 7.6 ms, flip angle 5°, in-plane resolution  $0.6 \times 0.6 \text{ mm}^2$ , slice thickness 1 mm, FOV  $210 \times 210 \times 100 \text{ mm}^3$ , dwell time 1.84  $\mu\text{s}$ , ramp length 0.15 ms, maximum gradient strength 30.36 mT/m, acquisition window 0.72 ms, 704 spokes, 393 samples, scan time of 6.15 min, and SENSE acceleration factor of 2 in the Cartesian-sampled dimension.

### 2.4 | In vivo measurements

In vivo imaging was performed in the knee of a healthy volunteer and in the lumbar spine of 4 patients with spine fractures after informed written consent by each subject and approval by the institutional review board (Klinikum rechts der Isar, Technical University of Munich, Munich, Germany). The spine fracture patients received an MR and a CT scan within 3 days after symptom onset. The CT scans were part of the clinical diagnostic workup.

For the knee measurements, 3D-UTE coronal and sagittal stack-of-stars dual echo measurements were performed with bipolar readout using a 16-channel transmit–receive knee coil and the following parameters: TE 0.14 ms/ 2.2 ms, TR 7.59 ms, flip angle 5°, in-plane resolution  $0.6 \times 0.6 \text{ mm}^2$ , slice thickness 1 mm, FOV  $190 \times 190 \times 164 \text{ mm}^3$ , ramp length 0.15 ms, maximum gradient strength 30.87 mT/m, dwell time 2  $\mu\text{s}$ , acquisition window 0.71 ms, 632 spokes, 355 samples, scan time of 9.2 min, and SENSE acceleration factor of 2 in the Cartesian-sampled dimension. For comparison, a Cartesian  $T_1$ -weighted gradient echo was acquired with an equal FOV  $190 \times 190 \times 164 \text{ mm}^3$ , equal resolution  $0.6 \times 0.6 \times 1.0 \text{ mm}^3$ , equal flip angle 5°, TE 2.3 ms, TR 4.3 ms and a scan time of 2 min,

and SENSE acceleration factor of 2 in the slice encoding dimension. For the subtraction of both echoes a scaling factor was estimated to suppress long  $T_2$  tissue components. A scaling factor of 1.5 gave the best water and fat suppression for a  $\Delta\text{TE}$  of 2.06 ms.

For the spine measurements, a single UTE was acquired using the built-in-table 16-channel posterior coil and the following parameters: TE 0.14 ms, TR 6.3 ms, flip angle 5°, in-plane resolution  $0.45 \times 0.45 \text{ mm}^2$ , slice thickness 3 mm, FOV  $250 \times 250 \times 279 \text{ mm}^3$ , ramp length 0.08 ms, maximum gradient strength 15.04 mT/m, dwell time 3.12  $\mu\text{s}$ , acquisition window 1.77 ms, 945 spokes, 568 samples, radial percentage of 85%, half-scan factor of 0.6 in slice direction, and scan time of 6.3 min.

The nominal and GIRF-corrected UTE spine images were independently read by 2 radiologists. The individual vertebrae, L1-L5 and S1, of 3 scanned subjects were scored with a 4-point Likert scale. The radiologists rated the GIRF-corrected and nominal-corrected images with respect to the diagnostic quality of cortical bone visualization from 1 (poor) to 4 (excellent).

### 2.5 | CT measurements

CT was performed on 1 of 2 CT scanners (Somatom Definition AS+, Siemens Healthineers, and IQon Spectral CT, Philips) with the following parameters according to routine clinical protocols: collimation, 0.6 mm; pixel spacing, 0.4/0.3 mm; pitch factor, 0.8/0.9; tube voltage (peak), 120kV; modulated tube current, 102–132 mA. Images were reformatted in 3 mm slice thickness using a bone-specific convolution kernel (I70H/YB).

## 3 | RESULTS

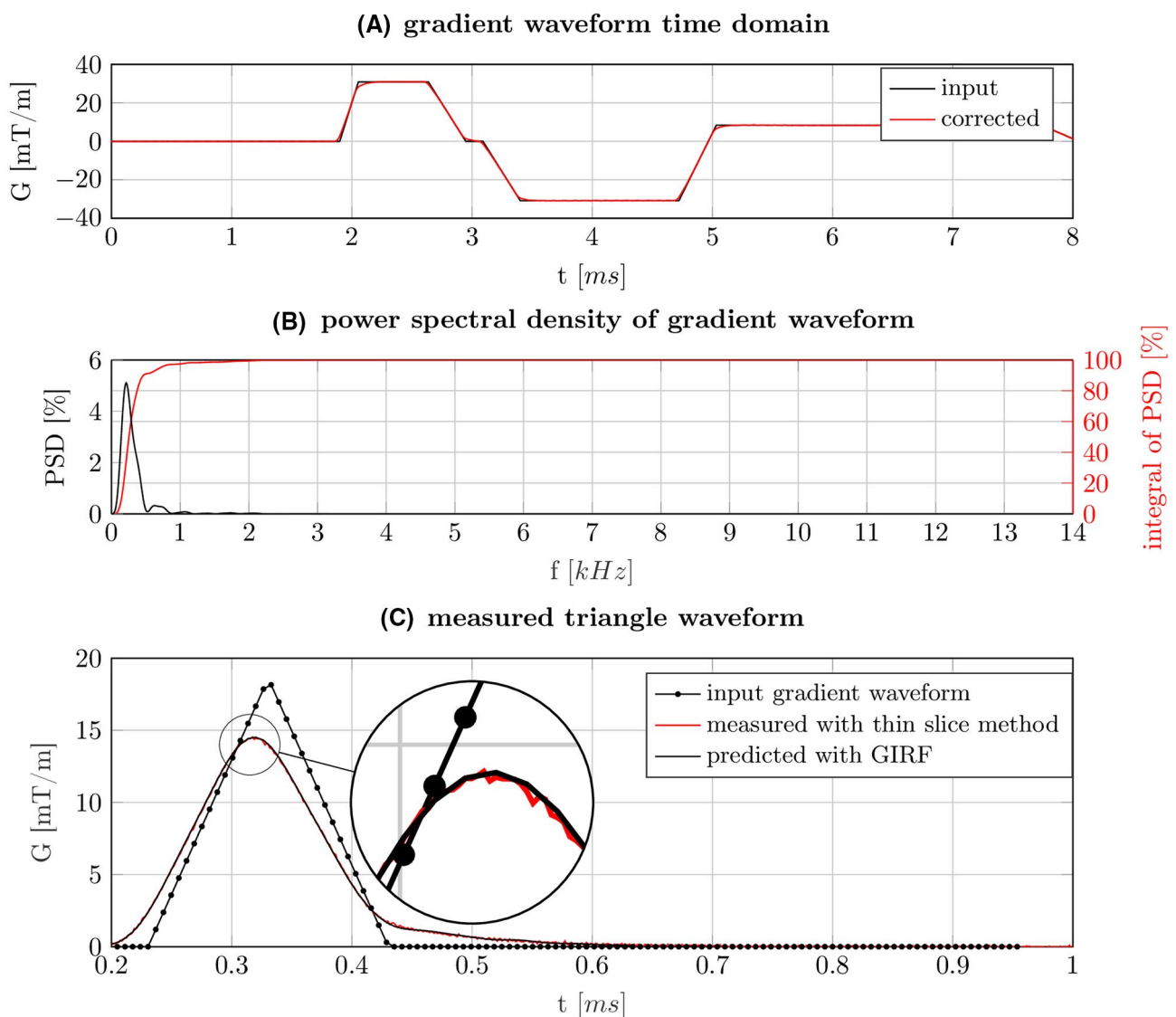
### 3.1 | GIRF measurement results

Figure 1 shows the magnitude and phase of the measured GMTF and depicts the GMTF's low-pass frequency behavior in all 3 axes. Small peaks are visible in the low frequency part of the GMTF, which correspond to mechanical resonances of the gradient coils, for example, at 1.2 kHz. The magnitude of the GMTF for all 3 axes behaved very similarly in the frequency range up to 3 kHz. For frequencies higher than 3 kHz, the  $x$  gradient and  $y$  gradient had lower transfer ratios than the  $z$  gradient, indicating anisotropic eddy current effects. The phase response varied slightly for frequencies of greater than 2 kHz and different gradient directions, indicating a different gradient delay for each axis (Supporting Information Figure S2). The structured noise between 2 kHz to 3 kHz can result from gradient amplifier nonlinearities that distorted the chirp

waveform. The noise in the GMTF measurement increased toward higher frequencies (Supporting Information Figure S3D). Higher frequencies were acquired at the end of the chirp impulse where the gradient strength decreased and the excited signal dropped, which can result in a smaller SNR. The measured GIRF contained information up to a frequency of 10 kHz. The power spectral density of a typical UTE readout gradient showed main contributions in the frequency range below 2 kHz. The integral of the power spectral density reached 95% of the energy after 2 kHz (Figure 3A,B). A comparison of measured gradient waveform and GIRF-predicted gradient waveform showed a good agreement (Figure 3C). There were no systematic changes of the GIRF observed

during repeated measurements over a time span of 1 month (Supporting Information Figure S4).

Figure 2B presents the input waveforms, the nominal-corrected waveforms, and the GIRF-corrected waveforms of the readout gradient as a function of time and after the excitation. The deviations during the FID readout were dominated by short-term effects. There was an increase in the size of deviations from the input gradient waveform during the ramping up of the gradients. Once the plateau was reached, eddy current effects decayed quickly. In comparison, the nominal-corrected gradients and the GIRF-corrected gradients diverged at the very beginning of the FID readout. Regarding the gradient echo readout, there was a short-lived eddy current



**FIGURE 3** (A) typical UTE readout gradient waveform in time domain and (B) its PSD in frequency domain. The measured GMTF based on a chirp test gradient contains information for frequencies up to 10 kHz. The PSD of a typical UTE readout gradient shows main contributions in the frequency range below 2 kHz. The integral of the PSD shows that after 2 kHz, 95% of the energy is reached. (C) Comparison of a measured triangular gradient waveform with the thin slice method, triangular input gradient waveform, and predicted waveform with the GIRF. On the right, the zoomed-in window shows in detail the difference between the GIRF-predicted waveform and the waveform measured with the thin slice measurement for the triangular gradient waveform. PSD, power spectral density

component that was still present at the beginning of the data acquisition window. These deviations at the beginning of the readout resulted in k-space trajectory errors at high frequencies in the radial spoke. Simulations were performed to study the effects of readout gradient waveform deviations on the reconstructed images (Supporting Information Figure S1). The deviations between the GIRF-corrected and nominal-corrected trajectories introduced blurring and an overshoot of signal intensity at object borders between regions with high and low signals.

### 3.2 | Phantom results

Figure 4 shows UTE images of the structural phantom reconstructed with the nominal-corrected and with the GIRF-corrected k-space trajectories, respectively. Line profiles depict the signal intensity along the white lines and highlight edge artifacts in the nominal-reconstructed images. Using the nominal-corrected gradient waveforms in the reconstruction resulted in an overshoot of the signal at borders between regions with signal and regions without signal. Further, in the nominal-reconstructed images, the halo effect was visible, and high-resolution features were blurred. The halo effect and the blurring were visible particularly at borders between regions with signal and regions without signal. Using the

GIRF-corrected gradient waveforms reduced the hyperintense edge artifacts, minimized the halo effect, and reduced blurring effects. The observed artifacts followed a similar pattern to those in the simulated data.

### 3.3 | In vivo results

In vivo images of a volunteer's knee joint are shown in Figure 5. Edge artifacts were present at the air–tissue borders in the images reconstructed with nominal-corrected gradients. Edge artifacts were also located near bone–soft-tissue borders. The signal of the cartilage next to the cortical bone was thus overestimated and blurred. Due to the blurring, the thin cortical bone structure was blurred and almost vanished. The aforementioned blurring was removed when the images were reconstructed with the GIRF-corrected trajectories.

Figure 6 shows a radial gradient echo image that was acquired after a UTE-FID readout and compares it to a Cartesian gradient echo image. The radial images were reconstructed by applying a k-space spoke alignment and using the GIRF-corrected gradient waveforms. The use of the GIRF-corrected gradient waveforms improved the contrast, enhanced the homogeneity, and achieved a better agreement of the signal variation with the Cartesian reference scan. In Figure 7, the radial gradient echoes were compared with the

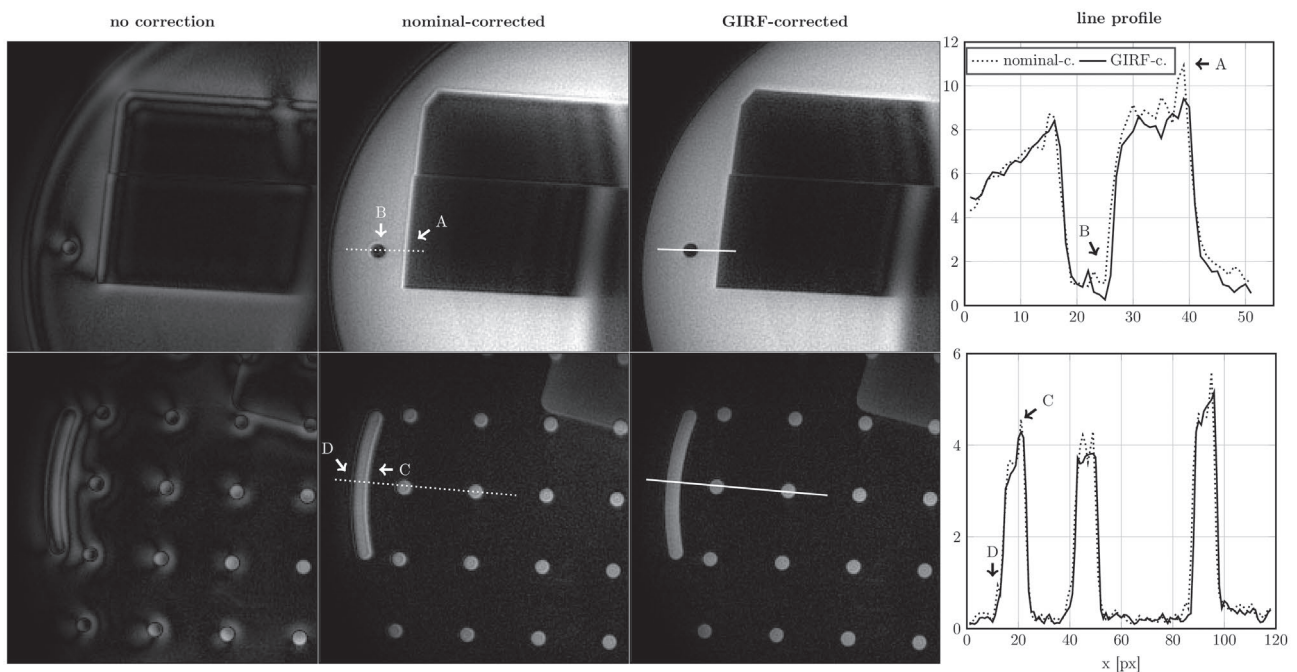


**FIGURE 4** UTE stack-of-stars images of a structural phantom that was scanned coronally. The phantom images were reconstructed using noncorrected, nominal-corrected, and GIRF-corrected trajectories. Line profiles depict the signal intensity along the white lines shown on the left. Artifacts are highlighted by arrows. The use of the nominal-corrected trajectories in the reconstruction resulted in edge artifacts. At borders between regions with signal and regions without signal (arrows A and C), the signal showed overshoots and formed hyperintense edges. As compared with the GIRF-corrected images, the nominal-corrected images showed a higher signal in the regions without signal (arrows B and D) and blurred high-resolution features

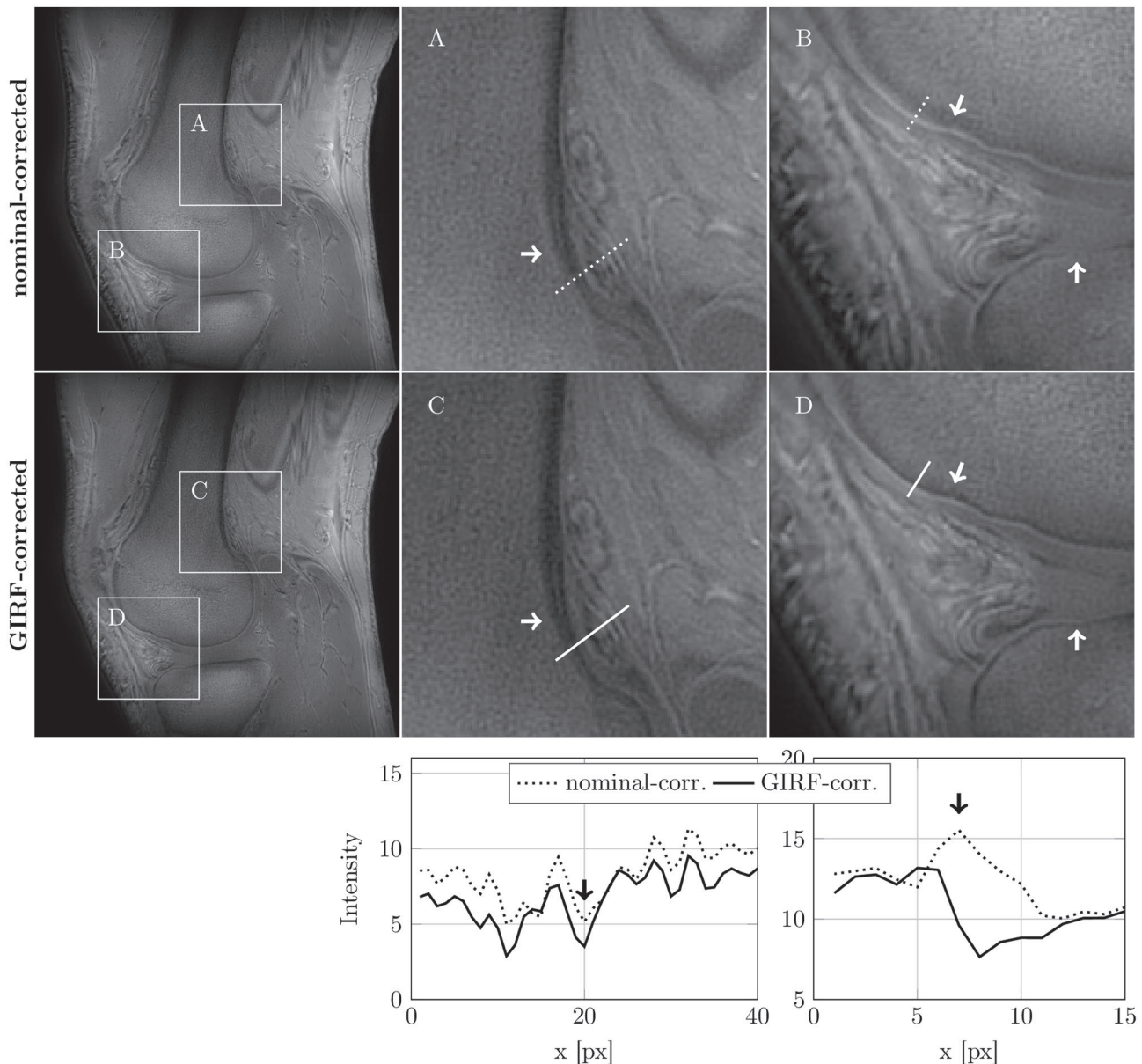


**FIGURE 5** In vivo UTE sagittal knee images with the Cartesian-encoded dimension being perpendicular to the shown slices. The UTE images were reconstructed using the nominal gradient waveforms and the GIRF-corrected waveforms. Line profiles depict the signal intensity along the white lines shown in the presented image. White arrows in the images and black arrows in the line plots highlight regions where thin cortical bone structures are blurred. In comparison to (A), the cortical bone shows higher contrast and appears slightly thinner in (C). In (B) the thin cortical bone at the cartilage border is barely visible, whereas the deep cartilage appears exaggerated and blurred. In (D), the cortical bone and the deep articular cartilage are sharper and better depictable

FID images of the same scan. The difference map highlights edge artifacts in the images reconstructed using the nominal-corrected trajectory for the FID and the k-space spoke alignment for the echo. Thin cortical bone structures were blurred and misclassified as soft tissue when not using the GIRF-corrected trajectories.

Figure 8 shows an in vivo sagittal lumbar spine UTE image of a patient with a spine fracture, reconstructed using nominal-corrected and GIRF-corrected gradient waveforms. The upper row of Figure 8 presents the reconstructed full-FOV with the natural contrast, whereas the contrast was inverted in the

bottom row of Figure 8 so that bone appears bright for a better visual comparison with the CT image. The CT and MRI data were manually coregistered in 3D with respect to the vertebra indicated by the blue cross. In the nominal-reconstructed UTE images, thin bone structures appeared bright in the natural contrast and were misclassified as soft-tissue because high-resolution features were blurred. The shape of the vertebra was better visualized with the GIRF-corrected reconstruction.

Figure 9 compares UTE images and CT images of 3 patients with spine fractures using zoomed-in sagittal slices of the lumbar spine. The contrast of the MR images was inverted

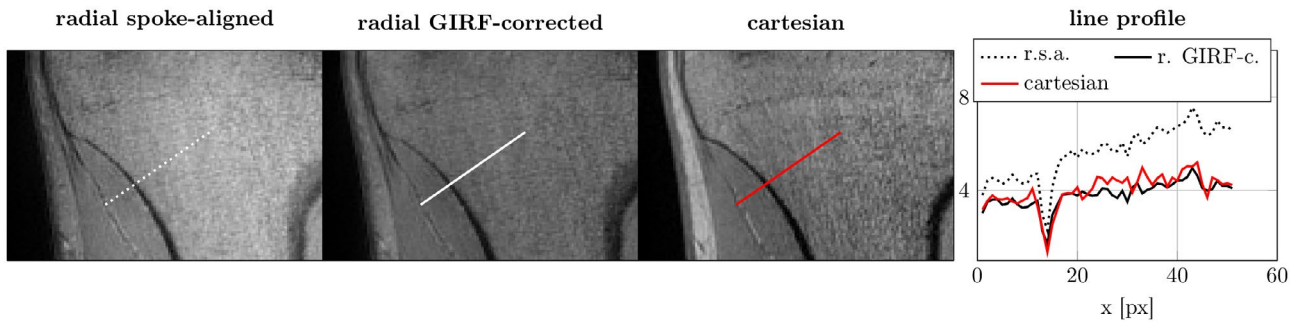


**FIGURE 6** In vivo radial and Cartesian gradient echo knee images. The radial gradient echo was acquired after a UTE-FID readout with an opposite gradient polarity to that of the UTE-FID readout. The images were reconstructed by applying k-space spoke alignment and with the GIRF-corrected gradient waveforms. A Cartesian gradient echo with the same TE was acquired for comparison. The line profile depicts the signal amplitude along the lines presented on the left. The contrast, homogeneity, and agreement between radial and Cartesian signal were improved by means of the GIRF-corrected gradient waveforms

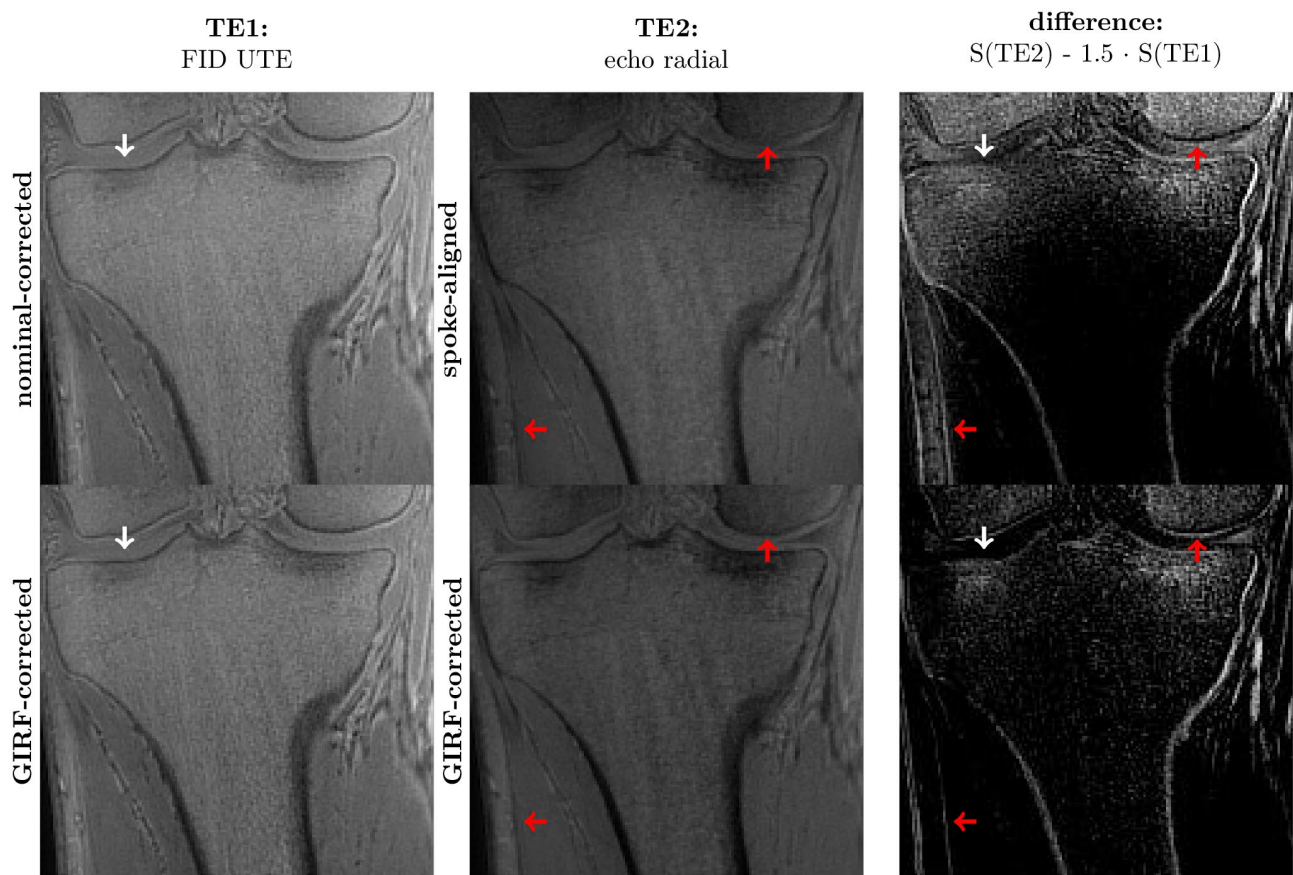


**FIGURE 7** In vivo UTE dual-echo knee images. Upper row: FID corrected with the nominal-corrected gradient waveforms, radial gradient echo image reconstructed after k-space spoke alignment, and the difference of the signals. Bottom row: Same as in the top row albeit with FID and radial gradient echo reconstructed with GIRF-corrected gradient waveforms. White and red arrows highlight improvements due to the GIRF-correction in the FID-UTE and the radial gradient echo images, respectively. In the nominal-reconstructed UTE and the k-space spoke aligned radial gradient echo images, high-resolution features were blurred. In the difference maps, these thin blurred structures disappeared and bone was misclassified as soft tissue. Further, the k-space spoke aligned radial gradient echo images appeared inhomogeneous, which is leading to a misclassification of soft tissue as bone. The GIRF-correction improved both the FID images and radial gradient echo images, reduced blurring, and amended the homogeneity

such that bone appears bright. In all scans, the image quality was improved using the GIRF-corrected gradient waveforms. The images were less blurry, had higher contrast, and the bone

structures became more visible when using GIRF-corrected versus nominal-corrected gradients. The shape of the vertebra in the GIRF-corrected images matched the shape of the



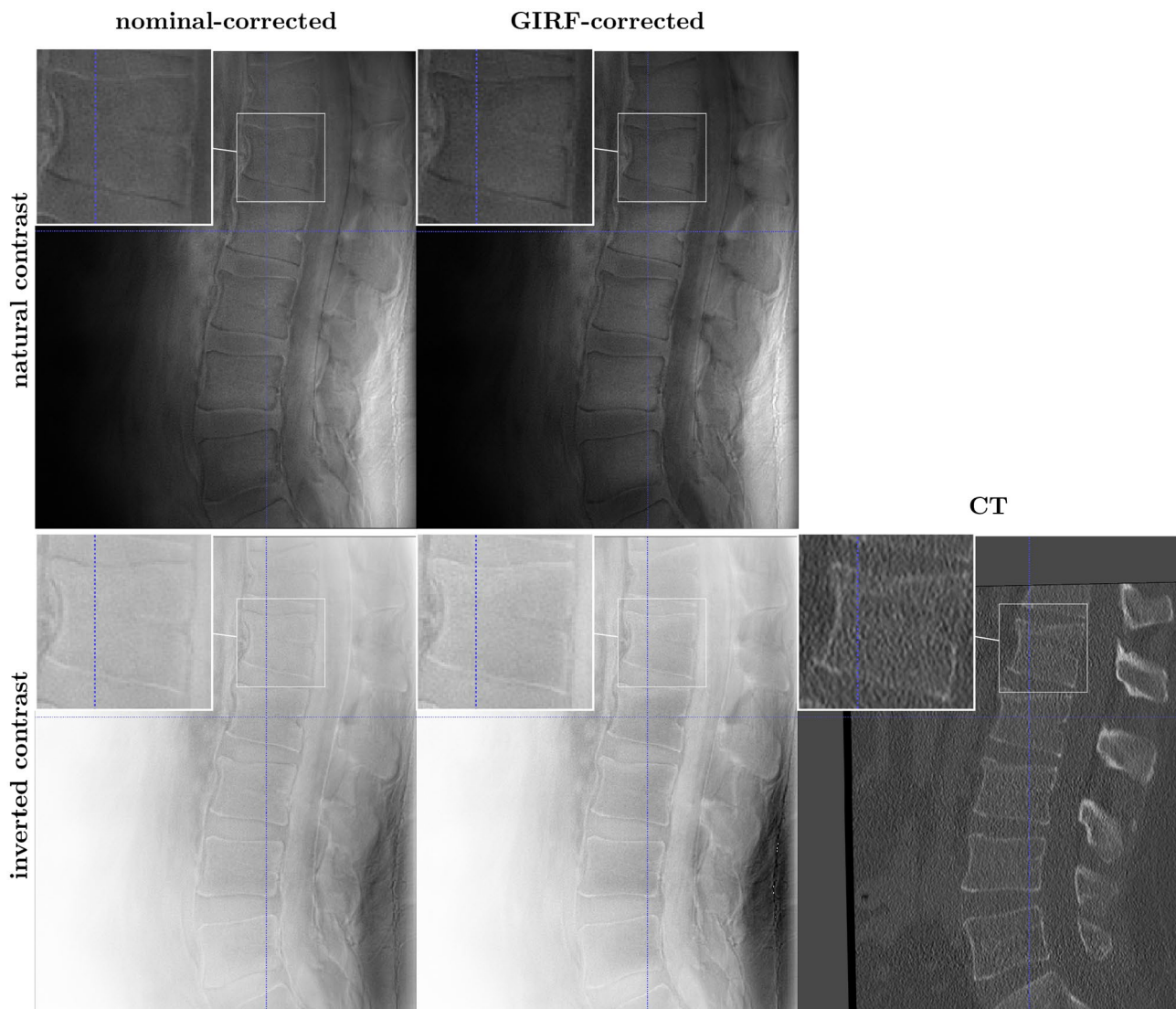


**FIGURE 8** In vivo UTE lumbar spine sagittal images of a patient with a spine fracture. The UTE images were reconstructed using the nominal-corrected gradient waveforms and GIRF-corrected waveforms. Upper row: the full FOV with the natural contrast. Bottom row: same as the upper row but the contrast was inverted for comparison with the CT image. The CT and MRI data were manually coregistered in 3D at the point indicated by the blue cross. In the nominal-reconstructed UTE images, high-resolution features were blurred. Thin bone structures appeared bright and were misclassified as soft tissue. The improvements due to the GIRF-corrected reconstruction made it easier to determine the shape of the vertebra

vertebra in the CT scans. In the nominal-corrected images, the thin bone structures were blurred, and the contrast could change from bright to dark in the inverted images, leading to the misclassification of bone as soft tissue or connective tissue. The rating of the diagnostic quality of the cortical bone visualization showed significant better results for the GIRF-corrected images than for the nominal corrected images and a high agreement among the readers. The median and SD scores of the rating for the GIRF-corrected images were  $3.17 \pm 0.79$  (good) for the first reader and  $3.28 \pm 0.83$  (good) for the second reader. The diagnostic quality of the nominal-corrected images was rated significantly lower than the GIRF-corrected images, with scores equal to  $1.78 \pm 0.64$  (moderate) for the first reader and  $1.83 \pm 0.70$  (moderate) for the second reader.

## 4 | DISCUSSION

Gradient chain miscalibration-induced artifacts are known to lead to errors in UTE MRI sequences, and it has been shown that eddy current and delay effects can be corrected for by measuring the k-space trajectories. This work demonstrated that, with a GIRF measured using the standard scanner hardware, the image quality of radial UTE images can be reliably improved. It was shown that the reduction of blurring and artifacts is especially crucial in high-resolution MSK imaging of thin bone structures and thin connective tissues. Without the GIRF-corrected reconstruction, such thin bone structures disappear or can become even misclassified as soft tissue. The improvements of a correction based on a GIRF

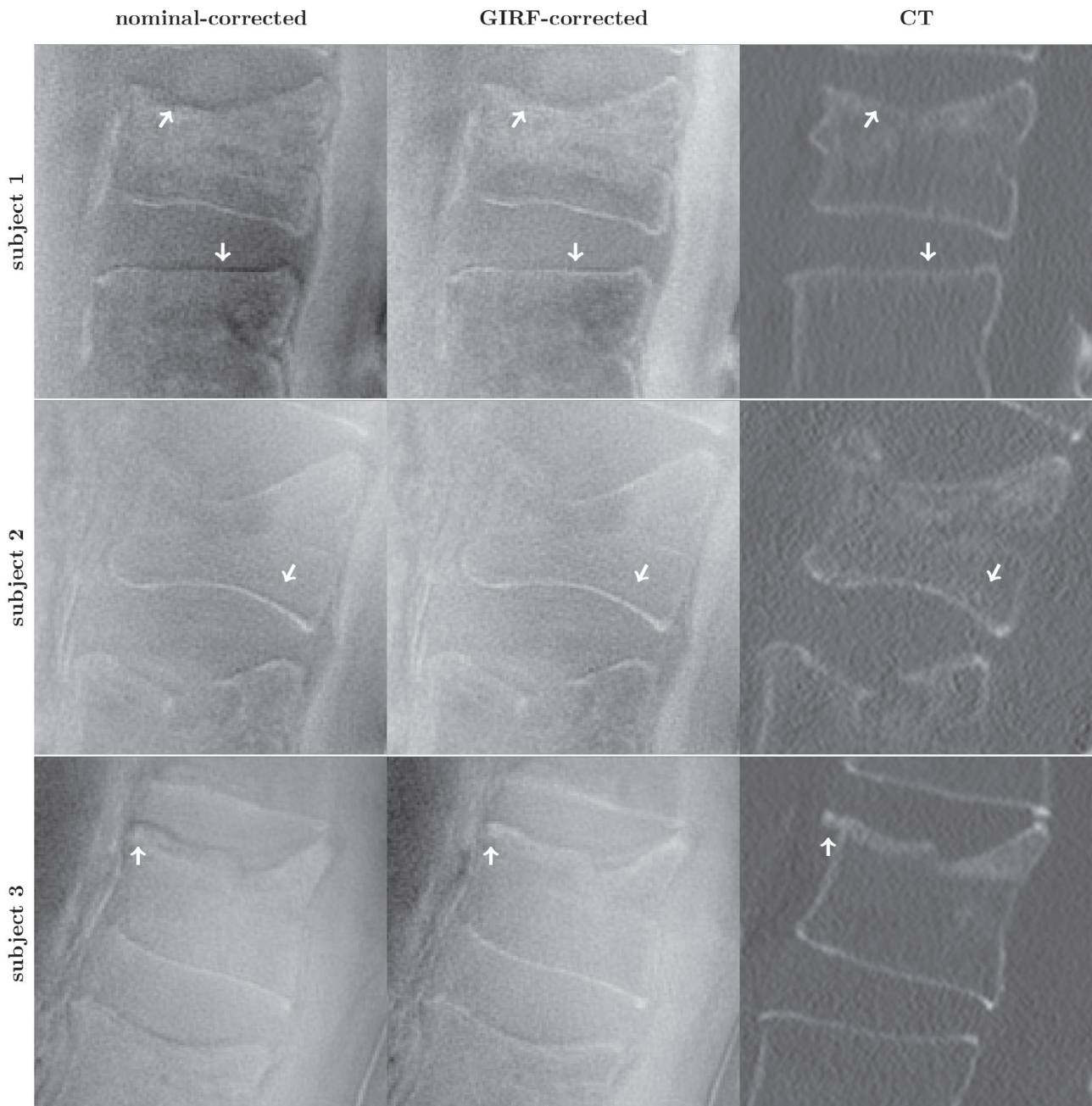


**FIGURE 9** In vivo UTE lumbar spine sagittal images of 3 patients with spine fractures. The contrast of the MR images was inverted such that bone appears bright. White arrows highlight improvements achieved with the GIRF-correction. In subject 1, thin bone structures appeared dark in the nominal-corrected images where a bright bone was expected as compared with the CT images. In subject 2, the vertebral body appeared blurred and with a less contrast in the nominal- versus the GIRF-corrected images. Subject 3 showed a sclerotic zone as a result of the fresh vertebral fracture. Once again, in comparison with the CT, areas with expected high signals appeared dark in the nominal-corrected images. In all scans, the image quality was improved using the GIRF-corrected gradient waveforms. In comparison with the CT images, the shapes of the vertebrae were depicted better in the GIRF-corrected images

acquired in a simple phantom scan were presently verified with phantom and in vivo measurements. The results not only reproduced prior reported improvements to UTE trajectory-correction methods for reducing both undershoot and overshoot of signal intensity at object-background borders but primarily highlighted the need of k-space trajectory correction in high-resolution UTE imaging.

Typically, eddy current correction methods measure directly the gradient with specialized NMR field probes,<sup>21,23,33,51</sup> perform separate calibration scans,<sup>24,30,52,53</sup> or extract information directly from the measured raw data without any additional calibration scans.<sup>31,32,54</sup> It was also previously reported that eddy currents can be corrected by measuring a transfer function to describe the gradient

characteristics.<sup>22,38,47,55</sup> Eddy current correction in the context of UTE imaging was done before by measuring the UTE gradient waveforms for a fixed parameter set with specialized NMR field probes<sup>33</sup> and by running calibration scans in a phantom before the actual measurements were performed.<sup>17,36,42</sup> The proposed GIRF measurement showed that the use of a chirp-based LTI model<sup>22,24,47</sup> is able to provide a transfer function that improves the reconstruction of UTE images independently of imaging parameters and required no additional hardware. The spectrum of the chirp waveform covered a large frequency range without blind spots and with high spectral density (12.5 Hz) and enabled a fast measurement (4 min) when compared to triangular input functions. However, at low frequencies (< 100 Hz), the chirp's spectral density approached 0, leading to a diverging intensity in the spectrum of the GIRF.<sup>56</sup> The proposed GIRF-based correction method for eddy-current correction has the advantage that only a 1-time calibration scan is needed, and the measured transfer function can be used in all subsequent image reconstructions. The measured GIRF indicates anisotropic eddy-current behavior that depends upon the gradient axis. No gradient terms of a second- or higher-order were measured with the phantom-based method, whereas such higher-order terms could be derived based on a field camera<sup>38,46</sup> or from a 3D phantom based approach using phase encoding.<sup>40</sup>

The performed simulations and phantom measurements investigated artifacts on the reconstructed images, originating from the readout gradient waveform deviations, including blurring, changes in background signal, and emphasized edge effects. An important aspect of the simulations was the introduction of a gradient delay to the low-pass model-based correction method. Approaches determining a single delay are widely used for radial acquisition schemes, for which the sampling is performed on the flat top of a trapezoidal gradient. The simulations showed that the simple model with an additional gradient delay is not sufficient as a k-space trajectory correction method for high-resolution UTE imaging. In addition, the simulations showed that the GIRF correction accounts for the dependence of the response on the readout gradient axis, whereas the model-based correction method cannot easily account for such effects. To obtain the best reconstruction result the accurate gradient waveform is needed with an exactly calibrated delay. The GIRF correction method is model-independent and requires no manual delay optimization. The analysis of the phantom experiments reproduced previously simulated artifacts such as blurring, background signal, and edge enhancement. All of these artifacts were reduced using the GIRF-corrected gradient waveforms, indicating that the GIRF-corrected gradient waveforms comprise important features of the real gradient waveforms such as the delay and the axis-dependent gradient shape. To summarize, the GIRF correction method is based on the transfer function

of the entire gradient system and thus describes better than any other correction models its behavior, thus allowing a better prediction of the k-space deviations induced by the gradients in UTE imaging.

In vivo, the GIRF correction was applied to high-resolution UTE images, showing the improvements for thin tissues in the knee such as cortical bone and cartilage. Further, the GIRF correction was applied to the FID-echo readout with opposite gradient polarities for the FID and the gradient echo. The correction of FID and gradient echo k-space trajectories were performed in 1 step. Conversely, traditional correction methods include 2 steps for the reconstruction of UTE-multi-echo data and correct the FID (using the nominal correction) and radial gradient echo data (using the k-space spoke alignment) separately. Such traditional correction methods can become slower and can lead to inconsistencies in the signal amplitude between the FID and the echo. Gradient waveform deviations can additionally lead to geometric distortions such as stretching and shifting. The GIRF correction treats FIDs and echoes in the same way. The GIRF-based correction method is therefore important if FIDs, and radial echoes are supposed to be matched, for example, to subtract both images to get rid of long  $T_2^*$  components and to highlight short  $T_2^*$  components.

The comparison of UTE in vivo spine images with CT images highlighted the importance of a GIRF-based correction method of UTE images for high-resolution features. Gradient waveform deviations can blur thin bone structures and fine connective tissues. Overestimated edges can lead to the misclassification of bone as soft tissue. The proposed methodology could therefore be particularly useful first for UTE CT-like imaging<sup>57</sup> or attenuation correction for PET/MRI,<sup>33,58</sup> where UTE sequences have been proposed to help to distinguish between cortical bone and air. Second, the proposed methodology could be useful for generating high-quality UTE-based CT-like images for diagnostic musculoskeletal imaging, especially in the evaluation of bone changes. MR-based CT-like imaging has been recently proposed, aiming at reducing the radiation burden on the patient, avoiding the need to perform additional X-ray and CT imaging when MR is already part of clinical care,<sup>59</sup> and achieving a hybrid contrast.<sup>60</sup> To further improve the image contrast of UTE imaging of bone structures, long  $T_2$  components could be further suppressed by employing inversion recovery and fat saturation techniques.<sup>61,62</sup>

The proposed correction method was shown to be beneficial not only in high-resolution single-echo UTE imaging but also in dual-echo imaging. Therefore, our results might imply a level of importance of the gradient corrections when UTE sequences are employed for UTE multi-echo imaging that acquires more than 1 TE per TR. Further, correcting the UTE trajectories could also be beneficial in the context of quantitative  $T_2^*$  measurements of short  $T_2^*$  tissues when employing

UTE multi-echo imaging and acquiring more than 1 TE per TR.<sup>62</sup>

The present work has several limitations: First, the present work does not address the effect of  $B_0$  eddy currents, which may promote unwanted phase accumulation of the sampled signal. We expect the effect to be small in UTE imaging because the k-space center is initially measured. However, because the  $B_0$  transfer function can be extracted from the acquired GIRF data, this correction could be readily implemented. Second, the measured GIRF contained information up to a frequency of 10 kHz. This is sufficient for typical UTE readout gradient waveforms yet may not be sufficient for arbitrary gradient waveforms. Third, the proposed correction method requires that the reconstruction is able to use the predicted trajectories in order to produce the corrected images. Therefore, an interface for providing the corrected trajectory to the gridding algorithm or the use of a custom-designed image reconstruction framework is required. Fourth, the GIRF-based correction method requires the precise knowledge of the input gradient waveforms in order to predict the real gradient waveform. Such knowledge may not be accessible for all vendor-specific sequences. The increased reconstruction complexity and the need of input waveforms to perform the correction might affect the future adoption of the GIRF-based correction method. Fifth, the presented CT-like images of the cortical bone in the lumbar spine by inverting the contrast of UTE images could be confounded by the fact that the UTE images are  $T_2^*$ -weighted,  $T_1$ -weighted, and proton density-weighted. This mixed weighting of UTE images could affect the ability of inverting the contrast of UTE images in resolving bone structures at least at the presently used parameters (TE, TR, and flip angle). Zero TE sequences have been recently used for CT-like imaging of bone structures by inverting the contrast of zero TE images, which have been considered to be primarily proton density-weighted.<sup>60,63,64</sup> The inversion of the contrast of UTE images was presently shown as only an example of the effect of UTE trajectory correction on a clinically relevant, high-resolution MSK imaging setting. The ability of inverted UTE images for CT-like bone imaging in the lumbar spine requires further investigation. Finally, the GIRF-based correction method does not adapt geometric distortions caused by spatial nonlinearities in the gradient fields at the edge of the FOV. These nonlinearities are static and do not account for dynamic trajectory errors from eddy currents.

## 5 | CONCLUSION

A simple phantom-based GIRF measurement and standard MRI scanner hardware were used to estimate k-space trajectories for high-resolution UTE MSK imaging, and in particular to improve cortical bone visualization. It was demonstrated that the correction based on the measured GIRF minimizes artifacts due to gradient waveform distortions in

comparison with a model-based trajectory correction method representing a typical implementation on a clinical system.

## ACKNOWLEDGMENT

The authors would like to thank Dr. Roland Krug for helpful discussions related to UTE imaging. The present work was supported by the European Research Council (grant agreement no. 677661, ProFatMRI). This work reflects only the authors' views and the European Union is not responsible for any use that may be made of the information it contains. Finally, the authors acknowledge research support from Philips Healthcare. Open access funding enabled and organized by Projekt DEAL.

## CONFLICT OF INTEREST

The authors PB and JR are employed by Philips GmbH Innovative Technologies.

## ORCID

Sophia Kronthaler  <https://orcid.org/0000-0001-7913-1238>

Jürgen Rahmer  <https://orcid.org/0000-0001-8514-4801>

## REFERENCES

1. Gatehouse PD, Bydder GM. Magnetic resonance imaging of short T2 components in tissue. *Clin Radiol*. 2003;58:1-19.
2. Robson MD, Gatehouse PD, Bydder M, Bydder GM. Magnetic resonance: An introduction to ultrashort TE (UTE) imaging. *J Comput Assist Tomogr*. 2003;27:825-846.
3. Weiger M, Pruessmann KP. Short-T2 MRI: Principles and recent advances. *Prog Nucl Magn Reson Spectrosc*. 2019;114-115:237-270.
4. Pauli C, Bae WC, Lee M, et al. Ultrashort-echo time MR imaging of the patella with bicomponent analysis: Correlation with histopathologic and polarized light microscopic findings. *Radiology*. 2012;264:484-493.
5. Gatehouse PD, He T, Puri BK, Thomas RD, Resnick D, Bydder GM. Contrast-enhanced MRI of the menisci of the knee using ultrashort echo time (UTE) pulse sequences: Imaging of the red and white zones. *Br J Radiol*. 2004;77:641-647.
6. Hodgson RJ, O'Connor PJ, Grainger AJ. Tendon and ligament imaging. *Br J Radiol*. 2012;85:1157-1172.
7. Du J, Bydder GM. Qualitative and quantitative ultrashort-TE MRI of cortical bone. *NMR Biomed*. 2013;26:489-506.
8. Chang EY, Du J, Chung CB. UTE imaging in the musculoskeletal system. *J Magn Reson Imaging*. 2015;41:870-883.
9. Robson MD, Bydder GM. Clinical ultrashort echo time imaging of bone and other connective tissues. *NMR Biomed*. 2006;19:765-780.
10. Qian Y, Williams AA, Chu CR, Boada FE. High-resolution ultrashort echo time (UTE) imaging on human knee with AWSOS sequence at 3.0 T. *J Magn Reson Imaging*. 2012;35:204-210.
11. Bae WC, Dwek JR, Znamirowski R, et al. Ultrashort echo time MR imaging of osteochondral junction of the knee at 3 T: Identification of anatomic structures contributing to signal intensity. *Radiology*. 2010;254:837-845.
12. Eckstein F, Glaser C. Measuring cartilage morphology with quantitative magnetic resonance imaging. *Semin Musculoskelet Radiol*. 2004;8:329-353.

13. Foreman SC, Ashmeik W, Baal JD, et al. Patients with type 2 diabetes exhibit a more mineralized deep cartilage layer compared with nondiabetic controls: A pilot study. *Cartilage*. 2019. <https://doi.org/10.1177/1947603519870853>
14. Ritzel H, Amling M, Posl M, Hahn M, Delling G. The thickness of human vertebral cortical bone and its changes in aging and osteoporosis: A histomorphometric analysis of the complete spinal column from thirty-seven autopsy specimens. *J Bone Miner Res*. 1997;12:89-95.
15. Johnson EM, Vyas U, Ghanouni P, Pauly KB, Pauly JM. Improved cortical bone specificity in UTE MR imaging. *Magn Reson Med*. 2017;77:684-695.
16. Lee H, Zhao X, Song HK, Zhang R, Bartlett SP, Wehrli FW. Rapid dual-RF, dual-echo, 3D ultrashort echo time craniofacial imaging: A feasibility study. *Magn Reson Med*. 2019;81:3007-3016.
17. Takizawa M, Hanada H, Oka K, Takahashi T, Yamamoto E, Fujii M. A robust ultrashort TE (UTE) imaging method with corrected k-space trajectory by using parametric multiple function model of gradient waveform. *IEEE Trans Med Imaging*. 2013;32:306-316.
18. Van Vaals JJ, Bergman AH. Optimization of eddy-current compensation. *J Magn Reson*. 1990;90:52-70.
19. Brodsky EK, Samsonov AA, Block WF. Characterizing and correcting gradient errors in non-cartesian imaging: Are gradient errors linear time-invariant (LTI)? *Magn Reson Med*. 2009;62:1466-1476.
20. Bernstein MA, King KF, Zhou XJ. *Handbook of MRI Pulse Sequences*. Burlington, MA: Elsevier; 2004.
21. De Zanche N, Barmet C, Nordmeyer-Massner JA, Pruessmann KP. NMR probes for measuring magnetic fields and field dynamics in MR systems. *Magn Reson Med*. 2008;60:176-186.
22. Liu H, Matson GB. Accurate measurement of magnetic resonance imaging gradient characteristics. *Materials (Basel)*. 2014;7:1-15.
23. Dietrich BE, Brunner DO, Wilm BJ, et al. A field camera for MR sequence monitoring and system analysis. *Magn Reson Med*. 2016;75:1831-1840.
24. Addy NO, Wu HH, Nishimura DG. Simple method for MR gradient system characterization and k-space trajectory estimation. *Magn Reson Med*. 2012;68:120-129.
25. Mason GF, Harshbarger T, Hetherington HP, Zhang Y, Pohost GM, Twieg DB. A method to measure arbitrary k-space trajectories for rapid MR imaging. *Magn Reson Med*. 1997;38:492-496.
26. Takahashi A, Peters T. Compensation of multi-dimensional selective excitation pulses using measured k-space trajectories. *Magn Reson Med*. 1995;34:446-456.
27. Harkins KD, Does MD, Grissom WA. Iterative method for pre-distortion of MRI gradient waveforms. *IEEE Trans Med Imaging*. 2014;33:1641-1647.
28. Alley MT, Glover GH, Pelc NJ. Gradient characterization using a Fourier-transform technique. *Magn Reson Med*. 1998;39:581-587.
29. Jang H, McMillan AB. A rapid and robust gradient measurement technique using dynamic single-point imaging. *Magn Reson Med*. 2017;78:950-962.
30. Duyn JH, Yang Y, Frank JA, van der Veen JW. Simple correction method for k-space trajectory deviations in MRI. *J Magn Reson*. 1998;132:150-153.
31. Deshmane A, Blaimer M, Breuer F, et al. Self-calibrated trajectory estimation and signal correction method for robust radial imaging using GRAPPA operator gridding. *Magn Reson Med*. 2016;75:883-896.
32. Kramer M, Biermann J, Reichenbach JR. Intrinsic correction of system delays for radial magnetic resonance imaging. *Magn Reson Imaging*. 2015;33:491-496.
33. Aitken AP, Giese D, Tsoumpas C, et al. Improved UTE-based attenuation correction for cranial PET-MR using dynamic magnetic field monitoring. *Med Phys*. 2014;41:012302.
34. Herrmann KH, Kramer M, Reichenbach JR. Time efficient 3D radial UTE sampling with fully automatic delay compensation on a clinical 3T MR scanner. *PLoS One*. 2016;11:e0150371.
35. Magland JF, Saligheh-Rad H, Wehrli FW. Correcting for gradient imperfections in ultra-short echo time imaging. In Proceedings of the 18th Scientific Meeting of ISMRM, Sweden, Stockholm, 2010. Abstract 3102.
36. Atkinson IC, Lu A, Thulborn KR. Characterization and correction of system delays and eddy currents for MR imaging with ultrashort echo-time and time-varying gradients. *Magn Reson Med*. 2009;62:532-537.
37. Latta P, Starcuk Z Jr, Gruwel ML, Weber MH, Tomanek B. K-space trajectory mapping and its application for ultrashort echo time imaging. *Magn Reson Imaging*. 2017;36:68-76.
38. Vannesjo SJ, Haeberlin M, Kasper L, et al. Gradient system characterization by impulse response measurements with a dynamic field camera. *Magn Reson Med*. 2013;69:583-593.
39. Brodsky EK, Klaers JL, Samsonov AA, Kijowski R, Block WF. Rapid measurement and correction of phase errors from B0 eddy currents: Impact on image quality for non-Cartesian imaging. *Magn Reson Med*. 2013;69:509-515.
40. Rahmer J, Mazurkewitz P, Bornert P, Nielsen T. Rapid acquisition of the 3D MRI gradient impulse response function using a simple phantom measurement. *Magn Reson Med*. 2019;82:2146-2159.
41. Gurney P, Pauly JM, Nishimura DG. A Simple Method for Measuring B0 Eddy Currents. In Proceedings of the 13th Annual Meeting of ISMRM, Miami, Florida, 2005. Abstract 866.
42. Zhao X, Lee H, Song HK, Cheng CC, Wehrli FW. Impact of gradient imperfections on bone water quantification with UTE MRI. *Magn Reson Med*. 2020;84:2034-2047.
43. Lee H, Zhao X, Song HK, Wehrli FW. Self-navigated three-dimensional ultrashort echo time technique for motion-corrected skull MRI. *IEEE Trans Med Imaging*. 2020;39:2869-2880.
44. Prince JL, Links JM. *Medical Imaging Signals and Systems*. Upper Saddle River, NJ: Pearson Prentice Hall; 2006.
45. Qian Y, Boada FE. Acquisition-weighted stack of spirals for fast high-resolution three-dimensional ultra-short echo time MR imaging. *Magn Reson Med*. 2008;60:135-145.
46. Vannesjo SJ, Graedel NN, Kasper L, et al. Image reconstruction using a gradient impulse response model for trajectory prediction. *Magn Reson Med*. 2016;76:45-58.
47. Campbell-Washburn AE, Xue H, Lederman RJ, Faranesh AZ, Hansen MS. Real-time distortion correction of spiral and echo planar images using the gradient system impulse response function. *Magn Reson Med*. 2016;75:2278-2285.
48. Ruschke S, Eggers H, Kooijman H, et al. Correction of phase errors in quantitative water-fat imaging using a monopolar time-interleaved multi-echo gradient echo sequence. *Magn Reson Med*. 2017;78:984-996.
49. Block KT, Uecker M. Simple method for adaptive gradient-delay compensation in radial MRI. In Proceedings of the 19th Annual Meeting of ISMRM, Montréal, Québec, Canada, 2011. Abstract 2816.

50. Untenberger M, Tan Z, Voit D, et al. Advances in real-time phase-contrast flow MRI using asymmetric radial gradient echoes. *Magn Reson Med.* 2016;75:1901-1908.
51. Vannesjo SJ, Dietrich BE, Pavan M, et al. Field camera measurements of gradient and shim impulse responses using frequency sweeps. *Magn Reson Med.* 2014;72:570-583.
52. Robison RK, Devaraj A, Pipe JG. Fast, simple gradient delay estimation for spiral MRI. *Magn Reson Med.* 2010;63:1683-1690.
53. Beaumont M, Lamalle L, Segebarth C, Barbier EL. Improved k-space trajectory measurement with signal shifting. *Magn Reson Med.* 2007;58:200-205.
54. Lee KJ, Paley MN, Griffiths PD, Wild JM. Method of generalized projections algorithm for image-based reduction of artifacts in radial imaging. *Magn Reson Med.* 2005;54:246-250.
55. Stich M, Wech T, Slawig A, et al. Gradient waveform pre-emphasis based on the gradient system transfer function. *Magn Reson Med.* 2018;80:1521-1532.
56. Mazurkewitz P, Rahmer J, Börnert P. GIRF measurement using a combination of triangular and chirp waveform input functions. In Proceedings of the 26th Annual Meeting of ISMRM, Paris, France, 2018. Abstract 0169.
57. Johansson A, Karlsson M, Yu J, Asklund T, Nyholm T. Voxel-wise uncertainty in CT substitute derived from MRI. *Med Phys.* 2012;39:3283-3290.
58. Keereman V, Fierens Y, Broux T, De Deene Y, Lonnew M, Vandenberghe S. MRI-based attenuation correction for PET/MRI using ultrashort echo time sequences. *J Nucl Med.* 2010;51:812-818.
59. Gersing AS, Bodden J, Neumann J, et al. Accelerating anatomical 2D turbo spin echo imaging of the ankle using compressed sensing. *Eur J Radiol.* 2019;118:277-284.
60. Argentieri EC, Koff MF, Breighner RE, Endo Y, Shah PH, Sneag DB. Diagnostic accuracy of zero-echo time MRI for the evaluation of cervical neural foraminal stenosis. *Spine (Phila Pa 1976).* 2018;43:928-933.
61. Carl M, Bydder GM, Du J. UTE imaging with simultaneous water and fat signal suppression using a time-efficient multispoke inversion recovery pulse sequence. *Magn Reson Med.* 2016;76:577-582.
62. Ma YJ, Chen Y, Li L, et al. Trabecular bone imaging using a 3D adiabatic inversion recovery prepared ultrashort TE cones sequence at 3T. *Magn Reson Med.* 2020;83:1640-1651.
63. Breighner RE, Endo Y, Konin GP, Gulotta LV, Koff MF, Potter HG. Technical developments: Zero echo time imaging of the shoulder: Enhanced osseous detail by using MR imaging. *Radiology.* 2018;286:960-966.
64. Wiesinger F, Sacolick LI, Menini A, et al. Zero TE MR bone imaging in the head. *Magn Reson Med.* 2016;75:107-114.

## SUPPORTING INFORMATION

Additional Supporting Information may be found online in the Supporting Information section.

**FIGURE S1** Upper row shows the simulated UTE images of a Shepp–Logan phantom (truth). The k-space data were generated using NUFFT encoding along the GIRF-corrected trajectories. Images were then reconstructed using the

nominal-corrected gradients, nominal-corrected and delayed-gradients and the GIRF-corrected gradients. A negative delay corresponds to a negative shift in time of the readout gradient. The time between two sampling points was 2  $\mu$ s. Bottom row shows differences between the input image (truth) and the correspondingly reconstructed images. Blurring was introduced in the UTE images reconstructed with the nominal-corrected trajectory. At the object-background border, the nominal reconstructed image had more energy in the background region (arrow A) and showed an overshoot of signal intensity at object borders between regions with high and low signals (arrow B). Delaying the readout gradient, positive or negative, did not improve the image quality

**FIGURE S2** Measurement of a spherical water phantom with the imaging plane being in three different geometrical orientations: coronal, sagittal and transversal. Here the z-axis points in feet-head direction, the y-axis points in anterior-posterior and the x-axis points in right-left direction. The line profiles on the right correspond the signal intensity along the arrows on the left

**FIGURE S3** Data processing steps of the GMTF estimation. A) Uncorrected phase evolution in time of the signal originating from off-center slices. The phase follows the applied chirp test gradient waveform (green) that was applied once in positive and once in negative readout direction. The measured phase in opposing readout direction yields the background corrected phase (right). Here the background corrected phase for four different off-center locations is shown in time. B) Background corrected phase at different points in time along the measured slice locations. C) Measured phase at one time point at four different off-center locations and the second order fit (left) and the corresponding root mean squared error (right). D) Root mean squared error of the second order fit for the four different locations and its evolution in time. The RMSE increases with increasing frequency of the chirp. For the highest frequencies and the highest RMSE the error is maximal  $\sim 0.06\%$

**FIGURE S4** Comparison of two independent GIRF measurements with a time separation of one month. A) and B) magnitude and phase of the first order GIRF. C) and D) difference in magnitude and phase of the two measured first order GIRFs

**How to cite this article:** Kronthaler S, Rahmer J, Börnert P, et al. Trajectory correction based on the gradient impulse response function improves high-resolution UTE imaging of the musculoskeletal system. *Magn Reson Med.* 2021;85:2001–2015. <https://doi.org/10.1002/mrm.28566>

## 7.2 Journal Publication II:

### Assessment of vertebral fractures and edema of the thoracolumbar spine based on water-fat and susceptibility-weighted images derived from a single ultra-short echo time scan

The publication entitled *Assessment of vertebral fractures and edema of the thoracolumbar spine based on water-fat and susceptibility-weighted images derived from a single ultra-short echo time scan* was published in *Magnetic Resonance in Medicine* (ISSN: 0740-3194) [186]. The manuscript was authored by Sophia Kronthaler, Christof Boehm, Georg Feuerriegel, Peter Börnert, Ulrich Katscher, Kilian Weiss, Marcus R. Makowski, Benedikt J. Schwaiger, Alexandra S. Gersing, Dimitrios C. Karampinos. It is available online (DOI: 10.1002/mrm.29078) as an open access article under the terms of the Creative Commons Attribution-NonCommercial-NoDerivs License. Preliminary results were also presented in the conference contribution C17, which was invited for oral presentation at the ISMRM annual meeting 2021. A summary of the publication is provided in Section 7.2.1, the author contributions are listed in Section 7.2.2 and the full text is included subsequently on the following pages.

#### 7.2.1 Abstract

##### Purpose

To develop a methodology to simultaneously perform single echo Dixon water-fat imaging and susceptibility weighted imaging (SWI) based on a single ultrashort echo time (sUTE) scan to assess vertebral fractures and degenerative bone changes in the thoracolumbar spine.

##### Methods

A methodology was developed to solve the smoothness-constrained inverse water-fat problem to separate water and fat while removing unwanted low-frequency phase terms. Additionally, the corrected UTE phase was used for SWI. UTE imaging (TE: 0.14 ms, 3T MRI) was performed in the lumbar spine of nine patients with vertebral fractures and bone marrow edema (BME). All images were reviewed by two radiologists. Water- and fat-separated images were analyzed in comparison with STIR and with respect to BME visibility. The visibility of fracture lines and cortical outlining of the UTE magnitude images were analyzed in comparison with computed tomography.

##### Results

Unwanted phase components, dominated by the  $B_1$  phase, were removed from the UTE phase images. The rating of the diagnostic quality of BME visualization showed a high preference for the sUTE-Dixon water- and fat-separated images in comparison with STIR. The UTE magnitude images enabled better visualizing fracture lines compared with STIR and slightly better visibility of cortical outlining. With increasing SWI weighting osseous structures and fatty tissues were enhanced.

**Conclusion**

The proposed sUTE-Dixon-SWI methodology allows the removal of unwanted low-frequency phases and enables water-fat separation and SWI processing from a single complex UTE image. The methodology can be used for the simultaneous assessment of vertebral fractures and BME of the thoracolumbar spine.

**7.2.2 Author contributions**

The first author implemented the reconstruction using Matlab (Mathworks, Natick, MA) and implemented the post-processing using Python (Python Software Foundation, Centrum voor Wiskunde en Informatica, Amsterdam). With the help and consultation from the coauthors; the first author designed and performed the experiments (MR measurements), analyzed and interpreted the data, and wrote the manuscript.



# Assessment of vertebral fractures and edema of the thoracolumbar spine based on water-fat and susceptibility-weighted images derived from a single ultra-short echo time scan

Sophia Kronthaler<sup>1</sup>  | Christof Boehm<sup>1</sup>  | Georg Feuerriegel<sup>1</sup> | Peter Börnert<sup>2</sup> | Ulrich Katscher<sup>2</sup>  | Kilian Weiss<sup>3</sup> | Marcus R. Makowski<sup>1</sup> | Benedikt J. Schwaiger<sup>4</sup> | Alexandra S. Gersing<sup>1</sup> | Dimitrios C. Karampinos<sup>1</sup>

<sup>1</sup>Department of Diagnostic and Interventional Radiology, Technical University of Munich, Munich, Germany

<sup>2</sup>Philips Research, Hamburg, Germany

<sup>3</sup>Philips GmbH, Hamburg, Germany

<sup>4</sup>Department of Diagnostic and Interventional Neuroradiology, School of Medicine, Technical University of Munich, Munich, Germany

## Correspondence

Sophia Kronthaler, Department of Diagnostic and Interventional Radiology, Klinikum rechts der Isar, Technische Universität München, Ismaninger Str. 22, 81675 Munich, Germany.  
Email: sophia.kronthaler@tum.de

## Funding information

The present work was supported by the European Research Council (grant agreement no. 677661, ProFatMRI). This work reflects only the authors' views and the European Union is not responsible for any use that may be made of the information it contains. Finally, the authors acknowledge research support from Philips Healthcare

**Purpose:** To develop a methodology to simultaneously perform single echo Dixon water-fat imaging and susceptibility-weighted imaging (SWI) based on a single echo time (TE) ultra-short echo time (UTE) (sUTE) scan to assess vertebral fractures and degenerative bone changes in the thoracolumbar spine.

**Methods:** A methodology was developed to solve the smoothness-constrained inverse water-fat problem to separate water and fat while removing unwanted low-frequency phase terms. Additionally, the corrected UTE phase was used for SWI. UTE imaging (TE: 0.14 ms, 3T MRI) was performed in the lumbar spine of nine patients with vertebral fractures and bone marrow edema (BME). All images were reviewed by two radiologists. Water- and fat-separated images were analyzed in comparison with short-tau inversion recovery (STIR) and with respect to BME visibility. The visibility of fracture lines and cortical outlining of the UTE magnitude images were analyzed in comparison with computed tomography.

**Results:** Unwanted phase components, dominated by the  $B_1$  phase, were removed from the UTE phase images. The rating of the diagnostic quality of BME visualization showed a high preference for the sUTE-Dixon water- and fat-separated images in comparison with STIR. The UTE magnitude images enabled better visualizing fracture lines compared with STIR and slightly better visibility of cortical outlining. With increasing SWI weighting osseous structures and fatty tissues were enhanced.

This is an open access article under the terms of the Creative Commons Attribution-NonCommercial License, which permits use, distribution and reproduction in any medium, provided the original work is properly cited and is not used for commercial purposes.

© 2021 The Authors. *Magnetic Resonance in Medicine* published by Wiley Periodicals LLC on behalf of International Society for Magnetic Resonance in Medicine.

**Conclusion:** The proposed sUTE-Dixon-SWI methodology allows the removal of unwanted low-frequency phases and enables water-fat separation and SWI processing from a single complex UTE image. The methodology can be used for the simultaneous assessment of vertebral fractures and BME of the thoracolumbar spine.

**KEYWORDS**

bone marrow edema, fat, magnetic resonance imaging (MRI), single-echo Dixon, susceptibility-weighted imaging (SWI), ultra-short echo time (UTE) imaging, vertebral fractures, water

## 1 | INTRODUCTION

In patients with vertebral fractures or degenerative changes of the spine, computed tomography (CT) and MRI are often performed.<sup>1</sup> A CT is preferred to assess the osseous status of the fractured vertebra as well as the adjacent segments for therapy selection and potential surgery planning. Acute vertebral fractures are often associated with bone marrow edema. To differentiate acute from chronic vertebral fractures MR imaging is the standard of reference for the evaluation of the bone marrow to see whether edema is present or not.<sup>2,3</sup> CT examinations of the spine are associated with radiation exposure, additional examination time, and costs. To assess the discoloration aspects, the soft tissue structures and the osseous components of the spine, it would be desirable to acquire all information in a single MRI examination.

MRI provides different approaches for depicting both the soft-tissue and osseous components. First, ultrashort-echo time (UTE) imaging enables signal detection from tissues with short  $T_2^*$  components, such as cortical bone.<sup>4</sup> Recent studies suggested the use of UTE and zero TE (ZTE) sequences for the depiction of cortical and trabecular bone.<sup>5-7</sup> It was further shown that UTE imaging enables the morphological assessment of fractures and degenerative bone changes in the spine<sup>8,9</sup> and joints.<sup>10,11</sup> In addition, susceptibility-weighted imaging (SWI), a technique that uses the different magnetic susceptibilities of tissues, is sensitive to tissues that distort the magnetic field by means of paramagnetic or diamagnetic effects.<sup>12</sup> In the past, SWI was mainly used in brain imaging, e.g., to differentiate bleedings from calcifications.<sup>12</sup> Recently, SWI was extended to other regions of the body: as calcified structures are diamagnetic, allowing SWI to visualize the calcified bone matrix.<sup>13-18</sup> SWI could, thus, be a promising technique to enhance the contrast of osseous tissue components. Second, Dixon sequences are commonly used in the clinical routine either for fat suppression or to generate water- and fat-separated images and to assess soft-tissue components. Dixon techniques exploit

the chemical shift-induced phase difference between water and fat signals and usually require the acquisition of multiple images at different TEs. However, due to the need for multiple echoes, Dixon sequences can prolong scan times.<sup>19-21</sup>

The combination of UTE data acquisition with conventional water-fat separation (UTE-Dixon) enables the depiction of both, the soft-tissue and the osseous components.<sup>22</sup> UTE-Dixon has applications in imaging and quantifying short  $T_2$  tissues, eliminating the necessity for fat suppression pulses that directly suppress the long  $T_2$  signals.<sup>22</sup> Previous studies have shown that an extension of the well-known IDEAL algorithm can be used to generate water, fat, and quantitative susceptibility maps.<sup>23,24</sup> Beyond that, the water- and fat-separated images were used to suppress long  $T_2$  components which proves itself beneficial in pseudo-CT imaging or in the context of PET attenuation map generation.<sup>22-28</sup> However, also typical UTE-Dixon imaging requires the acquisition of multiple echoes which prolong the repetition time (TR) and conventional Dixon does not consider the short  $T_2^*$  decay of water signal.<sup>29</sup>

Single-echo Dixon (sTE-Dixon) methods rely on a single complex TE image to decompose fat and water components directly from the complex MR signal.<sup>30</sup> However, the presence of unwanted phase terms corrupts the simple sTE-Dixon approaches based solely on the complex MR signal. To remove unwanted phase terms different techniques were previously reported that either use additional reference scans<sup>29,30</sup> or that use a region growing algorithm to estimate the unwanted phase terms.<sup>31</sup> The acquisition of additional reference scans yields longer scan times and errors due to patient motion or other sources of inconsistencies. Thus, double echo steady state (DESS) acquisition was recently combined with UTE to perform sTE-Dixon.<sup>32</sup> UTE-DESS acquires two complex signals and can solve for background phase terms in the sTE-Dixon processing. However, the acquisition of two complex signals prolongs the TR. In contrast, UTE imaging, based on single-echo spoiled gradient echo acquisition, acquires a single complex signal and has not yet been combined with sTE-Dixon

methods to generate water- and fat-separated images from a single-TE UTE (sUTE) acquisition without additional calibration scans. A sUTE acquisition would also minimize the effect of  $T_2^*$  decay on the water-fat separation.

The purpose of this work was to develop an approach to simultaneously performing single-UTE Dixon (sUTE-Dixon) imaging and SWI using one sUTE scan to assess the vertebral shape and bone marrow changes at the thoracolumbar spine in patients with vertebral fractures.

## 2 | METHODS

### 2.1 | Signal model

The complex water-fat signal  $S(t)$  at time  $t$  is comprised of the magnitude signal of water  $W$  and fat  $F$ , which, if one neglects  $T_2^*$  decay effects for short  $t$  and assumes a multi-peak fat spectrum, takes the form:

$$S(t) = (W + c(t)F) e^{i\phi(t)} \text{ with } c(t) = \sum_{p=1}^P \alpha_p e^{i2\pi\Delta f_p t} \quad (1)$$

The fat signal component consists of a fat spectrum  $c(t)$  with  $P$  spectral peaks with relative amplitudes  $\alpha_p$  and chemical shifts  $\Delta f_p$ .<sup>33</sup> The phase between the water and fat components is defined by

$$\theta(t) = \angle(c(t)) \quad (2)$$

$\phi(t)$  accounts for all phase terms that water and fat experience as a common phase.  $\Phi(t)$  comprises contributions from spatially dependent field  $B_0$  inhomogeneities,<sup>34</sup> eddy currents, signal delays in the receiver chains, and phase contributions due to the  $B_1$  transmit/receive phase.<sup>31</sup> In this work, eddy currents and signal delays were addressed by means of the gradient impulse response function based on measurements with the thin slice method.<sup>35</sup>

### 2.2 | Phase contributions

To achieve a water-fat separation based on a single TE, the chemical shift phase  $\theta(t)$  and the unwanted phase terms  $\phi(t)$  have to be known. At a UTE TE = 0.14 ms and 3T, the chemical shift induced phase difference between water and fat, assuming a nine-peak fat-model,<sup>36</sup> is  $\theta(TE) = 0.326$  rad. In UTE imaging, the phase contribution due to  $B_0$  inhomogeneities was expected to be small with respect to the short TE. Those  $B_0$  terms originate from the magnet inhomogeneity, the shim field, the object-based susceptibility, and residual terms from background fields.<sup>34</sup> For

the assessment, a Cartesian multi-echo reference scan was acquired to measure the  $B_0$  fieldmap in the thoracolumbar spine (Figure 1B). The 90% percentile of the phase  $\phi_{fm}$ , that resulted from the Cartesian fieldmap at TE = 0.14 ms, was in the range between 0 rad and 0.12 rad (Figure 1C). This phase, induced by the fieldmap, was small compared with the chemical shift phase  $\theta(TE)$ . However, the UTE phase contained a strong contribution of the  $B_1$  phase which varied slowly in the axial plane (Figure 1D–I), representing the dominant term in the UTE phase at TE = 0.14 ms when scanning the lumbar spine at 3T. The  $B_1$  phase is caused by the electric conductivity of tissue and has approximately a parabolic shape according to Maxwell's equations.<sup>37–39</sup>

### 2.3 | sUTE-Dixon processing

Under the assumption, that the unwanted phase terms primarily consisted of the  $B_1$  phase, which varies smoothly over the field of view (FOV),<sup>37–39</sup> we propose to solve the following smoothness-constrained non-linear inverse water-fat problem for the unwanted phase term  $\phi$ :

$$\begin{aligned} \phi &= \underset{\phi}{\operatorname{argmin}} \psi(\phi) \\ &= \underset{\phi}{\operatorname{argmin}} \frac{1}{2} \| (W + Fe^{i\theta(TE)}) e^{i\phi} - S_{\text{exp}}(TE) \|_2^2 + \lambda \| M \nabla \phi \|_2^2 \end{aligned} \quad (3)$$

where  $\phi$ : optimal solution which contains all unwanted phase components,  $W$ : magnitude of the water signal,  $F$ : magnitude of the fat signal,  $\theta(TE)$ : phase difference between water and fat due to the chemical shift,  $S_{\text{exp}}$ : measured signal,  $\lambda$ : regularization parameter,  $M$ : mask which was derived from the magnitude images and  $\nabla = (\frac{\partial}{\partial x}, \frac{\partial}{\partial y}, \frac{\partial}{\partial z})^T$  the 3D gradient in the coordinate system of the acquired image. The problem  $\psi$  was linearized as follows:

$$\psi(\phi + d\phi) = \frac{1}{2} \| (W + Fe^{i\theta(TE)}) e^{i\phi} (1 + id\phi) - S_{\text{exp}}(TE) \|_2^2 + \lambda \| M \nabla \phi + M \nabla d\phi \|_2^2 \quad (4)$$

The update  $d\phi$  was found by solving:

$$0 = \frac{\partial}{\partial \phi} \psi(\phi + d\phi) \quad (5)$$

$$\begin{aligned} & [ (W^2 + F^2 + 2WF \cos(\theta)) + 2\lambda \nabla^H M^2 \nabla ] \\ d\phi &= -\operatorname{Im} \left( (W + Fe^{i\theta(TE)}) e^{i\phi} S_{\text{exp}}^H(TE) \right) - 2\lambda \nabla^H M^2 \nabla \phi \end{aligned} \quad (6)$$

If  $\phi$  is known, water and fat can be calculated from Equations (1) and (2) as follows:

$$F = \frac{\operatorname{Im}(\hat{S})}{\sin(\theta(TE))} \quad (7)$$

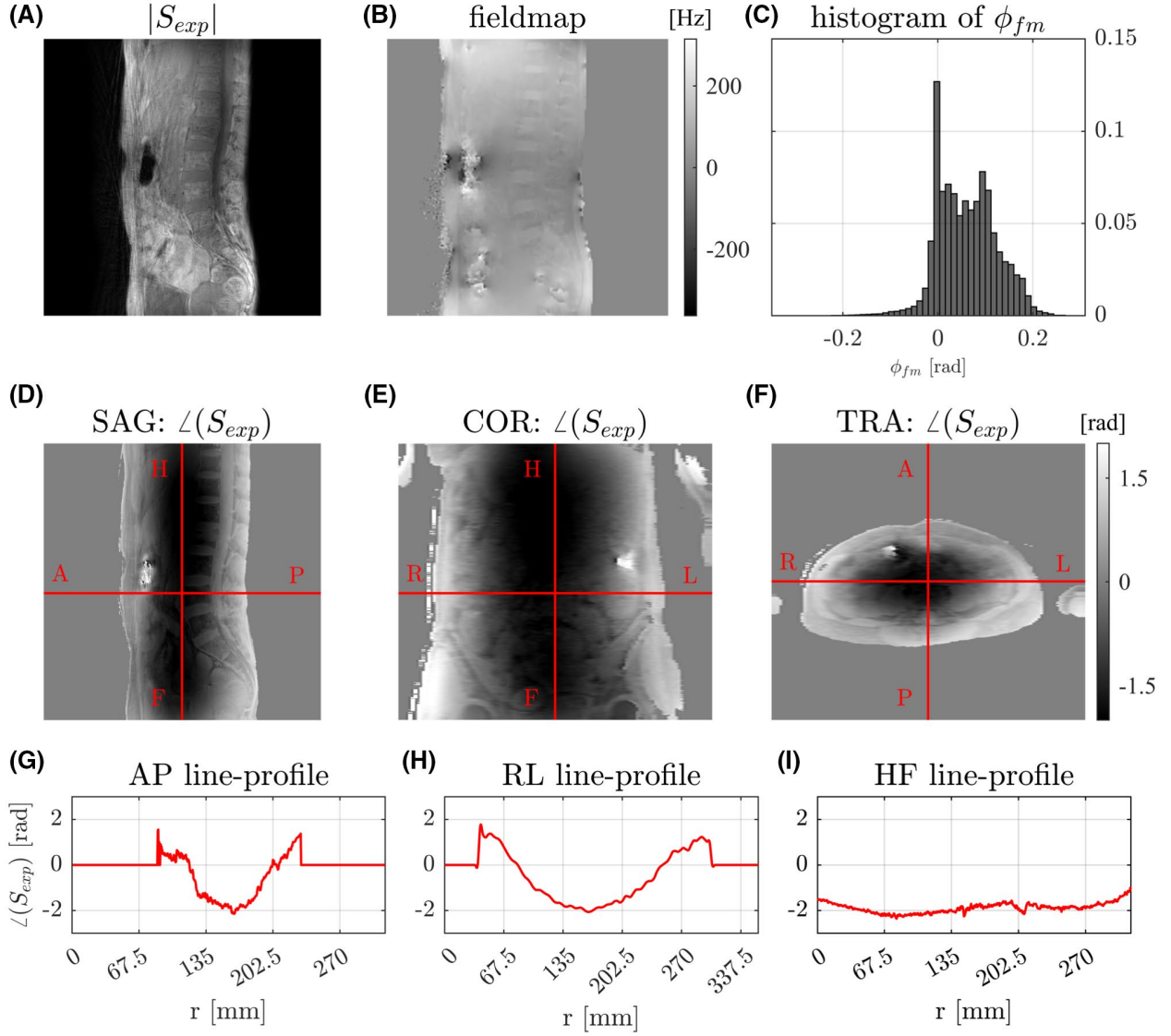


**FIGURE 1** Analysis of unwanted phase term components in a sagittal UTE scan of a patient's spine. (A) Magnitude image of the measured UTE signal  $|S_{exp}|$ . (B)  $B_0$  fieldmap obtained from a six-echo Cartesian multi-echo scan. (C) Histogram of the expected phase contribution  $\phi_{fm}$  to the UTE phase based on the Cartesian  $B_0$  fieldmap shown in (B). 90% of the fieldmap-based phase values were observed between 0 and 0.12 rad. (D–F) Phase of the sagittal UTE scan reformatted coronally and axially. (G–I) Corresponding line profiles of the UTE phase images. An unwanted phase term was observed in the UTE phase which was larger than the expected phase term (C) due to local field inhomogeneities and susceptibility effects. The unwanted phase term was prominent in AP and RL direction (G, H)

$$W = \text{Re}(\hat{S}) - |F|\cos(\theta(TE)) \quad (8)$$

where  $\hat{S} = S_{exp}(TE)e^{-i\phi}$  is the demodulated signal.

Finally, Equation (3) was solved using the conjugate gradient method as follows:

1. Unwrap the UTE phase in 2D
2. Choose a regularization parameter  $\lambda$  and set initial conditions with  $\phi_n$  being the unwanted phase term during the  $n$ -th iteration:  $\phi_{n=0} = 0; W = 0; F = 0$
3. Calculate the update  $d\phi_n$  according to Equation (6)
4. Update  $\phi_{n+1} = \phi_n + d\phi_n$

5. Demodulate unwanted phase terms  $\hat{S} = S_{exp}e^{-i\phi_{n+1}}$
6. Calculate  $F$  and  $W$  according to Equations (7) and (8)
7. Repeat steps 2–6 until the relative update  $\frac{\|d\phi_n\|_2}{\|\phi_n\|_2}$  is smaller than 0.01 with  $\phi_n$  being the solution after the  $n$ -th iteration step

To prevent phase wraps during the update steps, the phase was scaled to be between  $[-\pi, \pi]$  for steps 3–4 and rescaled for the demodulation step 5. A tissue mask was used in the regularizer to only perform the water-fat separation in areas with tissue components. Moreover, the mask prevents errors due to the abrupt increase at the border from signal to no-signal regions where the derivative

becomes very large. The signal magnitude was scaled between 0 and the 99<sup>th</sup> percentile of the maximum to remove outliers. The regularization parameter  $\lambda$  was optimized by visual inspection of the water-fat maps,  $\phi$  and the corrected signal phase. The problem was under-regularized if  $\phi$  contained non-smooth components. The problem was over-regularized if the corrected phase still contained slowly varying unwanted phase terms. All water and fat maps were obtained with a  $\lambda = 1$ . All sUTE-Dixon images were processed with the spectral fat model described in Ren et al.<sup>36</sup> To investigate the influence of the spectral fat model on the water-fat separation, the proposed processing was also tested with a wide range of biologically plausible fat spectrum models<sup>40–44</sup> (Supporting Information Figure S1, which is available online). The maximal RMSE, between the water image obtained with plausible fat spectrum models and water image obtained with the reference fat model,<sup>36</sup> was 1.81% (Supporting Information Table S1).

## 2.4 | SWI-processing

For the generation of SW images, the UTE phase was unwrapped and unwanted phase terms were removed using the result from the sUTE-Dixon processing. The phase was then used to generate a phase mask  $f$  as follows<sup>45</sup>:

$$S'_n = \left( f^n |S_{\text{exp}}| \right)^{-1} \text{ with } f = \begin{cases} \frac{\pi + (\angle(S_{\text{exp}}) - \phi)}{\pi} & \text{for } -\pi < \angle(S_{\text{exp}}) - \phi < 0 \\ 1 & \text{otherwise} \end{cases} \quad (9)$$

To increase bone contrast, the phase mask was scaled between 0 and 1 in areas with a phase between  $-\pi$  and 0 accordingly. In all areas with a large negative phase or a positive phase, means  $|\phi| < -\pi$ , the phase mask was set to 1 and thus there was no weighting added to the signal magnitude. For the generation of the SW image  $S'_n$  the phase mask was then  $n$ -times multiplied with the magnitude of the original UTE image  $|S_{\text{exp}}|$ . The contrast of the SWI was finally inverted such that bone appears bright.<sup>8,11</sup>

## 2.5 | In vivo measurements

In vivo imaging was performed in the lumbar spine of nine patients (seven female, two male; mean age  $65.9 \pm 15.8$  y) with spine fractures. Informed written consent and approval was obtained for each subject by the institutional review board (Klinikum rechts der Isar, Technical University of Munich, Munich, Germany). The spine fracture patients received an MR and a CT scan within 3 days

after symptom onset. The CT scans were part of the clinical diagnostic work up.

For the UTE measurements, a stack-of-stars UTE was acquired on a clinical 3.0T MR system (Ingenia Elition X, Philips Healthcare, The Netherlands) using the built-in-table 12-channel posterior coil, a 12-channel anterior coil and the following parameters: TE 0.14 ms, TR 6.3 ms, flip angle  $5^\circ$ , in-plane resolution  $0.45 \times 0.45 \text{ mm}^2$ , slice thickness 3 mm, FOV  $250 \times 250 \times 279 \text{ mm}^3$ , ramp length 0.08 ms, max. gradient strength 15.04 mT/m, sampling dwell time  $3.12 \mu\text{s}$  with 568 samples, acquisition window 1.77 ms, 945 number of spokes, with radial percentage of 85%, partial Fourier with a factor of 0.6 in slice direction and a resulting scan time of 6.3 minutes. sUTE-Dixon processing was performed solving Equation (3). All sUTE-Dixon processing computations were performed in Python on the graphics card of a workstation with GPU 24GiB RAM, 24 core CPU (Intel Xeon Gold) and 768 GB memory. In average the water-fat separation of a full UTE spine data sets took 160 s using 22 iteration steps. SWI processing was also performed using the mask of Equation (7) multiplied up to three times.

For conventional Dixon imaging and for comparison, a six-echo 3D monopolar time-interleaved multi-echo gradient-echo sequence was used<sup>46</sup> with following parameters: two interleaves with three echoes per TR and TR/TE1/ $\Delta$ TE: 8.2/1.3/1.1 ms, flip angle  $3^\circ$ , voxel size:  $1.8 \times 1.8 \times 1.8 \text{ mm}^3$ , FOV:  $626 \times 511 \times 102 \text{ mm}^3$ , receiver bandwidth: 1504 Hz/pixel, frequency direction A/P, scan time: 3.7 minutes. Water-fat maps were calculated using chemical shift encoding-based water-fat separation assuming a common  $T_2^*$  for water and fat and a multi-peak fat model, tuned specifically to bone marrow.<sup>36,47</sup> Furthermore, a sagittal short-tau inversion recovery (STIR) was acquired which is used in the standard clinical routine to detect bone marrow edema.

## 2.6 | CT measurements

CT was performed on one of two CT scanners (Somatom Definition AS+, Siemens Healthineers, and IQon Spectral CT, Philips) with the following parameters, according to routine clinical protocols: Collimation, 0.6 mm; pixel spacing, 0.4/0.3 mm; pitch factor, 0.8/0.9; tube voltage (peak), 120 kV; modulated tube current, 102–132 mA. Images were reformatted with 3 mm slice thickness using a bone-specific convolution kernel (I70H/YB).

## 2.7 | Radiological reading

The visual image analysis of the 6TE-Dixon, STIR, and sUTE-Dixon images was performed by two musculoskeletal

radiologists separately and independently (each with 3 y of clinical experience and 5 y of experience in musculoskeletal research), blinded to clinical and all other information. Images of the nine scanned patients were graded for overall diagnostic image quality on a five-point Likert scale (score of 1, inadequate; 2, poor; 3, moderate; 4, good; 5, excellent). Cohen's  $\kappa$  was used to determine the inter-reader agreement of the MR imaging findings. All patients were diagnosed with at least one acute vertebral fracture and showed a corresponding bone marrow edema. The radiologists rated STIR, inverted UTE magnitude, and sUTE-Dixon water-fat images with respect to image quality as well as assessment of bone marrow edema in comparison to STIR as standard of reference. The visibility of fracture lines and visibility of cortical outlining was compared with a corresponding CT scan. SW images were not included in the radiological reading.

### 3 | RESULTS

#### 3.1 | sUTE-Dixon processing results

To optimize the regularization parameter, sUTE-Dixon water-fat separation was performed for different regularization parameter values (Figure 2). Figure 2 shows the estimated unwanted phase components  $\phi$  after the 22th iteration, the UTE phase after the demodulation of these unwanted phase components and the resulting water and fat maps. Shown is a sagittal UTE scan of a patient with an acute fracture and edema in L2 (Figure 2 red arrows). For  $\lambda = 0.01$  the unwanted phase term contained high spatial frequency features which means the smoothness constraint was under-regularized. Useful phase information was demodulated from the UTE phase but the contrast between water and fat was poor. As  $\lambda$  was increased, the contrast of the water and fat images increased as well, and unwanted phase components were demodulated without loss of UTE phase information. For  $\lambda = 10$  the problem was over-regularized which resulted in maps that falsely identified subcutaneous fat as water (Figure 2, green arrow). The maps with the highest contrast between water and fat were obtained for  $\lambda = 1$ . The obtained phase  $\phi$  contained all smoothly varying background phase components leaving a corrected UTE phase that depicted a contrast mainly driven by chemical shift (Figure 3). To assess the image quality of the sUTE-Dixon water- and fat-separated images, a low-resolution Cartesian 6TE-Dixon based water-fat separation and STIR was used for comparison (Figure 4). The patient showed an acute wedge compression fracture and bone marrow edema in L3. The STIR, added here as a standard of reference, shows the build-up of fluid with a bright signal (Figure 4, red

arrows). In all water- and fat-separated images and with both methods, sUTE-Dixon and 6TE-Dixon, the compression fracture and the bone marrow edema were well depicted. Furthermore, the separation line between fluid and bone marrow was clearly visible in the fat images from both methods. Areas with prominent water or fat composition were correctly identified in the sUTE-Dixon maps when compared with the 6TE-Dixon maps. However, the anterior subcutaneous fat region was affected by abdominal breathing motion yielding errors in the sUTE-Dixon water and fat separation (Figure 4, green arrows).

#### 3.2 | UTE-SWI

Figure 5 shows the UTE-SWI results in comparison with a conventional CT. The patient had an acute compression fracture and bone marrow edema. The corrected phase image shows that tissue containing bone and tissue containing fat had a negative phase whereas tissues containing mainly water depicted a positive phase. The application of the phase masks decreased the signal amplitude in the UTE magnitude images in areas with a negative phase and increased the signal when the processed image was inverted. In the illustrated SW images  $S'_0 = |S(x)|$ ,  $S'_1$ ,  $S'_2$ ,  $S'_3$ , the contrast of osseous structures increased, when the magnitude of the original UTE image  $|S(x)|$  was multiplied up to three times with the phase mask. The fracture line as well as the visibility of the cortical outlining increased in the fractured vertebra (Figure 5, red arrows). In contrast, the visibility of the cortical outlining in the vertebra below decreased. Due to the negative phase in fatty tissue regions, changes in the bone marrow composition were additionally highlighted next to the osseous structures (Figure 5, white arrows). The green arrow points at a circumscribed sclerotic bone region which became more visible after multiple applications of the SWI weighting. The same osseous structure was detectable in the CT images. Although, the osseous structures were accentuated SNR decreased slightly with each SWI weighting step. Small amounts of noise were propagated to the SW images as a result from noise in the phase images and in the applied phase masks.

#### 3.3 | Reading results

To determine the performance of the proposed method over a larger number of patients, Table 1 sums up the reading by two radiologists. The rating of the diagnostic quality of the edema visualization showed high ratings for the sUTE-Dixon water- and fat-separated images in comparison with STIR, which was used as the standard

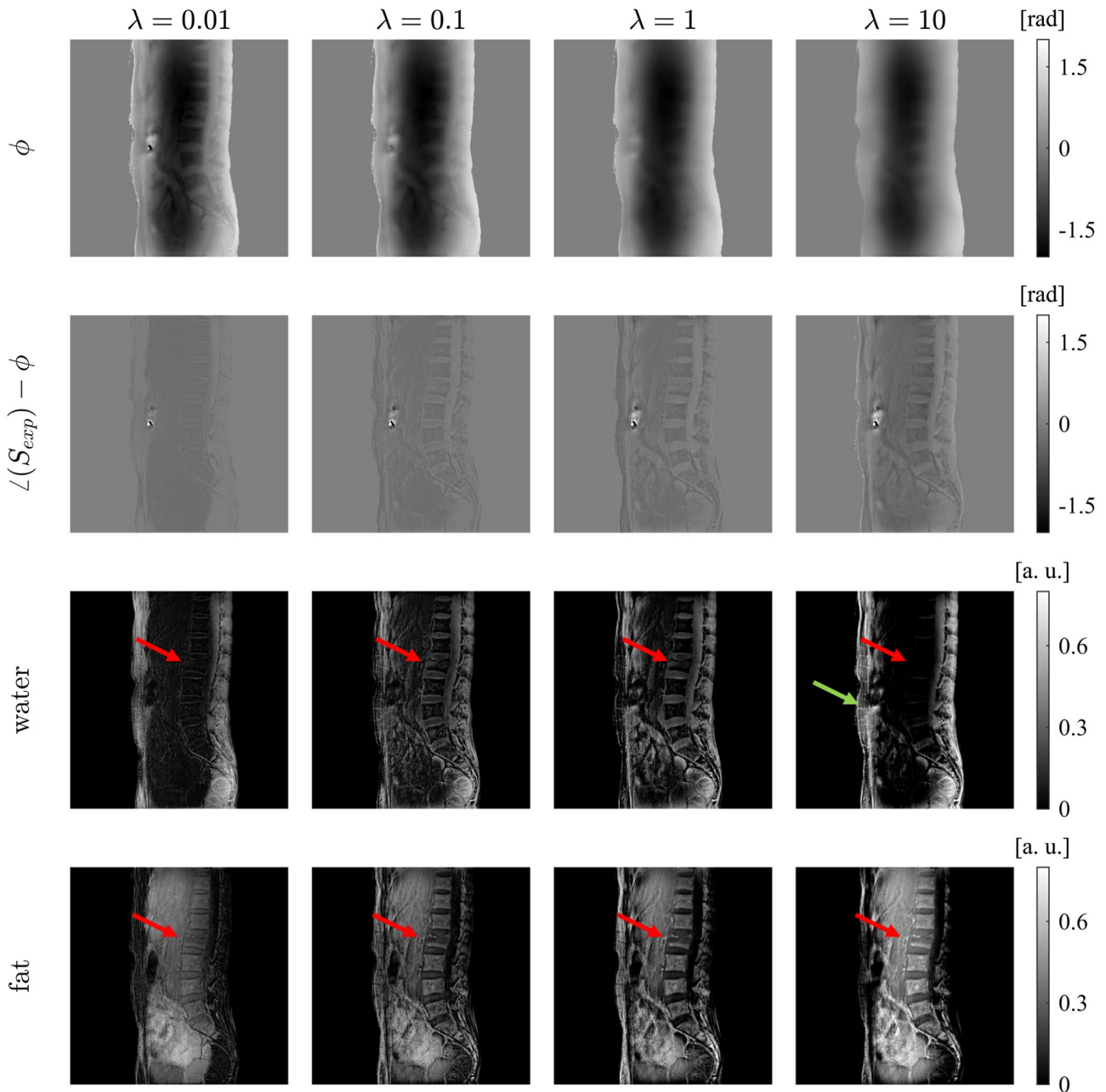


**FIGURE 2** Tuning of the regularization parameter  $\lambda$ . Shown are the sUTE-Dixon results after solving the non-linear inverse W-F problem with four different regularization parameters. For  $\lambda = 0.01$  the phase was under-regularized, which resulted in a solution  $\phi$  after  $n = 22$  iterations that contained non-smooth components. For  $\lambda = 10$ , the phase was over-regularized, which resulted in a corrected UTE phase that contained remaining unwanted smooth phase terms. In the over-regularized maps, the subcutaneous fat was falsely identified as water (green arrow). For a  $\lambda$  between 0.1 and 1, the unwanted phase terms were removed best. A  $\lambda$  of 1 gave the best water-fat separation and the visibility of an acute fracture with bone marrow edema (red arrows) was increased compared with the maps with  $\lambda = 0.1$

of reference. The interreader agreement was moderate for the water images and substantial for the fat images. The diagnostic quality of the sUTE-Dixon fat images with respect to edema visibility was rated equally high as the water-separated images (good by both readers). The UTE magnitude images enabled higher scores for visualizing fractures lines compared with STIR with a substantial interreader agreement. With respect to visibility of

cortical outlining, the inverted UTE magnitude images ( $S'_0$ ) reached slightly higher scores ( $3.1 \pm 0.3$  for reader 1 and  $3.2 \pm 0.4$  for reader 2) compared with the STIR images ( $2.9 \pm 0.6$  for reader 1 and  $2.9 \pm 0.6$  for reader 2).

Figure 6 shows three representative scans of patients included in the reading. Each subject showed signs of an acute vertebral fracture and bone marrow edema (Figure 6, red arrows). The build-up of fluid in the edema was

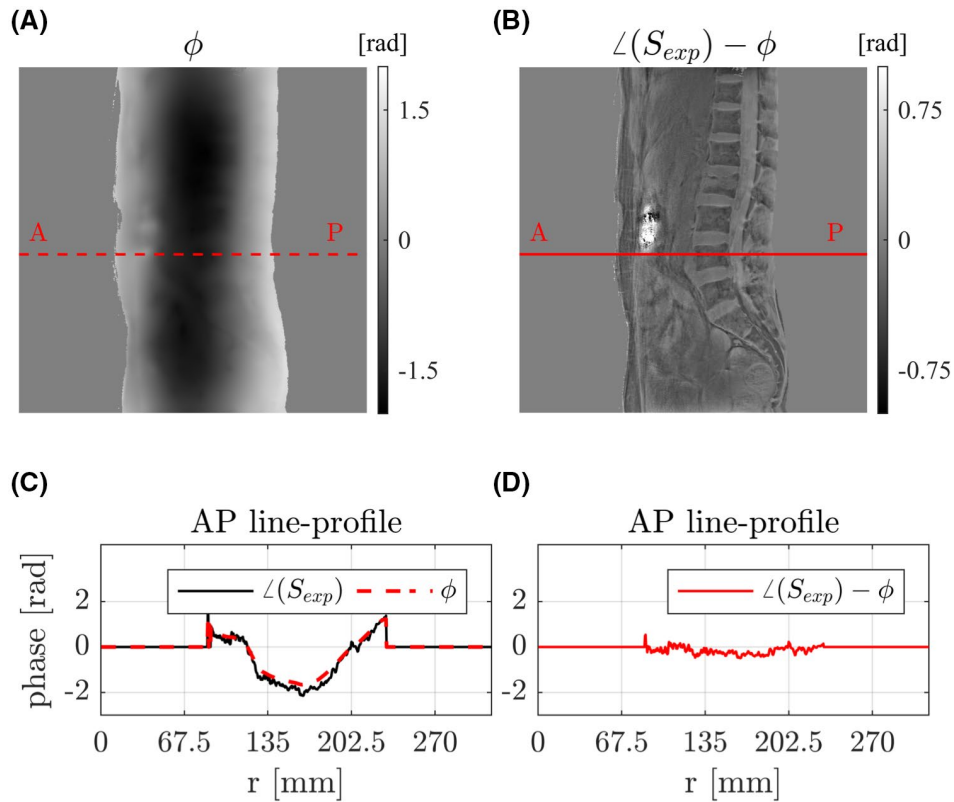


**FIGURE 3** In vivo result of a patient's spine after solving the non-linear inverse W-F problem with  $\lambda = 1$ . (A) Solution  $\phi$  for the phase which contains all unwanted phase components after the 22-th iteration step. Phase after removing the unwanted phase terms  $\phi$  (B) and the corresponding line profiles (C, D) drawn along the red line from anterior to posterior. The phase  $\phi$  contained all smoothly varying components leaving a corrected UTE phase that depicted a contrast mainly driven by chemical shift

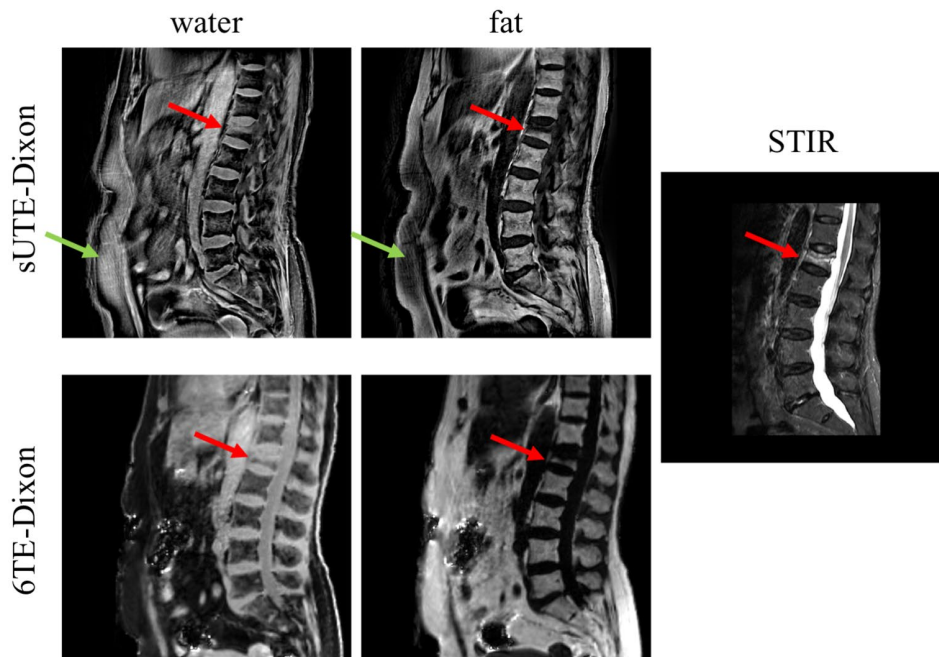


**FIGURE 4** Comparison of sUTE-Dixon, Cartesian 6TE-Dixon and STIR of a patient with an acute wedge compression fracture of L3 with bone marrow edema. The STIR showed an edema-equivalent signal alteration (red arrows). The UTE scan had a higher in-plane resolution and thicker slices compared with the STIR and the 6TE-Dixon scans. The bone marrow edema was visible in the sUTE-Dixon maps and the contrast between water and fat was comparable with the 6TE-Dixon maps. In the sUTE-Dixon water images, there was signal within the anterior subcutaneous fat region (green arrows), which is prone to artifacts due to abdominal breathing



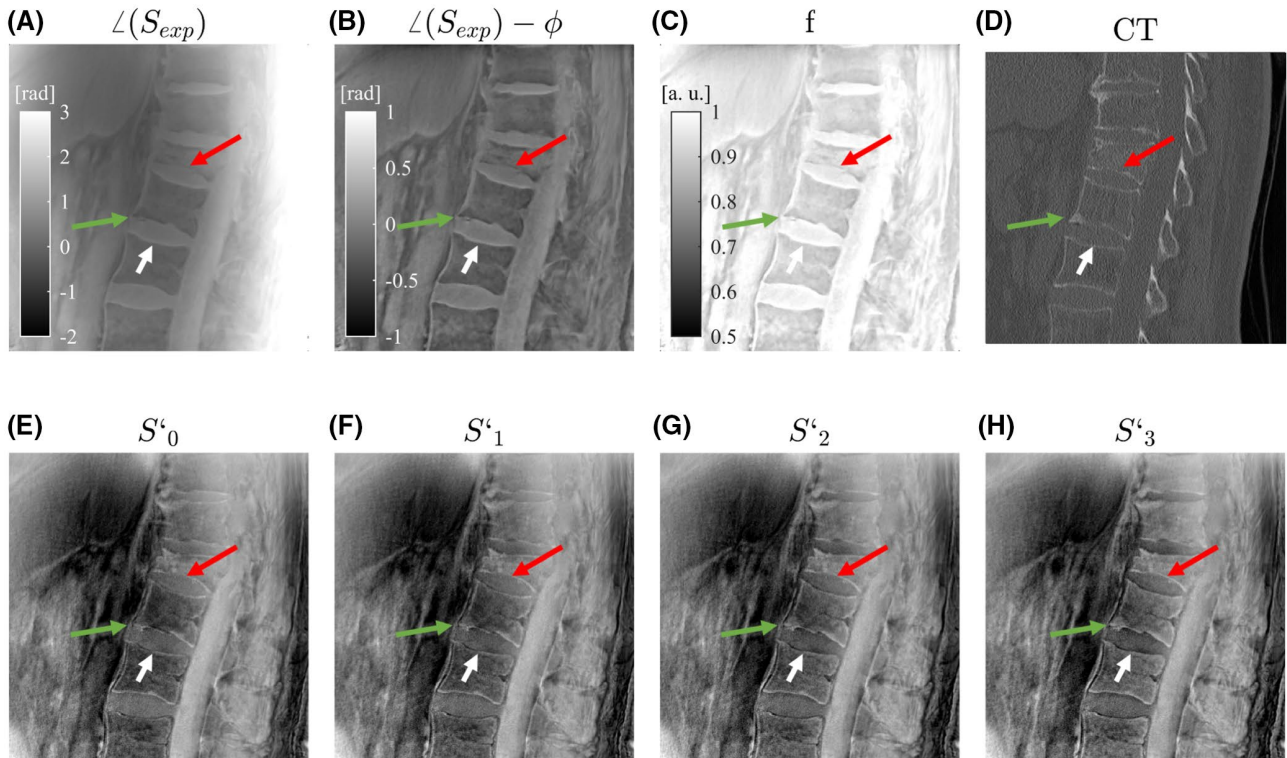


**FIGURE 5** Comparison of UTE-SWI and conventional CT in a patient showing a compression fracture in L1. (A) The input phase of the UTE. (B) The UTE phase was corrected to remove unwanted phase terms. (C) A phase mask  $f(x)$  was applied to the UTE magnitude image to highlight areas with negative phase. (D) Corresponding CT scan showed osseous structures. (E–H) Applying the phase mask multiple times increased the contrast of osseous structures as well as tissue containing fat. The red arrows highlight a cortical bone structure which contrast increased with increased SWI weighting. The white arrows point to a thin cortical bone structure where the osseous contrast decreased due to the connecting fatty tissue (SW-like image affected by both local field and chemical shift effects). The green arrows point to a thicker cortical bone structure which became visible after multiple applications of the SWI weighting

highlighted as bright signal in the STIR images. The edema was clearly visible in the sUTE-Dixon water- and fat-separated images. The sUTE-Dixon showed the vertebral fracture and the edema in the water- and fat-separated images.

## 4 | DISCUSSION

The proposed sUTE-Dixon-SWI methodology allows the removal of unwanted low-frequency background phases and enables simultaneous water-fat separation and SWI processing from a single echo complex UTE image. The formulated smoothness-constrained inverse problem solves the water fat problem while simultaneously removing the unwanted low-frequency phase terms. Therefore, no additional calibration scans are needed to remove unwanted phase components. Another novel aspect of the formulation is the use of a tissue mask in the regularizer and the scaling of the phase to prevent phase wraps during the unwanted low-frequency phase estimation update steps.

By analyzing carefully possible phase contributions, we have shown that the UTE phase in the present data acquired in the thoracolumbar spine at TE = 0.14 ms at 3T was mainly affected by the  $B_1$  transmit and receive phase. This  $B_1$  phase added in first order a low-frequency modulation to the UTE phase, which varied mainly in anterior-posterior (AP) and right-left (RL) direction. Caused by the electric conductivity of tissue, it has approximately a parabolic shape according to Maxwell's equations, and a corresponding postprocessing of the  $B_1$  phase yields quantitative values of the electric conductivity.<sup>37–39</sup> A comparison of the obtained conductivity with literature values<sup>48</sup> would in turn provide an additional criterium to identify the optimal value for  $\lambda$ . Phase contributions from  $B_0$  inhomogeneities or the local field changes were small, due to the short TE used. Similar arguments were recently presented while performing sTE-Dixon processing of UTE-DESS data.<sup>32</sup> UTE-DESS acquires two complex signals and can, therefore, solve directly for background phase contributions.<sup>32</sup> The present work instead removed the unwanted low-frequency phase terms based on a single

TABLE 1 Radiological Rating of STIR and sUTE-Dixon Derived Images

	STIR			sUTE-Dixon Water			sUTE-Dixon Fat			Inverted UTE Magnitude		
	Reader		$\kappa$	Reader		$\kappa$	Reader		$\kappa$	Reader		$\kappa$
	Reader 1	Reader 2		Reader 1	Reader 2		Reader 1	Reader 2		Reader 1	Reader 2	
Image quality	4.3 ± 0.9	4.2 ± 0.8	0.61	4.0 ± 1.0	4.2 ± 0.8	0.76	4.0 ± 0.7	4.0 ± 0.7	0.68	3.1 ± 0.6	3.2 ± 0.8	0.83
Visibility of edema in comparison with STIR	-	-	-	4.0 ± 0.9	4.0 ± 0.7	0.45	4.0 ± 0.7	4.0 ± 0.7	0.68	-	-	-
Visibility of fracture lines in comparison with CT	2.0 ± 1.0	2.0 ± 1.0	1.0	2.6 ± 0.5	2.8 ± 0.8	0.69	2.8 ± 0.4	2.8 ± 0.4	1.0	3.2 ± 0.4	3.3 ± 0.5	0.72
Visibility of cortical outlining in comparison with CT	2.9 ± 0.6	2.9 ± 0.6	1.0	2.6 ± 0.5	2.7 ± 0.5	0.77	3.0 ± 0.5	2.9 ± 0.6	0.77	3.1 ± 0.3	3.2 ± 0.4	0.61

All images were rated on a five-point Likert scale (score of 1, inadequate; 2, poor; 3, moderate; 4, good; 5, excellent). Interreader agreement was assessed using Cohen's  $\kappa$ . Five-point Likert scale (5 = best; 1 = worst).

\*Data given as means ± SDs.

complex signal using an iterative non-linear optimization approach.

The tuning of the regularization parameter showed that for  $\lambda = 1$  high contrast water- and fat-separated images were obtained. The sUTE-Dixon methodology performed consistently and reliably, produced high quality water- and fat-separated images for all nine patients, involved in this study, regardless of the patient's size using a fixed  $\lambda = 1$ . Thus, the data post-processing is fully automated which yields an advantage over filtering approaches, where the kernel size and filter type has to be defined for each subject.

In the presented study, we showed that the proposed sUTE-Dixon-SWI methodology allows the simultaneous assessment of vertebral fractures and edema of the thoracolumbar spine from a single MR sequence. The radiological reading suggested that the derived water/fat-sUTE-Dixon and SWI-UTE images can potentially replace the clinical standard of reference, STIR and CT images, in assessing edema and fracture lines, respectively. Compared with the 6TE-Dixon water- and fat-separated images, the sUTE-Dixon maps showed a good agreement and high contrast between water and fat. Thus, the proposed sUTE-Dixon-SWI technique presents several advantages: First, UTE scans are available on most clinical MR systems and the proposed technique could be realized as a data post processing step. Second, the patient can be scanned with one imaging modality. Beyond that, several sequences can be replaced with a single 3D scan acquired in a scan time of 6.3 minutes. The protocol has a large FOV and can potentially be transferred to other body regions. Due to the radial acquisition, the technique shows reduced sensitivity to motion along the frequency, in plane, and encoding direction.

While the present study shows the benefit of a single scan for water-fat separation and SW imaging, it has several limitations. Some limitations were specific to the thoracolumbar spine protocol and may depend on the imaged anatomy. First, water-fat separation can be challenging in anterior fat regions affected by respiratory motion which depends on the anatomy and the scan duration. Second, the UTE images were subject to slight fat blurring (water-fat shift of 0.74 pixel) due to the radial k-space trajectory. The influence of the fat blurring depends on the readout bandwidth and the in-plane resolution of the scan protocol. Finally, the implemented partial Fourier imaging in the slice encoding dimension affected SNR and might add blurring in the slice encoding direction. However, the partial Fourier imaging can be replaced by a parallel imaging acceleration in the future.

Several limitations were specific to the proposed sUTE-Dixon methodology and are independent of the imaged anatomy. First, noise was propagated from the phase

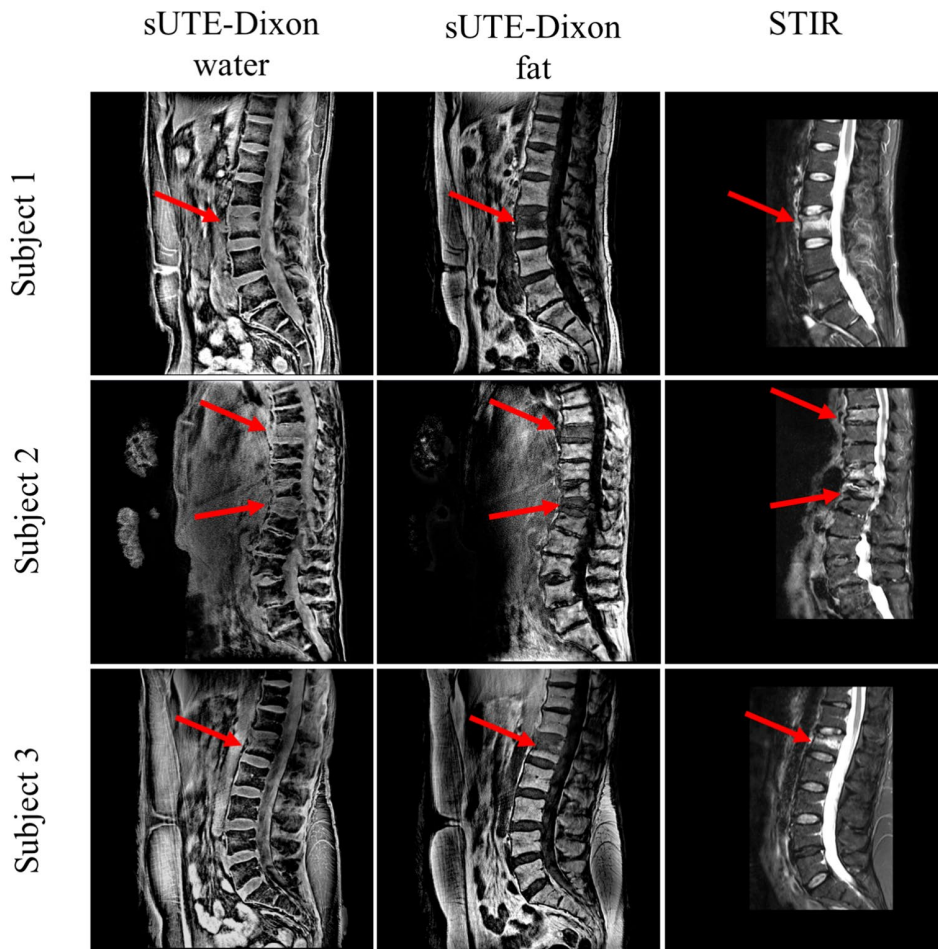


**FIGURE 6** In vivo UTE lumbar spine sagittal images of three patients with acute vertebral fractures (red arrows). The build-up of fluid in the edema was highlighted in the STIR images with a bright signal. The edema as well as the fracture line were clearly visible in the sUTE-Dixon water-fat images. In subject 2, the signal drops toward the anterior part because the subject was scanned without an anterior coil

masks into the SW images and, therefore, SNR decreased slightly at each weighting step. Appropriate denoising of the phase could help to prevent noise propagation and might be subject of future investigations. Second, in the SWI the phase information was used as a weighting in the magnitude. Therefore, not only the contrast of osseous structures is manipulated but also areas with high fat content are weighted. It is important to note that the contrast in the SW-like images comprises both susceptibility and chemical shift effects. Due to the similarity between the weighting of osseous tissue and fatty tissue, SW-like images must be evaluated carefully and were, therefore, not included in the radiological reading. Third, the TE of 0.14 ms was chosen based on the available minimum TE of the pulse sequence and the clinical system presently used. The minimum TE depends on the switching time of the RF system between transmission and reception. Potentially, shorter TEs may be achievable with a different scanner system, yet the question remains whether shorter

TEs are beneficial. For shorter TEs, the magnitude images include higher signal from short  $T_2^*$  components; however, the phase difference between water and fat is smaller. If TE increases, signals from short  $T_2^*$  components decrease, nonetheless the phase difference between water and fat increases and, thus, the contrast between water and fat increases. Estimating the optimal TE is a tradeoff between the short  $T_2^*$  magnitude signal and the water-fat phase contrast. In our study, we showed that, for TE = 0.14 ms, high quality water- and fat-separated images can be obtained with magnitude images that include short  $T_2^*$  signal components. However, future work is required to define the optimal TE. Finally, the sUTE-Dixon approach could be combined with a low-resolution calibration scan to estimate the fieldmap, which would involve only relatively little additional scan time. An a priori known low-resolution field-map could further improve quality of the water-fat separated images using the proposed processing and might enable quantitative applications using the proposed

processing. However, additional work would be required to investigate the additional value of a low-resolution calibration scan to estimate the fieldmap and any implications of such a scan for quantitative imaging applications.

## 5 | CONCLUSION

We proposed a methodology for the removal of unwanted low-frequency background phases, simultaneous water-fat separation and SWI processing from a single echo complex UTE image. The proposed method enabled the simultaneous assessment of vertebral fracture and edema of the thoracolumbar spine from a single MR sequence.

## ACKNOWLEDGMENTS

The present work was supported by the European Research Council (grant agreement no. 677661, ProFatMRI). This work reflects only the authors' views and the European Union is not responsible for any use that may be made of the information it contains. Finally, the authors acknowledge research support from Philips Healthcare. Open access funding enabled and organized by ProjektDEAL.

## CONFLICT OF INTEREST

Kilian Weiss, Peter Börnert, and Ulrich Katscher are employees of Philips Healthcare.

## ORCID

Sophia Kronthaler  <https://orcid.org/0000-0001-7913-1238>

[org/0000-0001-7913-1238](https://orcid.org/0000-0001-7913-1238)

Christof Boehm  <https://orcid.org/0000-0003-1321-5804>

Ulrich Katscher  <https://orcid.org/0000-0003-1379-1115>

## REFERENCES

- Shaneci AM, Kiczek M, Khan M, Jindal G. Spine anatomy imaging: an update. *Neuroimaging Clin N Am*. 2019;29:461-480.
- Piazzolla A, Solarino G, Lamartina C, et al. Vertebral bone marrow edema (VBME) in conservatively treated acute vertebral compression fractures (VCFs): evolution and clinical correlations. *Spine*. 2015;40:E842-E848.
- Mandalia V, Henson JH. Traumatic bone bruising—a review article. *Eur J Radiol*. 2008;67:54-61.
- Weiger M, Pruessmann KP. Short-T2 MRI: principles and recent advances. *Prog Nucl Magn Reson Spectrosc*. 2019;114-115:237-270.
- Ma YJ, Chen Y, Li L, et al. Trabecular bone imaging using a 3D adiabatic inversion recovery prepared ultrashort TE cones sequence at 3T. *Magn Reson Med*. 2020;83:1640-1651.
- Lu X, Jerban S, Wan L, et al. Three-dimensional ultrashort echo time imaging with tricomponent analysis for human cortical bone. *Magn Reson Med*. 2019;82:348-355.
- Wiesinger F, Sacolick LI, Menini A, et al. Zero TE MR bone imaging in the head. *Magn Reson Med*. 2016;75:107-114.
- Schwaiger BJ, Schneider C, Kronthaler S, et al. CT-like images based on T1 spoiled gradient-echo and ultra-short echo time MRI sequences for the assessment of vertebral fractures and degenerative bone changes of the spine. *Eur Radiol*. 2021;31:4680-4689.
- Argentieri EC, Koff MF, Breighner RE, Endo Y, Shah PH, Sneag DB. Diagnostic accuracy of zero-echo time MRI for the evaluation of cervical neural foraminal stenosis. *Spine*. 2018;43:928-933.
- Breighner RE, Bogner EA, Lee SC, Koff MF, Potter HG. Evaluation of osseous morphology of the hip using zero echo time magnetic resonance imaging. *Am J Sports Med*. 2019;47:3460-3468.
- Breighner RE, Endo Y, Konin GP, Gulotta LV, Koff MF, Potter HG. Technical developments: zero echo time imaging of the shoulder: enhanced osseous detail by using MR imaging. *Radiology*. 2018;286:960-966.
- Haacke EM, Mittal S, Wu Z, Neelavalli J, Cheng YC. Susceptibility-weighted imaging: technical aspects and clinical applications, part 1. *AJNR Am J Neuroradiol*. 2009;30:19-30.
- Böker SM, Adams LC, Bender YY, et al. Differentiation of predominantly osteoblastic and osteolytic spine metastases by using susceptibility-weighted MRI. *Radiology*. 2019;290:146-154.
- Boker SM, Adams LC, Fahlenkamp UL, Diederichs G, Hamm B, Makowski MR. Value of susceptibility-weighted imaging for the assessment of angle measurements reflecting hip morphology. *Sci Rep*. 2020;10:20899.
- Boker SM, Adams LC, Bender YY, et al. Evaluation of vertebral body fractures using susceptibility-weighted magnetic resonance imaging. *Eur Radiol*. 2018;28:2228-2235.
- Adams LC, Bressemer K, Boker SM, et al. Diagnostic performance of susceptibility-weighted magnetic resonance imaging for the detection of calcifications: a systematic review and meta-analysis. *Sci Rep*. 2017;7:15506.
- Engel G, Bender YY, Adams LC, et al. Evaluation of osseous cervical foraminal stenosis in spinal radiculopathy using susceptibility-weighted magnetic resonance imaging. *Eur Radiol*. 2019;29:1855-1862.
- Boker SM, Bender YY, Adams LC, et al. Evaluation of sclerosis in Modic changes of the spine using susceptibility-weighted magnetic resonance imaging. *Eur J Radiol*. 2017;88:148-154.
- Dixon WT. Simple proton spectroscopic imaging. *Radiology*. 1984;153:189-194.
- Glover GH. Multipoint Dixon technique for water and fat proton and susceptibility imaging. *J Magn Reson Imaging*. 1991;1:521-530.
- Glover GH, Schneider E. Three-point Dixon technique for true water/fat decomposition with B0 inhomogeneity correction. *Magn Reson Med*. 1991;18:371-383.
- Su KH, Friel HT, Kuo JW, et al. UTE-mDixon-based thorax synthetic CT generation. *Med Phys*. 2019;46:3520-3531.
- Jang H, von Drygalski A, Wong J, et al. Ultrashort echo time quantitative susceptibility mapping (UTE-QSM) for detection of hemosiderin deposition in hemophilic arthropathy: a feasibility study. *Magn Reson Med*. 2020;84:3246-3255.
- Wang K, Yu H, Brittain JH, Reeder SB, Du J. k-space water-fat decomposition with T2\* estimation and multifrequency fat

- spectrum modeling for ultrashort echo time imaging. *J Magn Reson Imaging*. 2010;31:1027-1034.
25. Su KH, Hu L, Stehning C, et al. Generation of brain pseudo-CTs using an undersampled, single-acquisition UTE-mDixon pulse sequence and unsupervised clustering. *Med Phys*. 2015;42:4974-4986.
  26. Qian P, Zheng J, Zheng Q, et al. Transforming UTE-mDixon MR abdomen-pelvis images into CT by jointly leveraging prior knowledge and partial supervision. *IEEE/ACM Trans Comput Biol Bioinform*. 2021;18:70-82.
  27. Gong K, Han PK, Johnson KA, El Fakhri G, Ma C, Li Q. Attenuation correction using deep Learning and integrated UTE/multi-echo Dixon sequence: evaluation in amyloid and tau PET imaging. *Eur J Nucl Med Mol Imaging*. 2021;48:1351-1361.
  28. Leynes AP, Yang J, Shanbhag DD, et al. Hybrid ZTE/Dixon MR-based attenuation correction for quantitative uptake estimation of pelvic lesions in PET/MRI. *Med Phys*. 2017;44:902-913.
  29. Jang H, Carl M, Ma Y, et al. Fat suppression for ultrashort echo time imaging using a single-point Dixon method. *NMR Biomed*. 2019;32:e4069.
  30. Yu H, Reeder SB, McKenzie CA, et al. Single acquisition water-fat separation: feasibility study for dynamic imaging. *Magn Reson Med*. 2006;55:413-422.
  31. Ma J. A single-point Dixon technique for fat-suppressed fast 3D gradient-echo imaging with a flexible echo time. *J Magn Reson Imaging*. 2008;27:881-890.
  32. Jang H, Ma Y, Carl M, Jerban S, Chang EY, Du J. Ultrashort echo time Cones double echo steady state (UTE-Cones-DESS) for rapid morphological imaging of short T2 tissues. *Magn Reson Med*. 2021;86:881-892.
  33. Yu H, Shimakawa A, McKenzie CA, Brodsky E, Brittain JH, Reeder SB. Multiecho water-fat separation and simultaneous R2\* estimation with multifrequency fat spectrum modeling. *Magn Reson Med*. 2008;60:1122-1134.
  34. Diefenbach MN, Ruschke S, Eggers H, Meineke J, Rummeny EJ, Karampinos DC. Improving chemical shift encoding-based water-fat separation based on a detailed consideration of magnetic field contributions. *Magn Reson Med*. 2018;80:990-1004.
  35. Kronthaler S, Rahmer J, Bornert P, et al. Trajectory correction based on the gradient impulse response function improves high-resolution UTE imaging of the musculoskeletal system. *Magn Reson Med*. 2021;85:2001-2015.
  36. Ren J, Dimitrov I, Sherry AD, Malloy CR. Composition of adipose tissue and marrow fat in humans by 1H NMR at 7 Tesla. *J Lipid Res*. 2008;49:2055-2062.
  37. Katscher U, van den Berg CAT. Electric properties tomography: biochemical, physical and technical background, evaluation and clinical applications. *NMR Biomed*. 2017;30:e3729.
  38. Kim DH, Choi N, Gho SM, Shin J, Liu C. Simultaneous imaging of in vivo conductivity and susceptibility. *Magn Reson Med*. 2014;71:1144-1150.
  39. van Lier AL, Brunner DO, Pruessmann KP, et al. B1(+) phase mapping at 7 T and its application for in vivo electrical conductivity mapping. *Magn Reson Med*. 2012;67:552-561.
  40. Hong CW, Mamidipalli A, Hooker JC, et al. MRI proton density fat fraction is robust across the biologically plausible range of triglyceride spectra in adults with nonalcoholic steatohepatitis. *J Magn Reson Imaging*. 2018;47:995-1002.
  41. Berglund J, Ahlström H, Kullberg J. Model-based mapping of fat unsaturation and chain length by chemical shift imaging-phantom validation and in vivo feasibility. *Magn Reson Med*. 2012;68:1815-1827.
  42. Peterson P, Månsson S. Simultaneous quantification of fat content and fatty acid composition using MR imaging. *Magn Reson Med*. 2013;69:688-697.
  43. Hamilton G, Yokoo T, Bydder M, et al. In vivo characterization of the liver fat 1H MR spectrum. *NMR Biomed*. 2011;24:784-790.
  44. Franz D, Diefenbach MN, Treibel F, et al. Differentiating supraclavicular from gluteal adipose tissue based on simultaneous PDFP and T2\* mapping using a 20-echo gradient-echo acquisition. *J Magn Reson Imaging*. 2019;50:424-434.
  45. Haacke EM, Xu Y, Cheng YC, Reichenbach JR. Susceptibility weighted imaging (SWI). *Magn Reson Med*. 2004;52:612-618.
  46. Ruschke S, Eggers H, Kooijman H, et al. Correction of phase errors in quantitative water-fat imaging using a monopolar time-interleaved multi-echo gradient echo sequence. *Magn Reson Med*. 2017;78:984-996.
  47. Diefenbach MN, Liu C, Karampinos DC. Generalized parameter estimation in multi-echo gradient-echo-based chemical species separation. *Quant Imaging Med Surg*. 2020;10:554-567.
  48. Gabriel S, Lau RW, Gabriel C. The dielectric properties of biological tissues: III. Parametric models for the dielectric spectrum of tissues. *Phys Med Biol*. 1996;41:2271-2293.

## SUPPORTING INFORMATION

Additional supporting information may be found in the online version of the article at the publisher's website.

**FIGURE S1** (A) Representative fat spectrum models. Shown are on the left side the different models for one parameter set (cl of 17.55, ndb of 1.9 and nmdb of 0.9) and on the right side the Peterson 8 peaks model for all different values of cl, ndb and nmdb. (B) Water maps obtained with the Ren marrow reference spectral model (left) and the water map obtained for the spectral model that resulted in the highest RMSE of 1.8% (right)

**TABLE S1** Simulation results using different spectral models. The root mean squared error (RMSE) was calculated between the water maps obtained by the Ren marrow reference spectral model and the specified spectral model. The maximal RMSE was 1.81% and is highlighted in red, the corresponding water map is shown in Figure S1B

**How to cite this article:** Kronthaler S, Boehm C, Feuerriegel G, et al. Assessment of vertebral fractures and edema of the thoracolumbar spine based on water-fat and susceptibility-weighted images derived from a single ultra-short echo time scan. *Magn Reson Med*. 2021;00:1-13. doi:[10.1002/mrm.29078](https://doi.org/10.1002/mrm.29078)

### 7.3 Journal Publication III:

#### On quantification errors of $R_2^*$ and proton density fat fraction mapping in trabecularized bone marrow in the static dephasing regime

The publication entitled *On quantification errors of  $R_2^*$  and proton density fat fraction mapping in trabecularized bone marrow in the static dephasing regime* was published in Magnetic Resonance in Medicine (ISSN: 0740-3194 ) [187]. The manuscript was authored by Sophia Kronthaler, Maximilian N. Diefenbach, Christof Boehm, Mark Zamskiy, Marcus R. Makowski, Thomas Baum, Nico Sollmann, Dimitrios C. Karampinos. It is available online (DOI: 10.1002/mrm.29279) as an open access article under the terms of the Creative Commons Attribution-NonCommercial-NoDerivs License. Preliminary results were presented in the conference contribution C18, which was awarded with an ISMRM Summa Cum Laude Merit Award and selected as an oral presentation at the ISMRM annual meeting 2021. A summary of the publication is provided in Section 7.3.1, the author contributions are listed in Section 7.3.2 and the full text is included subsequently on the following pages.

#### 7.3.1 Abstract

##### Purpose

To study the effect of field inhomogeneity distributions in trabecularized bone regions on the GRE signal with short TEs and to characterize quantification errors on  $R_2^*$  and PDFF maps when using a water-fat model with an exponential  $R_2^*$  decay model at short TEs.

##### Methods

Field distortions were simulated based on a trabecular bone micro CT dataset. Simulations were performed for different bone volume fraction (BV/TV) and for different bone-fat composition values. A multi-TE UTE acquisition was developed to acquire multiple UTEs with random order to minimize eddy currents. The acquisition was validated in phantoms and applied in vivo in a volunteer's ankle and knee. CSE-MRI based on a Cartesian multi-TE GRE scan was acquired in the spine of patients with metastatic bone disease.

##### Results

Simulations showed that signal deviations from the exponential signal decay at short TEs were more prominent for a higher BV/TV. UTE multi-TE measurements reproduced in vivo the simulation-based predicted behavior. In regions with high BV/TV, the presence of field inhomogeneities induced an  $R_2^*$  underestimation in trabecularized bone marrow when using CSE-MRI at 3T with a short TE.

##### Conclusion

$R_2^*$  can be underestimated when using short TEs (<2 ms at 3T) and a water-fat model with an exponential  $R_2^*$  decay model in multi-echo GRE acquisitions of trabecularized bone marrow.

### **7.3.2 Author contributions**

The first author performed the experiments (MR measurements), programmed the magnetic resonance pulse sequence (propriety hardware, specific libraries and software from Philips Medical Systems Best, The Netherlands), implemented the post-processing and the quantification process. With the help and consultation from the coauthors, the first author designed the experiment, analyzed and interpreted the data and wrote the manuscript.

## RESEARCH ARTICLE

# On quantification errors of $R_2^*$ and proton density fat fraction mapping in trabecularized bone marrow in the static dephasing regime

Sophia Kronthaler<sup>1</sup>  | Maximilian N. Diefenbach<sup>1</sup>  | Christof Boehm<sup>1</sup>  |

Mark Zamskiy<sup>1</sup> | Marcus R. Makowski<sup>1</sup> | Thomas Baum<sup>2</sup> |

Nico Sollmann<sup>2,3,4</sup> | Dimitrios C. Karampinos<sup>1</sup>

<sup>1</sup>Department of Diagnostic and Interventional Radiology, School of Medicine, Klinikum rechts der Isar, Technical University of Munich, Munich, Germany

<sup>2</sup>Department of Diagnostic and Interventional Neuroradiology, School of Medicine, Klinikum rechts der Isar, Technical University of Munich, Munich, Germany

<sup>3</sup>TUM-Neuroimaging Center, Klinikum rechts der Isar, Technical University of Munich, Munich, Germany

<sup>4</sup>Department of Diagnostic and Interventional Radiology, University Hospital Ulm, Ulm, Germany

## Correspondence

Sophia Kronthaler, Department of Diagnostic and Interventional Radiology, Klinikum rechts der Isar, Technische Universität München, Ismaninger Str. 22, 81675 Munich, Germany.  
Email: [sophia.kronthaler@tum.de](mailto:sophia.kronthaler@tum.de)

## Funding information

The present work was supported by the European Research Council (grant agreement no. 677661, ProFatMRI). The authors also acknowledge research support from DAAD (Project number: 57514573) and Philips Healthcare. Open Access funding enabled and organized by Projekt DEAL in the Technical University of Munich.

**Purpose:** To study the effect of field inhomogeneity distributions in trabecularized bone regions on the gradient echo (GRE) signal with short TEs and to characterize quantification errors on  $R_2^*$  and proton density fat fraction (PDFF) maps when using a water-fat model with an exponential  $R_2^*$  decay model at short TEs.

**Methods:** Field distortions were simulated based on a trabecular bone micro CT dataset. Simulations were performed for different bone volume fractions (BV/TV) and for different bone-fat composition values. A multi-TE UTE acquisition was developed to acquire multiple UTEs with random order to minimize eddy currents. The acquisition was validated in phantoms and applied in vivo in a volunteer's ankle and knee. Chemical shift encoded MRI (CSE-MRI) based on a Cartesian multi-TE GRE scan was acquired in the spine of patients with metastatic bone disease.

**Results:** Simulations showed that signal deviations from the exponential signal decay at short TEs were more prominent for a higher BV/TV. UTE multi-TE measurements reproduced in vivo the simulation-based predicted behavior. In regions with high BV/TV, the presence of field inhomogeneities induced an  $R_2^*$  underestimation in trabecularized bone marrow when using CSE-MRI at 3T with a short TE.

**Conclusion:**  $R_2^*$  can be underestimated when using short TEs (<2 ms at 3 T) and a water-fat model with an exponential  $R_2^*$  decay model in multi-echo GRE acquisitions of trabecularized bone marrow.

## KEYWORDS

chemical shift encoding (CSE), Gaussian decay, magnetically inhomogeneous tissues, PDFF mapping,  $R_2^*$  mapping, signal decay, static dephasing regime, trabecularized bone, ultra-short echo time (UTE)

This is an open access article under the terms of the Creative Commons Attribution-NonCommercial License, which permits use, distribution and reproduction in any medium, provided the original work is properly cited and is not used for commercial purposes.

© 2022 The Authors. *Magnetic Resonance in Medicine* published by Wiley Periodicals LLC on behalf of International Society for Magnetic Resonance in Medicine.



## 1 | INTRODUCTION

The clinical need for early diagnosis of osteoporosis, for assessment of fracture risk, and for therapy response monitoring has been driving the development of MRI methods to assess trabecular bone density and microstructure in vivo.<sup>1–3</sup> Trabecular bone consists of a complex network of bone tissue, which can comprise around 30% of the total tissue volume. The trabecular bone cavities are filled with fatty bone marrow.<sup>4</sup> Since bone signal decays rapidly with a very short  $T_2^*$ , in conventional MRI methods the signal of bone marrow was used indirectly to assess trabecular bone. First, high-resolution imaging was used to resolve the trabecular bone matrix as signal void within the bone marrow signal. However, high-resolution MR trabecular bone imaging is limited to distal skeletal sites and due to its low sensitivity and motion.<sup>2,5</sup> Beyond high-resolution trabecular bone imaging, trabecular bone has been typically indirectly evaluated by measurements of effective bone marrow properties.  $T_2^*$  and  $R_2^*$  measurements in trabecularized bone marrow have been correlated with the bone mineral density since early works<sup>5–9</sup> and  $R_2^*$  has been proposed as a biomarker for bone loss in osteoporosis.<sup>1,10–12</sup> More recently the proton density fat fraction (PDFF) has been introduced as a biomarker of bone marrow fat content changes associated with bone loss.<sup>1,2,12–14</sup> Therefore, chemical shift encoding-based (CSE) water-fat separation assuming a single  $R_2^*$  exponential signal decay has been proposed to simultaneously assess changes in the trabecular bone matrix by  $R_2^*$  quantification and in bone marrow fat content by PDFF quantification.<sup>1,2,13,15</sup>

The trabecular bone network presents an inherently complex topology with the bony trabeculae and the signal generating bone marrow in the intra-trabecular space. The susceptibility difference between bone and marrow and the underlying complex microstructure cause a large distribution of inhomogeneities of the induced magnetic field within each voxel. Due to the distribution of field inhomogeneities, spins dephase rapidly and consequently yield a decreased TR due to intravoxel dephasing. It was shown previously, in simulations<sup>16,17</sup> and in theoretical analyses,<sup>18,19</sup> that, in the static dephasing regime, the intra-voxel dephasing can be described as a mono-exponential decay with decay rate  $R_2^*$ . The static dephasing regime applies if diffusion effects become negligible as the dephasing field inhomogeneities are much stronger than the signal decay due to diffusive motion. The exponential decay originates from the assumption of Lorentzian distribution of field inhomogeneities. The frequency spectrum of an FID has a Lorentzian line shape with the FWHM of the Lorentzian distribution being equal to  $\frac{R_2^*}{\pi}$ .<sup>20</sup> In the static dephasing regime and within trabecular bone, it was shown that  $R_2^*$  depends on the bone density as well as the orientation

of trabecular bone with respect to the main magnetic field.<sup>7,9,18,21</sup>

The above described mono-exponential signal decay behavior, however, applies only for long TEs. In reality and for large field inhomogeneities, the distribution is not necessarily Lorentzian and resembles a Gaussian shape, which will affect the decay behavior for short TEs.<sup>18,19,22</sup> Therefore, at short TEs there are two effects that need to be considered. There is additional signal from short  $T_2^*$  tissue such as the bone matrix and, due to the underlying microstructure, the surrounding bone marrow signal follows a Gaussian decay. The characteristic TE, that defines the time point at which the Gaussian decay deviates from the mono-exponential decay, may be of the order of the shortest achievable TEs that are commonly used at CSE-MRI acquisitions of bone marrow.<sup>18,19,23,24</sup> In CSE-MRI, a typical acquisition strategy aims to minimize the first TE to increase the SNR, and water-fat signal modeling typically relies on the assumption of a mono-exponential single  $R_2^*$  signal decay. The question of the influence of large field inhomogeneities on the  $R_2^*$  signal decay at short TEs has not been addressed before and needs the ability to measure the decaying signal at UTE. Therefore, the purpose of this work is to investigate, with the help of a UTE acquisition, the quantification errors of  $R_2^*$  and PDFF maps in trabecularized bone marrow regions in the static dephasing regime when using a water-fat model with an exponential  $R_2^*$  decay model at short TEs.

## 2 | METHODS

### 2.1 | Bone cubes forward simulation

Similar to previous work on simulating magnetic fields, magnetic field offsets caused by a trabecular bone model were simulated.<sup>9,16,17</sup> Therefore, a micro computed tomography (CT) dataset was acquired with 45.6  $\mu\text{m}$  isotropic resolution of a healthy human femur bone cube with a size of  $180 \times 180 \times 180 \text{ mm}^3$ , containing only trabecular bone structure. From the micro-CT images, a bone mask was derived by applying a simple threshold at 50% (Figure 1A). The bone volume to total volume (BV/TV) ratio of each femoral cube was estimated by taking the mean inside the bounding box of the binary mask. A susceptibility map was obtained by assigning the susceptibility  $\chi$  of bone and marrow to the bone mask with  $\Delta\chi$  being defined as the difference between bone matrix to the surrounding marrow. According to the forward model as described earlier,<sup>25,26</sup> the relative distance field (RDF), deviations from the applied magnetic field, was simulated with one fixed  $B_0$ -direction, with varying  $\Delta\chi$  and with varying BV/TV ratios. The BV/TV ratio of the bone masks was

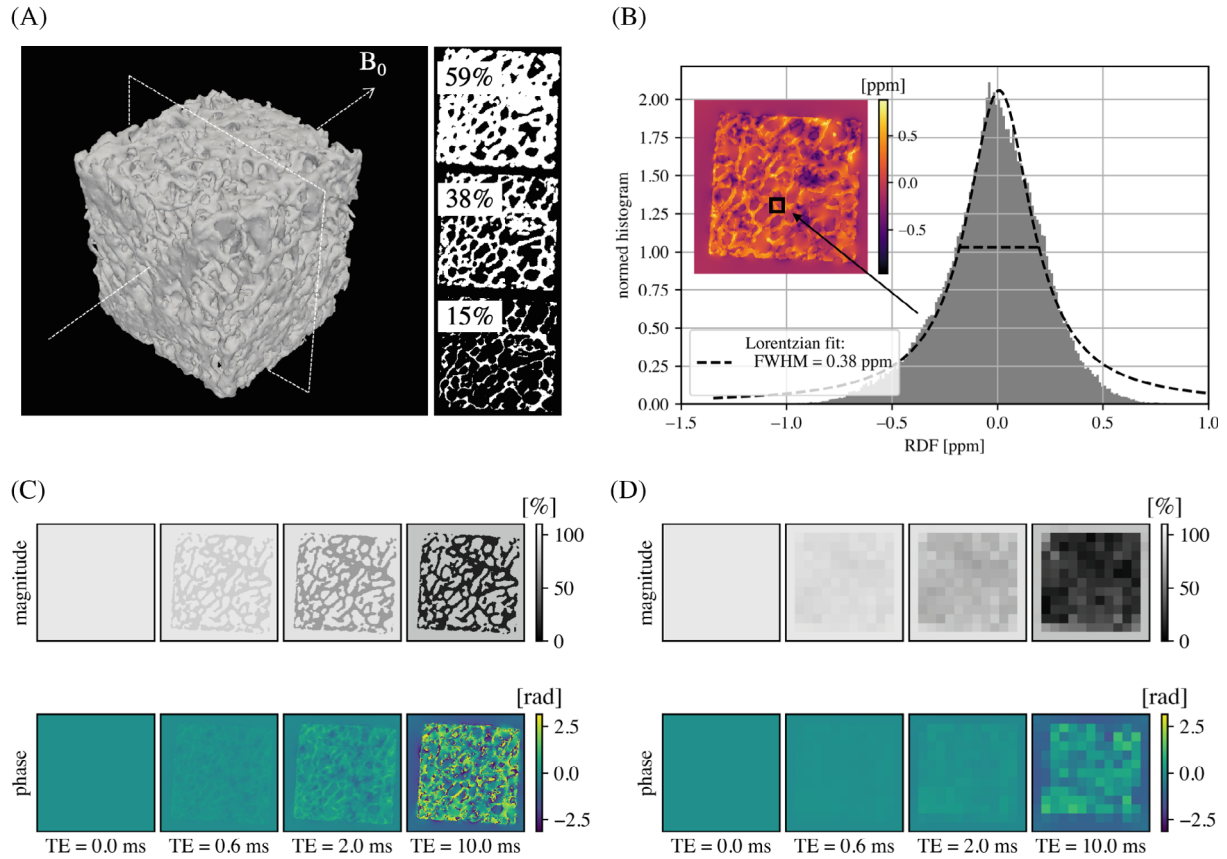


**FIGURE 1** Illustration of the bone cube simulations. A, A bone mask was generated from a microscopic CT scan of resolution  $45.6 \mu\text{m}$  (BV/TV 38%). B, The BV/TV was altered by erosion (BV/TV = 15%) and dilation (BV/TV = 59%). Forward simulated relative field map. The black square shows the size of a  $1.5 \times 1.5 \text{ mm}^2$  MR voxel and the distribution of the relative difference field (RDF) within the MR voxel. The FWHM of a Lorentzian fit was calculated to give an estimate of the signal decay due to the distribution of local inhomogeneities. With the field-map a signal for different TEs is generated on the microscopic CT scale (C) and down-sampled to the MR resolution of  $1.5 \times 1.5 \text{ mm}^2$  (D). RDF: relative distance field

altered by erosion and dilation with standard image processing tools (Python version 3.9.0, binary erosion/dilation from the `ndimage` `scipy` module with a nearest neighbor kernel, SciPy Version 1.7.1) to simulate the degeneration of trabecular bone comparable to the degeneration of bone in osteoporosis (Figure 1A). An auto-binned (Freedman Diaconis Estimator) histogram of all field values outside the trabecular bone was generated and shows the distribution of local field inhomogeneities within a  $1.5 \text{ mm} \times 1.5 \text{ mm} \times 1.5 \text{ mm}$  voxel (Figure 1B). The FWHM of the fitted Lorentzian curve was calculated to give an estimate of the reversible relaxation rate  $R_2'$ . The resulting RDF map was used to simulate a complex multi-echo signal at 3 T with TE = 0–10 ms and  $\Delta\text{TE} = 0.2 \text{ ms}$  (Figure 1C), assuming the following single-  $R_2^*$  bone signal model and single-  $R_2^*$  multi-fat-peak fat signal model.

$$S(t) = \begin{cases} \rho e^{-R_{2,B}^* t} & \text{in the bone matrix} \\ c(t) e^{-R_{2,F}^* t} e^{i2\pi f_{\text{RDF}} t} & \text{in the bone marrow} \end{cases}$$

$$\text{with } c(t) = \sum_{p=1}^P \alpha_p e^{i2\pi \Delta f_p t} \quad (1)$$

The fat signal was modeled by an a priori known spectrum  $c(t)$  with  $P$  spectral peaks with relative amplitudes  $\alpha_p$  and chemical shift  $\Delta f_p$ . The bone signal was modeled with a simple mono-exponential decay with  $\rho$  as the density of the bone matrix normalized by the density of the bone marrow. The simulated signal on the microscopic scale was down-sampled to the MR-like isotropic resolution of  $1.5 \text{ mm}$  by averaging the signal (Figure 1D). To assess the effect of local field inhomogeneities on the signal decay, caused by the susceptibility difference between bone and marrow, bone cube simulations with varying BV/TV ratios were performed (Figure 2A,B). Furthermore, the simulations were repeated for different signal models and a fixed BV/TV of 38% (Figure 2C,D): a) without bone matrix signal  $\rho = 0$  and with a single-fat-peak fat model  $T_{2,F} = 60 \text{ ms}$ ,<sup>27,28</sup>  $c(t) = 1$  b) without bone matrix signal ( $\rho = 0$ ) and with a nine-peak marrow fat spectrum model<sup>29</sup>

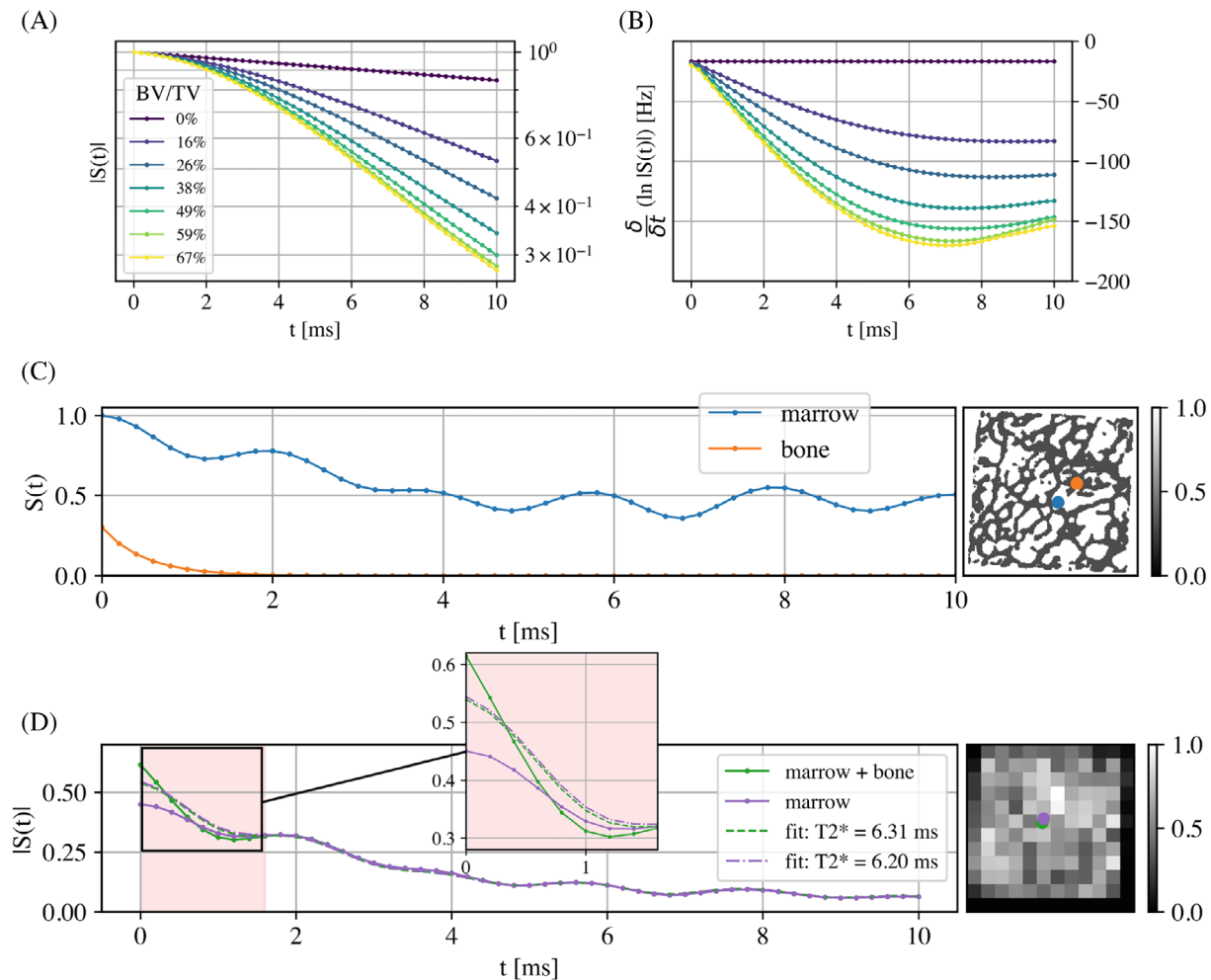


**FIGURE 2** Simulation results. A, Simulation of the macroscopic signal for varying BV/TV. Only the marrow signal was included in the simulation ( $\rho = 0$ ) with a single-fat-peak fat model ( $c(t) = 1$ ). For a BV/TV of 0%, the signal followed a mono-exponential decay with  $T_{2,F} = 60$  ms. B, The corresponding signal derivative shows that for a non-zero BV/TV the local distribution of RDFs yielded a Gaussian decay at low TEs and an exponential decay at larger TEs. C, Simulation of the microscopic signal for a voxel containing only bone and for a voxel containing only marrow. The bone signal followed a mono-exponential decay with  $T_{2,B}^* = 0.5$  ms. The marrow signal showed oscillations due to the nine-peak marrow fat spectrum. D, Simulation of the macroscopic signal including either only the signal of marrow or including the signal of both bone and marrow. The dashed lines show fitting results when only data points at TEs larger than 2 ms were included. The extrapolation of the fit at TEs < 2 ms resulted in a higher signal when compared to the simulation result (red area)

( $T_{2,F} = 60$  ms) and c) with bone matrix signal<sup>30</sup> ( $\rho = 0.3$ ,  $T_{2,B}^* = 0.5$  ms) and with a nine-peak marrow fat spectrum model<sup>29</sup> ( $T_{2,F} = 60$  ms).

## 2.2 | Multi-TE UTE pulse sequence

To measure the signal at short TEs, a 3D UTE stack-of-stars center-out radial sequence was employed<sup>31</sup> (Figure 3A). The non-selective RF excitation pulse was followed by a short phase-encoding gradient that adds a Cartesian dimension along the slice encoding direction. The duration of the phase-encoding gradient varied depending on the slice encoding. In addition, a variable delay  $dTE$  was

added, between the excitation pulse and slice encoding gradient, to achieve an arbitrary TE.<sup>32</sup> The delay was modified between TRs in a random order to prevent potential eddy current artifacts as described in<sup>32</sup> (Figure 3B). All TEs along one spoke were acquired first, before the acquisition of the next spoke. All spokes within one slice were acquired with a uniform, constant azimuthal angle sampling pattern. The minimal FID readout time of 0.14 ms was defined by the RF transmit–receive switching time of the system. A minimum TE of 0.19 ms was used for all measurements to give the coil system more time to tune the receive coil and eliminate remaining switching transients. All images were acquired on a 3T system (Elition X, Release 5.4; Philips Medical Systems).

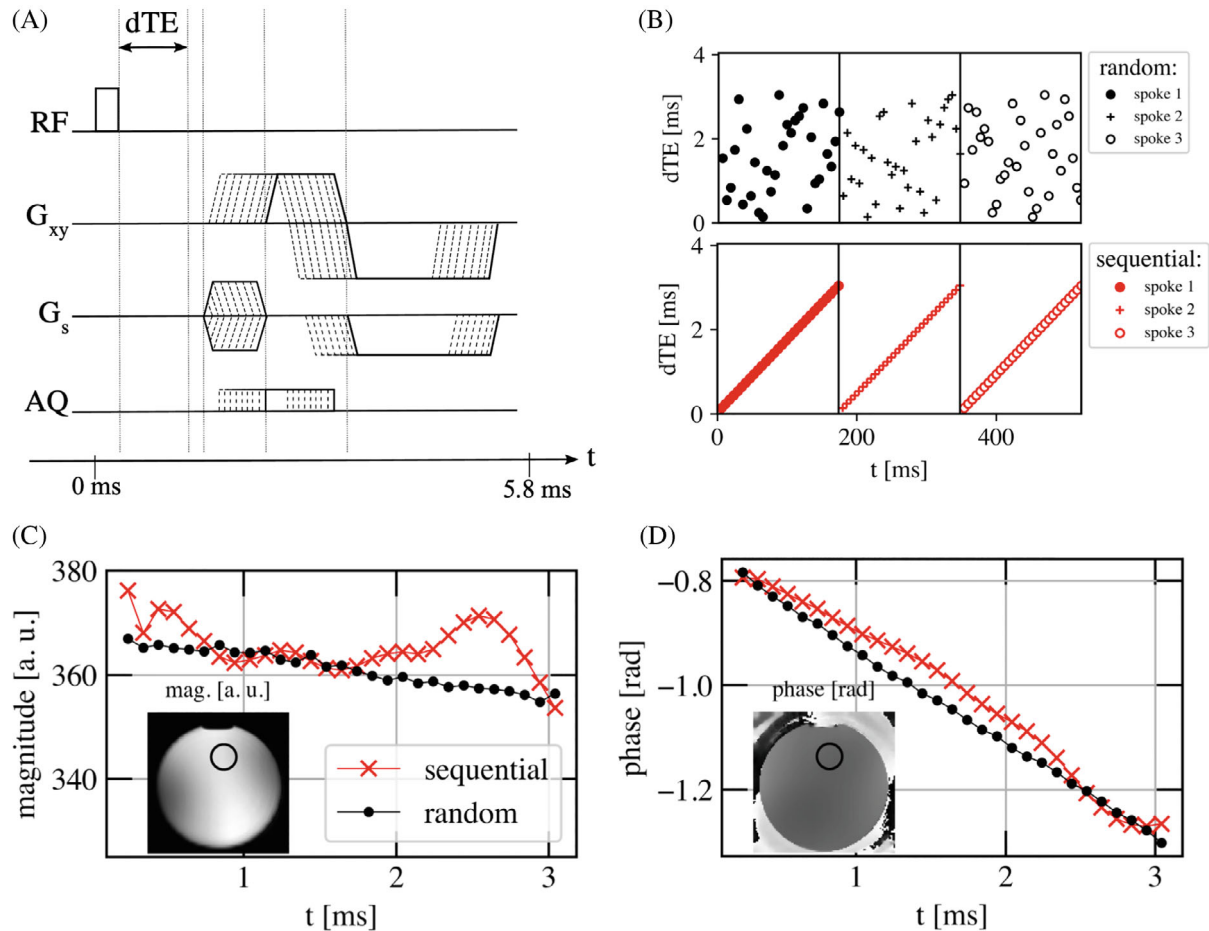


**FIGURE 3** 3D multi-TE UTE stack-of-stars acquisition: A, After the non-selective excitation, the FID readout started after a variable delay  $dTE$ . B, All TEs along one spoke were acquired in random order and before the readout of the next spoke. For comparison, the same acquisition was repeated with a sequential ordering of the TEs. C, D, Magnitude and phase over time of a phantom filled with water for the random (black) and the sequential (red) acquisition scheme

### 2.3 | Phantom measurements

To validate the signal stability of the multi-TE UTE acquisition strategy used, phantom measurements were performed in a water phantom and in water-fat phantoms with PDFF values of 0%, 5%, 15% and 100%.

For the measurement of the signal decay curves in the water phantom, an extensive coronal echo multi-TE UTE sampling was performed with 29 TEs in the range from 0.19 ms to 2.9 ms (Figure 1C, D) and the following scan parameters: TR 5.8 ms, flip angle (FA)  $5^\circ$ , in-plane resolution  $1.5 \times 1.5 \text{ mm}^2$ , slice thickness 3 mm, FOV  $180 \times 180 \times 116 \text{ mm}^3$ , receiver bandwidth 1440 Hz/pixel, and scan time of 16.4 min.

For the measurements of the PDFF phantoms a multi-TE UTE axial scan with 15 TEs was acquired with the following scan parameters: TE = [0.19, 0.24, 0.34, 0.44, 0.54, 0.64, 0.74, 0.84, 0.94, 1.04, 1.14, 2.24, 3.34, 4.44, 5.54, 6.64] ms, TR 9.2 ms, FA  $5^\circ$ , in-plane

resolution  $1.5 \times 1.5 \text{ mm}^2$ , slice thickness 5 mm, FOV  $100 \times 100 \times 250 \text{ mm}^3$ , receiver bandwidth 1426 Hz/pixel and scan time of 11.7 min.

For conventional Dixon imaging and for comparison, a 3D Cartesian six-echo monopolar time-interleaved multi-echo gradient-echo (GRE) sequence was used as described previously<sup>33</sup> with the following parameters: two interleaves with three echoes per TR and TR/TE<sub>1</sub>/ΔTE: 7.7/1.25/1.1 ms, FA  $3^\circ$ , voxel size  $1.5 \times 1.5 \times 5 \text{ mm}^3$ , FOV  $100 \times 100 \times 250 \text{ mm}^3$ , receiver bandwidth 1213 Hz/pixel, frequency direction anterior–posterior, scan time: 3.7 min.

### 2.4 | In vivo measurements

In vivo imaging was performed in the ankle and the knee of a healthy volunteer. Furthermore, clinical routine MR image data of the lumbar spine in three patients were retrospectively analyzed. The in vivo study part was approved

by the local institutional review board (Klinikum rechts der Isar, Technical University of Munich, Munich, Germany).

For the ankle measurements, a sagittal 3D multi-TE UTE measurement was performed with seven TEs, with a 16-channel ankle coil and the following parameters: TEs = [0.19 1.29 2.39 3.49 4.59 5.69 6.79] ms, FA 5°, FOV 220 × 220 × 90 mm<sup>3</sup>, voxel size 1.2 × 1.2 × 3 mm<sup>3</sup>, TR 3.4 ms, scan time 9.2 min, using a SENSE acceleration factor of 2 in the Cartesian-sampled dimension. Additionally, a Cartesian high-resolution balanced SSFP (bSSFP) reference scan was acquired with two phase cycles, TE 2.6 ms, FOV 220 × 220 × 90 mm<sup>3</sup>, voxel size 0.3 × 0.3 × 1.5 mm<sup>3</sup>.

For the knee measurements, a sagittal 3D multi-TE UTE measurement was performed with seven TEs, with a 16-channel transmit-receive knee coil and the following parameters: TE = [0.19 1.29 2.39 3.49 4.59 5.69 6.79] ms, FA 5°, FOV 130 × 130 × 105 mm<sup>3</sup>, voxel size 1.48 × 1.48 × 2 mm<sup>3</sup>, TR 10.1 ms, scan time 15.3 min, using a SENSE acceleration factor of 2 in the Cartesian-sampled dimension. Additionally, a Cartesian high-resolution bSSFP reference scan was acquired with two phase cycles, TE 2.6 ms, FOV 140 × 140 × 105 mm<sup>3</sup>, and voxel size 0.45 × 0.45 × 2 mm<sup>3</sup>.

For the calcaneus measurements, a sagittal Cartesian monopolar time-interleaved multi-echo gradient echo sequence was performed in three healthy volunteers. Scan parameters were: nine echoes in three acquisitions (three echoes per acquisition), TE<sub>1</sub>/ΔTE: 1.25/0.7 ms, readout direction feet-head, TR 13 ms, FA 5°, bandwidth/pixel = 1431.4 Hz, FOV 220 × 220 × 102 mm<sup>3</sup> and an isotropic voxel size of 1.5 mm. Additionally, all volunteer scans included a bSSFP sequence with two phase cycles, TE 3.4 ms, FOV 220 × 220 × 60 mm<sup>3</sup>, voxel size 0.3 × 0.3 × 0.9 mm<sup>3</sup>.

For the spine measurement, a sagittal Cartesian monopolar time-interleaved multi-echo gradient echo sequence was performed in the thoracolumbar spine of three patients where clinical MRI of the spine was performed either to assess degenerative disease or bone metastases. Subject 1: male, age 77, diagnosed with prostate cancer showed metastasis in L3 and extraosseous components. Subject 2: female, age 80, diagnosed with breast cancer showed diffuse metastases. Subject 3 male, age: 71, diagnosed with prostate cancer showed diffuse metastases. Scan parameters were: six echoes in two acquisitions (three echoes per acquisition), TE<sub>1</sub>/ΔTE: 1.12/0.96 ms, readout direction anterior–posterior, TR 8.3 ms, FA 5°, FOV 219.6 × 219.6 × 79.2 mm<sup>3</sup>, and an isotropic voxel size of 1.8 mm. A CT scan was acquired within 30 days before the MRI for clinical purposes and was evaluated for osteoblastic metastatic lesions using

consensus reading (two neuroradiologists with >5 y of experience).

## 2.5 | Reconstruction and postprocessing

For the reconstruction of the UTE images, an image reconstruction toolbox (ReconFrame) was used to grid the UTE data in two dimensions with the corresponding k-space trajectories, to Fourier transform in 3D, and to perform SENSE unfolding in the third Cartesian-sampled dimension. The UTE k-space trajectories were corrected by means of a gradient impulse response function.<sup>34</sup>

All water–fat maps were calculated using CSE-based water-fat separation assuming the widely used single- $R_2^*$  multi-fat-peak water-fat signal model,<sup>35,36</sup> tuned specifically to bone marrow.<sup>29,37</sup>

$$S(t) = (\rho_w + c(t)\rho_f) e^{-R_2^*t} e^{i2\pi f_B t} \quad (2)$$

with  $\rho_w$  and  $\rho_f$  the complex signal of water and fat components assuming an equal transverse relaxation rate  $R_2^*$  of water and fat,  $c(t)$  the chemical shift components due to the multi-peak fat spectrum as described in Equation (1) and  $f_B$  the field map.

Given the small flip angles in all measurements, minimal T1 weighting was assumed and T1 bias was neglected.<sup>38,39</sup>

In a first step, the field map was calculated based on all TEs and with a robust graph-cut field-mapping method with a variable-layer construction<sup>40</sup> and based on the signal model introduced in Equation (2). The field map was used as initialization for all subsequent CSE-based processing.

In a second step, CSE-based water-fat separation was performed<sup>37</sup> again with the signal model in Equation (2) and with the field map result obtained in the first step. The parameter estimation problem was iteratively solved via alternating Gauss-Newton updates of the linear and nonlinear parameters in a variable projection method (VARPRO).<sup>41</sup> The CSE-based water-fat separation was performed once including all TEs and once including only later TEs. Plotted fitted signal magnitude curves were calculated based on the fitting parameters of the CSE processing.

## 3 | RESULTS

### 3.1 | Bone cube simulations

Figure 2A shows the simulation result of the macroscopic MR signal, which only included signal from the fatty bone

marrow ( $\rho = 0$ ) with a single-fat-peak fat model ( $c(t) = 1$ ). For a BV/TV ratio of 0%, meaning no bone was present in the marrow and no local field inhomogeneities, the signal followed a mono-exponential decay with  $T_{2,F} = 60$  ms, which was the initial simulation parameter for the marrow relaxation rate. With an increase in BV/TV, two observations were made: (1) for TEs  $>6$  ms the signal followed an exponential decay with a  $T_{2,F}^* < 60$  ms and (2) for TEs  $<6$  ms the signal followed a Gaussian decay. The change in the signal decay is highlighted with the derivative of the logarithm of the signal (Figure 2B). For longer TEs, the curve converged toward a constant value. For shorter TEs, the derivative followed a straight line.

Figure 2C shows the extension of the bone cube simulations when a nine-peak marrow fat spectrum and bone signal was added. In the microscopic picture, the signal for a voxel containing only bone followed a mono-exponential decay with  $T_{2,B}^* = 0.5$  ms. The signal for a voxel containing only marrow showed a mono-exponential decay with  $T_{2,F} = 60$  ms and with oscillations due to the nine-peak marrow fat spectrum. Using only the marrow signal from Figure 2C to generate the down-sampled macroscopic image (Figure 2D) resulted in a lower  $T_2^* = 6.18$  ms when compared to the microscopic marrow signal. The extrapolation of the fit at TEs  $<2$  ms resulted in a higher signal when compared to the simulation result. Including bone signal with  $T_{2,B}^* = 0.5$  ms in the simulation yielded a  $T_2^* = 6.28$  ms. The behavior of the signal curve was very similar to the signal including only marrow for TE  $>2$  ms. Consequently, the difference between the fitted curves, including either only marrow or including bone and marrow, was small. For TE  $<1$  ms, the additional signal of bone resulted in a higher signal amplitude compared to the marrow-only signal decay curve. In the area between 1 ms and 2 ms, the fit resulted in an overestimation of the simulated signal.

### 3.2 | Phantom measurements

The signal decay curves in the water phantom using the multi-TE UTE acquisition strategy showed a mono-exponential decay of the magnitude (Figure 3C) and a linear decrease of the phase (Figure 3D) when the random acquisition scheme was used. In comparison, the signal decay curve acquired with a sequential ordered, suffered from eddy current artifacts. Specifically, the magnitude showed signal fluctuations and a non-exponential decay behavior. The PDFF evaluation using the multi-TE UTE acquisition in comparison with a conventional Cartesian CSE-MRI acquisition showed a good agreement. Both PDFFs, acquired with the UTE acquisition and with the Cartesian acquisition, deviated slightly from the actual

PDFF values of 0%, 5%, 15%, and 100%. The PDFF values measured with the cartesian multi-echo sequence were 1.3%, 6.7%, 16.3%, and 100%, respectively. The PDFF values measured with the multi-TE UTE sequence were  $-3.1\%$ , 3.7%, 16.1%, and 98.1%. For the Cartesian acquisition, the mean absolute error was 1.1% and for the UTE acquisition 1.9%.

### 3.3 | Multi-TE UTE in vivo measurements

To compare the signal decay at short TEs for different BV/TV ratios in vivo, a multi-TE UTE scan was performed in a healthy volunteer's ankle (Figure 4). The mean signal decay is shown for four selected regions of interest (ROIs). A Cartesian high-resolution bSSFP scan is shown as a reference and as an indicator for bone density. In the bSSFP scan, trabecular bone is only visible indirectly as the bone marrow presents strong MR signal and trabecular density is indicated by denser black signal drop out regions like in the subtalar. In regions with fewer trabeculae, bone marrow fills more volume and, consequently, MR signal is brighter as observed in the tuber calcanei. ROI 1 was placed within the cavum calcanei and showed a higher signal intensity in the bSSFP scan, higher fat content, compared to the other ROIs. ROI 2 was placed in the subtalar and showed the lowest signal intensity, higher BV/TV, compared to the other ROIs. The remaining ROIs (ROIs 3 and 4) were placed in the tuber calcanei and showed a higher signal intensity than ROI 1 and a lower signal intensity than ROI 4. In ROI 1, lower BV/TV ratios, the difference between the 7TEs fit and the 5TEs fit was small. For increasing BV/TV ratio, ROI 3 and 4, the difference at lower TEs increased as well. The largest difference was observed for ROI 2 with the largest BV/TV ratio. A voxel-wise comparison of the difference between the fits including all seven TEs or only the last five TEs is shown in Figure 5 by subtracting the two PDFF maps and the two  $R_2^*$  maps. The  $R_2^*$  difference maps showed a larger difference of 20% in  $R_2^*$  values for regions with higher bone densities such as the subtalar. The PDFF difference maps showed a small difference (5%) within the subtalar. Similar results were obtained in a healthy volunteer's knee (Figure 6), where the  $R_2^*$  differed in areas with higher bone density between fits over all TEs and fits over later TEs.

### 3.4 | Cartesian multi-GRE in vivo measurements

Figure 7 shows a comparison of  $R_2^*$  maps obtained with a Cartesian multi-GRE scan in the calcaneus of three

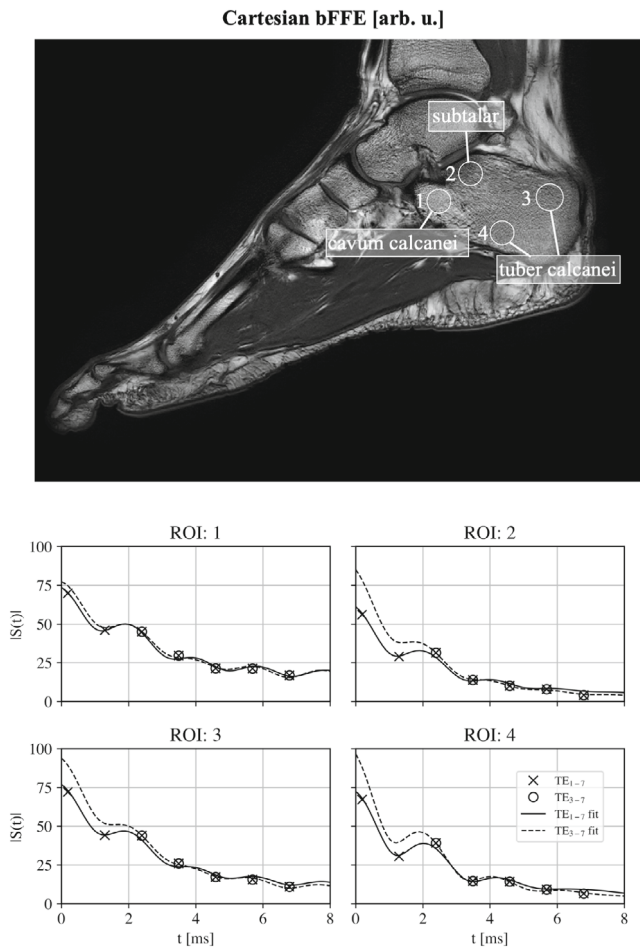


**FIGURE 4** Signal decay curves of a multi-TE UTE acquisition of the calcaneus. The signal decay is shown for selected regions of the calcaneus (top). A Cartesian high-resolution bSSFP scan is shown as a reference and as an indicator for bone density. The crosses represent the measurement points included in the seven TEs fit and the blank dots represent the measurement points that were included in the five TEs fit. Solid lines show the signal fitted with all TEs, dotted lines show the fitting with the latest five TEs. The cavum calcanei (ROI 1) has a high fat content and low trabecularization and minor differences using different TE regimes were visible. In ROI 2, a region with high trabecularization, signal deviation at the first TE compared to the fitted curve based on later TEs was observed. In the tuber calcanei (ROI 3, 4), characterized by lower fat content but also less trabecularized bone, signal deviations were visible

healthy volunteers. The  $R_2^*$  maps including  $TE_1$ - $TE_6$ , showed lower  $R_2^*$  values in regions with a higher BV/TV. Excluding the first echo ( $TE_{2-6}$ ) increased the  $R_2^*$  in areas with a high BV/TV. Supporting Information Figure S1, which is available online, shows the comparison of  $R_2^*$  maps when the processing included either  $TE_{2-6}$  or  $TE_{2-7}$ . The difference maps using  $TE_{2-6}$  and  $TE_{2-7}$  showed no significant change in areas with high BV/TV.

To evaluate  $R_2^*$  and PDFF quantification errors in a clinical routine scan, Cartesian multi-GRE spine scans were

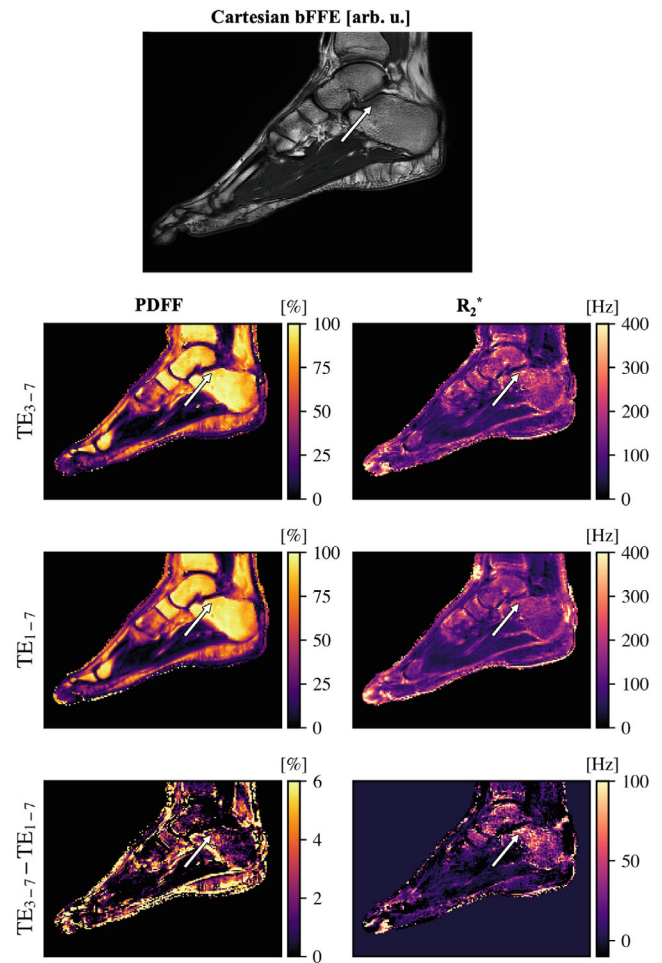


**FIGURE 5** Multi-TE UTE acquisition results. Top image shows a Cartesian high resolution bSSFP scan of the ankle in a healthy volunteer. The PDFF and  $R_2^*$  maps originate from a 3D UTE stack-of-stars acquisition processed with either all available seven TEs ( $TE_{1-7}$ ) or processed with only the later five TEs ( $TE_{3-7}$ ). The white arrow highlights a region with higher bone density. In this high BV/TV region,  $R_2^*$  obtained with  $TE_{3-7}$  was larger than  $R_2^*$  obtained with  $TE_{1-7}$ . The difference in PDFF was smaller compared to  $R_2^*$  difference and the PDFF difference was  $\sim 4\%$  in the region with high BV/TV area

performed in three patients. Two patients suffered from metastasized cancer and showed osteoblastic changes in the spine (Figure 8 and Supporting Information Figure S2), resulting in increased bone density within the vertebral bodies. The acquired CT images showed typical osteoblastic lesions within multiple vertebral bodies. Due to the replacement of fatty marrow with calcified tissue, the average signal over echoes  $\bar{S}$  showed low signal in the vertebral bodies. The signal decreased toward the anterior part as the subject was scanned without an anterior coil. The PDFF and the  $R_2^*$  map indicated pathological changes by presenting significantly reduced PDFF and increased  $R_2^*$  values. Supporting Information Figure S2 shows the mean

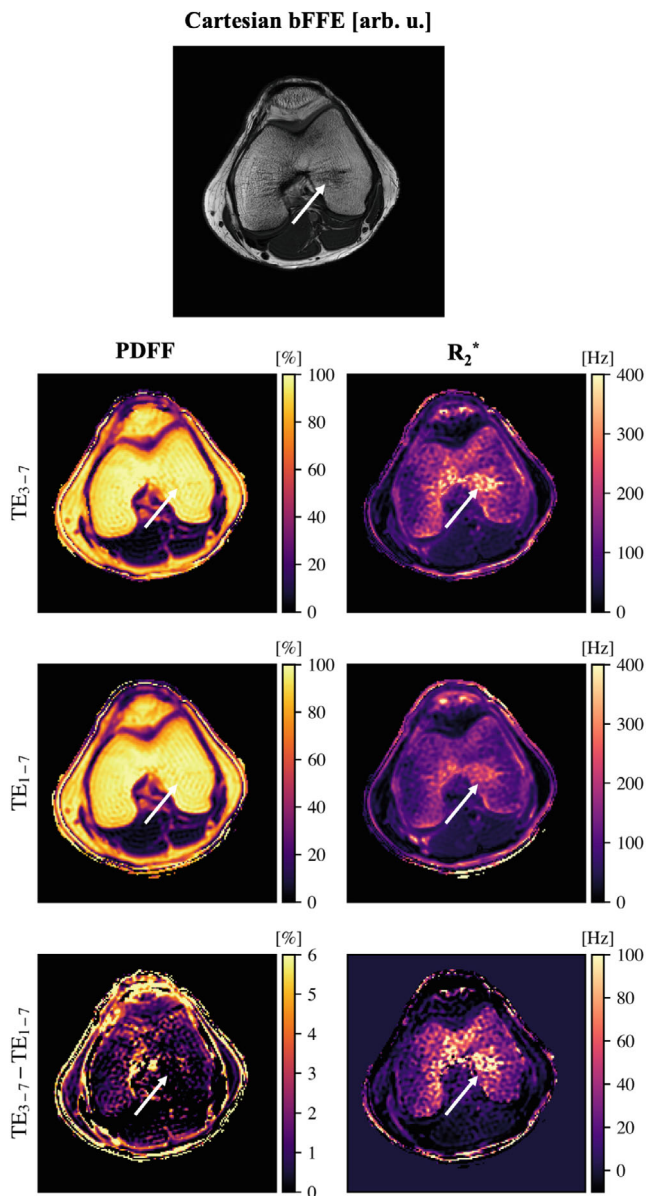


**FIGURE 6** Multi-TE UTE acquisition results. Top image shows a Cartesian high resolution bSSFP scan of a healthy volunteer's knee. Multi-TE 3D UTE acquisition was performed to obtain PDFF and  $R_2^*$  maps which were processed with either all available seven TEs ( $TE_{1-7}$ ) or processed with only the later five TEs ( $TE_{3-7}$ ). In the difference maps areas with higher bone density showed higher differences of  $R_2^*$  values (indicated with white arrow)

signal decay in the specified ROIs. ROI L3, L4, and L5 had lower bone density, which was indicated by a higher signal amplitude at the first TE. There, the fit evaluated with the last five TEs was able to predict the first measurement point at  $TE = 1.12$  ms. Regions with high trabecularization, T12 and L2, showed higher deviations of the signal at the first TE compared to the fit obtained from the last five TEs. The  $R_2^*$  difference maps (Figure 8) showed large differences in  $R_2^*$  and PDFF values within vertebrae

with higher BV/TV ratios (subjects 2 and 3). Specifically, the  $R_2^*$  difference maps show an underestimation of  $R_2^*$  including all TEs compared to  $R_2$  determined by including only the last five TEs. For comparison, a patient with a PDFF in the healthy range and no calcified tissue changes is shown (subject 1). The BV/TV ratio was small compared to subjects 2 and 3, and the difference in  $R_2^*$  was neglectable.

## 4 | DISCUSSION

In this work, we addressed the feasibility of UTE imaging to measure the influence of local field inhomogeneities on the signal of trabecularized bone marrow at short TEs. Modern CSE-MRI relies on a water-fat model with a single exponential  $R_2^*$  decay aiming at the simultaneous extraction of  $R_2^*$  and PDFF. We showed that using such a water-fat model with a single exponential  $R_2^*$  decay results in  $R_2^*$  and PDFF bias in the static dephasing regime. The bias relates to a deviation of the signal decay from an exponential decay at short TEs. The signal decay at short TEs is Gaussian rather than exponential, and the deviation from the exponential decay increases in regions with higher trabecular bone density. Therefore,  $R_2^*$  can be underestimated when using short TEs in multi-echo GRE acquisitions of trabecularized bone marrow processed with a water-fat model with a single  $R_2^*$  decay, especially in regions with high bone density.

The present work relies on the characterization of the influence of local field inhomogeneities on the signal of trabecularized bone marrow using both simulations and in vivo UTE measurements. First, realistic simulations with masks generated from real trabecular bone structures were performed. The simulations showed that the deviation of the signal from the exponential signal decay was more prominent for a higher BV/TV ratio, which is in accordance with previous theoretical descriptions.<sup>18,19</sup> Second, UTE multi-TE measurements in the calcaneus and the knee reproduced in vivo the simulation-based predicted behavior. In areas with a higher BV/TV ratio, the difference between Gaussian and exponential decay was larger. The UTE multi-TE essentially enabled the experimental in vivo verification of the above result previously described primarily in theory and simulations.<sup>17-19</sup> Finally, the influence of a Gaussian decay on  $R_2^*$  and PDFF mapping was investigated in Cartesian scans for bone marrow CSE-MRI at 3T. We showed that the occurrence of the Gaussian decay in the presence of field inhomogeneities induces an  $R_2^*$  underestimation in trabecularized bone marrow regions when using CSE-based water fat separation with a single exponential  $R_2^*$  decay with a short TE. If a TE longer than 2 ms is used at 3T, we did not observe quantification



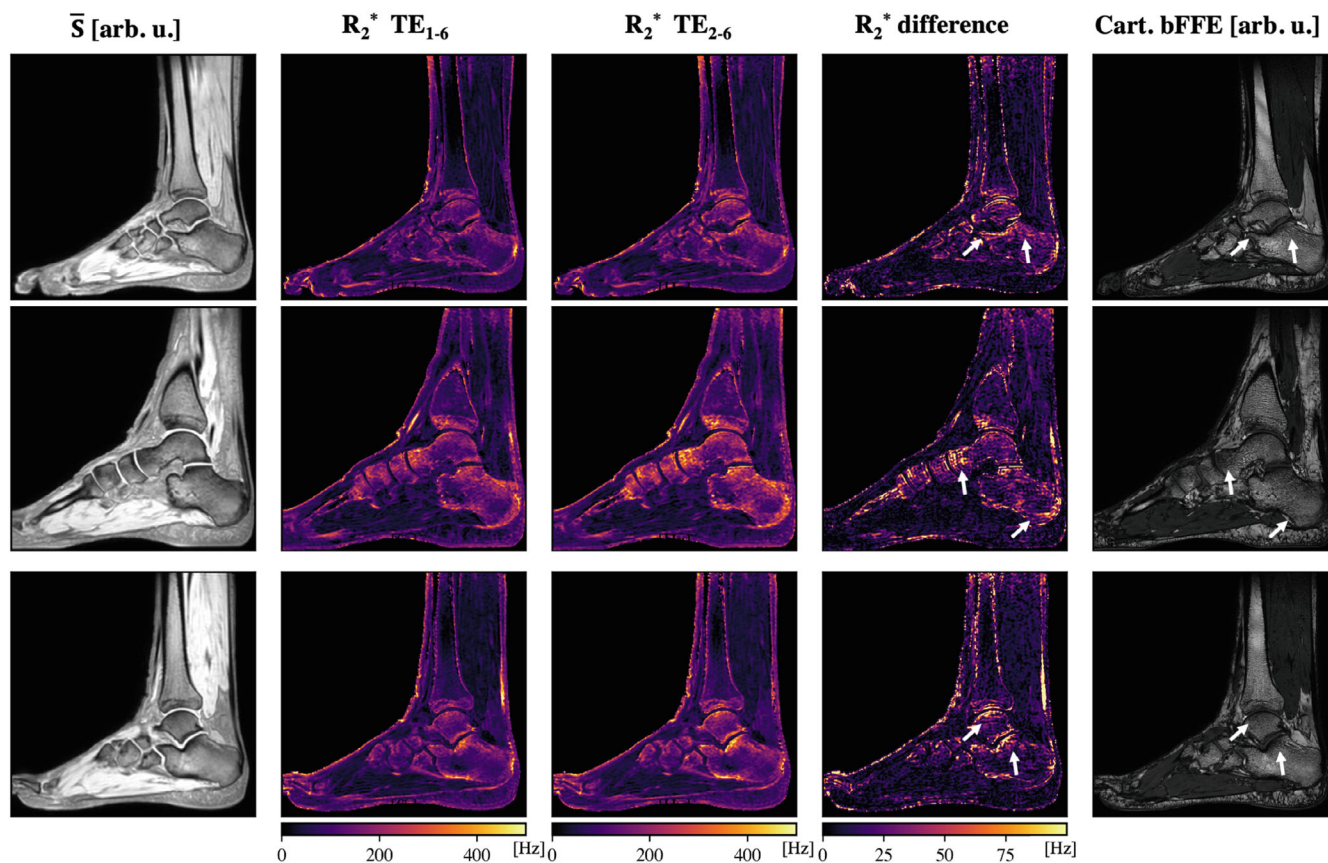


**FIGURE 7** Cartesian Dixon MR images and Cartesian high resolution bSSFP calcaneus scan images of three healthy volunteers.  $R_2^*$  maps were processed including the first echo  $TE_{1-6}$  or excluding the first echo  $TE_{2-6}$ . The white arrows highlight areas with high BV/TV and larger  $R_2^*$  differences

errors, but if shorter TEs were used the static dephasing regime effect should be considered. When decreasing the minimum TE, the PDFP quantification errors were in general smaller than the  $R_2^*$  quantification errors. Consequently, from the results included in this study, we recommend a minimum first TE of 2 ms at 3T for CSE-MRI of trabecularized bone marrow especially in regions with high BV/TV. However, the critical time where Gaussian decay effects become significant needs further investigation for various anatomies and various scans that are used in the clinical routine or research setting.

The present UTE measurements were based on a multi-TE UTE acquisition employing a special sampling scheme. Specifically, each spoke was acquired multiple times where the TE was shifted in a random order to prevent the influence of eddy currents. A similar acquisition scheme has already been proposed for applications in the brain to study ultrashort  $T_2$  components.<sup>32</sup> To the best of the authors' knowledge, the acquisition scheme has not yet been used and evaluated outside the brain. The present work uses the multi-UTE acquisition to experimentally verify the occurrence of the Gaussian signal decay in trabecularized bone marrow at short TEs. Such multi-UTE

acquisitions are associated with prolonged acquisition times, which might be difficult to adopt even in a research setting. However, the presented UTE results have two important implications. First, when using CSE-MRI to assess trabecularized bone marrow by performing simultaneous water-fat separation and  $R_2^*$  quantification with a water-fat model with a single exponential  $R_2^*$  decay, the minimum TE should be carefully selected such that the signal decay is exponential for the entire range of sampled TEs. Note, that the commonly used single exponential  $R_2^*$  decay signal model poorly describes the signal behavior at short TEs. Thus, each water-fat separation method<sup>41–44</sup> that relies on a single  $R_2^*$  exponential decay model underestimates  $R_2^*$  in areas with a distribution of local field inhomogeneities. Second, if the UTE signal of the trabecular bone matrix is of primary interest, the results suggest that UTE acquisitions combining fat and/or water suppression should be preferred, as described previously in.<sup>45</sup> At short TEs, the signal of the bone matrix becomes more significant, but the extraction of the bone matrix signal can be complicated further by the Gaussian decay of the bone marrow signal at short TEs, in the absence of fat suppression. However, additional work would be required

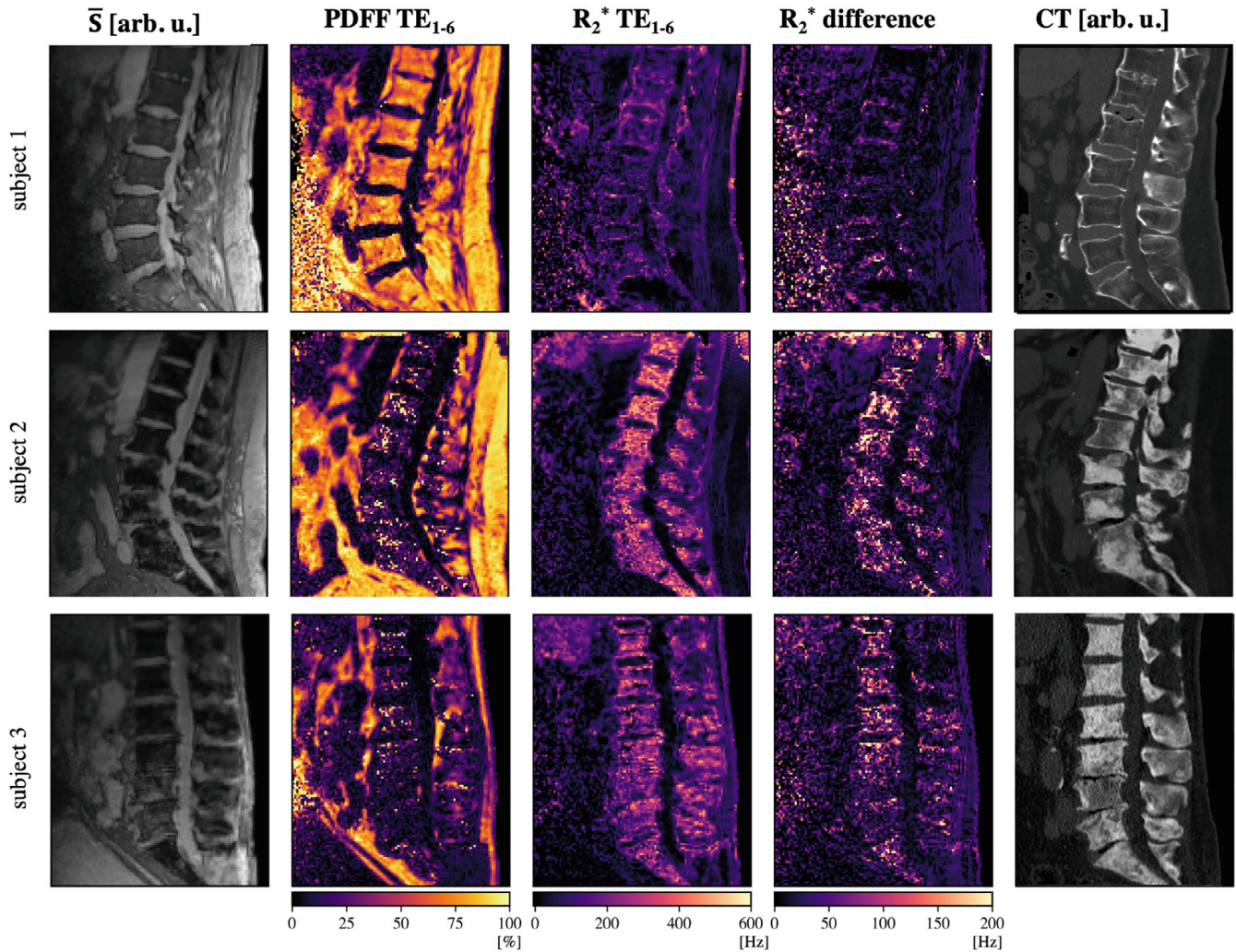


**FIGURE 8** Cartesian Dixon MR images and CT images of the thoracolumbar spine of three patients (subject 1 suffered from a degenerative spine disease; subject 2 and subject 3 showed osteoblastic bone metastases).  $\bar{S}$  shows the averaged signal over all echoes of the Cartesian multi-echo scan. Subject 1 showed a PDFF in the healthy range. In the patients with osteoblastic bone metastases, the fat fraction indicated pathological changes by showing significantly reduced fat fraction. The PDFF maps were obtained by including all TEs ( $TE_{1-6}$ ). The  $R_2^*$  difference maps showed an underestimation of  $R_2^*$  including all six TEs ( $TE = 1.12 \text{ ms} - 6.88 \text{ ms}$ ) compared to  $R_2^*$  determined by including only the last five TEs ( $TE = 2.08 \text{ ms} - 6.88 \text{ ms}$ ). In subject 1, with PDFF values in the healthy range, the difference in  $R_2^*$  was neglectable. For subjects 1 and 2, a significant difference in  $R_2^*$  was visible in vertebrae with low PDFF and strong osteoblastic bone changes, meaning high BV/TV ratios

to investigate the impact of fat suppression on the signal decay at short TEs using either conventional fat saturation and selective water excitation techniques or recently proposed simultaneous fat-water excitation techniques.<sup>46,47</sup>

The single  $R_2^*$  signal model used for data post-processing was based on a model frequently used in the literature,<sup>1</sup> but this model relies on several simplifications such as no T1 bias correction and no multi-exponential  $R_2^*$ -decay effects. T1 bias has been most commonly minimized by the selection of a small flip angle.<sup>38,39</sup>  $R_2^*$  can in general be different between the water and fat components. A dual  $R_2^*$  fitting can improve accuracy in fat fraction estimation, but it reduces the precision

in fat quantification. Therefore, models with a single  $R_2^*$  fitting have been used<sup>48,49</sup> and good agreement has been reported in vivo between MRS-based and image-based PDFF.<sup>48,50</sup>

While the present study shows potential  $R_2^*$  and PDFF quantification errors with a water-fat model with a single exponential  $R_2^*$  decay in trabecularized bone marrow, it has relevant limitations. First, since bone contains roughly 30% free water protons and has a very short  $T_2^*$ , an increase in bone density also means a decrease in SNR. Due to the lower SNR, the relative error of the fit increases. Second, the influence of the local field distribution on the signal decay at short TE was small. The Gaussian decay effect

was visible only in areas where the BV/TV ratio drastically changed. Third, in red bone marrow regions, the signal decay can be further complicated. Red bone marrow is composed of both hematopoietic cells and fat cell.<sup>1</sup> The signal of each chemical component, such as water, lipids and proteins, decays with a different  $R_2^*$ <sup>50</sup> and the assumption of a single  $R_2^*$  signal model might fail. Fourth, neither fat deblurring nor  $T_2^*$  deblurring was performed in this study, which could further improve image quality especially for the scans with higher resolution.<sup>51</sup> However, while image quality and resolution improve with deblurring methods, the ROI-based analysis should not be affected. Fifth, in this study two clinical scans were included which showed osteoblastic bone metastases. Additional subjects would be required to investigate further the exact range of quantification errors for various clinically relevant scans. Furthermore, additional work would be required to investigate the critical time and a signal model that describes the signal decay at short and long TEs in the presence of strong local field inhomogeneities.

## 5 | CONCLUSIONS

We showed with the help of simulations and UTE measurements that due to a distribution of local field inhomogeneities in trabecularized bone marrow regions  $R_2^*$  is underestimated when using a water-fat model with an exponential  $R_2^*$  decay model at short TEs. The bias relates to a Gaussian signal decay instead of an exponential decay at short TEs.  $R_2^*$  can be underestimated when using short TEs, shorter than 2 ms at 3 T, in multi-echo GRE acquisitions of trabecularized bone marrow, especially in regions with high bone density.

## ACKNOWLEDGMENTS


The present work was supported by the European Research Council (grant agreement no. 677661, Pro-FatMRI). The authors also acknowledge research support from DAAD (Project number: 57514573) and Philips Healthcare. Open Access funding enabled and organized by Project DEAL in the Technical University of Munich. The authors would also like to thank Carl Ganter for useful discussions.

## DATA AVAILABILITY STATEMENT


Example Python code of our implementation on trabecular bone simulations will be made freely available for download at [https://github.com/BMRRgroup/trabecular\\_bone\\_sim](https://github.com/BMRRgroup/trabecular_bone_sim). Example MATLAB code for graph-cut field-mapping from<sup>40</sup> is freely available at <https://github.com/BMRRgroup/fieldmapping-graph-cut>. Example MATLAB code to solve for chemical species separation

(CSS) as described in<sup>37</sup> is freely available for download at [https://github.com/BMRRgroup/MRI\\_field\\_contributions](https://github.com/BMRRgroup/MRI_field_contributions).

## ORCID

Sophia Kronthaler  <https://orcid.org/0000-0001-7913-1238>

Maximilian N. Diefenbach  <https://orcid.org/0000-0002-5581-885X>

Christof Boehm  <https://orcid.org/0000-0003-1321-5804>

## REFERENCES

- Karampinos DC, Ruschke S, Dieckmeyer M, et al. Quantitative MRI and spectroscopy of bone marrow. *J Magn Reson Imaging*. 2018;47:332-353.
- Sollmann N, Löffler MT, Kronthaler S, et al. MRI-based quantitative osteoporosis imaging at the spine and femur. *J Magn Reson Imaging*. 2021;54:12-35.
- Chang G, Boone S, Martel D, et al. MRI assessment of bone structure and microarchitecture. *J Magn Reson Imaging*. 2017;46:323-337.
- Burr DB, Allen MR. *Basic and Applied Bone Biology*. 2nd ed. Academic Press; 2019.
- Wehrli FW, Song HK, Saha PK, Wright AC. Quantitative MRI for the assessment of bone structure and function. *NMR Biomed*. 2006;19:731-764.
- Chung H, Wehrli FW, Williams JL, Kugelmas SD. Relationship between NMR transverse relaxation, trabecular bone architecture, and strength. *Proc Natl Acad Sci USA*. 1993;90:10250-10254.
- Majumdar S, Thomasson D, Shimakawa A, Genant HK. Quantitation of the susceptibility difference between trabecular bone and bone marrow: experimental studies. *Magn Reson Med*. 1991;22:111-127.
- Wehrli FW, Ford JC, Attie M, Kressel HY, Kaplan FS. Trabecular structure: preliminary application of MR interferometry. *Radiology*. 1991;179:615-621.
- Diefenbach MN, Meineke J, Ruschke S, Baum T, Gersing A, Karampinos DC. On the sensitivity of quantitative susceptibility mapping for measuring trabecular bone density. *Magn Reson Med*. 2019;81:1739-1754.
- Wu HZ, Zhang XF, Han SM, et al. Correlation of bone mineral density with MRI T2\* values in quantitative analysis of lumbar osteoporosis. *Arch Osteoporos*. 2020;15:18.
- Gao Y, Wang O, Guan W, et al. Bone mineral density and trabecular bone score in patients with 21-hydroxylase deficiency after glucocorticoid treatment. *Clin Endocrinol (Oxf)*. 2021;94:765-773.
- Kuhn JP, Hernando D, Meffert PJ, et al. Proton-density fat fraction and simultaneous R2\* estimation as an MRI tool for assessment of osteoporosis. *Eur Radiol*. 2013;23:3432-3439.
- Griffith JF, Yeung DK, Antonio GE, et al. Vertebral bone mineral density, marrow perfusion, and fat content in healthy men and men with osteoporosis: dynamic contrast-enhanced MR imaging and MR spectroscopy. *Radiology*. 2005;236:945-951.
- Baum T, Yap SP, Dieckmeyer M, et al. Assessment of whole spine vertebral bone marrow fat using chemical shift-encoding based water-fat MRI. *J Magn Reson Imaging*. 2015;42:1018-1023.

15. Schmeel FC, Luetkens JA, Feißt A, et al. Quantitative evaluation of T2\* relaxation times for the differentiation of acute benign and malignant vertebral body fractures. *Eur J Radiol.* 2018;108:59-65.
16. Majumdar S. Quantitative study of the susceptibility difference between trabecular bone and bone marrow: computer simulations. *Magn Reson Med.* 1991;22:101-110.
17. Ford JC, Wehrli FW, Chung H-W. Magnetic field distribution in models of trabecular bone. *Magn Reson Med.* 1993;30:373-379.
18. Yablonskiy DA. Quantitation of intrinsic magnetic susceptibility-related effects in a tissue matrix. *Phantom Study Magn Reson Med.* 1998;39:417-428.
19. Yablonskiy DA, Haacke EM. Theory of NMR signal behavior in magnetically inhomogeneous tissues: the static dephasing regime. *Magn Reson Med.* 1994;32:749-763.
20. Liang ZP, Lauterbur PC. *Principles of magnetic resonance imaging: a signal processing perspective.* SPIE Optical Engineering Press; 2000.
21. Song HK, Wehrli FW, Ma J. Field strength and angle dependence of trabecular bone marrow transverse relaxation in the calcaneus. *J Magn Reson Imaging.* 1997;7:382-388.
22. Ganter C. Static susceptibility effects in balanced SSFP sequences. *Magn Reson Med.* 2006;56:687-691.
23. Storey P, Novikov DS. Signatures of microstructure in R2\* decay: defining the limits of the weak field approximation. In *Proceedings of the 29th Scientific Meeting of ISMRM, Virtual Conference;* 2020:3248.
24. Martel D, Leporq B, Bruno M, Regatte RR, Honig S, Chang G. Chemical shift-encoded MRI for assessment of bone marrow adipose tissue fat composition: pilot study in premenopausal versus postmenopausal women. *Magn Reson Imaging.* 2018;53:148-155.
25. Sharma SD, Artz NS, Hernando D, Horng DE, Reeder SB. Improving chemical shift encoded water-fat separation using object-based information of the magnetic field inhomogeneity. *Magn Reson Med.* 2015;73:597-604.
26. Koch KM, Papademetris X, Rothman DL, Graaf RAD. Rapid calculations of susceptibility-induced magnetostatic field perturbations for in vivo magnetic resonance. *Phys Med Biol.* 2006;51:6381-6402.
27. Ruschke S, Syväri J, Dieckmeyer M, et al. Physiological variation of the vertebral bone marrow water T2 relaxation time. *NMR Biomed.* 2021;34:e 4439.
28. Dieckmeyer M, Ruschke S, Cordes C, et al. The need for T2 correction on MRS-based vertebral bone marrow fat quantification: implications for bone marrow fat fraction age dependence. *NMR Biomed.* 2015;28:432-439.
29. Ren J, Dimitrov I, Sherry AD, Malloy CR. Composition of adipose tissue and marrow fat in humans by 1H NMR at 7 tesla. *J Lipid Res.* 2008;49:2055-2062.
30. Weiger M, Pruessmann KP. Short-T2 MRI: principles and recent advances. *Prog Nucl Magn Reson Spectrosc.* 2019;114-115:237-270.
31. Qian Y, Boada FE. Acquisition-weighted stack of spirals for fast high-resolution three-dimensional ultra-short echo time MR imaging. *Magn Reson Med.* 2008;60:135-145.
32. Boucneau T, Cao P, Tang S, et al. In vivo characterization of brain ultrashort-T2 components. *Magn Reson Med.* 2018;80:726-735.
33. Ruschke S, Eggers H, Kooijman H, et al. Correction of phase errors in quantitative water-fat imaging using a monopolar time-interleaved multi-echo gradient echo sequence. *Magn Reson Med.* 2017;78:984-996.
34. Kronthaler S, Rahmer J, Bornert P, et al. Trajectory correction based on the gradient impulse response function improves high-resolution UTE imaging of the musculoskeletal system. *Magn Reson Med.* 2021;85:2001-2015.
35. Yu H, Shimakawa A, McKenzie CA, Brodsky E, Brittain JH, Reeder SB. Multiecho water-fat separation and simultaneous R2\* estimation with multifrequency fat spectrum modeling. *Magn Reson Med.* 2008;60:1122-1134.
36. Bydder M, Yokoo T, Hamilton G, et al. Relaxation effects in the quantification of fat using gradient echo imaging. *Magn Reson Imaging.* 2008;26:347-359.
37. Diefenbach MN, Liu C, Karampinos DC. Generalized parameter estimation in multi-echo gradient-echo-based chemical species separation. *Quant Imaging Med Surg.* 2020;10:554-567.
38. Karampinos DC, Yu H, Shimakawa A, Link TM, Majumdar S. T1-corrected fat quantification using chemical shift-based water/fat separation: application to skeletal muscle. *Magn Reson Med.* 2011;66:1312-1326.
39. Liu C-Y, McKenzie CA, Yu H, Brittain JH, Reeder SB. Fat quantification with IDEAL gradient echo imaging: correction of bias from T1 and noise. *Magn Reson Med.* 2007;58:354-364.
40. Boehm C, Diefenbach MN, Makowski MR, Karampinos DC. Improved body quantitative susceptibility mapping by using a variable-layer single-min-cut graph-cut for field-mapping. *Magn Reson Med.* 2021;85:1697-1712.
41. Hernando D, Haldar JP, Sutton BP, Ma J, Kellman P, Liang Z-P. Joint estimation of water/fat images and field inhomogeneity map. *Magn Reson Med.* 2008;59:571-580.
42. Reeder SB, Pineda AR, Wen Z, et al. Iterative decomposition of water and fat with echo asymmetry and least-squares estimation (IDEAL): application with fast spin-echo imaging. *Magn Reson Med.* 2005;54:636-644.
43. Hernando D, Kellman P, Haldar JP, Liang Z-P. Robust water/fat separation in the presence of large field inhomogeneities using a graph cut algorithm. *Magn Reson Med.* 2010;63:79-90.
44. Dong J, Liu T, Chen F, et al. Simultaneous phase unwrapping and removal of chemical shift (SPURS) using graph cuts: application in quantitative susceptibility mapping. *IEEE Trans Med Imaging.* 2015;34:531-540.
45. Ma YJ, Chen Y, Li L, et al. Trabecular bone imaging using a 3D adiabatic inversion recovery prepared ultrashort TE cones sequence at 3T. *Magn Reson Med.* 2020;83:1640-1651.
46. Liu J, Christiansen SD, Drangova M. Single multi-echo GRE acquisition with short and long echo spacing for simultaneous quantitative mapping of fat fraction, B0 inhomogeneity, and susceptibility. *Neuroimage.* 2018;172:703-717.
47. Bachrata B, Strasser B, Bogner W, et al. Simultaneous multiple resonance frequency imaging (SMURF): fat-water imaging using multi-band principles. *Magn Reson Med.* 2021;85:1379-1396.
48. Karampinos DC, Melkus G, Baum T, Bauer JS, Rummeny EJ, Krug R. Bone marrow fat quantification in the presence of trabecular bone: initial comparison between water-fat imaging and single-voxel MRS. *Magn Reson Med.* 2014;71:1158-1165.

49. Li G, Xu Z, Gu H, et al. Comparison of chemical shift-encoded water-fat MRI and MR spectroscopy in quantification of marrow fat in postmenopausal females. *J Magn Reson Imaging*. 2017;45:66-73.
50. Karampinos DC, Ruschke S, Dieckmeyer M, et al. Modeling of T2\* decay in vertebral bone marrow fat quantification. *NMR Biomed*. 2015;28:1535-1542.
51. Wang K, Yu H, Brittain JH, Reeder SB, Du J. K-space water-fat decomposition with T2\* estimation and multifrequency fat spectrum modeling for ultrashort echo time imaging. *J Magn Reson Imaging*. 2010;31:1027-1034.

### SUPPORTING INFORMATION

Additional supporting information may be found in the online version of the article at the publisher's website.

**Figure S1** The same Dixon MR images and Cartesian high resolution bSSFP calcaneus scan as shown in Figure 7.  $R_2^*$  maps were processed using either 6 or 7 echoes. In both cases the first echo was excluded. In areas with high BV/TV (white arrows) no significant  $R_2^*$  differences were observed.

**Figure S2** CT and Cartesian Dixon MR images of the thoracolumbar spine of a patient with osteoblastic bone metastases. The fat fraction and the  $R_2^*$  map indicate pathological changes by showing significantly reduced fat fraction and elevated  $R_2^*$ -values, respectively. In the right column signal decay curves for regions within specific vertebrae are shown. The fit including all 6 TEs (TE = 1.12 ms – 6.88 ms) deviated from the fit based on the last 5 TEs (TE = 2.08 ms – 6.88 ms). The deviation was largest for the first measurement point at TE = 1.12 ms and in regions with high trabecularization (T12 and L2).

**How to cite this article:** Kronthaler S, Diefenbach MN, Boehm C, et al. On quantification errors of  $R_2$  and proton density fat fraction mapping in trabecularized bone marrow in the static dephasing regime. *Magn Reson Med*. 2022;88:1126-1139. doi: 10.1002/mrm.29279

## 8 Discussion

The non-invasive measurement of bone mineral density and bone health would have tremendous implications in the field of osteoporosis as described in Chapter 2. UTE imaging is a promising technique to acquire signal from short  $T_2^*$  tissues such as bone. The need for CT-like MR imaging has been instigating the development of UTE imaging techniques over the last years. However, due to low SNR, accurate gradient calibration and scan time, the application of UTE imaging in clinical practice remains limited and is still challenging. The present dissertation provides a solution for some important technical challenges in UTE in vivo imaging and lays the foundation for the application of multi-TE UTE imaging in trabecular bone. In particular, JP-I and JP-II improve CT-like qualitative imaging of bone, while JP-III focuses on quantitative imaging of trabecular bone for osteoporosis screening.

### 8.1 Review of Existing Literature

The present work is based on several preceding technical publications in the field of musculoskeletal bone imaging. In the following sections, the existing literature is reviewed regarding the correction of gradient imperfections (Section 8.1.1), water-fat imaging and susceptibility weighted imaging (Section 8.1.2), and short  $T_2^*$  measurements in trabecular bone (Section 8.1.3).

#### 8.1.1 Correction of Gradient Imperfections

As described in Section 3.2.2, the rapidly time-varying gradients can cause system delays and eddy currents. Resulting gradient distortions, together with other filter characteristics of the entire gradient chain, can significantly degrade the UTE image quality [69, 80]. In the early days, eddy current compensation was performed with gradient pre-emphasis, which alters the input gradient waveform such that the eddy current effects are minimized during gradient switching [188–190]. In addition, active shielded gradients came into widespread use in the early 1990s [191, 192]. Nowadays, all modern MR scanners use actively shielded gradients to reduce currents in the cryostat and gradient pre-emphasis to minimize eddy current effects during gradient switching. However, many rapid and non-Cartesian sampling schemes are still vulnerable, even to small residual deviations of the acquisition trajectories. The hardware pre-emphasis is calibrated to meet defined filter characteristics and is limited by a finite number of time constants to correct long-term eddy currents [189], rendering them imperfect for correcting short-time constant eddy currents.[169, 193] In addition to other hardware optimizations, the most

common methods for correcting dynamic field imperfections are improved pre-compensation of the gradient waveform and post-correction of acquired data. Both methods rely on the accurate characterization of the acquisition trajectory.

A rather simple trajectory characterization approach, introduced 1994 by Liu et al. [194], is to measure eddy currents and model their behavior to predict the true k-space trajectory. However, modeling eddy currents requires assumptions that are reasonable under many

conditions, yet may differ from one system to the next. Further model-based approaches necessitate a model that accurately considers not only eddy current effects but also other system delays and potentially mechanical vibrations. Another approach to obtain the true k-space trajectory is to measure the played-out gradient waveform. The earliest method of measuring the actual gradient waveform was presented 1987 by Onodera et al. [195] who utilized the FID signal obtained from a water phantom for the gradient measurements. This idea was refined and adapted 10 years later with the advent of spiral imaging to correct for non-Cartesian spiral trajectories [88, 90, 196]. Duyn et al. showed 1998 [92] that trajectory calibration can be performed directly on a subject using off-center slice selection, which enabled the measurement of the real gradient waveform at different locations. 20 years later De Zanche et al. [93] introduced a special field camera with NMR probes to measure magnetic fields with a high spatiotemporal resolution [197]. Currently, the field camera is the most advanced and accurate method for measuring the gradient response of the system, yet it requires specialized hardware and special additional equipment that is expensive [94, 95]. The measurement of the k-space trajectory is typically performed in a separate calibration scan for each specific parameter set. Calibrating each individual sampling trajectory is impractical and time consuming. A more efficient approach is to estimate the actual trajectory as a linear combination of the individual physical gradient channels [84]. Further, Brodsky et al. [193] showed that the MRI gradient chain can be modeled by a linear time invariant (LTI) system. This assumption allows the prediction of k-space trajectories scanned in arbitrary directions with only a few measurements in the three main gradient directions [87]. Another important concept was introduced by Addy et al. [87], who described the gradient characteristics itself for arbitrary k-space trajectories with a GIRF. Ideally, the GIRF incorporates all LTI influences on the gradient waveform between the console and the magnet bore [86, 87, 198–201].

Besides gradient pre-emphasis and trajectory correction, in radial imaging some techniques were introduced that extract the necessary information on gradient delays directly from the measured raw data without any additional calibration scans [81, 82, 202].

A number of techniques for gradient imperfection correction have been presented, specifically in the context of UTE imaging. Some measured the k-space trajectories immediately before each UTE measurement for the given set of scan parameters, which prolongs the total scan time [85, 203, 204]. Other approaches relied on eddy current models and calibrated model parameters to achieve a correction for arbitrary UTE scan settings [80, 83, 205]. A preliminary study of GIRF requirements for correcting UTE images was presented by Stich et al. [206]. In addition, it has been recently shown how gradient imperfections can impose spatially dependent artifacts in UTE images. These artifacts can compromise the bone water quantification. [207, 208]

### 8.1.2 Separation of Water and Fat in UTE Imaging

The diagnostically important signal of water in body MRI can be overshadowed by signals from fat. When the fat spectrum is broad or susceptibility-induced distortions of the main magnetic field are present, common fat suppression approaches like STIR [209] and SPAIR [210] face limitations. Unlike fat suppression techniques, water-fat separation techniques with CSE, which form the foundation of WFI, rely on algorithmic fitting of a chosen water-fat signal model to a sampled MR signal evolution. CSE-based water-fat imaging was first presented by Thomas Dixon in 1984 when he proposed a modified spin echo sequence [139] that acquired two echoes at distinct echo times. In the resulting images, the water and fat signals were in-phase and out-of-phase. By combining in-phase and out-of-phase images Dixon generated

water-only and fat-only images. WFI has an advantage over fat suppression approaches in that the fat signal information is fully evaluated and may be used to calculate a PDFFF of the imaged region. Until recently, a primary focus in WFI, besides Dixon-based fat suppression, has been on precise PDFFF estimation. As a result, Dixon’s dual-echo technique was expanded to include the acquisition of complex multi-echo MR signals, the use of more realistic water-fat signal models, and more advanced fitting algorithms. A signal model that is commonly used nowadays is the complex single  $T_2^*$  signal model [152], which accounts for the spectral nature of the fat signal [211], MR relaxation effects [212] and magnetic field distortions [178]. The number of echoes required increases with the complexity of the signal model, which increases the scan time [140, 141, 144, 154].

The various benefits of the established WFI approach, especially the improved fat suppression, were subsequently extended to short  $T_2$  MRI. UTE-Dixon, which combines UTE imaging and multi-echo Dixon imaging, was used to image and quantify short  $T_2$  tissues, removing the need for fat suppression pulses that suppress the long  $T_2$  signals directly [143]. Further, the IDEAL algorithm was extended to include also short  $T_2$  components to generate water, fat, and susceptibility maps [14]. The method was applied to detect hemosiderin deposition in hemophilic arthropathy [213] and to quantify susceptibility and density of cortical bone [214]. However, the decay of the short  $T_2^*$  of water has not been explicitly considered in the signal model so far. Besides quantitative approaches WFI proved itself beneficial to suppress both fat and long  $T_2$  water components which is important in pseudo-CT imaging [161, 162, 164] and in the context PET attenuation map generation [163, 165].

As previously stated, UTE-Dixon imaging necessitates the acquisition of multiple echoes, which increases the TR. In an attempt to reduce the number of echoes needed for WFI, Yu et al. [166] introduced 2006 single acquisition water-fat separation, which was based on an idea already introduced in the 1980s using quadrature encoding [215–217]. Single-echo Dixon (sTE-Dixon) methods rely on a single TE image to decompose fat and water components directly from the complex MR signal [166]. In the quadrature encoding method, the echo time is chosen such that the phase difference between water and fat is  $90^\circ$ . Yu et al. extended the formulation to allow for arbitrary echo times and arbitrary phase differences. In general, the simple sTE-Dixon methods, relying only on a single complex MR signal, are perturbed by unwanted phase terms arising, for example, from  $B_0$  inhomogeneities or residual  $B_1$  transmit-receive phases. Various strategies for removing undesired phase terms have previously been published, including the use of extra reference scans [104, 166], or the use of a region growing algorithm to estimate the unwanted phase terms [167]. It was shown recently that single-echo Dixon can be combined with UTE imaging to suppress fat in UTE images [104]. To remove the unwanted, and at short TEs more dominant,  $B_1$  transmit-receive phase term an additional reference scan was necessary. Acquiring additional reference scans result in longer scan times and errors due to patient movement or other sources of inconsistency.

Another approach that combines dual-echo imaging and sTE-Dixon methods, was presented by Jang et al. 2021 who used a DESS acquisition in combination with UTE imaging to suppress fat or water [97]. UTE-DESS acquires two complex signals, by a pair of balanced spiral-out and spiral-in readout gradients separated by an unbalanced spoiling gradient in between. The acquired two complex signals can solve for background phase terms in the sTE-Dixon processing but at the cost of an extended TR.



### 8.1.3 Measurement of Bone Density and Short $T_2^*$ in Trabecular Bone

As describe in Section 2.3 bone signal decays rapidly with a very short  $T_2^*$  and therefore conventional MRI methods use the signal of bone marrow to indirectly assess trabecular bone. Trabecular bone imaging started in the 1990s when high-resolution MR imaging was used to resolve the trabecular bone matrix as signal voids within the bone marrow signal [47, 218–222]. In the beginning high-resolution imaging was applied on human trabecular bone samples and later applied in-vivo in distal skeletal regions [8, 26]. However, a major limitation of high-resolution trabecular MR bone imaging is that it is limited to distal skeletal regions because of its low sensitivity and motion [8, 26]. In the 2000s, researchers demonstrated that bone marrow, which fills the cavities of trabecular bone, may play an important role in bone health and metabolism [54, 55]. The PDFF of bone marrow was found to be an important biomarker for bone marrow fat content changes that are associated with bone loss [24, 26, 55, 223–226]. The bone marrow fat fraction is usually analyzed with MRS or CSE-MRI [26]. CSE-MRI can provide another key biomarker when analyzing the trabecular bone matrix. Already in the early works  $T_2^*$  was successfully correlated with bone mineral density in preliminary studies [8, 47, 218, 227] and later  $T_2^*$  was proven to be a biomarker for bone loss in osteoporosis [24, 52, 223, 228, 229].

In general, the literature applying short  $T_2^*$  UTE measurements in vivo in trabecular bone is very limited. Ma et al. [119] showed in 2020 the first in vivo short  $T_2^*$  measurement in the spine. The researchers used a 3D IR-UTE-Cones sequence with a broadband adiabatic inversion to suppress signals from long  $T_2$  tissues. The remaining signal contained only short  $T_2^*$  signal from the trabecular bone matrix. A multi-spoke UTE readout was used to determine the mono-exponential signal decay at different TEs which allowed to measure  $T_2^*$ . After proving that long  $T_2$  components were suppressed the bone density was estimated from a single IR-UTE scan with an additional proton density reference. Because of the IR pulses and the limitation to specific TR and inversion time (TI), the presented sequence has low SNR, high SAR, and long scan times, limiting the application to research setups, and the clinical value and application has not been investigated further.

In the absence of any fat suppression, the signal evolution in trabecular bone is complex and non-trivial. In the beginning, researchers used simulations [218, 230] and analytical methods [231, 232] to try to understand the complex signal behavior. In general, the difference in susceptibility between bone and marrow, as well as the underlying complex microstructure, result in a wide distribution of field inhomogeneities within each voxel. It has previously been demonstrated [218, 230–232] that intravoxel dephasing can be described as a mono-exponential decay with decay rate  $T_2^*$  [172]. It was also shown that  $T_2^*$  is affected by bone density as well as the orientation of trabecular bone with respect to the main magnetic field [52, 218, 232, 233]. According to the simulations and theoretical analysis, the above-described mono-exponential signal decay behavior applies only for long TEs and differs at short TEs below a specific characteristic time point. The simulations and analytical analysis suggested that at short TEs, due to the underlying microstructure, the bone marrow signal follows a Gaussian decay [230, 232, 234, 235].

The signal behavior at short TEs in trabecular bone without fat suppression has never been measured in vivo. A potential measurement technique was presented in 2018 by Boucneau [236] for applications in the brain to study ultrashort  $T_2$  components. The researchers used a multi-TE UTE acquisition method with a unique random sampling scheme. To avoid the influence of eddy currents, each spoke was acquired multiple times with the TE shifted in a random order.

## 8.2 Present Work

The present work includes several contributions to the field of qualitative and quantitative UTE imaging in musculoskeletal MR. Qualitative CT-like imaging of bone was improved by removing artifacts in JP-I and by enabling simultaneous water-fat separation, which is presented in JP-II. In particular, JP-I emphasizes the importance of trajectory error correction in high-resolution cortical bone UTE imaging. JP-II proposes a new method for separating water and fat from a single UTE scan while also producing susceptibility-weighted magnitude images. An application of the new methodology for the assessment of vertebral fractures and edema is presented. Finally, JP-III investigates quantitative imaging of short  $T_2^*$  species. Therefore, in vivo multi-TE UTE measurements are performed to investigate quantification errors in  $R_2^*$  and PDFF mapping in trabecularized bone marrow at short TEs.

### 8.2.1 Novelty

The trajectory correction demonstrated in JP-I shows the importance of the precise knowledge of the gradient waveform in UTE imaging. Previously, no systematic investigation of the impact of gradient imperfections in high-resolution UTE MSK imaging had been conducted. Artifacts in reconstructed images caused by readout gradient deviations were investigated using simulations and phantom measurements. Nominal methods that use simple gradient delay models were shown to be insufficient and it was demonstrated that precise waveform information during ramp up was necessary. Especially for high-resolution applications, accurate waveform information during ramp-up is critical, and simple gradient delays, as commonly used, were found to be inadequate. Furthermore, in a study of spine fractures, a comparison of UTE in vivo spine images with CT images confirmed the diagnostic importance of an elaborate UTE image correction method for high-resolution imaging.

The new sUTE-Dixon-SWI methodology, developed in JP-II, improves the use of single echo Dixon water-fat separation in UTE imaging. The proposed method allows for the removal of unwanted low-frequency background phases, separation of water and fat, and SWI processing from a single echo complex UTE image. The formulated smoothness-constrained inverse problem solves the water fat problem while removing the undesirable low-frequency phase terms. As a result, no additional calibration scans are required to remove unwanted phase components, as was previously the case. Another novel aspect of the formulation is the use of a tissue mask in the regularizer and phase scaling to prevent phase wraps during the undesirable low-frequency phase estimation update steps. The proposed method was used in a thoracolumbar spine study and allowed for the simultaneous assessment of vertebral fracture and edema using a single MR sequence.

Finally, JP-III demonstrated the feasibility of using UTE imaging to assess the influence of local field inhomogeneities on the signal of trabecularized bone marrow at short TEs. Previous work predicted the Gaussian signal decay behavior at short TEs only through simulations and in theoretical analysis. Advanced modeling would be expected to aid in extracting the short  $T_2^*$  species component from the total signal. This work is the first in vivo measurement and analysis of signal at short TEs in trabecular bone in the presence of fat and demonstrated that advanced modeling would require a very high sensitivity. Furthermore, realistic simulations were carried out using masks generated from real trabecular bone structures. Finally, the influence of a Gaussian decay on  $T_2^*$  and PDFF mapping was investigated in Cartesian scans for bone marrow CSE-MRI at 3T.

## 8.2.2 Impact

Given the potential that non-invasive and radiation free measurement of cortical and trabecular bone health would offer in the field of CT-like bone imaging and osteoporosis (see Chapter 2), the impact of the presented methods is deemed high.

JP-I demonstrated that by using a GIRF measured with standard scanner hardware, the image quality of radial UTE images can be consistently improved. The reduction of blurring and artifacts was proven to be especially important in high-resolution MSK imaging of thin cortical bone structures and thin connective tissues. Without the GIRF-corrected reconstruction, such thin bone structures become indistinguishable or are misidentified as soft tissue. The findings not only reproduced previously reported improvements to UTE trajectory-correction methods, but also highlighted the importance of k-space trajectory correction in high-resolution UTE imaging. The established and validated method in JP-I was essential for obtaining high quality, artifact-free UTE images for the work presented in JP-II and JP-III.

In JP-II, a new method was proposed for removing unwanted low-frequency background phases from a single echo complex UTE image, as well as simultaneous water-fat separation and SWI processing. The proposed method was evaluated on nine patients in a clinical study of the thoracolumbar spine, and it successfully demonstrated the simultaneous assessment of vertebral fractures and edema from a single MR sequence. Using a fixed regularization parameter, the sUTE-Dixon methodology consistently and reliably produced high quality water- and fat-separated images for all study patients, regardless of the patient's size. According to the radiological reading, the derived water-fat images and SWI-UTE images can potentially replace the clinical standard of reference, STIR and CT images, in assessing edema and fracture lines. Several advantages are provided by the proposed sUTE-Dixon-SWI technique: First and foremost, UTE scans are available on the majority of clinical MR systems, and the proposed technique could be implemented as a data post-processing step. The data post-processing is fully automated, which has an advantage over simple filtering approaches, in which the kernel size and filter type are defined for each subject. Furthermore, only one imaging modality can be used to scan the patient. Several sequences can be replaced by a single 3D scan acquired in 6.3 minutes. Because only one UTE image is needed, the technique could be expanded to different anatomical locations.

The methods presented in JP-I and JP-II are clinically applicable and have been tested using standard clinical MRI hardware. The proposed methods are also currently being used in clinical studies. The list of related publications includes all the subsequent and related work that has already been published.

For the first time, the work presented in JP-III investigated the accuracy of measuring PDFF and  $R_2^*$  in trabecular bone at short TEs in vivo. It was demonstrated using simulations and UTE measurements that  $R_2^*$  is underestimated at short TEs due to a distribution of local field inhomogeneities in trabecularized bone marrow regions when using a water-fat model with an exponential  $R_2^*$  decay model. The bias relates to a Gaussian signal decay instead of an exponential decay at short TEs.  $R_2^*$  can be underestimated even in multi-echo GRE acquisition with a TE shorter than 2 ms at 3T, especially in regions with high bone density in trabecularized bone marrow. The findings presented in JP-III have two important implications for future research: First, when using CSE-MRI to assess trabecularized bone marrow, for PDFF mapping and  $R_2^*$  quantification, with a single  $R_2^*$  water-fat model, the minimum TE should be carefully chosen so that the signal decay is exponential across the entire range of sampled TEs. It should be noted that the commonly used single exponential

$R_2^*$  decay signal model does not adequately describe signal behavior at short TEs. As a result, each water-fat separation method [158, 178, 237, 238] that relies on a single  $R_2^*$  exponential decay model underestimates  $R_2^*$  in areas with a distribution of local field inhomogeneities. Second, if the UTE signal of the trabecular bone matrix is of primary interest, the findings indicate that UTE acquisitions combining fat or water suppression should be preferred, as described previously in [119]. Consequently, the work demonstrated that the bone matrix signal becomes more significant at short TEs, but the extraction of the bone matrix signal can be complicated further by the Gaussian decay of the bone marrow signal at short TEs in the absence of fat suppression. This finding provides a foundation for future research on UTE imaging of trabecular bone to assess bone quality in osteoporosis.

### 8.2.3 Limitations

UTE imaging, in general, faces a number of challenges that limit the use of UTE imaging in routine clinical practice. First, as a clinical imaging technique, UTE sequences have relatively long scan times, which in the presented work limited the resolution and FOV in all employed scans and necessitated radial undersampling, parallel imaging (SENSE) or partial Fourier encoding, and non-isotropic voxels with relatively large slice thickness (1.5 - 3 mm). Consequently, SNR is reduced due to the employed acceleration and undersampling to reduce the scan time.

Second, UTE imaging in bone already suffers from low SNR since bone contains roughly 30% free water protons and has a very short  $T_2^*$ . Thus, SNR was a limiting factor in the presented work. An increase in bone density, as investigated in JP-III, means a decrease in SNR. Thus, due to the lower SNR the relative error of the fitted signal curves in JP-III increased. In JP-II, noise was propagated from the phase masks into the susceptibility weighted (SW) images and, therefore, SNR decreased slightly at each weighting step. Appropriate denoising of the phase could help to prevent noise propagation and might be subject of future investigations. To specifically maximize SNR, in the work presented in this thesis, no fat or long  $T_2$  suppression was employed. In previous studies, it was observed that fat and long  $T_2$  suppression techniques reduce SNR drastically because the short  $T_2^*$  components are not fully recovered after the signal inversion of the long  $T_2$  components. However, long  $T_2$  signals can contaminate UTE images which can lead to quantification errors and confounded contrast.

Third, in JP-I and JP-II images of the cortical bone in the lumbar spine were compared with inverted UTE magnitude images. The UTE images are  $T_2^*$ -weighted, T1-weighted, and proton density weighted. This mixed weighting of UTE images may have an impact on the ability to invert the contrast of UTE images in resolving bone structures, at least at the presently used parameters such as TE, TR, and flip angle. In contrast, ZTE sequences have been recently used for CT-like imaging of bone structures by inverting the contrast of ZTE images, which have been considered to be primarily proton density-weighted [111? , 112]. The inversion of UTE image contrast was presented in this work as only one example of the effect of UTE trajectory correction on a clinically relevant, high-resolution MSK imaging setting. Further research is required to determine the potential of inverted UTE images for CT-like bone imaging in the lumbar spine.

Fourth, in the absence of fat suppression, off-resonance artifacts are present, as described in Section 5.5. In UTE imaging, the center-out radial or spiral sampling of k-space uses a different direction for each readout. Because of the ring-shaped point spread function, off-resonance artifacts appear as blurring which produces artifacts that differ from those seen in Cartesian sampling of k-space. Center-out radial artifacts must be identified because they can mimic

normal structures and disease. The work presented in this thesis did not include fat deblurring or  $T_2^*$  deblurring, which could further improve image quality, especially for high-resolution scans [143]. However, while deblurring methods could improve image quality and resolution, region of interest (ROI)-based analysis, as used in JP-III, should not be affected.

Despite the success of the presented UTE imaging methods and investigations, the presented work has several limitations. The presented GIRF-based correction method in JP-I does not account for the effect of  $B_0$  eddy currents, which may cause unwanted phase accumulation of the sampled signal. We expect the effect to be small in UTE imaging because the data acquisition starts in the k-space center. In addition, the GIRF-based correction method does not account for geometric distortions caused by spatial nonlinearities in the gradient fields at the edge of the FOV. Furthermore, the increased reconstruction complexity and the requirement of input waveforms to perform the GIRF-based correction may have an impact on the method's future applicability in the clinical routine. The proposed GIRF-based correction method requires that the reconstruction is able to use the predicted trajectories in order to produce the corrected images. As a result, an interface for providing the corrected trajectory to the gridding algorithm is required. Further, the GIRF-based correction method requires the precise knowledge of the input gradient waveform in order to predict the real gradient waveform. Such knowledge may not be accessible for all vendor-specific sequences.

There are several limitations to the developed methodology presented in JP-II: First, the phase information was used as a weighting in the magnitude in the SWI. As a result, not only is the contrast of osseous structures manipulated, but areas with high fat content are weighted as well. The contrast in the SW-like images is composed of both susceptibility and chemical shift effects. Because the weighting of osseous tissue and fatty tissue is similar, SW-like images must be evaluated carefully and were therefore excluded from the radiological reading. Second, the minimum TE depends on the switching time of the RF system between transmission and reception, which was 0.14 ms in the presented study. Shorter TEs may be feasible with a different scanner system, but the question remains whether shorter TEs are useful. The optimal TE is a tradeoff between the short  $T_2^*$  magnitude signal and the water-fat phase contrast and future work is required to define the optimal TE. Finally, the presented sUTE-Dixon method could be combined with a low-resolution calibration scan to estimate the fieldmap, requiring only a relatively small amount of additional scan time. Using the proposed processing in combination with an a priori known low-resolution field-map could further improve the quality of the water-fat separated images and enable quantitative applications. However, additional research would be needed to determine the additional value of a low-resolution calibration scan for estimating the fieldmap, as well as any implications of such a scan for quantitative imaging applications.

The  $R_2^*$  measurements presented in JP-III have several limitations: First, the influence of the local field distribution on the signal decay at short TE was small. The Gaussian decay effect was only visible in areas where the BV/TV ratio changed drastically. Second, signal decay in red bone marrow regions can be more complicated, which the study did not account for. The single  $R_2^*$  signaling model used in this study might fail considering the different  $R_2^*$  of each chemical component in red bone marrow [239]. Finally, in the presented study two clinical scans were included which showed osteoblastic bone metastases. Additional subjects would be needed to further investigate the exact range of quantification errors for different clinically relevant scans.

### 8.3 Perspectives

The methods and results presented in this work, when combined, allow to include UTE imaging in future research settings and clinical studies.

The work presented in JP-I lays the foundation to acquire high-quality high-resolution UTE images, which is an important basis for future qualitative as well as quantitative analyses, such as presented recently by Zamskiy et al. [78]. The GIRF-based correction method is a versatile technique and can be used to correct trajectory errors in non-UTE imaging sequences. The implemented correction methods have built the foundation for an already ongoing research project on the correction of gradient chain-induced fat quantification errors in radial multi-echo SOS acquisition. Preliminary results were recently presented by Zöllner et al. [240].

The developed sUTE-Dixon-SWI methodology presented in JP-II, may serve as basis for future studies in assessing edema and fracture lines with a single UTE scan and potentially replace the clinical standard of reference, STIR and CT. The UTE scan protocol and the fully automated post-processing enables the incorporation of the method in several clinical studies. In a preliminary study, the robustness of the methodology across different musculoskeletal anatomies was tested and the sUTE-Dixon-SWI method was able to provide high quality UTE, water, and fat images [241]. Furthermore, a clinical study was conducted that included the proposed water-fat separated images and CT-like susceptibility-weighted images from 30 patients with vertebral fractures and degenerative changes in the spine. Such a study is the first step to translate the presented technique to a clinical application. In addition, the developed methodology allows the estimation and removal of the  $B_1$  transmit and receive phase. The phase term is caused by electric conductivity of tissue and a corresponding post-processing of the  $B_1$  phase could potentially yield quantitative values of the electric conductivity [242–244]. A comparison of the obtained conductivity with literature values [245] would in turn provide an additional criteria to identify the optimal value for the regularization parameter.

The work presented in JP-III, establishes a framework for short  $T_2^*$  studies in trabecular bone, which opens new perspectives for future research. The measurements presented here enable further investigation of the signal decay at short and long TEs in the presence of strong field inhomogeneities. Understanding the signal behavior, and also learning more about the critical time, opens the possibility to fit the signal evolution with an adequate model and potentially measure trabecular bone density.

In general, in the emerging field of short  $T_2$  MRI and UTE imaging, the clinical usefulness needs to be investigated for applications that are easily accessible with existing clinical scanners. Most published results in the literature cover healthy bone imaging and the application in subjects with bone diseases or injuries would help to understand the potential of UTE imaging. Furthermore, most clinical scanners do not offer the possibility to acquire high-quality UTE images at TEs  $\sim 100 \mu s$ . Further, the reduction of scan time with elaborate acceleration and reconstruction techniques will be necessary to implement UTE imaging in clinical practice. On the technical side, advances in high-bandwidth capabilities of MR scanner hardware in terms of gradient strength and duty cycles, as well as RF switching speed, will be an important factor for future discoveries in short  $T_2$  research [69]. Finally, most UTE sequences are developed at 3T, though some studies report UTE imaging at 7T. Higher field strength, stronger gradients, and dedicated extremity coils could be desirable for UTE imaging of short  $T_2$  tissues, which typically have low SNR [246, 247].

## 9 Conclusion

The present dissertation is an important step towards the application of UTE imaging in clinical practice, specifically in qualitative CT-like imaging for radiological diagnostics of bone pathologies and quantitative imaging of trabecularized bone in osteoporosis research. UTE imaging is a promising technique for obtaining signals from short  $T_2^*$  tissues like bone. The demand for CT-like MR imaging has fueled the development of UTE imaging techniques in recent years. Due to low SNR, accurate gradient calibration and scan time, the application of UTE imaging in clinical practice was previously limited. Based on the three embedded journal publications the presented methodologies provides a solution for some important technical challenges in high-resolution CT-like qualitative imaging of cortical bone and quantitative imaging of trabecularized bone on a clinical MR scanner. First, artifacts in high-resolution imaging caused by gradient errors were corrected for high-quality quantitative imaging of bone. Second, a time efficient single echo time UTE acquisition was extended to provide information not only on short  $T_2$  tissues but also on water and fat for high-quality qualitative imaging of bone pathologies. Third, based on the correction method of the first publication, a foundation was established for quantitative imaging of trabecular bone in osteoporosis screening.

The proposed methods for qualitative, ct-like, bone imaging can potentially replace the clinical standard of reference, STIR and CT images, in assessing edema and fracture lines respectively. Single TE UTE scans are available on the majority of clinical MR systems, and the proposed post-processing technique is fully automated. Thus only one imaging modality can be used to scan the patient. Several sequences can be replaced by a fast single 3D scan which can be expanded to different anatomical locations. In the field of osteoporosis the non-invasive and quantitative measurement of bone mineral density could eventually work as a marker for disease activity, progression and therapy effectiveness. Implementing the presented measurement techniques into clinical practice will eventually have an impact on the medical treatment of a large number of patients.

# Acknowledgments

First of all, I would like to express my heartfelt appreciation to all the people who have supported me during this dissertation. Without these people, the content and scope of the work would not have been possible. People who have supported my personal development during this work, through all the ups and downs of this roller coaster ride, who have inspired and motivated me, and who celebrated all of my achievements with me.

My deepest gratitude goes to Professor Dimitrios Karampinos, who leads an exceptional group. I owe a great deal of my professional and personal development to him. Thank you for always supporting me, for pushing me when necessary, for helping me control my hypercritical nature, and for always having an open ear. Your work ethic is unparalleled and I especially appreciate the great trust you have in the students. How open you are with developments and decisions and value the opinions of your group. How you are interested in making the Ph.D. experience the best for everyone, not forgetting to reward hard work appropriately.

Working in a medical setting is a very motivating experience. However, as researchers, we need the help and support of people with medical backgrounds to improve and establish our methods. I would like to thank Alexandra Gersing, Benedikt Schwaiger, and Georg Feuerriegel, who have been very supportive of my work, helped with setting up studies and shared their rich medical knowledge with me. Their contribution has improved my understanding and motivated me. I would also like to thank Ernst J. Rummeny, who supported our research and ensured that our work was rewarded.

I would like to thank my collaborators at Phillips Healthcare Kilian Weiss, Jürgen Rahmer, Ulrich Katscher, and Peter Börnert. Thank you for being so supportive, for openly sharing your techniques and knowledge, and for giving me detailed feedback. Thank you, Peter and Jürgen, for your encouraging words during a daunting review process. Thank you Kilian for pushing the visibility of my project. I appreciate you joining the group, sharing your deep MR knowledge, and helping me wherever you can, even with problems that weren't part of your job description.

I would also like to thank my second supervisor, Professor Björn Menze, for his support during this dissertation. Your input was always very welcome.

My deep-felt thankfulness goes to the members of my research group. The BMRR group is an excellent, supportive, and inspiring working environment where work is fun. Research can be frustrating at times, and I have learned the importance of group cohesion. There was never any doubt that I would find someone to help me when I had a difficult problem to solve. Thanks to Stefan, Barbara, Max, Dominik, Jan, Sarah, Christoph, Sean, Julio, Chris, Mingming, Yupeng, Carl, Ely, and Mark. And also to the newer members that I didn't get to spend much time with, Aizada, Jonathan, Johannes, Philipp, and Alex. Thanks also to the BMRR family friends Stephan and Ronja. Thank you all for giving me this experience, and thank you also for so much fun during my Ph.D. years! A special thanks to Max, who supported me and took me under his wing, especially during my first ISMRM deadline. Thanks to Dominik, whom I asked many questions in the beginning and whose optimistic nature I really appreciate. Thanks also for the many templates I have copied from you over the years. Thank you, Christoph, for keeping up the team spirit and making it so



much fun to work here. Thanks also for all the after-hours beer chats. Thank you, Ming you've always been a great source of motivation and enthusiasm, especially during the Corona lockdown and home office phase. I am especially grateful for that. Your bubbly, fun, and strict nature is contagious. Thank you, Chris, for your tireless support, it has been especially fun and inspiring to work with you on various projects.

Finally, I want to express my gratitude to my friends and the Kronthaler family. Without your support and love, I would not have reached this point in my professional life. Thank you for having my back and helping me to take things step by step. Especially during the times of Corona lockdown and home office, you helped me to stay motivated and balanced. I would like to give a special mention to Anton Kronthaler, first and foremost, as he insisted on being mentioned and secondly, his realistic world view always helps me to focus and not get lost in details. Last but not least, I would like to thank Mikkell, my husband. Thank you for all your support, love, and encouragement. I am very grateful for having you in my life.

# List of Abbreviations

<b>2D</b>	two-dimensional
<b>3D</b>	three-dimensional
<b>BW</b>	band width
<b>BM</b>	bone marrow
<b>BME</b>	bone marrow edema
<b>BMD</b>	bone mineral density
<b>BV/TV</b>	bone volume fraction
<b>CSE-MRI</b>	chemical shift encoding-based water-fat MRI
<b>CSE</b>	chemical shift encoding
<b>CS</b>	compressed sensing
<b>CT</b>	computed tomography
<b>CTI</b>	continuous time imaging
<b>DESS</b>	dual echo steady state
<b>DXA</b>	dual-energy x-ray absorptiometry
<b>FSE</b>	fast spin echo
<b>FOV</b>	field of view
<b>FA</b>	flip angle
<b>FT</b>	Fourier transform
<b>FID</b>	free induction decay
<b>GRE</b>	gradient echo
<b>GIRF</b>	gradient impulse response function
<b>HR-QCT</b>	high-resolution QCT
<b>IP</b>	in-phase
<b>IR</b>	inversion recovery

<b>IFFT</b>	inverse fast Fourier transform
<b>IDEAL</b>	iterative decomposition with echo asymmetry and least squares estimation
<b>LTI</b>	linear time invariant
<b>MR</b>	magnetic resonance
<b>MRI</b>	magnetic resonance imaging
<b>MRS</b>	magnetic resonance spectroscopy
<b>MSK</b>	musculoskeletal
<b>NUFFT</b>	non-uniform fast Fourier transform
<b>NMR</b>	nuclear magnetic resonance
<b>OP</b>	out-of-phase
<b>PI</b>	parallel imaging
<b>PSF</b>	point spread function
<b>PET</b>	positron emission tomography
<b>PD</b>	proton density
<b>PDFF</b>	proton density fat fraction
<b>QCT</b>	quantitative computed tomography
<b>QSM</b>	quantitative susceptibility mapping
<b>RF</b>	radio frequency
<b>ROI</b>	region of interest
<b>SENSE</b>	sensitivity encoding
<b>STIR</b>	short-tau inversion recovery
<b>SNR</b>	signal-to-noise ratio
<b>SPI</b>	single point imaging
<b>sUTE</b>	single ultrashort echo time
<b>SAR</b>	specific absorption rate
<b>SPAIR</b>	spectral attenuated inversion recovery
<b>SPIR</b>	spectral presaturation with inversion recovery
<b>SOS</b>	stack-of-stars

<b>SW</b>	susceptibility weighted
<b>SWI</b>	susceptibility weighted imaging
<b>TE</b>	echo time
<b>TI</b>	inversion time
<b>TR</b>	repetition time
<b>TB</b>	trabecular bone
<b>UTE</b>	ultrashort echo time
<b>UTESI</b>	ultrashort echo time with spectroscopic imaging
<b>VARPRO</b>	variable projection
<b>VOI</b>	voxel of interest
<b>WFI</b>	water-fat imaging
<b>WHO</b>	world health organization
<b>ZTE</b>	zero echo time

# List of Figures

3.1	Gradient Echo: The first readout gradient $G_r$ with positive polarity after the excitation RF pulse causes a dephasing of the spins. This dephasing is recovered by a second gradient with opposite polarity. After a time interval TE, the time integral of both gradients match and an echo is generated. The real and imaginary parts are shown as a solid black and dotted line, respectively. Slice selection is achieved with a frequency selective RF pulse and a slice encoding gradient $G_s$ . TE: echo time; RF: radio-frequency pulse; $G_r$ : readout encoding gradient; $G_s$ : slice encoding gradient; $G_p$ : phase encoding gradient; AQ: receiver channel; $T_{AQ}$ : time of the acquisition window. . . . .	12
3.2	Free Induction Decay measurement with a UTE sequence: The signal's real and imaginary parts are shown as a solid black and dotted line, respectively. A) After the RF excitation pulse, data acquisition starts as soon as possible. TE is defined from the center of the RF pulse to the start of data acquisition. B) K-space representation of A). Data acquisition begins at the center of k-space with a radial center-out readout (along arrow). The signal decay during the data acquisition window $T_{AQ}$ reduces the signal at the outer k-space points, resulting in blurring in the image space. C-D) To reduce $T_2^*$ blurring, stronger readout gradients are used to traverse k-space faster and reduce $T_{AQ}$ . TE: echo time; RF: radio-frequency pulse; $G_r$ : readout encoding gradient; AQ: receiver channel; $T_{AQ}$ : time of the acquisition window. . . . .	13
3.3	UTE sequence diagrams: In all sequences, $G_{x,y}$ encodes the imaging plane and $G_z$ the slice direction. A) 2D UTE sequence with two half-sinc slice selective RF pulses that belong to the acquisition of one k-space spoke. The slice excitation gradient has opposing polarities for each half pulse excitation, which result in a conventional sinc pulse slice profile. B) 3D non-selective excitation pulse followed by 3D radial Koosh ball readout. C) 3D non-selective excitation pulse followed by a slice phase encoding gradient $G_z$ and a SOS in-plane radial readout. D) 3D volume-selective excitation combined with the same 3D SOS encoding as in C). RF: radio-frequency pulse; $G_{x,y}$ : imaging plane encoding gradient; $G_z$ : slice encoding gradient; $k_z$ : k-space in slice direction; AQ: receiver channel; SOS: stack-of-stars. . . . .	17

4.1	UTE multi-TE sequence diagrams. a) UTE multi-acquisition technique: The various TEs (shown is here a dual-echo acquisition) are acquired in successive sequence repetitions. The difference between two successive repetitions are depicted with the solid and dotted lines. While this acquisition scheme provides greater TE flexibility, it reduces scan time efficiency. b) UTE multi-echo technique: The various TEs are acquired in each sequence repetition. This method reduces the scan time when compared to the multi-acquisition method. However, TE is constrained by the system's smallest achievable echo distance and thus also by the desired spatial resolution. c) Interleaved UTE multi-echo techniques: Multiple echoes are acquired after each RF excitation. The entire multi-TE readout is shifted between repetitions, allowing for more flexible TEs. Thus, the interleaved acquisition method combines the scan time efficiency of multi-echo readout with the multi-acquisition method's greater TE flexibility. RF: radio-frequency pulse; G <sub>x,y</sub> : imaging plane encoding gradient; AQ: receiver channel. . . . .	22
5.1	Illustration of the Cartesian (left) and radial center-out (right) sampling scheme. Shown are sampling points in k-space with $dk$ and $dk'$ being the distance between to sampling points. The arrows depict the readout direction and sampling points that are acquired during one acquisition. . . . .	29
5.2	Point spread function (top row) and corresponding reconstruction of the Shepp-Logan phantom (bottom row) for variable radial density. A radial density of 100% corresponds to $\pi \cdot n$ number of spokes. . . . .	29
5.3	Cartesian and non-Cartesian reconstruction pipeline. A) The Cartesian k-space data is transformed to image space data by a straightforward IFFT. B) The non-Cartesian k-space data is gridded to a Cartesian k-space before the Fourier transform of k-space to image space. The NUFFT directly transforms any non-Cartesian data from k-space to image space. IFFT: inverse fast Fourier transform; NUFFT: non-uniform fast Fourier transform; $k_x, k_y$ : Cartesian k-space coordinates; $k_\phi, k_r$ : polar k-space coordinates. . . . .	30
5.4	Comparison of gridding parameters and NUFFT. Regridding reconstruction without oversampling (ovs = 1) shows clearly visible aliasing artifacts. Regridding reconstruction with artificially increased FOV (ovs = 2) shifts the artifacts away from the object. A wider kernel (w = 4) increases computation time yet also reduces aliasing artifacts. NUFFT: non-uniform fast Fourier transform; ovs: gridding oversampling factor; w: kernel width in $dk$ ; t: computation time for an image with 512 x 512 pixels. . . . .	31

- 
- 5.5 Off-resonance artifacts obtained for Cartesian, radial and radial center-out sampling. Graphical acquisition time maps are shown in the top row of the corresponding k-space trajectories (arrows). Points acquired at the beginning of the acquisition window are represented with darker shading and points acquired at the end of the acquisition window are represented with light shading. The phase accumulated due off-resonance effects leads to distortions. Middle row shows the PSF in k-space for water (on resonance) in red and for fat (frequency shift of 440 Hz) in white. Bottom row shows reconstructions of a water-fat phantom left. In the water map, the white represents voxels that contain 100% water, and gray represents 50% water. Similarly, in the fat map 100% fat is shown in white, and 50% fat gray. PSF: point spread function;  $k_x, k_y$ : Cartesian k-space coordinates;  $x, y$ : Cartesian images space coordinates. . . . . 33

# List of Tables

2.1	Effective radiation doses for x-ray based imaging methods. Table adapted from [38]. . . . .	8
2.2	Overview of major advantages and disadvantages of the different MR techniques currently applied to quantitative osteoporosis imaging at the spine and femur, including information on the basis of the tissue signal. Table adapted from [26].	10
3.1	Overview of major advantages and disadvantages of basic techniques for short $T_2$ MRI. Table adapted from [69]. . . . .	15
3.2	Overview of major qualitative MRI techniques for bone imaging and application. Table modified from [13]. . . . .	21



# Bibliography

- [1] R. Damadian, “Tumor detection by nuclear magnetic resonance,” *Science*, vol. 171, no. 3976, pp. 1151–1153, 1971.
- [2] P. C. Lauterbur, “Image formation by induced local interactions: Examples employing nuclear magnetic resonance,” *Nature*, vol. 242, no. 5394, pp. 190–191, 1973.
- [3] A. N. Garroway, P. K. Grannell, and P. Mansfield, “Image formation in NMR by a selective irradiative process,” *Journal of Physics C: Solid State Physics*, vol. 7, pp. L457–L462, Dec. 1974.
- [4] A. Kumar, D. Welte, and R. R. Ernst, “NMR Fourier zeugmatography,” *Journal of Magnetic Resonance*, vol. 213, no. 2, pp. 495–509, 2011.
- [5] J. T. Lin and J. M. Lane, “Osteoporosis: a review.,” *Clinical orthopaedics and related research*, pp. 126–34, Aug 2004.
- [6] C. S. Parenteau, E. C. Lau, I. C. Campbell, and A. Courtney, “Prevalence of spine degeneration diagnosis by type, age, gender, and obesity using medicare data,” *Scientific Reports*, vol. 11, p. 5389, Mar. 2021.
- [7] E. S. Siris, S. K. Brenneman, E. Barrett-Connor, P. D. Miller, S. Sajjan, M. L. Berger, and Y.-T. Chen, “The effect of age and bone mineral density on the absolute, excess, and relative risk of fracture in postmenopausal women aged 50-99: results from the National Osteoporosis Risk Assessment (NORA),” *Osteoporosis International*, vol. 17, pp. 565–574, Apr. 2006.
- [8] F. W. Wehrli, H. K. Song, P. K. Saha, and A. C. Wright, “Quantitative mri for the assessment of bone structure and function,” *NMR in Biomedicine*, vol. 19, no. 7, pp. 731–764, 2006.
- [9] S. Emdin and J. Creyghton, “High resolution nmr imaging in solids,” *Physica B+C*, vol. 128, no. 1, pp. 81–83, 1985.
- [10] M. D. Robson, P. D. Gatehouse, M. Bydder, and G. M. Bydder, “Magnetic resonance: An introduction to ultrashort te (ute) imaging,” *Journal of Computer Assisted Tomography*, vol. 27, no. 6, 2003.
- [11] M. Weiger and K. P. Pruessmann, *MRI with Zero Echo Time*, p. 311–322. John Wiley & Sons, Ltd, 2012.
- [12] G. M. Bydder, G. D. Fullerton, and I. R. Young, *MRI of Tissues with Short T2s or T2\*s*. Chichester, United Kingdom: John Wiley & Sons Ltd, 2012.
- [13] S. Jerban, D. G. Chang, Y. Ma, H. Jang, E. Y. Chang, and J. Du, “An update in qualitative imaging of bone using ultrashort echo time magnetic resonance,” *Frontiers in Endocrinology*, vol. 11, p. 777, 2020.

- 
- [14] Y.-J. Ma, S. Jerban, H. Jang, D. Chang, E. Y. Chang, and J. Du, “Quantitative ultrashort echo time (ute) magnetic resonance imaging of bone: An update,” *Frontiers in Endocrinology*, vol. 11, p. 667, 2020.
- [15] P. Fratzl and R. Weinkamer, “Nature’s hierarchical materials,” *Progress in Materials Science*, vol. 52, pp. 1263–1334, Nov. 2007.
- [16] D. H. Pahr and A. G. Reisinger, “A review on recent advances in the constitutive modeling of bone tissue,” *Current Osteoporosis Reports*, vol. 18, pp. 696–704, Dec. 2020.
- [17] D. H. Copp and S. S. Shim, “The homeostatic function of bone as a mineral reservoir,” *Oral Surgery, Oral Medicine, Oral Pathology*, vol. 16, pp. 738–744, June 1963.
- [18] V. Bousson, C. Bergot, A. Meunier, F. Barbot, C. Parlier-Cuau, A.-M. Laval-Jeantet, and J.-D. Laredo, “Ct of the middiaphyseal femur: Cortical bone mineral density and relation to porosity,” *Radiology*, vol. 217, no. 1, pp. 179–187, 2000. PMID: 11012442.
- [19] D. M. L. Cooper, J. R. Matyas, M. A. Katzenberg, and B. Hallgrímsson, “Comparison of microcomputed tomographic and microradiographic measurements of cortical bone porosity,” *Calcified tissue international*, vol. 74, pp. 437–47, May 2004.
- [20] B. Clarke, “Normal bone anatomy and physiology,” *CLIN J AM SOC NEPHROL*, vol. 3, p. S131, Nov. 2008.
- [21] J.-Y. Rho, L. Kuhn-Spearing, and P. Zioupos, “Mechanical properties and the hierarchical structure of bone,” *Medical Engineering & Physics*, vol. 20, pp. 92–102, Mar. 1998.
- [22] D. B. Burr and M. R. Allen, *Basic and Applied Bone Biology*. Academic Press, 2nd edition ed., Feb. 2019.
- [23] M. Granke, M. D. Does, and J. S. Nyman, “The role of water compartments in the material properties of cortical bone,” *Calcified Tissue International*, vol. 97, pp. 292–307, Sept. 2015.
- [24] D. C. Karampinos, S. Ruschke, M. Dieckmeyer, M. Diefenbach, D. Franz, A. S. Gersing, R. Krug, and T. Baum, “Quantitative mri and spectroscopy of bone marrow,” *J. Magn. Reson. Imaging*, vol. 47, pp. 332–353, Feb. 2018.
- [25] J. E. Compston, M. R. McClung, and W. D. Leslie, “Osteoporosis,” *The Lancet*, vol. 393, pp. 364–376, Jan. 2019.
- [26] N. Sollmann, M. T. Löffler, S. Kronthaler, C. Böhm, M. Dieckmeyer, S. Ruschke, J. S. Kirschke, J. Carballido-Gamio, D. C. Karampinos, R. Krug, and T. Baum, “MRI-Based Quantitative Osteoporosis Imaging at the Spine and Femur,” *Journal of Magnetic Resonance Imaging*, vol. 54, no. 1, pp. 12–35, 2021.
- [27] J.-Y. Reginster and N. Burlet, “Osteoporosis: A still increasing prevalence,” *Bone*, vol. 38, pp. 4–9, Feb. 2006.
- [28] S. C. Manolagas, “Birth and death of bone cells: Basic regulatory mechanisms and implications for the pathogenesis and treatment of osteoporosis\*,” *Endocr Rev*, vol. 21, pp. 115–137, Apr. 2000.

- [29] L. J. Melton III, E. A. Chrischilles, C. Cooper, A. W. Lane, and B. L. Riggs, "Perspective how many women have osteoporosis?," *J Bone Miner Res*, vol. 7, pp. 1005–1010, Sept. 1992.
- [30] A. Randell, P. N. Sambrook, T. V. Nguyen, H. Lapsley, G. Jones, P. J. Kelly, and J. A. Eisman, "Direct clinical and welfare costs of osteoporotic fractures in elderly men and women," *Osteoporosis International*, vol. 5, pp. 427–432, Nov. 1995.
- [31] I. Hallberg, M. Bachrach-Lindström, S. Hammerby, G. Toss, and A.-C. Ek, "Health-related quality of life after vertebral or hip fracture: a seven-year follow-up study," *BMC Musculoskeletal Disorders*, vol. 10, p. 135, Nov. 2009.
- [32] J.-E. Tarride, N. Burke, W. D. Leslie, S. N. Morin, J. D. Adachi, A. Papaioannou, L. Bessette, J. P. Brown, L. Pericleous, S. Muratov, and R. B. Hopkins, "Loss of health related quality of life following low-trauma fractures in the elderly," *BMC Geriatrics*, vol. 16, p. 84, Apr. 2016.
- [33] D. Bliuc, N. D. Nguyen, T. V. Nguyen, J. A. Eisman, and J. R. Center, "Compound risk of high mortality following osteoporotic fracture and refracture in elderly women and men," *J Bone Miner Res*, vol. 28, pp. 2317–2324, Nov. 2013.
- [34] L. J. Melton III, E. J. Atkinson, C. Cooper, W. M. O’Fallon, and B. L. Riggs, "Vertebral fractures predict subsequent fractures," *Osteoporosis International*, vol. 10, pp. 214–221, Sept. 1999.
- [35] C. H. Wilkins, "Osteoporosis screening and risk management.," *Clinical interventions in aging*, vol. 2, pp. 389–94, 2007.
- [36] J. A. Kanis, C.-C. Glüer, and I. O. F. for the Committee of Scientific Advisors, "An update on the diagnosis and assessment of osteoporosis with densitometry," *Osteoporosis International*, vol. 11, pp. 192–202, Mar. 2000.
- [37] J. A. Kanis, J. D. Adachi, C. Cooper, P. Clark, S. R. Cummings, M. Diaz-Curiel, N. Harvey, M. Hilgsmann, A. Papaioannou, D. D. Pierroz, S. L. Silverman, P. Szulc, T. Epidemiology, and Q. of Life Working Group of IOF, "Standardising the descriptive epidemiology of osteoporosis: recommendations from the epidemiology and quality of life working group of iof," *Osteoporosis International*, vol. 24, pp. 2763–2764, Nov. 2013.
- [38] T. M. Link, "Osteoporosis imaging: State of the art and advanced imaging," *Radiology*, vol. 263, pp. 3–17, Apr. 2012.
- [39] P. Ammann and R. Rizzoli, "Bone strength and its determinants," *Osteoporosis International*, vol. 14, pp. 13–18, Mar. 2003.
- [40] S. C. E. Schuit, M. van der Klift, A. E. A. M. Weel, C. E. D. H. de Laet, H. Burger, E. Seeman, A. Hofman, A. G. Uitterlinden, J. P. T. M. van Leeuwen, and H. A. P. Pols, "Fracture incidence and association with bone mineral density in elderly men and women: the rotterdam study," *Bone*, vol. 34, pp. 195–202, Jan. 2004.
- [41] D. M. Black, S. L. Greenspan, K. E. Ensrud, L. Palermo, J. A. McGowan, T. F. Lang, P. Garnero, M. L. Bouxsein, J. P. Bilezikian, and C. J. Rosen, "The effects of parathyroid hormone and alendronate alone or in combination in postmenopausal osteoporosis," *N Engl J Med*, vol. 349, pp. 1207–1215, Sept. 2003.

- 
- [42] C. Bergot, A. M. Laval-Jeantet, K. Hutchinson, I. Dautraix, F. Caulin, and H. K. Genant, "A comparison of spinal quantitative computed tomography with dual energy x-ray absorptiometry in european women with vertebral and nonvertebral fractures," *Calcified Tissue International*, vol. 68, pp. 74–82, Feb. 2001.
- [43] J. Damilakis, J. E. Adams, G. Guglielmi, and T. M. Link, "Radiation exposure in x-ray-based imaging techniques used in osteoporosis," *European Radiology*, vol. 20, pp. 2707–2714, Nov. 2010.
- [44] D. NIH Consensus Development Panel on Osteoporosis Prevention and Therapy, "Osteoporosis prevention, diagnosis, and therapy," *JAMA*, vol. 285, pp. 785–795, Feb. 2001.
- [45] S. Boutroy, M. L. Bouxsein, F. Munoz, and P. D. Delmas, "In vivo assessment of trabecular bone microarchitecture by high-resolution peripheral quantitative computed tomography," *J Clin Endocrinol Metab*, vol. 90, pp. 6508–6515, Dec. 2005.
- [46] R. Krug, A. J. Burghardt, S. Majumdar, and T. M. Link, "High-resolution imaging techniques for the assessment of osteoporosis," *Radiologic Clinics of North America*, vol. 48, pp. 601–621, May 2010.
- [47] F. W. Wehrli, J. C. Ford, M. Attie, H. Y. Kressel, and F. S. Kaplan, "Trabecular structure: Preliminary application of MR interferometry," *Radiology*, vol. 179, no. 3, pp. 615–621, 1991.
- [48] S. Majumdar, D. Thomasson, A. Shimakawa, and H. K. Genant, "Quantitation of the susceptibility difference between trabecular bone and bone marrow: Experimental studies," *Magnetic Resonance in Medicine*, vol. 22, no. 1, pp. 111–127, 1991.
- [49] R. Krug, S. Banerjee, E. T. Han, D. C. Newitt, T. M. Link, and S. Majumdar, "Feasibility of in vivo structural analysis of high-resolution magnetic resonance images of the proximal femur," *Osteoporosis International*, vol. 16, pp. 1307–1314, Nov. 2005.
- [50] S. Majumdar and H. K. Genant, "In vivo relationship between marrow  $t_2^*$  and trabecular bone density determined with a chemical shift–selective asymmetric spin-echo sequence," *J. Magn. Reson. Imaging*, vol. 2, pp. 209–219, Mar. 1992.
- [51] J. R. Reichenbach, F. Schweser, B. Serres, and A. Deistung, "Quantitative susceptibility mapping: Concepts and applications," *Clinical Neuroradiology*, vol. 25, pp. 225–230, Oct. 2015.
- [52] M. N. Diefenbach, J. Meineke, S. Ruschke, T. Baum, A. Gersing, and D. C. Karampinos, "On the sensitivity of quantitative susceptibility mapping for measuring trabecular bone density," *Magnetic Resonance in Medicine*, vol. 81, no. 3, pp. 1739–1754, 2019.
- [53] Y. Wang and T. Liu, "Quantitative susceptibility mapping (qsm): Decoding mri data for a tissue magnetic biomarker," *Magnetic Resonance in Medicine*, vol. 73, pp. 82–101, Jan. 2015.
- [54] P. K. Fazeli, M. C. Horowitz, O. A. MacDougald, E. L. Scheller, M. S. Rodeheffer, C. J. Rosen, and A. Klibanski, "Marrow fat and bone—new perspectives," *J Clin Endocrinol Metab*, vol. 98, pp. 935–945, Mar. 2013.

- [55] J. F. Griffith, D. K. Yeung, G. E. Antonio, F. K. Lee, A. W. Hong, S. Y. Wong, E. M. Lau, and P. C. Leung, "Vertebral bone mineral density, marrow perfusion, and fat content in healthy men and men with osteoporosis: Dynamic contrast-enhanced MR imaging and MR spectroscopy," *Radiology*, vol. 236, no. 3, pp. 945–951, 2005.
- [56] P. T. Callaghan and C. D. Eccles, "Sensitivity and resolution in nmr imaging," *Journal of Magnetic Resonance (1969)*, vol. 71, pp. 426–445, Feb. 1987.
- [57] J. Rahmer, P. Börnert, J. Groen, and C. Bos, "Three-dimensional radial ultrashort echo-time imaging with t2 adapted sampling," *Magnetic Resonance in Medicine.*, vol. 55, pp. 1075–1082, May 2006.
- [58] S. Choi, X.-W. Tang, and D. G. Cory, "Constant time imaging approaches to nmr microscopy," *Int. J. Imaging Syst. Technol.*, vol. 8, pp. 263–276, Jan. 1997.
- [59] B. J. Balcom, R. P. Macgregor, S. D. Beyea, D. P. Green, R. L. Armstrong, and T. W. Bremner, "Single-Point Ramped Imaging with T1 Enhancement (SPRITE)," *Journal of Magnetic Resonance, Series A*, vol. 123, pp. 131–134, Nov. 1996.
- [60] P. Gatehouse and G. Bydder, "Magnetic resonance imaging of short t2 components in tissue," *Clinical Radiology*, vol. 58, no. 1, pp. 1–19, 2003.
- [61] J. E. Holmes and G. M. Bydder, "MR imaging with ultrashort TE (UTE) pulse sequences: Basic principles," *Radiography*, vol. 11, pp. 163–174, Aug. 2005.
- [62] M. D. Robson and G. M. Bydder, "Clinical ultrashort echo time imaging of bone and other connective tissues," *NMR in Biomedicine*, vol. 19, pp. 765–780, nov 2006.
- [63] J. Du and G. M. Bydder, "Qualitative and quantitative ultrashort-TE MRI of cortical bone," *NMR in Biomedicine*, vol. 26, no. 5, pp. 489–506, 2013.
- [64] E. Y. Chang, J. Du, and C. B. Chung, "UTE imaging in the musculoskeletal system," *Journal of Magnetic Resonance Imaging*, vol. 41, no. 4, pp. 870–883, 2015.
- [65] B. H. Suits and D. White, "Nmr imaging in solids," *Solid State Communications*, vol. 50, pp. 291–295, Apr. 1984.
- [66] S. Hafner, "Fast imaging in liquids and solids with the back-projection low angle shot (blast) technique," *Magnetic Resonance Imaging*, vol. 12, pp. 1047–1051, Jan. 1994.
- [67] D. P. Madio and I. J. Lowe, "Ultra-fast imaging using low flip angles and fids," *Magnetic Resonance in Medicine.*, vol. 34, pp. 525–529, Oct. 1995.
- [68] D. J. Tyler, M. D. Robson, R. M. Henkelman, I. R. Young, and G. M. Bydder, "Magnetic resonance imaging with ultrashort te (ute) pulse sequences: Technical considerations," *J. Magn. Reson. Imaging*, vol. 25, pp. 279–289, Feb. 2007.
- [69] M. Weiger and K. P. Pruessmann, "Short-t2 mri: Principles and recent advances," *Progress in Nuclear Magnetic Resonance Spectroscopy*, vol. 114-115, pp. 237–270, 2019.
- [70] P. J. Prado, B. J. Balcom, S. D. Beyea, R. L. Armstrong, and T. W. Bremner, "Concrete thawing studied by single-point ramped imaging," *Solid State Nuclear Magnetic Resonance*, vol. 10, pp. 1–8, Dec. 1997.

- 
- [71] M. Bruschewski, H. Kolkmann, K. John, and S. Grundmann, “Phase-contrast single-point imaging with synchronized encoding: a more reliable technique for in vitro flow quantification,” *Magnetic Resonance in Medicine*, vol. 81, pp. 2937–2946, May 2019.
- [72] F. Springer, G. Steidle, P. Martirosian, C. D. Claussen, and F. Schick, “Effects of in-pulse transverse relaxation in 3d ultrashort echo time sequences: Analytical derivation, comparison to numerical simulation and experimental application at 3t,” *Journal of Magnetic Resonance*, vol. 206, pp. 88–96, Sept. 2010.
- [73] J. M. Pauly, *Selective Excitation for Ultrashort Echo Time Imaging*, pp. pp. 381 – 387. in: eMagRes, John Wiley & Sons, Ltd, 2012.
- [74] S. Josan, J. M. Pauly, B. L. Daniel, and K. B. Pauly, “Double half rf pulses for reduced sensitivity to eddy currents in ute imaging,” *Magnetic Resonance in Medicine.*, vol. 61, pp. 1083–1089, May 2009.
- [75] K. D. Harkins, M. D. Does, and W. A. Grissom, “Iterative method for predistortion of MRI gradient waveforms,” *IEEE Transactions on Medical Imaging*, vol. 33, no. 8, pp. 1641–1647, 2014.
- [76] P. T. Gurney, B. A. Hargreaves, and D. G. Nishimura, “Design and analysis of a practical 3d cones trajectory,” *Magnetic Resonance in Medicine.*, vol. 55, pp. 575–582, Mar. 2006.
- [77] Y. Qian and F. E. Boada, “Acquisition-weighted stack of spirals for fast high-resolution three-dimensional ultra-short echo time MR imaging,” *Magnetic Resonance in Medicine*, vol. 60, no. 1, pp. 135–145, 2008.
- [78] M. Zamskiy, S. Kronthaler, D. Weidlich, I. Ball, A. Gersing, M. Makowski, J. Herzen, and D. Karampinos, “Bone imaging of the spine and pelvis using an improved 3d adiabatic inversion recovery-prepared ultrashort te sequence at 3t,” *In Proceedings of the Scientific Meeting of ESMRMB, Virtual Conference, p. L01.36.*, 2020.
- [79] M. Yoneyama, I. Ball, M. Azuma, T. Hirai, and M. V. Cauteren, “3d broadband ir-prepared ute bone imaging for assessment of ossification of the posterior longitudinal ligament (opll) in the cervical spine,” *In Proceeding of the 27th Scientific Meeting of ISMRM, Canada, Montreal, p. 2873*, p. p. 2873, 2019.
- [80] M. Takizawa, H. Hanada, K. Oka, T. Takahashi, E. Yamamoto, and M. Fujii, “A Robust Ultrashort TE (UTE) imaging method with corrected k-space trajectory by using parametric multiple function model of gradient waveform,” *IEEE Transactions on Medical Imaging*, vol. 32, no. 2, pp. 306–316, 2013.
- [81] A. Deshmane, M. Blaimer, F. Breuer, P. Jakob, J. Duerk, N. Seiberlich, and M. Griswold, “Self-calibrated trajectory estimation and signal correction method for robust radial imaging using GRAPPA operator gridding,” *Magnetic Resonance in Medicine*, vol. 75, no. 2, pp. 883–896, 2016.
- [82] M. Krämer, J. Biermann, and J. R. Reichenbach, “Intrinsic correction of system delays for radial magnetic resonance imaging,” *Magnetic Resonance Imaging*, vol. 33, no. 4, pp. 491–496, 2015.

- 
- [83] P. Latta, Z. Starčuk, M. L. Gruwel, M. H. Weber, and B. Tomanek, “K-space trajectory mapping and its application for ultrashort Echo time imaging,” *Magnetic Resonance Imaging*, vol. 36, pp. 68–76, 2017.
- [84] D. C. Peters, J. A. Derbyshire, and E. R. McVeigh, “Centering the projection reconstruction trajectory: Reducing gradient delay errors,” *Magnetic Resonance in Medicine*, vol. 50, pp. 1–6, July 2003.
- [85] K.-H. Herrmann, M. Krämer, and J. R. Reichenbach, “Time efficient 3d radial uterine sampling with fully automatic delay compensation on a clinical 3t mr scanner,” *PLOS ONE*, vol. 11, p. e0150371, Mar. 2016.
- [86] S. J. Vannesjo, N. N. Graedel, L. Kasper, S. Gross, J. Busch, M. Haeberlin, C. Barmet, and K. P. Pruessmann, “Image reconstruction using a gradient impulse response model for trajectory prediction,” *Magnetic Resonance in Medicine*, vol. 76, no. 1, pp. 45–58, 2016.
- [87] N. O. Addy, H. H. Wu, and D. G. Nishimura, “Simple method for MR gradient system characterization and k-space trajectory estimation,” *Magnetic Resonance in Medicine*, vol. 68, no. 1, pp. 120–129, 2012.
- [88] G. F. Mason, T. Harshbarger, H. P. Hetherington, Y. Zhang, G. M. Pohost, and D. B. Twieg, “A method to measure arbitrary k-space trajectories for rapid MR imaging,” *Magnetic Resonance in Medicine*, vol. 38, no. 3, pp. 492–496, 1997.
- [89] A. Takahashi and T. Peters, “Compensation of multi-dimensional selective excitation pulses using measured k-space trajectories,” *Magnetic Resonance in Medicine*, vol. 34, no. 3, pp. 446–456, 1995.
- [90] M. T. Alley, G. H. Glover, and N. J. Pelc, “Gradient characterization using a fourier-transform technique,” *Magnetic Resonance in Medicine*, vol. 39, no. 4, pp. 581–587, 1998.
- [91] H. Jang and A. B. McMillan, “A rapid and robust gradient measurement technique using dynamic single-point imaging,” *Magnetic Resonance in Medicine*, vol. 78, no. 3, pp. 950–962, 2017.
- [92] J. H. Duyn, Y. Yang, J. A. Frank, and J. W. Van Der Veen, “Simple Correction Method for k-Space Trajectory Deviations in MRI,” *Journal of Magnetic Resonance*, vol. 132, no. 1, pp. 150–153, 1998.
- [93] N. De Zanche, C. Barmet, J. A. Nordmeyer-Massner, and K. P. Pruessmann, “NMR Probes for measuring magnetic fields and field dynamics in MR systems,” *Magnetic Resonance in Medicine*, vol. 60, no. 1, pp. 176–186, 2008.
- [94] H. Liu and G. B. Matson, “Accurate measurement of magnetic resonance imaging gradient characteristics,” *Materials*, vol. 7, no. 1, pp. 1–15, 2014.
- [95] B. E. Dietrich, D. O. Brunner, B. J. Wilm, C. Barmet, S. Gross, L. Kasper, M. Haeberlin, T. Schmid, S. J. Vannesjo, and K. P. Pruessmann, “A field camera for MR sequence monitoring and system analysis,” *Magnetic Resonance in Medicine*, vol. 75, no. 4, pp. 1831–1840, 2016.

- 
- [96] E. M. Johnson, U. Vyas, P. Ghanouni, K. B. Pauly, and J. M. Pauly, "Improved cortical bone specificity in UTE MR Imaging," *Magnetic Resonance in Medicine*, vol. 77, no. 2, pp. 684–695, 2017.
- [97] H. Jang, Y. Ma, M. Carl, S. Jerban, E. Y. Chang, and J. Du, "Ultrashort echo time Cones double echo steady state (UTE-Cones-DESS) for rapid morphological imaging of short T2 tissues," *Magnetic Resonance in Medicine*, vol. 86, no. 2, pp. 881–892, 2021.
- [98] E. Deininger-Czermak, A. Euler, S. Franckenberg, T. Finkenstaedt, C. Villefort, D. Gascho, and R. Guggenberger, "Evaluation of ultrashort echo-time (ute) and fast-field-echo (fracture) sequences for skull bone visualization and fracture detection - a postmortem study," *Journal of Neuroradiology*, Nov. 2021.
- [99] J. Du, M. Bydder, A. M. Takahashi, M. Carl, C. B. Chung, and G. M. Bydder, "Short t2 contrast with three-dimensional ultrashort echo time imaging," *Magnetic Resonance Imaging*, vol. 29, pp. 470–482, May 2011.
- [100] Y. H. Lee, S. Kim, H.-T. Song, I. Kim, and J.-S. Suh, "Weighted subtraction in 3d ultrashort echo time (ute) imaging for visualization of short t2 tissues of the knee," *Acta Radiologica*, vol. 55, no. 4, pp. 454–461, 2014.
- [101] E. C. A. Araujo, N. Azzabou, A. Vignaud, G. Guillot, and P. G. Carlier, "Quantitative ultrashort te imaging of the short-t2 components in skeletal muscle using an extended echo-subtraction method," *Magnetic Resonance in Medicine.*, vol. 78, pp. 997–1008, Sept. 2017.
- [102] J. Rahmer, U. Blume, and P. Börnert, "Selective 3d ultrashort te imaging: comparison of "dual-echo" acquisition and magnetization preparation for improving short-t2 contrast," *Magnetic Resonance Materials in Physics, Biology and Medicine*, vol. 20, p. 83, Mar. 2007.
- [103] P. E. Z. Larson, P. T. Gurney, K. Nayak, G. E. Gold, J. M. Pauly, and D. G. Nishimura, "Designing long-t2 suppression pulses for ultrashort echo time imaging," *Magnetic Resonance in Medicine.*, vol. 56, pp. 94–103, July 2006.
- [104] Y. J. Ma, S. Jerban, H. Jang, E. Y. Chang, and J. Du, "Fat suppression for ultrashort echo time imaging using a novel soft-hard composite radiofrequency pulse," *Magnetic Resonance in Medicine*, vol. 82, no. 6, pp. 2178–2187, 2019.
- [105] M. A. Pauly JM, Conolly SM, "Suppression of long-t2 components for short-t2 imaging," *In: Proceedings of the 10th Annual Meeting of SMRI, New York, New York, USA p. 330.*, 1992.
- [106] P. E. Z. Larson, S. M. Conolly, J. M. Pauly, and D. G. Nishimura, "Using adiabatic inversion pulses for long-t2 suppression in ultrashort echo time (ute) imaging," *Magnetic Resonance in Medicine.*, vol. 58, pp. 952–961, Nov. 2007.
- [107] M. Carl, G. M. Bydder, and J. Du, "UTE imaging with simultaneous water and fat signal suppression using a time-efficient multispoke inversion recovery pulse sequence," *Magnetic Resonance in Medicine*, vol. 76, no. 2, pp. 577–582, 2016.



- 
- [108] S. Anumula, J. Magland, S. L. Wehrli, H. Zhang, H. Ong, H. K. Song, and F. W. Wehrli, "Measurement of phosphorus content in normal and osteomalacic rabbit bone by solid-state 3d radial imaging," *Magnetic Resonance in Medicine*, vol. 56, pp. 946–952, Nov. 2006.
- [109] A. C. Seifert and F. W. Wehrli, "Solid-state quantitative  $^1\text{H}$  and  $^{31}\text{P}$  mri of cortical bone in humans," *Current Osteoporosis Reports*, vol. 14, pp. 77–86, June 2016.
- [110] E. C. Argentieri, M. F. Koff, R. E. Breighner, Y. Endo, P. H. Shah, and D. B. Sneag, "Diagnostic Accuracy of Zero-Echo Time MRI for the Evaluation of Cervical Neural Foraminal Stenosis," *Spine*, vol. 43, no. 13, pp. 928–933, 2018.
- [111] R. E. Breighner, Y. Endo, G. P. Konin, L. V. Gulotta, M. F. Koff, and H. G. Potter, "Zero echo time imaging of the shoulder: Enhanced osseous detail by using MR imaging," *Radiology*, vol. 286, pp. 960–966, mar 2018.
- [112] F. Wiesinger, L. I. Sacolick, A. Menini, S. S. Kaushik, S. Ahn, P. Veit-Haibach, G. Delso, and D. D. Shanbhag, "Zero TE MR bone imaging in the head," *Magnetic Resonance in Medicine*, vol. 75, pp. 107–114, jan 2016.
- [113] S. Jerban, Y. Ma, L. Li, H. Jang, L. Wan, T. Guo, A. Searleman, E. Y. Chang, and J. Du, "Volumetric mapping of bound and pore water as well as collagen protons in cortical bone using 3d ultrashort echo time cones mr imaging techniques," *Bone*, vol. 127, pp. 120–128, Oct. 2019.
- [114] S. Jerban, Y. Ma, H. Jang, B. Namiranian, N. Le, H. Shirazian, M. E. Murphy, J. Du, and E. Y. Chang, "Water proton density in human cortical bone obtained from ultrashort echo time (ute) mri predicts bone microstructural properties," *Magnetic Resonance Imaging*, vol. 67, pp. 85–89, Apr. 2020.
- [115] R. A. Horch, D. F. Gochberg, J. S. Nyman, and M. D. Does, "Clinically compatible mri strategies for discriminating bound and pore water in cortical bone," *Magnetic Resonance in Medicine*, vol. 68, pp. 1774–1784, Dec. 2012.
- [116] M. K. Manhard, S. Uppuganti, M. Granke, D. F. Gochberg, J. S. Nyman, and M. D. Does, "Mri-derived bound and pore water concentrations as predictors of fracture resistance," *Bone*, vol. 87, pp. 1–10, June 2016.
- [117] S. Jerban, Y. Ma, J. H. Wong, A. Nazaran, A. Searleman, L. Wan, J. Williams, J. Du, and E. Y. Chang, "Ultrashort echo time magnetic resonance imaging (ute-mri) of cortical bone correlates well with histomorphometric assessment of bone microstructure," *Bone*, vol. 123, pp. 8–17, June 2019.
- [118] M. C. Wurnig, M. Calcagni, D. Kenkel, M. Vich, M. Weiger, G. Andreisek, F. W. Wehrli, and A. Boss, "Characterization of trabecular bone density with ultra-short echo-time mri at 1.5, 3.0 and 7.0 t - comparison with micro-computed tomography," *NMR Biomed.*, vol. 27, pp. 1159–1166, Oct. 2014.
- [119] Y. J. Ma, Y. Chen, L. Li, Z. Cai, Z. Wei, S. Jerban, H. Jang, E. Y. Chang, and J. Du, "Trabecular bone imaging using a 3D adiabatic inversion recovery prepared ultrashort TE Cones sequence at 3T," *Magnetic Resonance in Medicine*, vol. 83, no. 5, pp. 1640–1651, 2020.

- 
- [120] W. C. Bae, S. Patil, R. Biswas, S. Li, E. Y. Chang, S. Statum, D. D. D’Lima, C. B. Chung, and J. Du, “Magnetic resonance imaging assessed cortical porosity is highly correlated with microct porosity,” *Bone*, vol. 66, pp. 56–61, Sept. 2014.
- [121] J. Du, J. C. Hermida, E. Diaz, J. Corbeil, R. Znamirovski, D. D. D’Lima, and G. M. Bydder, “Assessment of cortical bone with clinical and ultrashort echo time sequences,” *Magnetic Resonance in Medicine.*, vol. 70, pp. 697–704, Sept. 2013.
- [122] A. Akbari, S. Abbasi-Rad, and H. S. Rad, “T1 correlates age: A short-te mr relaxometry study in vivo on human cortical bone free water at 1.5t,” *Bone*, vol. 83, pp. 17–22, Feb. 2016.
- [123] X. Wang and Q. Ni, “Determination of cortical bone porosity and pore size distribution using a low field pulsed nmr approach,” *J. Orthop. Res.*, vol. 21, pp. 312–319, Mar. 2003.
- [124] R. A. Horch, J. S. Nyman, D. F. Gochberg, R. D. Dortch, and M. D. Does, “Characterization of 1h nmr signal in human cortical bone for magnetic resonance imaging,” *Magnetic Resonance in Medicine.*, vol. 64, pp. 680–687, Sept. 2010.
- [125] E. Diaz, C. B. Chung, W. C. Bae, S. Statum, R. Znamirovski, G. M. Bydder, and J. Du, “Ultrashort echo time spectroscopic imaging (utesi): an efficient method for quantifying bound and free water,” *NMR Biomed.*, vol. 25, pp. 161–168, Jan. 2012.
- [126] B. J. Schwaiger, C. Schneider, S. Kronthaler, F. T. Gassert, C. Böhm, D. Pfeiffer, T. Baum, J. S. Kirschke, D. C. Karampinos, M. R. Makowski, K. Woertler, M. Wurm, and A. S. Gersing, “CT-like images based on T1 spoiled gradient-echo and ultra-short echo time MRI sequences for the assessment of vertebral fractures and degenerative bone changes of the spine,” *European Radiology*, vol. 31, no. 7, pp. 4680–4689, 2021.
- [127] A. M. Afsahi, A. F. Lombardi, Z. Wei, M. Carl, J. Athertya, K. Masuda, M. Wallace, R. R. Lee, and Y.-J. Ma, “High-contrast lumbar spinal bone imaging using a 3d slab-selective ute sequence,” *Frontiers in Endocrinology*, vol. 12, 2022.
- [128] I. L. H. Reichert, M. D. Robson, P. D. Gatehouse, T. He, K. E. Chappell, J. Holmes, S. Girgis, and G. M. Bydder, “Magnetic resonance imaging of cortical bone with ultrashort te pulse sequences,” *Magnetic Resonance Imaging*, vol. 23, pp. 611–618, June 2005.
- [129] Y.-J. Ma, Y. Zhu, X. Lu, M. Carl, E. Y. Chang, and J. Du, “Short t2 imaging using a 3d double adiabatic inversion recovery prepared ultrashort echo time cones (3d dir-ute-cones) sequence,” *Magnetic Resonance in Medicine.*, vol. 79, pp. 2555–2563, May 2018.
- [130] J. Du, M. Bydder, A. M. Takahashi, and C. B. Chung, “Two-dimensional ultrashort echo time imaging using a spiral trajectory,” *Magnetic Resonance Imaging*, vol. 26, pp. 304–312, Apr. 2008.
- [131] J. Du, A. M. Takahashi, and C. B. Chung, “Ultrashort te spectroscopic imaging (utesi): Application to the imaging of short t2 relaxation tissues in the musculoskeletal system,” *J. Magn. Reson. Imaging*, vol. 29, pp. 412–421, Feb. 2009.

- [132] J. Du, A. M. Takahashi, W. C. Bae, C. B. Chung, and G. M. Bydder, “Dual inversion recovery, ultrashort echo time (dir ute) imaging: Creating high contrast for short-t2 species,” *Magnetic Resonance in Medicine*, vol. 63, pp. 447–455, Feb. 2010.
- [133] A. Nazaran, M. Carl, Y. Ma, S. Jerban, Y. Zhu, X. Lu, J. Du, and E. Y. Chang, “Three-dimensional adiabatic inversion recovery prepared ultrashort echo time cones (3d ir-ute-cones) imaging of cortical bone in the hip,” *Magnetic Resonance Imaging*, vol. 44, pp. 60–64, Dec. 2017.
- [134] H. Jang, M. Carl, Y. Ma, S. Jerban, T. Guo, W. Zhao, E. Y. Chang, and J. Du, “Fat suppression for ultrashort echo time imaging using a single-point dixon method,” *NMR in Biomedicine*, vol. 32, p. e4069, May 2019.
- [135] M. Garwood, D. Idiyatullin, C. A. Corum, R. Chamberlain, S. Moeller, N. Kobayashi, L. J. Lehto, J. Zhang, R. O’Connell, M. Tesch, M. J. Nissi, J. Ellermann, and D. R. Nixdorf, *Capturing Signals from Fast-relaxing Spins with Frequency-Swept MRI: SWIFT*. John Wiley & Sons, Ltd, 2012.
- [136] D. M. Grodzki, P. M. Jakob, and B. Heismann, “Ultrashort echo time imaging using pointwise encoding time reduction with radial acquisition (petra),” *Magnetic Resonance in Medicine*, vol. 67, pp. 510–518, Feb. 2012.
- [137] E. Ljungberg, T. C. Wood, A. B. Solana, S. C. R. Williams, G. J. Barker, and F. Wiesinger, “Motion corrected silent ZTE neuroimaging,” *Magnetic Resonance in Medicine*, vol. n/a, Apr. 2022.
- [138] M. Weiger, M. Wu, M. C. Wurnig, D. Kenkel, A. Boss, G. Andreisek, and K. P. Pruessmann, “Zte imaging with long-t2 suppression,” *NMR Biomed.*, vol. 28, pp. 247–254, Feb. 2015.
- [139] W. T. Dixon, “Simple proton spectroscopic imaging,” *Radiology*, vol. 153, no. 1, pp. 189–194, 1984.
- [140] G. H. Glover, “Multipoint dixon technique for water and fat proton and susceptibility imaging,” *Journal of Magnetic Resonance Imaging*, vol. 1, no. 5, pp. 521–530, 1991.
- [141] G. H. Glover and E. Schneider, “Three-point dixon technique for true water/fat decomposition with b0 inhomogeneity correction,” *Magn. Reson. Med.*, vol. 18, pp. 371–383, Apr. 1991.
- [142] S. B. Reeder, Z. Wen, H. Yu, A. R. Pineda, G. E. Gold, M. Markl, and N. J. Pelc, “Multicoil dixon chemical species separation with an iterative least-squares estimation method,” *Magnetic Resonance in Medicine*, vol. 51, no. 1, pp. 35–45, 2004.
- [143] K. Wang, H. Yu, J. H. Brittain, S. B. Reeder, and J. Du, “k-Space water-fat decomposition with T2\* estimation and multifrequency fat spectrum modeling for ultrashort echo time imaging,” *Journal of Magnetic Resonance Imaging*, vol. 31, no. 4, pp. 1027–1034, 2010.
- [144] M. N. Diefenbach, C. Liu, and D. C. Karampinos, “Generalized parameter estimation in multi-echo gradient-echo-based chemical species separation,” *Quantitative Imaging in Medicine and Surgery*, vol. 10, no. 3, pp. 554–567, 2020.

- 
- [145] J. Ma, “Dixon techniques for water and fat imaging,” *Journal of Magnetic Resonance Imaging*, vol. 28, no. 3, pp. 543–558, 2008.
- [146] T. E. Skinner and G. H. Glover, “An extended two-point dixon algorithm for calculating separate water, fat, and b0 images,” *Magnetic Resonance in Medicine*, vol. 37, no. 4, pp. 628–630, 1997.
- [147] A. Kovanlikaya, C. Guclu, C. Desai, R. Becerra, and V. Gilsanz, “Fat quantification using three-point dixon technique: In vitro validation1,” *Academic Radiology*, vol. 12, no. 5, pp. 636–639, 2005.
- [148] J. Szumowski, W. R. Coshov, F. Li, and S. F. Quinn, “Phase unwrapping in the three-point dixon method for fat suppression mr imaging,” *Radiology*, vol. 192, no. 2, pp. 555–561, 1994.
- [149] B. D. Coombs, J. Szumowski, and W. Coshov, “Two-point dixon technique for water-fat signal decomposition with b0 inhomogeneity correction,” *Magnetic Resonance in Medicine*, vol. 38, no. 6, pp. 884–889, 1997.
- [150] L. Zhi-Pei, “A model-based method for phase unwrapping,” *IEEE Transactions on Medical Imaging*, vol. 15, no. 6, pp. 893–897, 1996.
- [151] S. M.-H. Song, S. Napel, N. J. Pelc, and G. H. Glover, “Phase unwrapping of mr phase images using poisson equation,” *IEEE Transactions on Image Processing*, vol. 4, no. 5, pp. 667–676, 1995.
- [152] H. Yu, A. Shimakawa, C. A. McKenzie, E. Brodsky, J. H. Brittain, and S. B. Reeder, “Multiecho water-fat separation and simultaneous R<sup>2</sup> estimation with multifrequency fat spectrum modeling,” *Magnetic Resonance in Medicine*, vol. 60, no. 5, pp. 1122–1134, 2008.
- [153] C. D. Hines, H. Yu, A. Shimakawa, C. A. McKenzie, J. H. Brittain, and S. B. Reeder, “T1 independent, t2\* corrected mri with accurate spectral modeling for quantification of fat: Validation in a fat-water-spio phantom,” *Journal of Magnetic Resonance Imaging*, vol. 30, no. 5, pp. 1215–1222, 2009.
- [154] M. N. Diefenbach, S. Ruschke, H. Eggers, J. Meineke, E. J. Rummeny, and D. C. Karampinos, “Improving chemical shift encoding-based water-fat separation based on a detailed consideration of magnetic field contributions,” *Magnetic Resonance in Medicine*, vol. 80, no. 3, pp. 990–1004, 2018.
- [155] H. Yu, S. B. Reeder, A. Shimakawa, J. H. Brittain, and N. J. Pelc, “Field map estimation with a region growing scheme for iterative 3-point water-fat decomposition,” *Magnetic Resonance in Medicine*, vol. 54, no. 4, pp. 1032–1039, 2005.
- [156] C. Cui, X. Wu, J. D. Newell, and M. Jacob, “Fat water decomposition using globally optimal surface estimation (goose) algorithm,” *Magnetic Resonance in Medicine*, vol. 73, no. 3, pp. 1289–1299, 2015.
- [157] C. Cui, A. Shah, X. Wu, and M. Jacob, “A rapid 3d fat-water decomposition method using globally optimal surface estimation (r-goose),” *Magnetic Resonance in Medicine*, vol. 79, no. 4, pp. 2401–2407, 2018.

- 
- [158] D. Hernando, P. Kellman, J. P. Haldar, and Z.-P. Liang, "Robust water/fat separation in the presence of large field inhomogeneities using a graph cut algorithm," *Magn. Reson. Med.*, vol. 63, pp. 79–90, Jan. 2010.
- [159] C. Boehm, M. N. Diefenbach, M. R. Makowski, and D. C. Karampinos, "Improved body quantitative susceptibility mapping by using a variable-layer single-min-cut graph-cut for field-mapping," *Magnetic Resonance in Medicine*, vol. 85, no. 3, pp. 1697–1712, 2021.
- [160] J. Du, G. Hamilton, A. Takahashi, M. Bydder, and C. B. Chung, "Ultrashort echo time spectroscopic imaging (utesi) of cortical bone," *Magnetic Resonance in Medicine*, vol. 58, no. 5, pp. 1001–1009, 2007.
- [161] K. H. Su, H. T. Friel, J. W. Kuo, R. Al Helo, A. Baydoun, C. Stehning, A. N. Crisan, M. S. Traughber, A. Devaraj, D. W. Jordan, P. Qian, A. Leisser, R. J. Ellis, K. A. Herrmann, N. Avril, B. J. Traughber, and R. F. Muzic, "UTE-mDixon-based thorax synthetic CT generation," *Medical Physics*, vol. 46, no. 8, pp. 3520–3531, 2019.
- [162] P. Qian, J. Zheng, Q. Zheng, Y. Liu, T. Wang, R. Al Helo, A. Baydoun, N. Avril, R. J. Ellis, H. Friel, M. S. Traughber, A. Devaraj, B. Traughber, and R. F. Muzic, "Transforming UTE-mDixon MR Abdomen-Pelvis Images into CT by Jointly Leveraging Prior Knowledge and Partial Supervision," *IEEE/ACM Transactions on Computational Biology and Bioinformatics*, vol. 18, no. 1, pp. 70–82, 2021.
- [163] K. Gong, P. K. Han, K. A. Johnson, G. El Fakhri, C. Ma, and Q. Li, "Attenuation correction using deep Learning and integrated UTE/multi-echo Dixon sequence: evaluation in amyloid and tau PET imaging," *European Journal of Nuclear Medicine and Molecular Imaging*, vol. 48, no. 5, pp. 1351–1361, 2021.
- [164] K. H. Su, L. Hu, C. Stehning, M. Helle, P. Qian, C. L. Thompson, G. C. Pereira, D. W. Jordan, K. A. Herrmann, M. Traughber, R. F. Muzic, and B. J. Traughber, "Generation of brain pseudo-CTs using an undersampled, single-acquisition UTE-mDixon pulse sequence and unsupervised clustering," *Medical Physics*, vol. 42, no. 8, pp. 4974–4986, 2015.
- [165] A. P. Leynes, J. Yang, D. D. Shanbhag, S. S. Kaushik, Y. Seo, T. A. Hope, F. Wiesinger, and P. E. Z. Larson, "Hybrid zte/dixon mr-based attenuation correction for quantitative uptake estimation of pelvic lesions in pet/mri," *Med. Phys.*, vol. 44, pp. 902–913, Mar. 2017.
- [166] H. Yu, S. B. Reeder, C. A. McKenzie, A. C. Brau, A. Shimakawa, J. H. Brittain, and N. J. Pelc, "Single acquisition water-fat separation: Feasibility study for dynamic imaging," *Magnetic Resonance in Medicine*, vol. 55, no. 2, pp. 413–422, 2006.
- [167] J. Ma, "A single-point dixon technique for fat-suppressed fast 3D gradient-echo imaging with a flexible echo time," *Journal of Magnetic Resonance Imaging*, vol. 27, no. 4, pp. 881–890, 2008.
- [168] E. Haacke, R. Brown, M. Thompson, and V. R., *Magnetic Resonance Imaging: Physical Principles and Sequence Design*, ch. 14, pp. 297–324. John Wiley & Sons, Ltd, 2014.

- 
- [169] M. A. Bernstein, K. F. King, and X. J. Zhou, *Handbook of MRI Pulse Sequences*. Elsevier, 2004.
- [170] L. Feng, L. Axel, H. Chandarana, K. T. Block, D. K. Sodickson, and R. Otazo, “Xd-grasp: Golden-angle radial mri with reconstruction of extra motion-state dimensions using compressed sensing,” *Magnetic Resonance in Medicine.*, vol. 75, pp. 775–788, Feb. 2016.
- [171] X. Zhu, M. Chan, M. Lustig, K. M. Johnson, and P. E. Z. Larson, “Iterative motion-compensation reconstruction ultra-short te (imoco ute) for high-resolution free-breathing pulmonary mri,” *Magnetic Resonance in Medicine*, vol. 83, pp. 1208–1221, Apr. 2020.
- [172] Z.-P. Liang and P. C. Lauterbur, *Principles of magnetic resonance imaging*. SPIE Optical Engineering Press Bellingham, 2000.
- [173] A. Rosenfeld and A. Kak, “Digital picture processing,” *New York: Academic Press*, vol. 30, no. 4, pp. 694–695, 1988.
- [174] J. D. O’Sullivan, “A fast sinc function gridding algorithm for fourier inversion in computer tomography,” *IEEE Transactions on Medical Imaging*, vol. 4, no. 4, pp. 200–207, 1985.
- [175] J. Fessler and B. Sutton, “Nonuniform fast fourier transforms using min-max interpolation,” *IEEE Transactions on Signal Processing*, vol. 51, no. 2, pp. 560–574, 2003.
- [176] K. T. Block, H. Chandarana, S. Milla, M. Bruno, T. Mulholland, G. Fatterpekar, M. Hagiwara, R. Grimm, C. Geppert, B. Kiefer, and D. K. Sodickson, “Towards routine clinical use of radial stack-of-stars 3d gradient-echo sequences for reducing motion sensitivity,” *J Korean Soc Magnetic Resonance in Medicine*, vol. 18, pp. 87–106, June 2014.
- [177] J. G. Pipe, “Motion correction with propeller mri: Application to head motion and free-breathing cardiac imaging,” *Magnetic Resonance in Medicine.*, vol. 42, pp. 963–969, Nov. 1999.
- [178] S. B. Reeder, A. R. Pineda, Z. Wen, A. Shimakawa, H. Yu, J. H. Brittain, G. E. Gold, C. H. Beaulieu, and N. J. Pelc, “Iterative decomposition of water and fat with echo asymmetry and least-squares estimation (ideal): Application with fast spin-echo imaging,” *Magnetic Resonance in Medicine.*, vol. 54, pp. 636–644, Sept. 2005.
- [179] T. Benkert, L. Feng, D. K. Sodickson, H. Chandarana, and K. T. Block, “Free-breathing volumetric fat/water separation by combining radial sampling, compressed sensing, and parallel imaging,” *Magnetic Resonance in Medicine.*, vol. 78, pp. 565–576, Aug. 2017.
- [180] K. P. Pruessmann, “Encoding and reconstruction in parallel mri,” *NMR Biomed.*, vol. 19, pp. 288–299, May 2006.
- [181] N. Seiberlich, F. A. Breuer, M. Blaimer, K. Barkauskas, P. M. Jakob, and M. A. Griswold, “Non-cartesian data reconstruction using grappa operator gridding (grog),” *Magnetic Resonance in Medicine.*, vol. 58, pp. 1257–1265, Dec. 2007.
- [182] M. Lustig, D. Donoho, and J. M. Pauly, “Sparse mri: The application of compressed sensing for rapid mr imaging,” *Magnetic Resonance in Medicine.*, vol. 58, pp. 1182–1195, Dec. 2007.

- 
- [183] L. Feng, R. Grimm, K. T. Block, H. Chandarana, S. Kim, J. Xu, L. Axel, D. K. Sodickson, and R. Otazo, “Golden-angle radial sparse parallel mri: Combination of compressed sensing, parallel imaging, and golden-angle radial sampling for fast and flexible dynamic volumetric mri,” *Magnetic Resonance in Medicine*, vol. 72, pp. 707–717, Sept. 2014.
- [184] L. Wan, W. Zhao, Y. Ma, S. Jerban, A. C. Searleman, M. Carl, E. Y. Chang, G. Tang, and J. Du, “Fast quantitative 3d ultrashort echo time mri of cortical bone using extended cones sampling,” *Magnetic Resonance in Medicine*, vol. 82, pp. 225–236, July 2019.
- [185] S. Kronthaler, J. Rahmer, P. Börnert, M. R. Makowski, B. J. Schwaiger, A. S. Gersing, and D. C. Karampinos, “Trajectory correction based on the gradient impulse response function improves high-resolution UTE imaging of the musculoskeletal system,” *Magnetic Resonance in Medicine*, vol. 85, no. 4, pp. 2001–2015, 2021.
- [186] S. Kronthaler, C. Boehm, G. Feuerriegel, P. Börnert, U. Katscher, K. Weiss, M. R. Makowski, B. J. Schwaiger, A. S. Gersing, and D. C. Karampinos, “Assessment of vertebral fractures and edema of the thoracolumbar spine based on water-fat and susceptibility-weighted images derived from a single ultra-short echo time scan,” *Magnetic Resonance in Medicine*, 2021.
- [187] S. Kronthaler, M. N. Diefenbach, C. Boehm, M. Zamskiy, M. R. Makowski, T. Baum, N. Sollmann, and D. C. Karampinos, “On quantification errors of  $r_2^*$  and proton density fat fraction mapping in trabecularized bone marrow in the static dephasing regime,” *Magnetic Resonance in Medicine*, vol. 88, no. 3, pp. 1126–1139, 2022.
- [188] P. Jehenson, M. Westphal, and N. Schuff, “Analytical method for the compensation of eddy-current effects induced by pulsed magnetic field gradients in nmr systems,” *Journal of Magnetic Resonance (1969)*, vol. 90, pp. 264–278, Nov. 1990.
- [189] J. J. Van Vaals and A. H. Bergman, “Optimization of eddy-current compensation,” *Journal of Magnetic Resonance (1969)*, vol. 90, no. 1, pp. 52–70, 1990.
- [190] R. E. Wysong, D. P. Madio, and I. J. Lowe, “A novel eddy current compensation scheme for pulsed gradient systems,” *Magnetic Resonance in Medicine*, vol. 31, pp. 572–575, May 1994.
- [191] P. B. Roemer and J. S. Hickey, “Self-shielded gradient coils for nuclear magnetic resonance imaging,” U.S. Patent 4737716, 1988.
- [192] R. Bowtell and P. Mansfield, “Gradient coil design using active magnetic screening,” *Magnetic Resonance in Medicine*, vol. 17, pp. 15–21, Jan. 1991.
- [193] E. K. Brodsky, A. A. Samsonov, and W. F. Block, “Characterizing and correcting gradient errors in non-Cartesian imaging: Are gradient errors Linear Time-Invariant (LTI)?,” *Magnetic Resonance in Medicine*, vol. 62, no. 6, pp. 1466–1476, 2009.
- [194] Q. Liu, D. G. Hughes, and P. S. Allen, “Quantitative characterization of the eddy current fields in a 40-cm bore superconducting magnet,” *Magnetic Resonance in Medicine*, vol. 31, pp. 73–76, Jan. 1994.

- 
- [195] T. Onodera, S. Matsui, K. Sekihara, and H. Kohno, “A method of measuring field-gradient modulation shapes. application to high-speed nmr spectroscopic imaging,” *Journal of Physics E: Scientific Instruments*, vol. 20, pp. 416–419, Apr. 1987.
- [196] N. G. Papadakis, A. A. Wilkinson, T. A. Carpenter, and L. D. Hall, “A general method for measurement of the time integral of variant magnetic field gradients: Application to 2d spiral imaging,” *Magnetic Resonance Imaging*, vol. 15, pp. 567–578, Jan. 1997.
- [197] C. Barmet, N. D. Zanche, and K. P. Pruessmann, “Spatiotemporal magnetic field monitoring for mr,” *Magnetic Resonance in Medicine*, vol. 60, pp. 187–197, July 2008.
- [198] S. J. Vannesjo, M. Haerberlin, L. Kasper, M. Pavan, B. J. Wilm, C. Barmet, and K. P. Pruessmann, “Gradient system characterization by impulse response measurements with a dynamic field camera,” *Magnetic Resonance in Medicine*, vol. 69, no. 2, pp. 583–593, 2013.
- [199] A. E. Campbell-Washburn, H. Xue, R. J. Lederman, A. Z. Faranesh, and M. S. Hansen, “Real-time distortion correction of spiral and echo planar images using the gradient system impulse response function,” *Magnetic Resonance in Medicine*, vol. 75, no. 6, pp. 2278–2285, 2016.
- [200] M. Stich, T. Wech, A. Slawig, R. Ringler, A. Dewdney, A. Greiser, G. Ruyters, T. A. Bley, and H. Köstler, “Gradient waveform pre-emphasis based on the gradient system transfer function,” *Magnetic Resonance in Medicine*, vol. 80, no. 4, pp. 1521–1532, 2018.
- [201] J. Rahmer, P. Mazurkewitz, P. Börnert, and T. Nielsen, “Rapid acquisition of the 3D MRI gradient impulse response function using a simple phantom measurement,” *Magnetic Resonance in Medicine*, vol. 82, pp. 2146–2159, Dec. 2019.
- [202] K. J. Lee, M. N. Paley, P. D. Griffiths, and J. M. Wild, “Method of generalized projections algorithm for image-based reduction of artifacts in radial imaging,” *Magnetic Resonance in Medicine*, vol. 54, no. 1, pp. 246–250, 2005.
- [203] A. P. Aitken, D. Giese, C. Tsoumpas, P. Schleyer, S. Kozerke, C. Prieto, and T. Schaeffter, “Improved UTE-based attenuation correction for cranial PET-MR using dynamic magnetic field monitoring,” *Medical Physics*, vol. 41, no. 1, p. 12302, 2014.
- [204] J. F. Magland, H. Saligheh-Rad, and F. W. Wehrli, “Correcting for gradient imperfections in ultra-short echo time imaging,” *In Proceedings of the 18th Scientific Meeting of ISMRM, Sweden, Stockholm, p. 3102*, vol. 50, no. 1, p. 50068, 2010.
- [205] I. C. Atkinson, A. Lu, and K. R. Thulborn, “Characterization and correction of system delays and eddy currents for MR imaging with ultrashort echo-time and time-varying gradients,” *Magnetic Resonance in Medicine*, vol. 62, no. 2, pp. 532–537, 2009.
- [206] M. Stich, L. Pereira, T. Wech, A. Weng, R. Ringler, and T. Bley, “Trajectory correction for a 3D-ultrashort echo time (UTE) sequence using the gradient system transfer function,” *In Proceedings of the 26th Annual Meeting of ISMRM, Paris, France, p. 0941*, 2018.
- [207] X. Zhao, H. Lee, H. K. Song, C. C. Cheng, and F. W. Wehrli, “Impact of gradient imperfections on bone water quantification with UTE MRI,” *Magnetic Resonance in Medicine*, vol. 84, no. 4, pp. 2034–2047, 2020.



- 
- [208] H. Lee, X. Zhao, H. K. Song, and F. W. Wehrli, “Self-Navigated Three-Dimensional Ultrashort Echo Time Technique for Motion-Corrected Skull MRI,” *IEEE Transactions on Medical Imaging*, vol. 39, no. 9, pp. 2869–2880, 2020.
- [209] G. Krinsky, N. M. Rofsky, and J. C. Weinreb, “Nonspecificity of short inversion time inversion recovery (stir) as a technique of fat suppression: pitfalls in image interpretation.,” *American Journal of Roentgenology*, vol. 166, pp. 523–526, Mar. 1996.
- [210] E. Kaldoudi, S. C. R. Williams, G. J. Barker, and P. S. Tofts, “A chemical shift selective inversion recovery sequence for fat-suppressed mri: Theory and experimental validation,” *Magnetic Resonance Imaging*, vol. 11, pp. 341–355, Jan. 1993.
- [211] X. Wang, D. Hernando, and S. B. Reeder, “Sensitivity of chemical shift-encoded fat quantification to calibration of fat mr spectrum,” *Magn. Reson. Med.*, vol. 75, pp. 845–851, Feb. 2016.
- [212] H. Yu, C. A. McKenzie, A. Shimakawa, A. T. Vu, A. C. S. Brau, P. J. Beatty, A. R. Pineda, J. H. Brittain, and S. B. Reeder, “Multiecho reconstruction for simultaneous water-fat decomposition and  $t_2^*$  estimation,” *J. Magn. Reson. Imaging*, vol. 26, pp. 1153–1161, Oct. 2007.
- [213] H. Jang, A. von Drygalski, J. Wong, J. Y. Zhou, P. Aguero, X. Lu, X. Cheng, S. T. Ball, Y. Ma, E. Y. Chang, and J. Du, “Ultrashort echo time quantitative susceptibility mapping (UTE-QSM) for detection of hemosiderin deposition in hemophilic arthropathy: A feasibility study,” *Magnetic Resonance in Medicine*, vol. 84, no. 6, pp. 3246–3255, 2020.
- [214] A. V. Dimov, Z. Liu, P. Spincemaille, M. R. Prince, J. Du, and Y. Wang, “Bone quantitative susceptibility mapping using a chemical species-specific signal model with ultrashort and conventional echo data,” *Magn. Reson. Med*, vol. 79, pp. 121–128, Jan. 2018.
- [215] C. B. Ahn, S. Y. Lee, O. Nalcioglu, and Z. H. Cho, “Spectroscopic imaging by quadrature modulated echo time shifting,” *Magnetic Resonance Imaging*, vol. 4, p. 110, Jan. 1986.
- [216] P. JL, H. EM, and H. JE, “Water/fat separation and chemical shift artifact correction using a single scan,” *In Proceedings of the 4th Annual Scientific Meeting of the Society of Magnetic Resonance of Medicine, New York, NY, USA. p 174–175.*, 1985.
- [217] P. Z, “Separate water and lipids images obtained by a single scan.,” *In Proceedings of the 4th Annual Scientific Meeting of the Society of Magnetic Resonance of Medicine, New York, NY, USA. p 172–173.*, 1985.
- [218] S. Majumdar, “Quantitative study of the susceptibility difference between trabecular bone and bone marrow: Computer simulations,” *Magnetic Resonance in Medicine*, vol. 22, no. 1, pp. 101–110, 1991.
- [219] S. Majumdar, M. Kothari, P. Augat, D. C. Newitt, T. M. Link, J. C. Lin, T. Lang, Y. Lu, and H. K. Genant, “High-resolution magnetic resonance imaging: Three-dimensional trabecular bone architecture and biomechanical properties,” *Bone*, vol. 22, pp. 445–454, May 1998.

- [220] S. Majumdar, D. Newitt, A. Mathur, D. Osman, A. Gies, E. Chiu, J. Lotz, J. Kinney, and H. Genant, “Magnetic resonance imaging of trabecular bone structure in the distal radius: Relationship with x-ray tomographic microscopy and biomechanics,” *Osteoporosis International*, vol. 6, pp. 376–385, Sept. 1996.
- [221] X. Ouyang, K. Selby, P. Lang, K. Engelke, C. Klifa, B. Fan, F. Zucconi, G. Hottya, M. Chen, S. Majumdar, and H. K. Genant, “High resolution magnetic resonance imaging of the calcaneus: Age-related changes in trabecular structure and comparison with dual x-ray absorptiometry measurements,” *Calcified Tissue International*, vol. 60, pp. 139–147, Feb. 1997.
- [222] H.-W. Chung, F. W. Wehrli, J. L. Williams, and S. L. Wehrli, “Three-dimensional nuclear magnetic resonance microimaging of trabecular bone,” *J Bone Miner Res*, vol. 10, pp. 1452–1461, Oct. 1995.
- [223] J. P. Kühn, D. Hernando, P. J. Meffert, S. Reeder, N. Hosten, R. Laqua, A. Steveling, S. Ender, H. Schröder, and D. T. Pillich, “Proton-density fat fraction and simultaneous R2\*estimation as an MRI tool for assessment of osteoporosis,” *European Radiology*, vol. 23, no. 12, pp. 3432–3439, 2013.
- [224] T. Baum, S. P. Yap, M. Dieckmeyer, S. Ruschke, H. Eggers, H. Kooijman, E. J. Rummeny, J. S. Bauer, and D. C. Karampinos, “Assessment of whole spine vertebral bone marrow fat using chemical shift-encoding based water-fat mri,” *J. Magn. Reson. Imaging*, vol. 42, pp. 1018–1023, Oct. 2015.
- [225] S. Ruschke, H. Eggers, H. Kooijman, M. N. Diefenbach, T. Baum, A. Haase, E. J. Rummeny, H. H. Hu, and D. C. Karampinos, “Correction of phase errors in quantitative water-fat imaging using a monopolar time-interleaved multi-echo gradient echo sequence,” *Magnetic Resonance in Medicine*, vol. 78, no. 3, pp. 984–996, 2017.
- [226] S. Ruschke, J. Syväri, M. Dieckmeyer, D. Junker, M. R. Makowski, T. Baum, and D. C. Karampinos, “Physiological variation of the vertebral bone marrow water T2 relaxation time,” *NMR in Biomedicine*, vol. 34, no. 2, p. e4439, 2021.
- [227] H. Chung, F. W. Wehrli, J. L. Williams, and S. D. Kugelmass, “Relationship between NMR transverse relaxation, trabecular bone architecture, and strength,” *Proceedings of the National Academy of Sciences of the United States of America*, vol. 90, no. 21, pp. 10250–10254, 1993.
- [228] H. Z. Wu, X. F. Zhang, S. M. Han, L. Cao, J. X. Wen, W. J. Wu, and B. L. Gao, “Correlation of bone mineral density with MRI T2\* values in quantitative analysis of lumbar osteoporosis,” *Archives of Osteoporosis*, vol. 15, no. 1, p. 18, 2020.
- [229] Y. Gao, O. Wang, W. Guan, X. Wu, J. Mao, X. Wang, W. Yu, and M. Nie, “Bone mineral density and trabecular bone score in patients with 21-hydroxylase deficiency after glucocorticoid treatment,” *Clinical Endocrinology*, vol. 94, no. 5, pp. 765–773, 2021.
- [230] J. C. Ford, F. W. Wehrli, and H.-W. Chung, “Magnetic field distribution in models of trabecular bone,” *Magn. Reson. Med.*, vol. 30, pp. 373–379, Sept. 1993.

- [231] D. A. Yablonskiy and E. M. Haacke, "Theory of NMR signal behavior in magnetically inhomogeneous tissues: The static dephasing regime," *Magnetic Resonance in Medicine*, vol. 32, no. 6, pp. 749–763, 1994.
- [232] D. A. Yablonskiy, "Quantitation of intrinsic magnetic susceptibility-related effects in a tissue matrix. Phantom study," *Magnetic Resonance in Medicine*, vol. 39, no. 3, pp. 417–428, 1998.
- [233] H. K. Song, F. W. Wehrli, and J. Ma, "Field strength and angle dependence of trabecular bone marrow transverse relaxation in the calcaneus," *Journal of Magnetic Resonance Imaging*, vol. 7, no. 2, pp. 382–388, 1997.
- [234] P. Storey and D. S. Novikov, "Signatures of microstructure in  $R_2^*$  decay : defining the limits of the weak field approximation," *In Proceedings of the 28th Scientific Meeting of ISMRM, Virtual Conference, p. 3102*, vol. 12, pp. 7–10, 2020.
- [235] C. Ganter, "Static susceptibility effects in balanced SSFP sequences," *Magnetic Resonance in Medicine*, vol. 56, no. 3, pp. 687–691, 2006.
- [236] T. Boucneau, P. Cao, S. Tang, M. Han, D. Xu, R. G. Henry, and P. E. Larson, "In vivo characterization of brain ultrashort-T2 components," *Magnetic Resonance in Medicine*, vol. 80, no. 2, pp. 726–735, 2018.
- [237] D. Hernando, J. P. Haldar, B. P. Sutton, J. Ma, P. Kellman, and Z.-P. Liang, "Joint estimation of water/fat images and field inhomogeneity map," *Magn. Reson. Med.*, vol. 59, pp. 571–580, Mar. 2008.
- [238] J. Dong, T. Liu, F. Chen, D. Zhou, A. Dimov, A. Raj, Q. Cheng, P. Spincemille, and Y. Wang, "Simultaneous phase unwrapping and removal of chemical shift (spurs) using graph cuts: Application in quantitative susceptibility mapping," *IEEE Transactions on Medical Imaging*, vol. 34, no. 2, pp. 531–540, 2015.
- [239] D. C. Karampinos, S. Ruschke, M. Dieckmeyer, H. Eggers, H. Kooijman, E. J. Rummeny, J. S. Bauer, and T. Baum, "Modeling of  $T_2^*$  decay in vertebral bone marrow fat quantification," *NMR in Biomedicine*, vol. 28, no. 11, pp. 1535–1542, 2015.
- [240] C. Zöllner, S. Kronthaler, S. Ruschke, H. Eggers, J. Rahmer, P. Börnert, R. Braren, D. Franz, and D. Karampinos, "Correcting gradient chain-induced fat quantification errors in multi-echo SoS acquisition using the gradient impulse response function," *In Proceedings of the 28th Scientific Meeting of ISMRM, Virtual Conference, p. 517*, 2020.
- [241] S. Kronthaler, G. Feuerriegel, C. Boehm, A. S. Gersing, B. J. Schwaiger, K. Weiss, and D. C. Karampinos, "On the robustness of single ute-dixon for simultaneous short  $t_2^*$ , water and fat imaging across skeletal anatomies," *In Proceeding of the 31th Scientific Meeting of ISMRM, UK, London, p. 6791*, 2022.
- [242] U. Katscher and C. A. van den Berg, "Electric properties tomography: Biochemical, physical and technical background, evaluation and clinical applications," *NMR in Biomedicine*, vol. 30, no. 8, 2017.
- [243] D. H. Kim, N. Choi, S. M. Gho, J. Shin, and C. Liu, "Simultaneous imaging of in vivo conductivity and susceptibility," *Magnetic Resonance in Medicine*, vol. 71, no. 3, pp. 1144–1150, 2014.

- [244] A. L. Van Lier, D. O. Brunner, K. P. Pruessmann, D. W. Klomp, P. R. Luijten, J. J. Lagendijk, and C. A. Van Den Berg, “B1+ phase mapping at 7 T and its application for in vivo electrical conductivity mapping,” *Magnetic Resonance in Medicine*, vol. 67, no. 2, pp. 552–561, 2012.
- [245] S. Gabriel, R. W. Lau, and C. Gabriel, “The dielectric properties of biological tissues: III. Parametric models for the dielectric spectrum of tissues,” *Physics in Medicine and Biology*, vol. 41, no. 11, pp. 2271–2293, 1996.
- [246] A. M. Afsahi, Y. Ma, H. Jang, S. Jerban, C. B. Chung, E. Y. Chang, and J. Du, “Ultrashort echo time magnetic resonance imaging techniques: Met and unmet needs in musculoskeletal imaging,” *J Magn Reson Imaging*, vol. n/a, Dec. 2021.
- [247] R. Krug, P. E. Z. Larson, C. Wang, A. J. Burghardt, D. A. C. Kelley, T. M. Link, X. Zhang, D. B. Vigneron, and S. Majumdar, “Ultrashort echo time mri of cortical bone at 7 tesla field strength: A feasibility study,” *J. Magn. Reson. Imaging*, vol. 34, pp. 691–695, Sept. 2011.